THE EFFECTS OF THE BACK CLEARANCE SIZE AND THE BALANCE HOLES ON THE BACK CLEARANCE FLOW OF THE CENTRIFUGAL PUMP WITH SEMI-OPEN IMPELLER

A Dissertation

by

SANG HYUN PARK

Submitted to the Office of Graduate Studies of
Texas A&M University
in partial fulfillment of the requirements for the degree of

DOCTOR OF PHILOSOPHY

December 2008

Major Subject: Mechanical Engineering

THE EFFECTS OF THE BACK CLEARANCE SIZE AND THE BALANCE HOLES ON THE BACK CLEARANCE FLOW OF THE CENTRIFUGAL PUMP WITH SEMI-OPEN IMPELLER

A Dissertation

by

SANG HYUN PARK

Submitted to the Office of Graduate Studies of
Texas A&M University
in partial fulfillment of the requirements for the degree of

DOCTOR OF PHILOSOPHY

Approved by:

Chair of Committee,	Gerald L. Morrison
Committee Members,	Je Chin Han
	N. K. Anand
	Robert Randall
Head of Department,	Dennis L. O'Neal

December 2008

Major Subject: Mechanical Engineering

ABSTRACT

The Effects of the Back Clearance Size and the Balance Holes on the Back Clearance Flow of the Centrifugal Pump with Semi-Open Impeller. (December 2008)

Sang Hyun Park, B.S., Yonsei University, Korea;

M.S., Texas A&M University

Chair of Advisory Committee: Dr. Gerald Morrison

Conventionally the size of the back clearance played a great importance on reducing the axial clearance by utilizing the concept that the decreased axial clearance results in lower axial force acting on the impeller. However, from the previous works on the effect of the back clearance on the hydrodynamic forces upon the semi-open impeller showed the opposite trend: increasing the back clearance results in the reduced axial loading. In this work, the computational fluid dynamics (CFD) simulation of an entire pump and detailed analysis on the back clearance flow are performed.

By utilizing the commercially available software, meshing and CFD simulations are performed. LDA data, unsteady pressure data, and pressure distributions on the housing are used to validate the CFD model. The flow field prediction of the back clearance flow is then compared with other researcher's works of the gap flow analysis between the rotating and stationary disks. The flow field inside the impeller passage, which is very sensitive to the back clearance size, is also studied. The empirical equation for the leakage loss through the balance holes is produced using the CFD predictions.

DEDICATION

To my loving parents and my lovely wife

ACKNOWLEDGEMENTS

I would like to thank my committee chair, Dr. Gerald Morrison, and my committee members, Dr. Han, Dr. Anand, and Dr. Randall, for their guidance and support throughout the course of this research.

Thanks also go to Won Pill Lee and Ji Sun Lee. Without their support, I could not accomplish this.

Thanks to Dr. Arun Suryanarayanan, Dr. Ahmed Gamal, and Dr. Adolfo Delgado.

NOMENCLATURE

A	Area
β	Tangential velocity of fluid
β_r	Non-dimensional radial velocity
β_θ	Non-dimensional tangential velocity
C_μ	Friction coefficient
γ	Specific weight
d_b	Diameter of balance hole (0.0067m)
E	Gap ratio of the axial clearance to the radius of the imepller
g	Gravitational acceleration
ΔH	Head drop (m)
H_p	Static head (m)
H_v	Velocity head or dynamic head (m)
H_{EU}	Euler head (m)
h	Impeller blade height (0.022 m)
η	Efficiency of the pump
θ	Angular position in polar coordinate
K_p	Turbulent kinetic energy
L	Head loss (m)
μ	Viscosity
ν	Kinetic viscosity
$\overline{P}$	Time-averaged pressure
ΔP	Pressure drop
ΔP_b	Pressure drop across the inlet and the outlet of the balance hole

P_t	Total pressure (Pa)
$P_{t,in}$	Total pressure supply (Pa)
Q	Flow rate through the pump (liter/sec)
Q_b	Flow rate through the balance hole (liter/sec)
Q_s	Flow coefficient through the pump
$Q_{s,b}$	Flow coefficient through the balance hole
ρ	Density (kg/m^3)
r_o	The radius of the impeller (0.17 m)
s	Axial clearance (m)
T	Torque (N·m)
U	Impeller velocity at the radial position (m/s)
U_2	Impeller velocity at the periphery of the impeller (m/s)
u'	X velocity fluctuation
v'	Y velocity fluctuation
φ	Flow coefficient
V_θ	Tangential velocity (m/s)
V_m	Meridional velocity (m/s)
V_x	Velocity in x-direction (m/s)
V_y	Velocity in y-direction (m/s)
V_z	Velocity in z-direction (m/s)
V_x'	Relative velocity in x-direction (m/s)
V_y'	Relative velocity in y-direction (m/s)
W	Relative velocity vector
W_m	Meridional relative velocity (m/s)

Ψ	Angular position of the window for LDA measurement (either 45˚ or -
ψ	Head coefficient
X	Head coefficient for balance hole
y^*	Wall function parameter
y_p	Distance from the wall in normal direction
Z	Z coordinate
Ω	Angular velocity of the impeller (146.6 rad/sec)

TABLE OF CONTENTS

Page

Page

LIST OF FIGURES

Page

Page

LIST OF TABLES

Page

I INTRODUCTION

Pumps are subject to various kinds of forces and torques which are generated by motions within the pump. Of all contributors to the loads acting upon the pump, hydrodynamic forces due to pressure fluctuations and mean pressure imbalances inside the pump and the rotordynamic forces due to the imbalance are the major elements. The impeller or the shaft is prone to fatigue failure under the influence of the following hydrodynamic loadings.

1. pressure difference between the front and the back of the impeller
2. momentum change taking place at the inlet portion of the impeller
3. pressure imbalance on the impeller blades
4. pressure pulsation from the rotor-stator interaction

The first and second contributors are called axial loading. This axial loading imposes high levels of stress on the bearing or the seal components of the pump. The third contributor acts as a form of torque on the impeller and the shaft. Dynamic torque can inflict fatigue failure on the impeller shaft. The fourth element of hydrodynamic loading is sometimes called “noise”.

It has been a dominant opinion that increasing back clearance increases axial thrust in a centrifugal pump. However, from Hossain’s (2002) work, it was determined that, for an open faced impeller with a fixed front clearance, axial thrust is reduced by increasing the back clearance at on and off design conditions. By maintaining a constant front clearance, the pumps performance remained the same for all back clearances when no balance holes were present. Hossain’s work showed that decreasing the back clearance of an open faced impeller increased the axial loading of

This dissertation follows the style of Journal of Fluids and Structures.

the shaft up to 23%. While other researchers maintained the total sum of front and back clearance, thereby changing the pumps performance Hossain increased the back clearance and maintained the front clearance, which results in an increase of the total clearance. Moreover, the pump Hossain had used in his experiment had no balancing chamber, while previous researchers utilized semi-open or double shrouded pumps with balancing chambers. Portions of the back shroud had been removed as an alternative form of balancing the axial thrust. All of these configurations are commonly found in industrial pumps, but complicated leakage flow, flow over the cut away, and any balance holes make the hydrodynamic analysis very difficult without 3-D CFD analysis.

The noise, unsteady pressure pulsation, can cause a cyclic loading on the impeller shaft which will lead to fatigue failure. The pressure fluctuation is caused by several factors such as rotordynamic instability and the interaction between the tongue of the volute (the cutwater) and the rotating impeller tips (blade passing frequency and its multiple harmonics). There are ample possibilities that one of these frequencies from the pressure fluctuation can excite the natural frequency of the pump or pipeline. Hossain measured unsteady pressure fluctuations on various locations inside the pump. He found that, in power spectrum plots, larger back clearance and balance holes reduce the amplitude of the pressure fluctuation and reduced higher harmonics.

A Axial Thrust in the Centrifugal Pumps

Polhemus et al. (1929) identified sources of axial thrust in dredge pumps, which are the forces acting on the front and back of the shroud and the vacuum created by the

pump at the inlet portion. Stepanoff (1932) conducted a series of experiments where the axial thrust and leakage flow in centrifugal pumps were observed. In his work, he tried to explain the phenomenon which affects the axial trust and head loss due to the leakage flow. He suggested that two factors contributing to the axial thrust were pressure acting on the shroud of the impeller due to the radial velocity difference between the upper shroud and the bottom shroud (hub) along the streamlines and the second factor was cavitation. The former factor is mainly due to the momentum change brought about by the 90-degree turn at the inlet position. Brkich (1946) summarized the means by which axial thrust in single-stage centrifugal pumps is reduced. He pointed out that inlet suction pressure plays a significant role in generating axial thrust.

The flow field inside the pump with a semi-open faced impeller is significantly different than that of a pump with the double shrouded impeller in that the flow at the front clearance interacts with the flow inside the impeller passages. The more in-depth research on axial thrust specifically on semi-open impeller was conducted by Thorne (1973). He predicted the pressure distribution on the back of the impeller based upon the assumption of tangential velocity ratio (β/ω) (tangential velocity of the fluid between the back clearance to that of the impeller at a given radius) being the same at any given position on the back and the front of the impeller. He also conducted a series of experiments on the axial thrust while changing the back clearance and modifying the impeller by adding balance holes and cutaways on the back shroud. He measured the pressure distribution on the back of the shroud and concluded that increasing β/ω by any means, such as back vanes, results in a more abrupt decrease in pressure head and

lower pressures acting on the back of the impeller. However, his measurements were made using an impeller with back vanes. These vanes create a more controlled pressure distribution due to the forced vortex motion caused by the back vanes compared to the case without back vanes. He pointed out that, from several experimental results, front clearance plays a less significant role in changing axial thrust without providing a detailed physical explanation.

Gyulai and Popoviciu (1975) derived an equation for β/ω as function of radial position (r) and compared their results with experimental data. The β/ω ratio is important in that this parameter is directly related to the pressure distribution on the back of the impeller. According to simple Couette flow theory, the β/ω ratio of the fluid between two walls is 0.5: the velocity of fluid is a half of that of sliding boundary. However, the flow between the back shroud and the casing of the pump is much more complicated than simple Couette flow, and requires a more in-depth analysis. Gyulai and Popoviciu suggested that β/ω is a function of radial position (r) whenever the flow rate through the pump is not zero and β/ω is simply 0.5 for no flow through the pump. Using the relationship for β/ω, they derived an equation for the pressure coefficient within the clearance under the assumptions: constant wall friction coefficient and no secondary flow within the clearance (entire flow is either centrifugal or centripetal). Gyulai and Popoviciu based their bulk flow assumption on the fact that the flow inside the clearance is fully turbulent flow. They have discovered that pressure difference between the fixed wall and the rotating wall at the same radius was up to 20%, which indicates the presence of a secondary flow. They concluded that there is secondary

flow inside the clearance and this secondary flow creates severe discrepancies between the experimental data and theoretical β/ω values from their equation. They also claimed that the axial increase of the clearance increases the effect of secondary flow based upon the fact that increasing the clearance decreases the β/ω ratio, which agrees with Thorne's results.

Kurokawa et al. (1994) performed a theoretical analysis to acquire the axial thrust of the LOX pump of a rocket engine. This turbo pump utilized a self-balancing mechanism such as balancing pistons (one near the radial tip of the impeller and another one at the gap near the shaft on the back of the impeller) and balance holes. The back clearance acted as a spring for the impeller to stabilize itself into pressure equilibrium in the axial direction (zero axial thrust). They set up a momentum conservation equation (lateral and circumferential) and a continuity equation on a gap flow at the balancing pistons. Then using the precise boundary conditions and a couple of correction equations necessary due to the geometry of the balance pistons and the bolt grooves, they calculated the velocity of the gap flow, and the pressure. They pointed out that the most influential parameters on the axial thrust are the leakage parameter, the tangential velocity ratio of the leakage before entering the gap, the axial space ratio, the relative surface roughness, and the Reynolds number. They found that the axial thrust increased as the back clearance increased. The change of the back clearance was made by moving the impeller in the axial direction inside the housing, which is different than that of Hossain in that Hossain changed the back clearance by moving the impeller and the back casing closer together.

B Rotor-Stator Interaction

Dean et al. (1960) developed a theoretical model of the flow at the exit of an impeller. According to Dean and previous investigators, flow at the exit consists of jet and wake regions: the jet being near the pressure side and the wake being near the suction side of the impeller vane. In their work, they developed equations of momentum and total pressure distribution as a function of the radial coordinate, and predicted that distortion due to the jet and wake flows can significantly affect the flow in a vaneless diffuser. Chu (1995a, 1995b) observed in their experimental investigation that a series of vortex trains developed from the jet and wake interactions with the volute tongue (diffuser tip of a vane less diffuser). Other researchers have developed theoretical models of noise generation from simplified 2-D models of pumps. Kubota et al. (1983) setup a theoretical model that can predict the pressure fluctuation at an arbitrary point on the impeller caused by rotor-stator interaction by using a simple vibration model without applying any hydrodynamics. Based upon Kubota's work, Bolleter (1988) analyzed vibration characteristics such as blade passage tone and its harmonics using simple Fourier series decomposition of pressure fluctuation. In his work, he suggested a method of calculating frequencies and the rotational speed of vibration force vectors in terms of the number of the impeller and the diffuser blades.

Guelich et al. (1992) performed a series of case studies on pressure pulsations inside pumps. They pointed out that measurement of the pressure at the suction or the outlet pipe will not show the actual pressure fluctuations inside the pump. They collected statistical data and performed case studies on pressure pulsations instead of

performing theoretical or empirical analysis on a particular pump. They concluded that the pressure pulsation is caused by several design factors which can not be predicted by a single theoretical approach. The general characteristics of the pressure pulsations are due to several design factors such as impeller geometry, pumping system's configuration, and types of impeller (i.e. specific speed). The results are summarized in their work.

The potential adverse effect of pressure pulsations at the blade-passing frequency have been studied by Rzentkowski (1996) as he performed experimental studies on a whole piping system's resonance characteristics at the blade passing frequency. He also summarized the different kinds of acoustic sources found in the centrifugal pumps. More fundamental studies on the noise or the pressure pulsation due to the rotor-stator interaction were performed by Langthjem et al. (2004a, 2004b). In their work, they categorized the vortices inside the pump as free vortices shed from the impeller blades, source panels (casing surfaces including volute tongue), and the bound vortices created from impeller blade surfaces. They modeled the behavior of these vortices with a 2-D computational model using the discrete vortex model (DVM). The rotor-stator interaction was simulated with the interaction between the free vortices and the source panel. From their analysis, the pressure fluctuation could be calculated. Their theoretical DVM was in good agreement with the experimental data on ducted and un-ducted fans with air as the medium. However, due to slower dissipation of kinetic energy of the pressure wave in water, the prediction of the behavior of the wave in the centrifugal pump resulted in poorer agreement with experimental data. They

concluded that this poor agreement is caused by the fact that the flow disturbance due to the reflection of waves from the walls inside the pump is much stronger than in the fan.

Gonzalez et al. (2002) conducted a series of CFD analyses on rotor-stator interaction with the same CFD tool (Fluent) as used in this work. They compared unsteady pressure fluctuation data from an experiment with the CFD results. They installed 36 pressure transducers along the circumference of the pump at the impeller radius. They compared the unsteady data at the blade passing frequency with CFD data and determined that there is a special (in terms of angular coordinate) pressure fluctuation pattern. They also simulated fluid-solid interactions by utilizing 3D-FEM models of the pump structures. Pavesi et al. (2005) conducted a series of experiments and numerical simulations using commercial CFD software (CFX 2.12) to investigate rotor-stator interaction. The resulting pressure and velocity data correlation and coherence calculation between inlet and outlet of the impeller were quiet meaningful in that stall phenomenon, which occurred during off-design loading of the pump, was found to be related to the jet-wake phenomenon

C CFD and Its Validation

Although numerical analyses of pumps date back to the 1970s, numerical analyses that utilize 3-D turbulent RANs scheme began in the late 1990s. Specifically for semi-open impellers, Cao et al. (1998) conducted a CFD analysis. Other than RANs scheme, Byskov et al. (2003) used a Large Eddy Simulation (LES) scheme for the flow field analysis of an impeller. Benra et al. (2004) conducted CFD simulations of a 3-D

model of a centrifugal pump using commercial software and compared their results with experimental data. In Gonzalez et al. (2006), they tried to confirm the presence of a secondary flow inside the volute by investigating the helicity which accounts for the transport of the vorticity. Before doing so, the "global variables" such as head, required power, and efficiencies, computed using CFD were compared to experimental data. There was a slight underestimation on the required power, but the time averaged data agreed well. Yedidiah (2006a, 2006b) tried to establish a methodology that would optimize the design process of a pump. He emphasized how one can select information one needs to improve a whole pump's performance instead of improving specific features of the pump using CFD data and the pumps' actual performance data.

D Pressure and Velocity Measurement

Before LDV (Laser Doppler Velocimeter) was employed for the measurement of the flow field inside rotating machinery, Pitot tube probes accompanied with an yaw meter, hot wire/film anemometry, yaw probes (Murakami et al. (1980)), hydrogen bubble visualization, and various other methods were used. These apparatuses were able to measure the mean velocity, but they were inadequate to measure velocity fluctuations inside the impeller to ascertain the turbulent nature of the flow. LDV has been widely used in measuring velocity of fluid for decades. LDV is used for many flow field measurement applications where its robustness, no need for calibration, high temporal resolution, and lack of physical probe in the flow are desirable. When LDV is applied to the measurement of rotating machinery, such as pump or turbines, an ensemble average is used to acquire mean velocity. LDV measurements of velocity

components (x-, y-, and z- direction) and Reynolds stress components were made to investigate the interaction between the rotor and stator in a centrifugal pump by Ubaldi et al. (1998). They investigated the interaction between the volute tongue and the impeller blades by looking inside the impeller channels and the casing separately.

More detailed investigations on the flow field inside the impeller passage were performed by Pedersen et al. (2003) using PIV (Particle Image Velocimeter) and LDV. They compared the results obtained with PIV and LDV and found that a ensemble average using large amounts of PIV data can produce satisfactory accuracy comparable to LDV data. While LDV provides fairly high accuracy on temporal flow structures, PIV can offer the ability to identify instantaneous spatial flow structures. Dong et al. (1992a, 1992b) utilized Particle Displacement Velocimery (PDV), which is based upon the same principle as PIV, in the measuring of the velocity field. Detailed flow field study of the rotor-stator interaction was performed by Chu (1995a). They showed the comparison between the pressure data which was measured directly on the surface of the casing and the calculated pressure data with velocity data using time averaged Reynolds Navier-Stokes equation. They measured the velocity and Reynolds stress on the center plane of the housing. They assumed no velocity gradient along the z-direction for calculating pressure and achieved good agreement with direct pressure measurement. However, along the volute tongue, the z-velocity gradient was too large to assume horizontal flow, and agreement was poor.

Soong et al. (2003) performed an intensive visualization study on the flow inside the gap between two rotating disks. They studied the flow field characteristics

inside the gap using smoke with three different gap sizes and three different Reynolds numbers. In their work, they indentified a single cell circulation which is a flow that comes from the outside then turns, and returns to the outside the disk inside the gap. With decreased gap size, the rate of circulation decreased due to the obstruction of fluid ingestion. They also have found that the flow spirals outward as the Reynolds number increases, but this phenomenon could not be found in the flow between co-rotating and counter rotating disks. The pressure data of the gap between the rotating disks can be found in the work of Bayley et al. (1964), in which they measure the pressure using a bank of manometers.

II OBJECTIVES

While the previous works on the effect of the back clearance on the hydrodynamic forces in the centrifugal pumps are based upon simple leakage flow theories and intuitive reasoning using the discrete experimental data with help of overly simplified equations, full 3-D computational fluid dynamics (CFD) simulations will be performed to investigate the mechanisms of the back clearance effects upon the axial forces and the pressure fluctuations.

A preliminary computer simulation of the flow field using commercial CFD software has shown that the net force acting on the impeller predicts the same trend as Hossain's experimental data on the axial loading, which is counter to the commonly accepted concept of a small clearance causing more pump-out of the fluid between the housing and impeller back thus reducing the pressure and decreasing the axial loading. The details of what is occurring in the clearance area of the pump are essential to understanding the effect of back clearance. These details will be supplied by the CFD simulations. For this study, CFD simulations of the entire pump will be performed and the results will be validated with experimental data consisting of global time averaged variables (head, required power, efficiency, axial loading, and phase averaged velocity field measurements inside the impeller and the inlet pipe) and unsteady variables (pressure fluctuations). The investigation on the effect of the back clearance size on the flow inside the back clearance will be performed using the disk gap flow analysis which is established by many workers. Detailed analysis on the effect of the back clearance on the axial thrust and leakage flow analysis is applicable to other pumps,

since this semi-open pump has many common factors shared with many other industrial pumps operating at the same specific speed range such as standard semi-open faced impeller with back swept blades and single volute tongue (vaneless diffuser).

With the validated CFD prediction, values of the forces and moments acting on the impeller will be presented in terms of the back clearance size. These data are extremely difficult and expensive to acquire by any type of experimental methodology. Moreover the study on the leakage flow rate through the balance hole, which is valuable information for providing the leakage loss, will also be performed.

III PROCEDURES

Performing in-depth analysis of the flow field inside a pump using CFD requires verification of the simulation's accuracy by comparing the CFD data with actual experimental data. The data which one can acquire from the pump facility at the Turbomachinery Laboratory at Texas A&M University are dynamic pressure measurements, mean wall pressure measurements, and LDV measurements. One can infer the physical phenomenon inside pump from the measurements but those are limited to regions where the measurements were performed such as the windows on the pump casing which only cover 20% of the total surface of the casing. The flow field of interest in this study, behind the impeller, is mostly inaccessable to velocity measurement apparatus. In this study, the pressure fluctuation data acquired from dynamic pressure sensors will be used to verify the dynamic results (unsteady) of the CFD data, especially at the casing surface. LDV data obtained in this study and by Berchane and mean pressure data obtained by Hossain will be used to verify the time averaged velocity field inside the impeller passage.

A Pump Facility

The pump to be used in this work is a 10.2 X 7.6 X 33 cm Ingersoll-Rand pump. It has a 33.65 cm diameter impeller with five backswept blades. In this work, the impeller will be rotated at 1400 rpm and will be equipped with and without balance holes. In previous work, the best efficiency was acquired with no balance holes, a 0.65mm front clearance, and a 1.87mm back clearance, although closing all balance

holes will result in highest bending moment and axial thrust upon the impeller. To prevent cavitation, the upstream flow is pressurized, which results in higher NPSHA than the NPSHR. This facility is described in detail by Hossain (2002).

The pump speed will be maintained at a constant speed of 1400 rpm through the use of an adjustable frequency drive on the electric motor. The drive is controlled by a remote potentiometer connected to the logical board of the drive. By turning the potentiometer, the motor speed is varied and set to the desired value. This speed is 78 % of the rated speed for the IR pump. The pump can not be operated at higher speeds due to the power limitations of the Westinghouse motor. In the work by Hossain, it was determined that the best efficiencies were obtained for the geometric configuration having a back clearance of 1.87 mm, a front clearance of 0.65 mm, and no balance holes. The best efficiency point (BEP) for that configuration was at a flow rate of 31 Liters/sec. For this work, these same running conditions are chosen to investigate the flow at the BEP. Brass bolts were manufactured to seal the balance holes already drilled in the eye of the impeller for the non-balance hole case. The back clearance was set to 1.87 mm by adding brass washers of known thickness onto the shaft of the impeller, which in turn is screwed into the shaft of the IR pump.

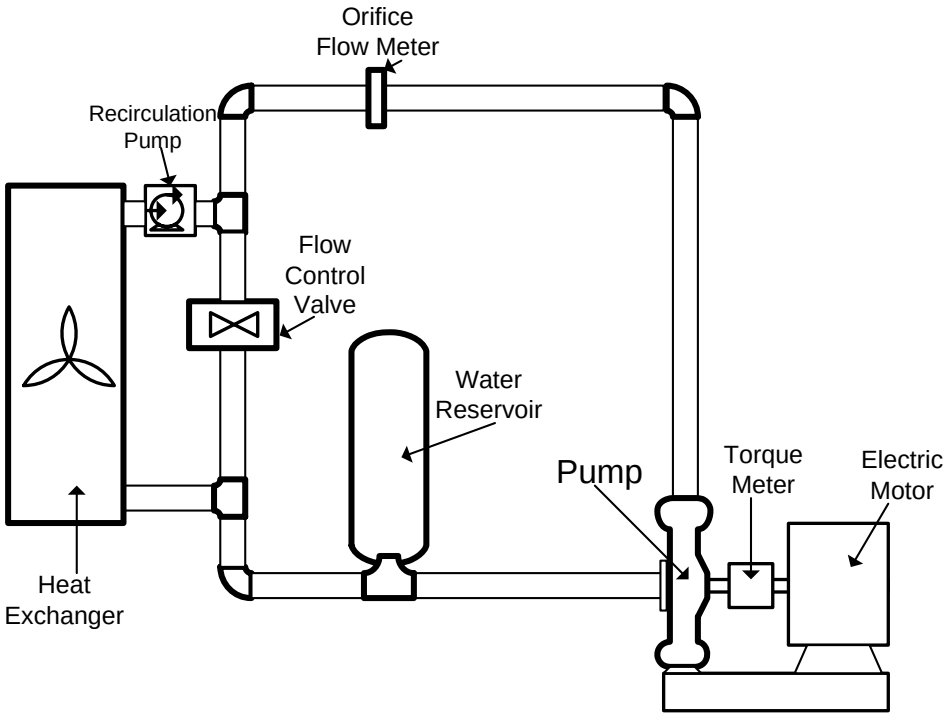

Figure 1 The pump test facility for velocity measurement

To keep the front clearance constant at 0.65 mm, gaskets (provided by the pump manufacturer) are inserted or taken out from the front casing accordingly. The flow rate is measured by an orifice meter and set to 10, 20, and 31 Liters/sec by manually adjusting the flow control valve (Figure 1). The two lower flow rates are included to determine how off design operating conditions effect the flow field and the accuracy of CFD simulations.

B LDA System

The fluid velocity measurement system is composed of a laser source, a TSI Laser Doppler Velocimetry System, and a three dimensional traverse. Measuring the flow is accomplished using a one-dimensional LDV system in operating backscatter

mode (Figure 2). The LDV system consists of the base-plate, laser source, transmitting optics, receiving optics, seed particles, photo-detector, and the signal processor. The laser source is a Coherent 35 mw He-Ne laser, lasing at a wavelength of 632.8 nm.

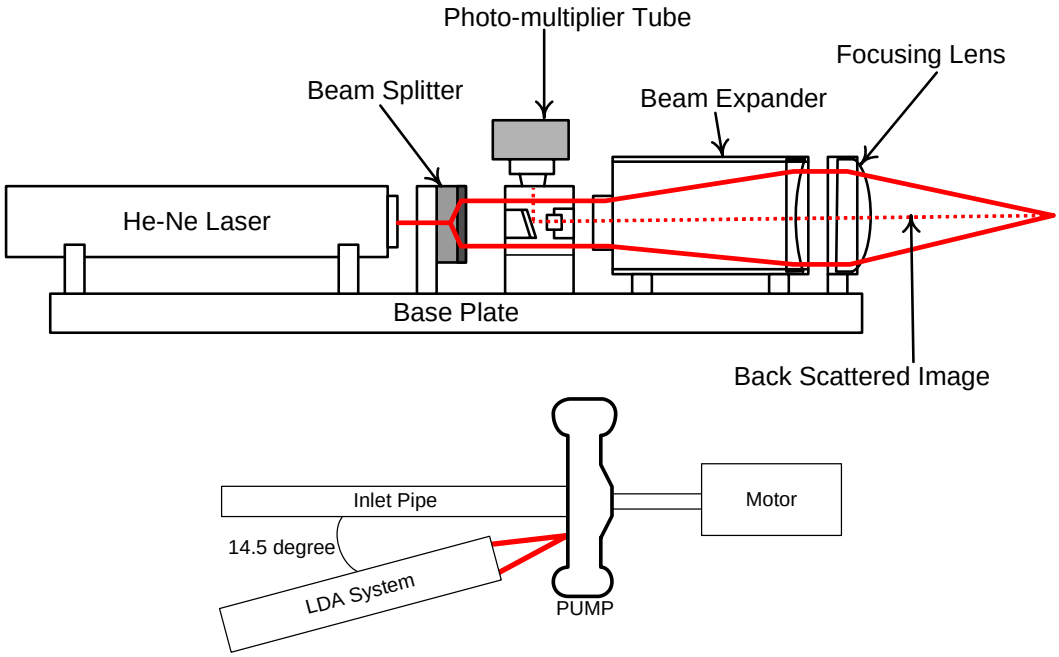

Figure 2 Components of LDA system

The base (model 9123-150) is a black anodized aluminum rail. The laser source, transmitting optics, receiving optics, and the photo-detector are all mounted and fixed to the base-plate. The transmitting optical train consists of a polarization rotator, a beam splitter, a beam expander, and a focusing lens. By using a beam splitter (model 9115-2), the incident beam from the laser source is split into two equal intensity parallel beams that are focused to a point in space by the focusing lens (model 9169-450) to form fringes. The orientation of the fringes is parallel to the LDV axis, and

perpendicular to the plane formed by the intersecting beams. The distance between adjacent fringes (fringe spacing) is a function of both the laser wavelength (λ) and the half angle κ, and is given by the following equation:

$$d_f = \lambda/(2 \sin \kappa) \quad (1)$$

where κ is equal to half the angle formed between the two intersecting beams. Thus by knowing the laser wavelength and the half angle we can calculate the fringe spacing. The point at which the two beams interfere is called the probe volume and it is defined as a portion of the beam waist enclosed by the surface whereupon the peak light intensity falls to $1/e^2$ of its maximum value. The diameter of the probe volume is given by the following equation:

$$d_m = \frac{4\lambda f}{\pi D_{e^{-2}} \cos\kappa} \quad (2)$$

where d_m is the probe volume diameter, λ is the laser wavelength, f is the focal length of the focusing lens, $D_{e^{-2}}$ is the diameter of the incident laser beams, and κ is the half-angle. A beam expander (model 9189) was also incorporated, the purpose of which was to increase the diameter of the two beams to achieve a smaller probe volume. This also results in a higher light intensity in the probe volume and as a result, a better signal to noise ratio. The parameters of LDV system mentioned above are summarized in Table 1.

Table 1 The specification of the LDV system

λ	The laser wavelength	632.8 nm
κ	The half angle	7.71°
d_m	The probe volume diameter	61.5 μm
f	The focal length of the focusing lens	480 mm
$D_{e^{-2}}$	The diameter of the incident laser beams	6.345 mm
d_f	The fringe spacing	2.35 μm

The flow is seeded with Polystyrene Latex particles averaging 6 μm in diameter with a specific gravity of 1.2. The choice of scattering particles is very critical in LDV as it has a very significant effect on the intensity of the reflected light detected by the photo-multiplier tube. In general, larger particles reflect more light, but to achieve accurate readings the particles should be able to follow the flow fairly well and thus should have the minimum required aerodynamic size. As the scattering particle passes through the interference pattern, it reflects light in a sinusoidal manner. This sinusoidal wave (Doppler burst) has a frequency that is proportional to the velocity of the scattering particle. By knowing the fringe spacing in the interference zone and the frequency of the Doppler burst, the velocity of the particle can be calculated:

$$u_i = f_d * d_f \tag{3}$$

where f_d is the frequency of the Doppler burst, and u_i is the velocity of the scattering particle perpendicular to the fringes, that is perpendicular to the LDV system axis, and in the plane formed by the two intersecting beam. Thus, the LDV system can be used

to obtain different velocity components by changing the orientation of the plane formed by the two intersecting beams. This can be done by rotating the beam splitter.

The light scattered by the flowing particles is then collected and focused onto a photo-multiplier tube (model 9162). This is accomplished by the use of a collecting lens (TSI model 9169-450) and a receiving focusing lens. The photo-multiplier tube converts the total flux of light energy striking the detector into a voltage that is the input to the signal processor (Figure 3).

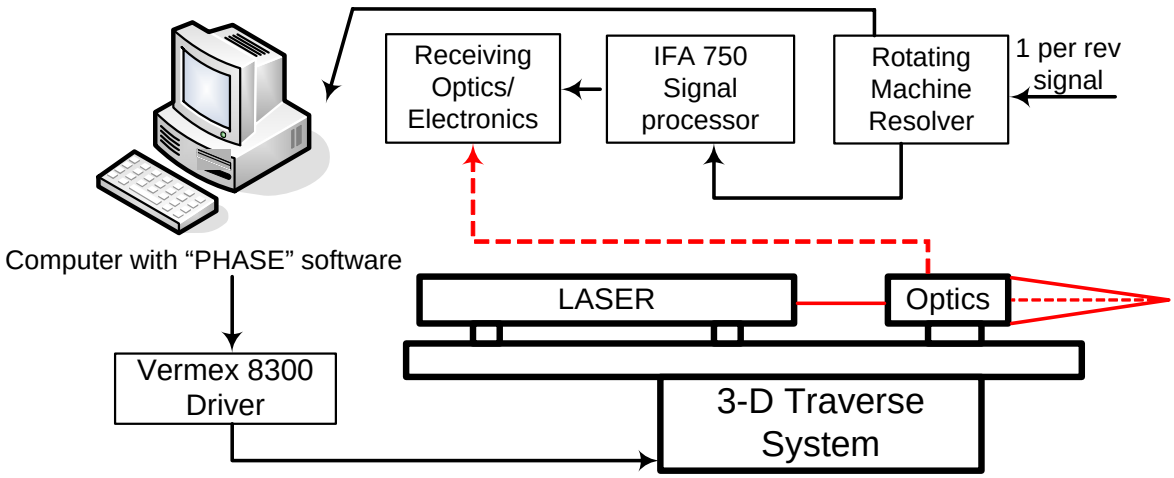

Figure 3 LDA signal processing system configuration

C Signal Processing

An IFA 750 Digital Burst Correlator is used to extract and measure the Doppler frequency. To accomplish this accurately, the Doppler signal has to be separated from the pedestal and background noise by passing through band pass filters. A high-pass filter eliminates the pedestal while a low-pass filter reduces the amplitude of the wide-

band noise. For this work, the filter settings are chosen on a trial and error basis through the phase software according to the signal acquired through the LDV. A low pass filter of 10 Mhz and a high pass filter of 1 Mhz were determined to be appropriate. After amplifying the signal, it is clipped to provide a quantized signal that is then fed into a burst detector. The burst detector is used to discriminate between the Doppler signal and the noise. When a signal is detected it is digitally sampled at multiple-sampling frequencies, and once the optimum sampling rate of the signal is determined, 256 samples from the center portion of the signal burst are transferred to the auto-correlator. The frequency of the incoming signal is calculated by determining the number of time delays that occur between contiguous validated cycles of the autocorrelation function. By knowing the sampling time period and the number of time delays and the number of cycles in the correlation function, the frequency is determined and sent to the computer.

A TSI Rotating Machinery Resolver (model 1989) is incorporated into the system to record the rotor angle with each velocity measurement. A photoelectric switch mounted on the shaft of the impeller provides the Rotating Machinery Resolver with a once per revolution reference signal. The interface between both the Correlator and the Resolver with the LDV system is made through the Phase software that was developed by TSI.

A three dimensional traverse which has a 0.02 mm resolution in all three axes is controlled by a Velmex 8300 series control/driver, which can be operated manually or automatically through a computer. The laser sources along with the optical train are

mounted on the base-plate which is bolted to the traverse. This makes it possible to investigate the flow at different azimuthal and radial points along different axial planes inside the pump.

D Data Acquisition Locations

Figure 4 shows the optical windows and the LDV measurement locations inside the pump. Measurements are taken at 13 radial locations (from r = 80 mm to 140 mm at a point to point spacing of 5mm) and five axial planes (z/h of 0.11, 0.29, 0.47, 0.66, and 0.84). The radial lines along which the probe is traversed are at azimuthal angles of 45° in window B, and -45° in window A.

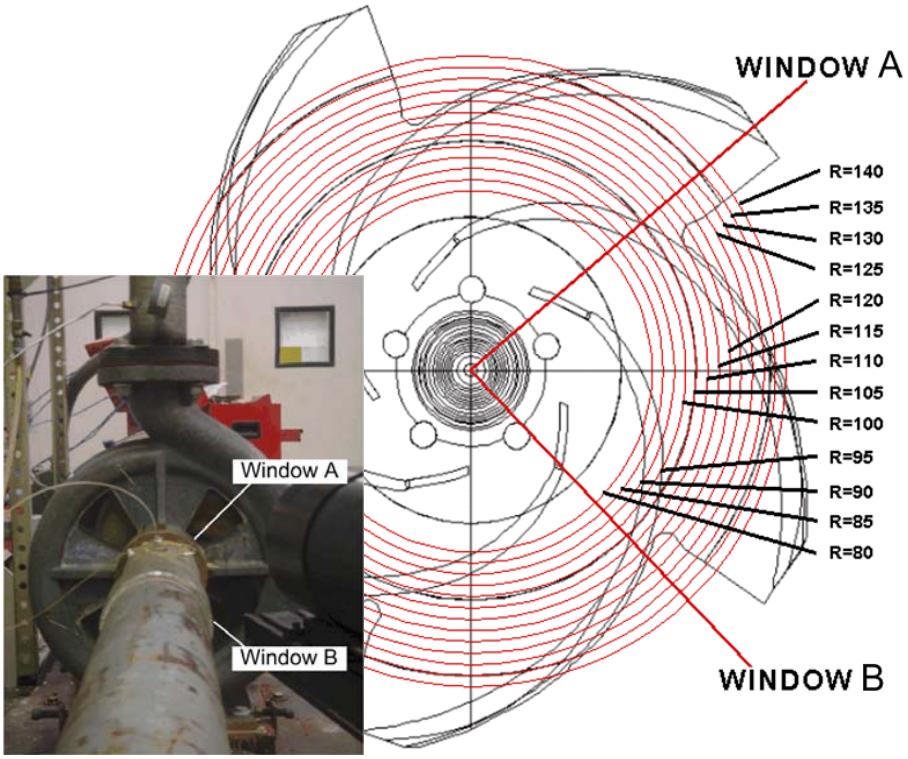

Figure 4 LDA measurement positions

Azimuthal angles are measured counter clockwise from the horizontal line as the observer faces the suction side of the pump. A pinhole was glued onto the pump housing and was used as a reference spatial location for the probe volume.

The traverse was controlled automatically through the Phase software. Position files were written and then automatically executed as part of the data acquisition process. About 350,000 measurements were performed at each physical location and phase averaged for every 1° increment of rotor position. Five axial positions for the LDA measurements are shown in Figure 5. "z/h" represents the depth at which the measurements were made (h is height of impeller blade-22mm). In summary, there are 360 X 13 X 5 = 23,400 measurement points. This requires approximately 8,000,000,000 individual velocity measurements performed for one velocity component measured for one pump operating condition.

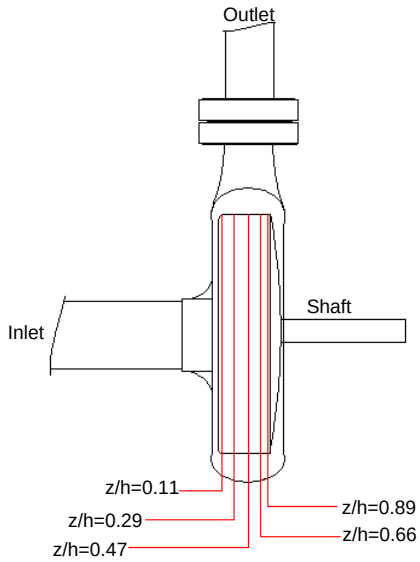

Figure 5 Side view of pump showing depth designation z/h

The flow inside the pump where the LDA measurements were performed on the impeller and into the volute was assumed to be two dimensional. Two different velocity components were measured in order to calculate the velocity vector and the turbulence kinetic energy in planes parallel to the rotor disk. Thus at each physical location, velocity measurements were performed twice, each time measuring a different component (vertical and horizontal). For this purpose, the plane of intersection of the two beams was oriented at two different angles (vertical and horizontal). By performing these measurements, the mean and fluctuating value of the flow was attained at each of those locations.

The velocity information was then post processed through several C++ programs to reach the final form that is to be presented. As part of the data reduction process, the vertical and horizontal data were phase averaged to obtain the mean vertical and horizontal velocities as well as the vertical and horizontal variances for every 1° increment of the rotor position from 1 to 360°. The mean velocity was calculated at each angular position by the following equation:

$$\overline{U} = \frac{\sum_1^n u_i}{n} \tag{5}$$

where u_i is the instantaneous velocity measurement and n is the total number of points that have the same blade angle associated with it. The variance was calculated by the following equation.

$$Var = \frac{\sum_1^n (\overline{U} - u_i)^2}{n} \quad \text{or} \quad Var = \frac{\sum_1^n (u')^2}{n} \tag{6}$$

The angle between the LDV system and the pump axis was then accounted for in the mean velocities but not in the variances. This was done by multiplying the

horizontal velocities (V_h) by cos(γ), where γ is the angle difference between the pump and LDV x-axis which is equal to 14.5º (Figure 2). The vertical velocity V_v was left unchanged because the y-axis of the pump and the LDV coincide and thus $V_v = V_y$. The absolute velocity vector was then resolved into the tangential and radial components by the following equations:

$$V_\theta = -V_x \sin\theta + V_y \cos\theta \tag{7}$$

$$V_r = V_x \cos\theta + V_y \sin\theta \tag{8}$$

where θ is the angle between the radial line of measurement and the positive x-axis, which is ± 45° in our case.

Finally, since the magnitude of $\overline{u'u'}$ and $\overline{u'u'}$ are comparably similar (maximum 15% difference), the turbulence kinetic energy was estimated assuming isotropic turbulence from the equation:

$$k_p = \frac{1.5}{2}(\overline{u'u'} + \overline{v'v'}) \tag{9}$$

where u' and v' are the velocity fluctuations in the horizontal and vertical directions respectively. This isotropic turbulence model is also utilized in selecting the κ-ε turbulence model for the CFD simulation.

E Pressure Measurement

Dynamic pressure will be measured with high resolution ICP (piezoelectric pressure sensor model 112A22) transducers from the PCB Company. These sensors have average sensitivity of 100mV/psi (14.5 mV/kPa), lowest sensible frequency of 0.50Hz, resonant frequency higher than 250 kHz, and operation range of 50 psi. A total

of six of these sensors are installed on the housing of the pump. They are mounted flush with the inner surface of the housing. It would be most desirable to place pressure sensors at every one-degree (azimuthally) position and compare data with the CFD results. For the limited budget, it is thought that pressure fluctuation data from four positions are sufficient to validate the unsteady CFD result. To determine the four locations that can best-validate the pressure fluctuation predictions, the CFD simulation results were utilized. Four positions, starting from the location near the volute tongue and spaced by 90 degrees were selected. Signals from these sensors are amplified by the built-in pre-amplifier and then conditioned by a PCB 442B104 signal conditioner.

F Numerical Simulation

Four computers with Pentium 4 3.4 Ghz processors are used for the CFD analysis. Meshing of the pump required approximately 900,000 hexahedral elements (structured and unstructured) and 1,000,000 calculation nodes. Gambit software from Fluent was used to construct the grid. The numerical simulation of the pump is performed using Fluent (version 6.3.26). The turbulent models κ-ε or κ-ω are utilized based on the fact that κ-ω model is known to handle time averaged flow within the rotating machinery with multiple reference frames very well and the κ-ε model with unsteady simulation due to the fact that this model is proven to work well by other researchers. Some workers prefer the Reynolds Stress Transport model in highly 3-D flow simulation in that this model can eliminate the error from isotropic turbulence viscosity model. However, since the computer has rather limited system resources (other researchers working with RST model use supercomputers), either the κ-ε or κ-ω

model is used. Lastly an LES (large eddy simulation) model is available in the Fluent software, but this model is known to demand a very refined grid (for normal pump applications, more than 1,500,000 nodes are required) and to have high gird dependence. Ergo, in this research this model will not be used. Figure 6 shows a representative mesh model of the pump that is used in this work.

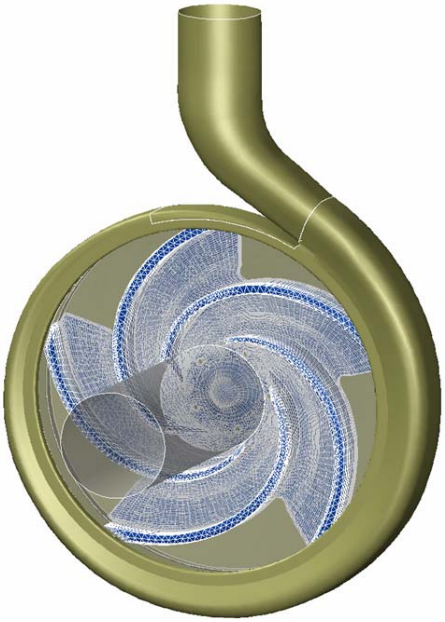

Figure 6 Mesh model of the pump with a semi-open impeller

Three mesh models of the pump with three back clearance sizes are generated and the simulation is conducted under the conditions specified in Table 2.

Table 2 Simulation conditions and available test data

Back Clearance	Balance Holes (ϕ6.7mm)	Flow Rate (liter/sec)	Available Experimental Data
0.91mm	Yes	31	Axial Thrust, Head, BHP
		28	Axial Thrust, Head, BHP
		25	Axial Thrust, Head, BHP
	No	31	Axial Thrust, Head, BHP
		28	Axial Thrust, Head, BHP
		25	Axial Thrust, Head, BHP
1.87mm	Yes	31	Axial Thrust, Head, BHP
		28	Axial Thrust, Head, BHP
		25	Axial Thrust, Head, BHP
	No	31	Axial Thrust, Head, BHP, LDA Measurement, Pressure Fluctuations Measurement
		28	Axial Thrust, Head, BHP, Pressure Fluctuations Measurement
		25	Axial Thrust, Head, BHP, Pressure Fluctuations Measurement
		20	Axial Thrust, Head, BHP, LDA Measurement, Pressure Fluctuations Measurement
		10	Axial Thrust, Head, BHP, LDA Measurement, Pressure Fluctuations Measurement
3.17mm	Yes	31	Axial Thrust, Head, BHP
		28	Axial Thrust, Head, BHP
		25	Axial Thrust, Head, BHP
	No	31	Axial Thrust, Head, BHP
		28	Axial Thrust, Head, BHP
		25	Axial Thrust, Head, BHP

IV RESULTS AND DISCUSSION

A CFD Validation (Appendix A)

A grid independence study was performed to verify whether the number of nodes of the mesh model used in this study is large enough to justify no further improvement on the mesh model. Other factors that affect the quality of the mesh model are the uncertainty in digitizing the real pump geometry into a computer model and the physical and the chemical properties assumed such as the wall roughness and the density and the viscosity of the liquid. As stated above, it is assumed that the chemical properties of water are constant regardless of the operating temperature. The wall roughness is a property that is inevitably decided by trial and error.

1 CFD Grid Independence Study

This study assumes that grid independence is achieved when there is no further change in head, power input, and the axial thrust with further increase in the number of the nodes. Quality of the whole pump mesh model can be judged by investigating the changes in head and power input as the number of nodes increase. Monitoring of grid independence of the impeller gird alone is performed by evaluating the variance of the axial thrust. Improvement of the mesh model is carried out by refining the mesh in zones that have abrupt pressure changes (pressure curvature). The Fluent program calculates the magnitude of the curvature of pressure by calculating the Laplacian of the pressure using following equation by Warren et al. (1992).

$$CurvatureValue = (A_{cell})^{1/2}\left|\nabla^2 p\right| = \sqrt{A_{cell}}\left|\frac{\partial^2 p}{\partial x^2} + \frac{\partial^2 p}{\partial y^2} + \frac{\partial^2 p}{\partial z^2}\right|$$, (unit: Pa / m).

Then, by increasing the number of the nodes in the regions that have high curvature, one can reduce the curvature (pressure gradient).

Three mesh models are generated for three different back clearances, but the differences among them are only the number of nodes on the back clearance. Due to this similarity among three models, it was decided that the mesh model for the 0.91mm back clearance be used for the grid independence study. The two other mesh models (1.87mm and 3.17mm clearance models) are also improved in the same manner as the mesh model for the 0.91mm back clearance. A total of nine grid adaption processes are conducted (Table A 1). As shown in the table, the initial maximum pressure curvature was 64.8. This was reduced to 22.3 after nine adaptions. These adaptions were performed for the entire pump mesh, but the highest pressure curvature was found in the outlet pipe where the flow changes direction. As the pressure curvature value approaches 22, high pressure curvature regions were also found at the tips of the impeller. Figure A 1 and Figure A 2 show the change in head and power required (BHP) as the pressure curvature maximum value is decreased. The figures show that both the head and the BHP do not change as the number of nodes increases after the first adaption. One can presumably conclude that this mesh model is now grid-independent after one or two grid adaptions. Figure A 3 shows the change in the axial force in terms of the number of the nodes. Even though the head and the BHP are grid-independent after two adaptions, the axial thrust is still not grid-independent. As the figure shows, one can suggest that the mesh model is fully grid-independent after the

fourth adaption. These changes in head, BHP, and the axial thrust with increases in the number of the nodes is more evident in Figure A 4 where the % change for each adaption are presented . From these observations, the other two mesh models with different back clearances have undergone grid adaptions until the pressure curvature value is below 22 which is average value for the entire pump.

2 Turbulence y* Value

Grid quality is evaluated in terms of the turbulence y* value. The y* value is simliar to the y+ value conventionally used in turbulent flow analysis. According to the Fluent manual, the y* value is equivalent to the y+ value when the first node layer is placed where the log-law is valid (y*<300). The y* value is defined in the following equation.

$$y^* = \frac{\rho C_\mu^{1/4} K_P^{1/2} y_P}{\mu}$$

(ρ : density, C_μ : Friction Coefficient, K_P : Turbulent Kinetic Energy, and y_P : distance from the wall in normal direction)

Because this study uses the standard wall function, the y* value should be less than 300 for accurate turbulent flow depiction. In Figure A 23 through Figure A 28, the distribution of the maximum y* value on each of zones which define the pump surfaces for different pump configurations are shown. Zone ID on the abscissa represents the face zone shown in Table A2. High y* values on the front impeller surface are found near the suction side (Figure 7).

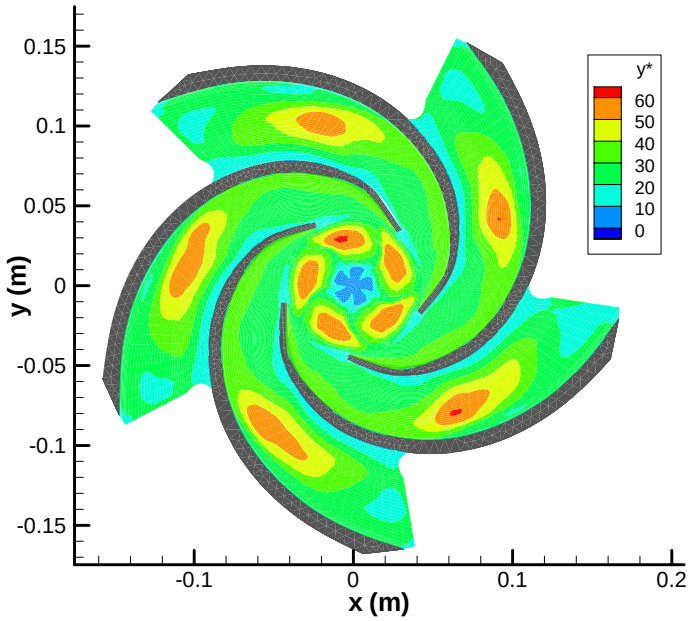

Figure 7 y* distribution on the front wall of the impeller at 31 liter/sec

The slightly larger y* on the suction side (zone 2) is caused by higher turbulent kinetic energy at the top portion of the blade where the back step flow occurs (Figure 8). At this position flow through the front clearance from the previous passage flows over the blade and merges with the flow in the next passage.

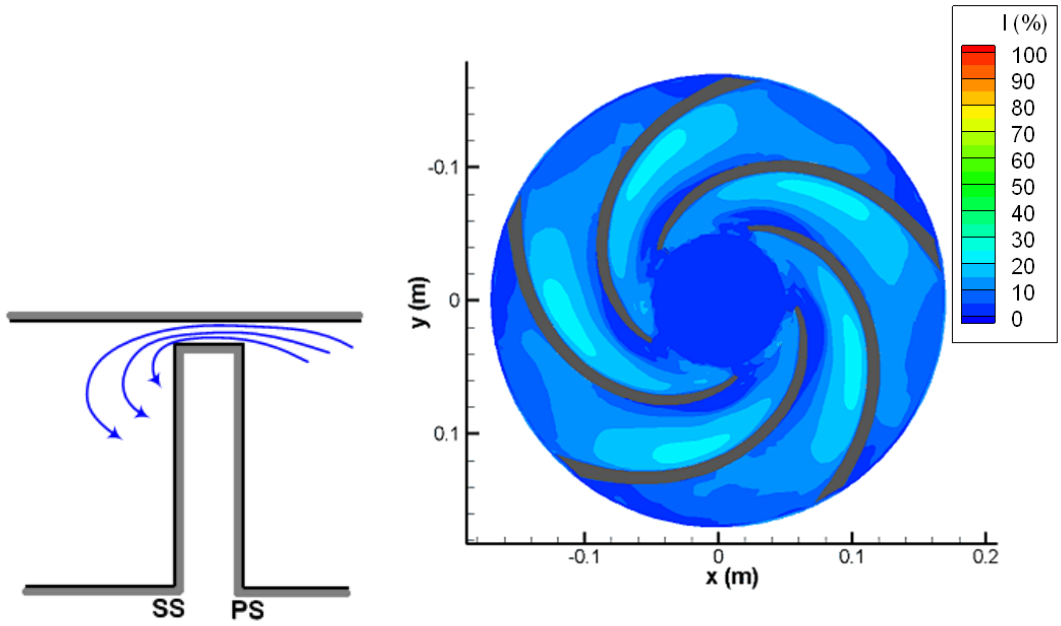

Figure 8 Turbulence intensity near the front wall of the housing and the flow depiction over the blade

Also the y* value is relatively high at the eye of the impeller where most of the conversion of the axial momentum of the incoming flow into the radial momentum takes place (Figure 9). The regions of the impeller mentioned above are the sections which the fine mesh should be used to reduce the y* value.

The grid adaption could have been accomplished by adapting the mesh using the grid-adaption tool in Fluent. However, this author found that, if the grid adaption for y* value is performed once the mesh is loaded onto Fluent, the hanging nodes created by the adaption process cause fatal program errors. Due to this reason, the grid adaption for y* value is a trial and error process. It is performed by the author creating new meshes which have the best quality in terms of y* value using the Gambit program.

The y* value plots show the y* values are well under 300 in every pump configurations and every operating conditions.

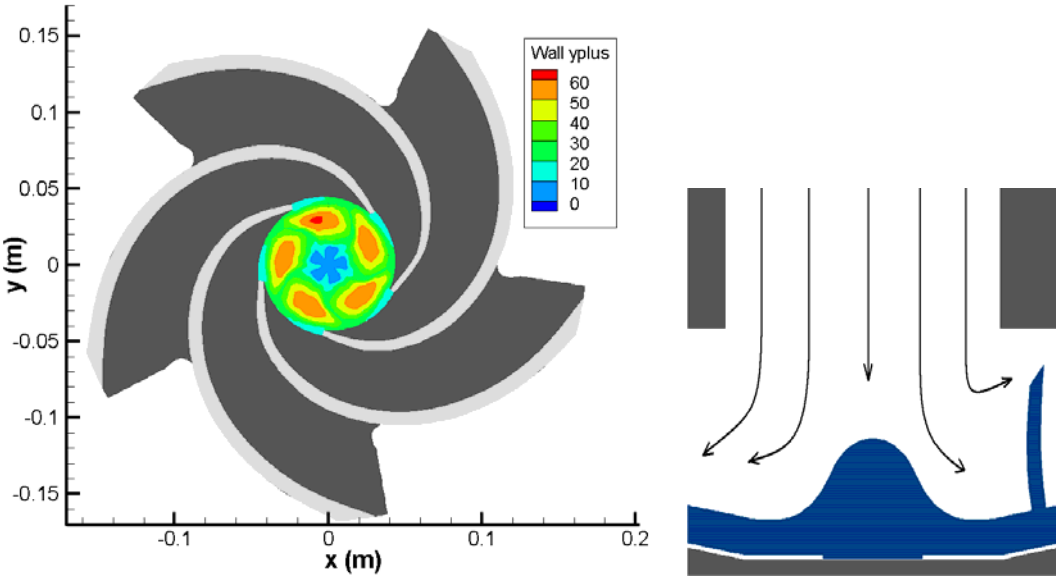

Figure 9 The y* value at the eye portion of the impeller and the typical flow near eye section

The reason why the y* value adaption study is not performed on the housing part is that, due to the topological reason, the meshing of the housing can only be performed in one way so that the hexahedral grid element can be used. This way of meshing facilitates a less fine mesh on the housing wall, which results in the maximum y* value of order of 1000 at the outlet pipe. However, on the crucial part such as the cut-water, the wall near the exit of the impeller, and the front and the back wall of the housing are meshed with finer grid so that these parts have the y* value well below 300.

3 Boundary Conditions

Three boundary conditions are available for the inlet and the outlet. The first boundary condition pair defines pressure on the inlet and the outlet of the pump. The flow simulation is conducted based on the fixed inlet and outlet pressures. However, the prediction of the steady and the unsteady pressure distribution is poor compared to the experimental data because in reality the inlet and the outlet pressures fluctuate as the pump operates. Due to this reason, the first boundary condition pair was not used. The second method is called “mass inlet” condition. This method specifies the mass flow rate at the inlet, and sets the outlet condition as “outflow”. An outflow boundary condition extrapolates variables at the boundary using interior domain information. One is required to assure that there is no back flow when using the outflow boundary condition. Gonzales et al. (2002) claimed that the mass inlet condition predicts poorly compared to the “target mass flow rate” condition. However, this author assumes that the ability to predict pressure accurately also depends upon the model’s ability to depict the pump facility’s characteristics as well, not solely on the depiction of the pump itself. Ergo, since the facility used in this work is different than other researchers, using the boundary condition which is known to work well in one condition blindly will not necessarily guarantee good results. The third boundary condition called “target mass flow rate” specifies the mass flow rate at the outlet and lets the inlet pressure fluctuate according to the outlet condition at each time step. The validity of these two boundary conditions were examined by comparing the mass inlet condition (with adapted grid) using the steady performance data as shown in Figures A 5 through A 10

in terms of the non-dimensional coefficients (ψ and φ). ψ and φ are the head coefficient and the flow coefficient, respectively, and are defined in the following equations.

$$\psi = \frac{g\Delta H}{U_2^2}$$

$$\varphi = \frac{Q}{\Omega r_o^3}$$

As one can see, the mass inlet boundary condition without any grid adaption based on pressure curvature results in poor predictions, and the other two boundary conditions – mass inlet with grid adaption and target mass flow rate– results in almost the same predictions of head for a given flow rate. The mass inlet condition without any grid improvement shows the largest difference from the experimental data. Especially for the case with a 0.91mm back clearance performance prediction which shows a maximum 7% difference from the experimental data. Other than the case with 0.91mm back clearance, the mass inlet condition without any grid improvement results in the same performance prediction as the performance prediction with the target mass boundary condition. In both cases (with and without the balance holes), the mass inlet boundary condition (with grid adaption) results in a decrease in the head coefficient as the back clearance increases. The experimental data shows such trends only for the case with balance holes. However, the predictions for the unsteady data show many differences between "mass inlet" and "target mass flow rate" conditions. Figures A11 through A22 show the pressure amplitude spectra of the pump with the 1.87mm back clearance and no balance holes. The spectra contain three data: experimental data taken by this author, CFD data obtained using the mass inlet boundary condition, and CFD

data obtained using the target mass boundary condition. Unsteady pressure data are recorded at four locations: 30 degrees, 110 degrees, 180 degrees, and 250 degrees at a radius of 0.17m (6.7in: impeller radius) on the back of the housing. Methodology for the pressure data acquisition in the experiment is presented in a previous section. While the pump facility is able to execute experiments with other back clearance configuration, it was assumed that unsteady pressure data validation for one back clearance case with various operating conditions would be sufficient to assure the simulations represent the other cases with different back clearances. For all azimuthal locations (30, 110, 180, and 250 degree) both the mass inlet boundary condition and the target mass boundary condition produce excellent agreement with experimental data for the 3^{rd}, 4^{th}, 5^{th}, and 6^{th} harmonics. However, at the blade passing frequency and twice the blade passing frequency, "target mass flow rate" predicts a trend opposite to the "mass inlet" boundary condition's results as illustrated in Figures A 11, A 12, A 14, A 15, A 16, A 18, and A 21. All of these opposite trends can be found at azimuthal positions of 30, 110, and 250 degrees. At 180 degrees, both boundary conditions predict unsteady behavior of the pump fairly well. The reason for this is that at the 180 degree position - the opposite side of the cutwater region (30 degrees), pressure fluctuations are mainly dominated by local pressure pulsation from the jet-wake mixing at the impeller tip, which has a weak relationship to the inlet condition or the cutwater. On the other hand, at the 25lit/sec operating condition (80% of B.E.P.), the target mass flow rate boundary condition's unsteady pressure prediction at 30 degree agrees well with experimental data. However, at 180 degrees, the target mass flow rate boundary

condition predicts much lower amplitude for the 2nd harmonic than that of the mass inlet boundary condition. For this case, the mass inlet boundary condition consistently produces better simulations.

Based upon the comparisons between the CFD predictions experimental data for both the steady and the unsteady conditions, the mass inlet condition with grid adaption is selected to be used in this study.

4 Steady Data

a) LDA Data (Appendix B)

LDA data were recorded by Berchane (2004) and Park (2005) using the same LDA apparatus. Berchane measured the X and Y velocity and the turbulent kinetic energy using the standard deviation of the LDA data. The radial velocity (V_r), the tangential velocity (V_θ), and the relative velocity vectors (V'_x, V'_y) were calculated using following equations.

$$V_r = V_x Cos\Psi + V_y Sin\Psi$$

$$V_\theta = -V_x Sin\Psi + V_y Cos\Psi$$

$$V'_x = (V_y - U * Cos\Psi) * Cos(\theta + \Psi) + (V_x - U * Cos\Psi) * Sin(\theta + \Psi)$$

$$V'_y = (V_y - U * Cos\Psi) * Sin(\theta + \Psi) - (V_x - U * Cos\Psi) * Cos(\theta + \Psi)$$

where θ is the angle in the polar plot, which represents the time stamp for each radial slice, Ψ is the azimuthal angle for either window A (45˚) or the window B (-45˚), and $U = r * \Omega$ is the impeller's tangential velocity.

Park measured the flow field inside the pump at off-design conditions of 1/3 and 2/3 of design flow. Figure B1 through Figure B18 contain Park's LDA data along with Berchane's data for the purpose of self-completeness of this work. CFD data are reduced in the same manner as the LDA data were reduced. For a given azimuthal location (window A or window B), a stationary measurement plane was set, and as the impeller rotates, the velocity data were collected. LDA data that were taken in this manner show that the velocity distribution of one impeller passage passing one particular azimuthal location. These LDA data are supposedly the same for all five impeller passages. However, minute differences exist inside individual impeller passages and these differences are due to slightly different surface roughness in the five impeller passages. Figure B1 through Figure B18 show the contour plots of absolute velocity magnitude and the relative velocity vector plot. The axial depths (z/h) of 0.47, 0.66, and 0.87 are shown with both window A and window B.

For the 31 liter/sec operating condition, the simulation shows that, as the axial depth increases, the magnitude of the velocity reduces while the experimental data shows the rate of decrease of the velocity as the depth increase is smaller at the inlet section. The experiment shows retarded radial velocity in the middle of the passage near the inlet (the first and the second radial arcs in Figure B 2, Figure B 4, Figure B 5, and Figure B 6). For window B, this trait is thought to be due to, as Murakami et al.

(1980) measured in their experiment, the effect of the thickness of the blade resulting in the flow near the pressure side of the blade to have a secondary flow towards the suction side and the flow near the suction side of the blade to have a secondary flow towards the pressure side. At the inlet, the same trend which Murakami et al. witnessed is more evident for the 20 liter/sec flow condition. The CFD simulation predicts this trait as well.

The retarded velocity zone is located at the middle span of the passage for both windows. Along with these slow velocity zones, there are regions where the flow is fanning out towards the suction side of the blade despite the mainstream passage flow. A possible cause for these trends is that a flow from the inlet rebounds from the eye of the impeller into the front housing wall. This upward flow pushes the flow toward the suction side of the blade (Figure 10). This trend can also be seen at the 20 liter/sec operating condition. The CFD predicts the same kind of the passage flow which flows toward the suction side, however there are only small or no zones with the retarded radial velocity present.

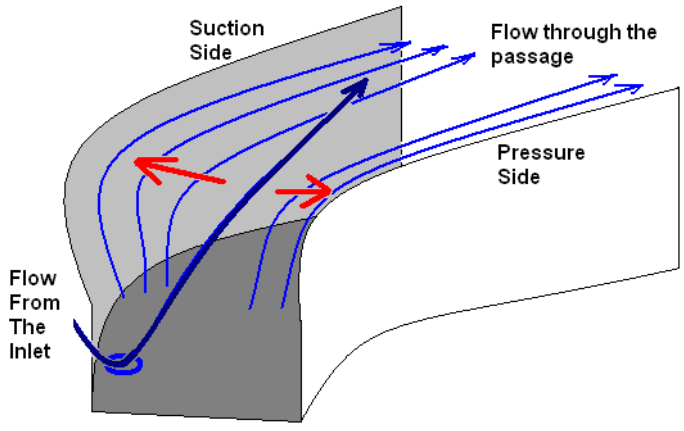

Figure 10 The schematic diagram of the flow inside the passage

At the outlet of the impeller, for the 20 liter/sec operating condition (Figure B7 through Figure B 12), the flow starts to be deflected and to have less radial velocity. The CFD predicts much lower radial velocity than that of the experiment and this discrepancy is larger in window B than window A.

Throughout the operating conditions and different depths, the inlet flow from the CFD prediction shows a flow which is less skewed toward the pressure side than the experimental results. This discrepancy was also observed by Byskov et al' (2003). In their work, at the off-design condition, the vectors at the middle span near the inlet in the passage in an LES simulation shows more stream-lined flow while PIV data shows the vectors skewed toward the pressure side of the blade. They have explained that the reason for this discrepancy is that the pre-rotation from the inlet pipe is not resolved in the LES simulation. This discrepancy at the near-inlet section becomes larger as the axial depth increases (Figure B5 and Figure B6) even though the vectors from the CFD simulation also show the skewed vectors.

At the 31 liter/sec Berchane (2002) flow rate both CFD and the experiment show no recirculation zones but the stream-lined flow near the pressure side of the blade. However, the velocity magnitude gradient prediction from CFD shows a gradual change along the span wise direction with little indentation on the suction side of the blade while the experimental data shows a larger indentation (Figure 11).

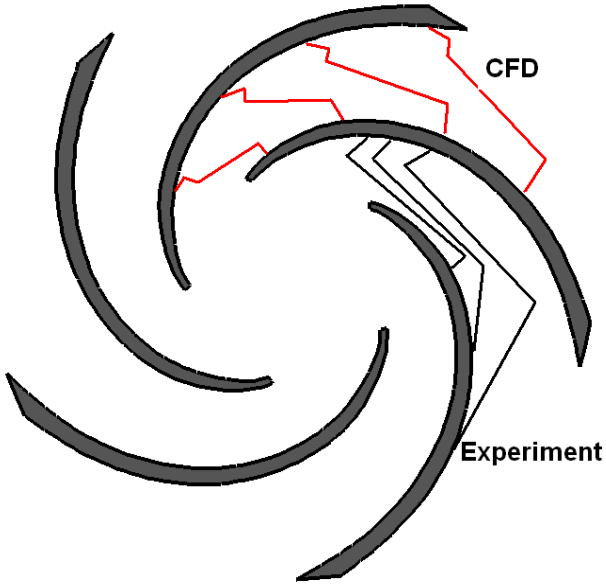

Figure 11 Absolute velocity magnitude distribution in the blade passage

As the depth increases (Figure B 3 through Figure B 6), CFD predicts a lower velocity magnitude at the entrance region than the LDA measurement. This feature clearly shows that CFD predicts steeper transition from axial momentum to radial momentum ('**a**' from Figure 12), while LDA shows more gradual change ('**b**' from Figure 12).

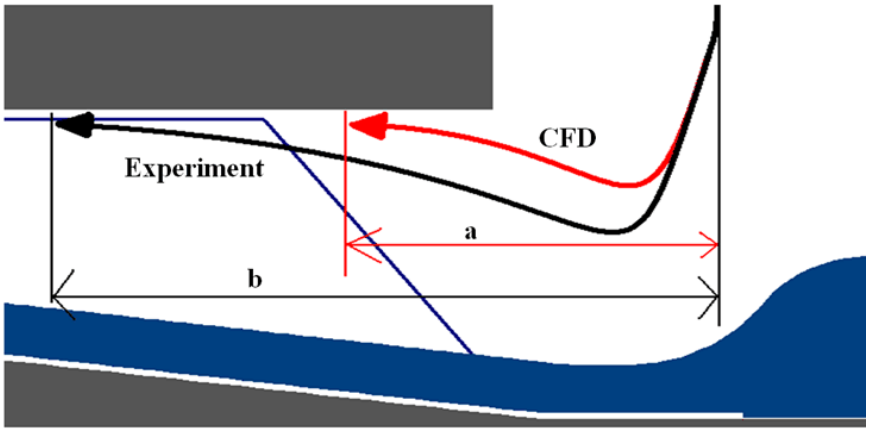

Figure 12 The radial distance for the momentum conversion

In other words, the velocity magnitude prediction in X-Y plane shows higher values than that from the LDA in the entrance region, which explains why LDA shows higher axial momentum in the same area where CFD prediction predicts less axial momentum.

This is thought to be due to the fact that CFD under-predicts the radial length over which the axial momentum converts itself into radial momentum. This change in momentum is affected by the geometry of the impeller, the surface roughness at the inlet, the cavitation characteristics, and the pump facility's characteristics. Since the CFD model used in this work does not have a model equation for cavitation characteristics, and the surface roughness at the inlet corner is rather guess work, the flow field near the entrance possesses discrepancies. Plus there is a limit to what CFD can reproduce of the pump facility's characteristics. The available boundary conditions that could be facilitated into the CFD analysis are either "target mass flow rate" or "mass flow rate". As shown in the previous section, "target mass flow rate with

pressure designation" provided the least accurate performance prediction and the unsteady characteristics predictions are less accurate than that of "mass flow rate" boundary conditions. Provided the fact that the best available models are used, the discrepancies between CFD and LDA are a minimum. However, once the flow is dominated by the radial momentum as the flow approaches the tip of the impeller, both CFD and LDA are in a good agreement. Even at off-design conditions (2/3 and 1/3 of design flow) CFD and LDA show fairly good agreement (Figure B 7 through Figure B 18). This illustrates the viability of the CFD since more distortion on the flow field results at off-design conditions. However, at the depth of z/h=0.47, CFD still predicts steep changes of momentum from axial to radial: deeper penetration of the incoming flow.

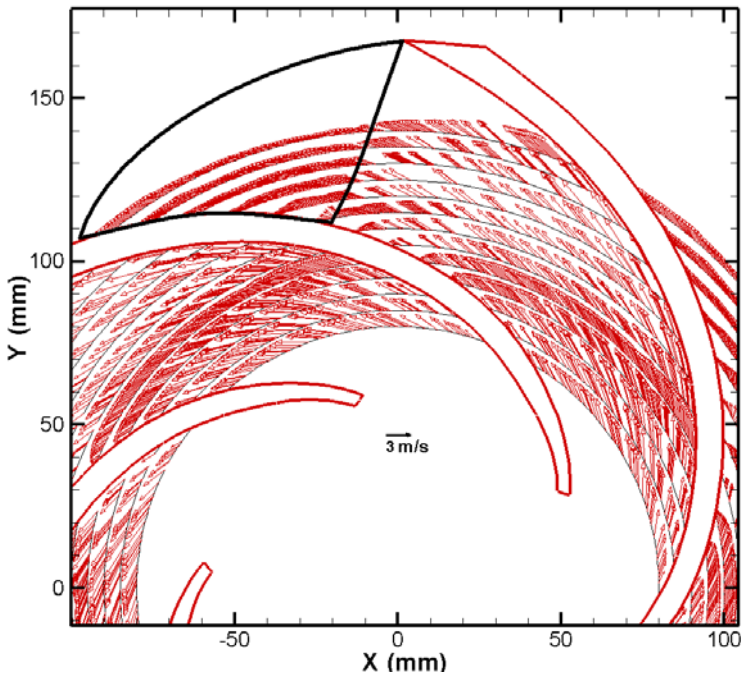

Figure 13 Flow at the cutaway region

At the 20 liter/sec operating condition in window B, Figure B 10 and Figure B12 show sudden increases in the tangential velocity and decreases in the radial velocity near the outlet region (Figure 13). The black pie-shaped region is where the cutaway zone is located. Due to the pump running under the designed capacity and the cutaway zone, the flow exiting the passage near the pressure side of the blade slows down due to the increase in the flow path height, but maintains its angular momentum. As Chen et al. (1990) stated in their work, the flow exiting the passage will circulate through the other passage. Only the passage which does not have any stall will have the flow exiting the passage. This stalled flow is more evident in Figure B12 where the CFD and the experiment show the same trends.

At 10 liter/sec, which is 1/3 of the designed flow condition, both the CFD and the experiment show the recirculation zone near the pressure side of the blade at the exit of the passage. However, this recirculation zone (stall) seems to occur only at window A (Figure B 13, Figure B 15, and Figure B 17) where the cut water is located. The schematic diagram of the path of this recirculation flow is shown in the Figure 14. At the window B position only the large magnitude of the stagnation is present (Figure B 14, Figure B 16, and Figure B 18).

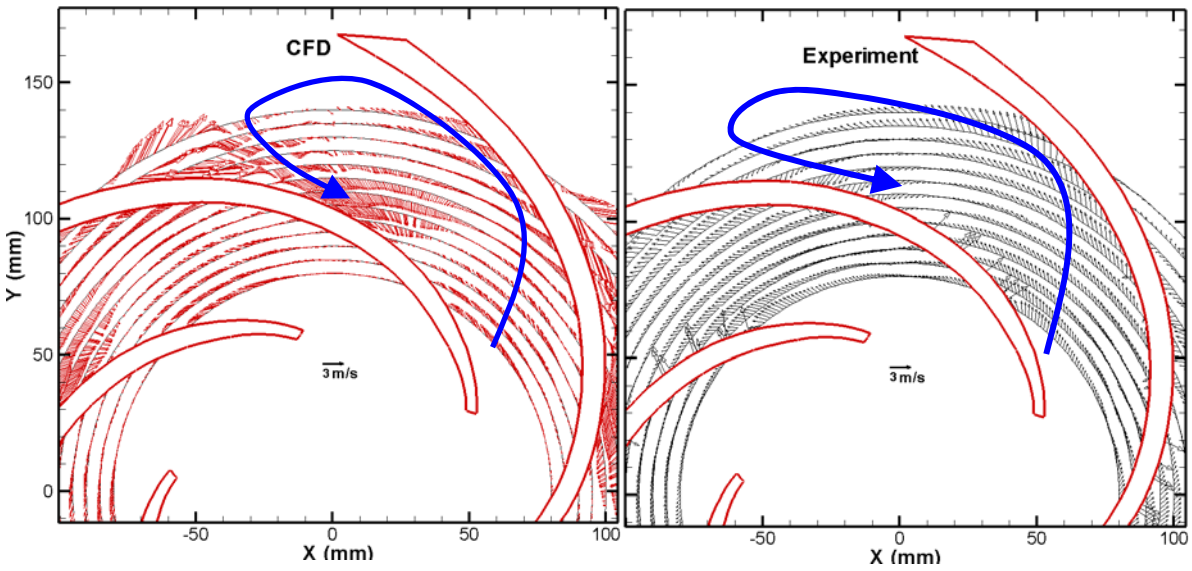

Figure 14 The stalled passage (window A)

At window A, the sizes of the backward flow region for the CFD and the experiment show good agreement. The difference is the magnitude of the backward velocity. The CFD predicts large backward flow even at the mid span region and the magnitude of the backward velocity decreases as the depth increases while the experiment shows almost no change in the magnitude.

Byskov et al. (2003) showed good agreement using an LES prediction at the design condition, but rather poor predictions at off-design conditions. They explained that their discrepancy resulted from the inlet pre-rotation which is hard to specify for the CFD simulation. Although this work uses a rather relatively coarser mesh grid than Byskov's CFD model, in this work the simulation appears to predict the flow field inside the pump better, not only at the design conditions, but also at the off-design conditions. One thing that should be emphasized is that the scope of this study is mainly on the phenomenon taking place at the tip and the bottom plate of the impeller.

b) Performance Data (Appendix C)

From Hossain's data, the performance curve is available for the pump used in this study. Although his data cover flow rates of 25 through 33 liter/sec, his data are complete enough to verify the CFD prediction of the pump performance. Comparing global parameters such as head and efficiency will assure the validity of the CFD predictions of the whole pump simulation as opposed to the independent CFD prediction of the impeller. The meshing of the housing was conducted by digitizing the original drawing of the housing. However, due to the corrosion inside the pump housing, the exact inner profile of the housing could not be depicted in the mesh model. From Figure C 1 to Figure C 12, the performance curve from the experiment and the CFD predictions are shown.

RPM of the impeller and the flow rate measured in the experiment could not be held at a constant value, while RPM and the flow rate were constant for the CFD simulation. For the purpose of comparing the flow rate and the head under different RPM, non-dimensional variables (ψ and φ) are used. The efficiency is defined as following equation.

$$\eta = \frac{\rho g Q \Delta H}{\Omega T}$$

Both graphs show good agreement. The CFD predicted an overall average of 3.14% more head than the experiment. Although the CFD simulation with the target-mass boundary condition shows overall average of 4.71% over-prediction, the prediction on the unsteady performance of the pump showed some discrepancy. This

will be discussed in the unsteady data validation section. Between the cases without balance holes (Figure C 3 and Figure C 5) and with balance holes (Figure C 4 and Figure C 6), the head coefficients are lower for the cases with balance holes. However the magnitudes of these head discrepancies are an order of magnitude smaller than the values. For the case with 0.91mm back clearance, the case with balance holes results in more head in the experiment, but the opposite is the case in the CFD prediction (Figure C1 and Figure C2). The clue for the reason why the balance holes reduce the head developed by the impeller can be found in Thorne and Bower's work (1973). In their work, they measure the front and the back pressure distribution of the 2 inch impeller with four 0.5 inch diameter balance holes. With balance holes, the head development on the front and the back of the impeller is smaller than that without the balance holes. The balance holes re-circulate the fluid from the back of the impeller to the front eye of the impeller. This re-circulation reduces the impeller exit pressure because the impeller energy is wasted providing energy to the flow through the balance holes, which also reduces the entire back pressure until the re-circulation and the pressure distribution is stabilized (Figure 15).

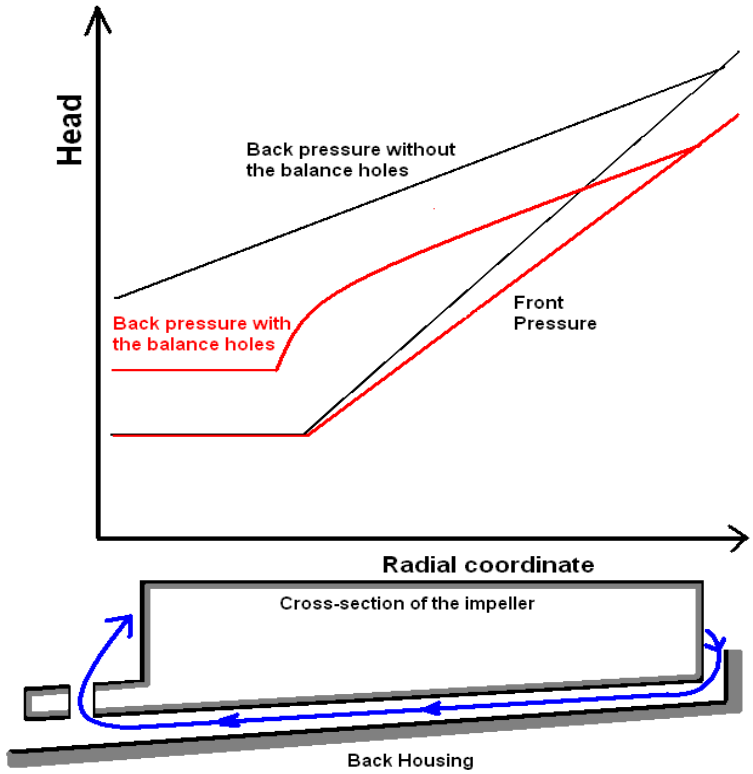

Figure 15 The schematic diagram of the flow recirculation through the balance holes

The pressure difference between the front and the back of the impeller is fundamentally the axial thrust. This is smaller for the impeller with balance holes.

The efficiencies of the cases with balance holes show lower values and the effect of the balance hole is more evident on the case with a back clearance of 1.87mm (Figure C 9 and Figure C 10) in the CFD prediction. However, in other cases, the CFD predicts almost no effect on the efficiency. It is speculated that the reason why the effect of the balance holes is minute is that the size of the balance holes (6.7mm) is a fourth of what the manufacturer specified to use, and thus the effects on the overall performance of the pump is small. Nonetheless, the effect of these small balance holes on the axial thrust is significant. The reduction in the axial thrust by having the balance holes is up

to %20 of the axial thrust without the balance holes. Further study on the axial thrust will be performed on the next section.

c) Axial Thrust Prediction (Appendix C)

As stated in a previous section, axial thrust data from Hossain's experiment is measured by integrating the pressure distribution on the front and the back of the housing. His methodology involved measuring the steady state pressures at 120 locations on six azimuthal locations evenly spaced so the pressure distribution could be measured on the entire front and back housing. However, for the purpose of comparing the CFD prediction and the experimental data, the CFD data is presented in the same way Hossain reduced his data. This produces a value different from that obtained using the fine mesh on the impeller. Figure C 13 through Figure C 18 show comparisons between axial thrust prediction and experimental results from Hossain's work. For the purpose of self-completeness, Hossain's data of pressure distributions are presented with CFD results from Figure C 19 to Figure C 54. Pressure distribution values are normalized pressure which is defined with following equation.

$$\text{Normalized Pressure} = \frac{\overline{P}}{\Delta P}$$

($\overline{P}$: averaged pressure and ΔP : pressure difference between the inlet and the outlet section)

Again the CFD results are presented only at the locations where Hossain made measurements. The reason why the specific pressure distributions on the front and the back of the housing are presented here is that, while the overall integration of pressure shows good agreement, this agreement could be achieved despite the trends of the pressure distribution being different between the CFD results and the experimental results. Integrated axial thrust prediction for the case with the 0.91mm clearance (Figure C 13 and Figure C 14) shows higher value than that from the experiment for both the one with balance holes and without balance holes. Corresponding pressure contour plots are Figure C 19 through Figure C 30). Axial thrust prediction of the case of the back clearance of 1.87mm and 3.17mm shows excellent agreement with the experiment (Figure C 15 through Figure C 18). The difference between the CFD and the experiment in Figure C13 can be attributed to the CFD predicting lower pressure on the outer rim where the area which is subject to the pressure is the outer rim where cutaway portions are than from the experiment. Also the pressure at the back of the housing from the CFD prediction on the middle span shows that a larger area is subject to higher pressure where the area on which the force from the pressure is exerted is mostly the impeller back face. In other words, while the CFD predicts higher pressure on the larger area, the experiment shows higher pressure on the smaller region. This is why the CFD is predicting much higher axial thrust than the experiment. This trend also can be seen in the other cases with 1.87 mm and 3.17 mm back clearance without the balance holes, but the difference in the back pressure mentioned above is much smaller in these cases. These smaller differences result in better agreement between the

CFD and the experiment. The probable explanation for the large difference in the back pressure in Figure C 19 through Figure C 24 is that the experiment used a brass ring with a specified thickness to create 0.91 mm clearance while the CFD mesh for the back clearance is generated with constant back clearance throughout the whole back face region. This author was aware of the fact that the back face of the impeller and the back face of the housing are not absolutely in parallel, however there was no way of measuring the exact clearance thorough the region of interest. The uncertainty in the size of the back clearance is thought to be the reason for the difference in the back face pressure distribution in the case with the back clearance of 0.91 mm without the balance holes. In the same sense, in the case with 1.87 mm back clearance, the difference in axial thrust between the CFD and the experiment can be explained, however as the back clearance increases from 0.91 mm to 3.17 mm, the difference becomes smaller. This may be due to the sensitivity of the effects of the back clearance to the size of the back clearance. As for the cases with balance holes (Figure C 14, Figure C 16, and Figure C18), the discrepancies are much smaller than the cases without the balance holes, or the prediction of axial thrust from the CFD almost coincide with the experimental data on the cases with the back clearance size of 1.87 mm and 3.17 mm. One could deduce the conclusion that the CFD prediction on the axial thrust is accurate on those cases, but the pressure contour plots from the experiment (Figure C 25, Figure C 27, Figure C 29, Figure C 37, Figure C 39, Figure C 41, Figure C 49, Figure C 51, and Figure C 53) show large drops in pressure on the outer rims at two azimuthal locations, which are absent in the CFD prediction. This

pressure drop is consistent in all cases with balance holes, and, although Hossain did not explained the reason for this pressure drop near the cut-water region, it could be attributed to the different flow field in the back clearance than that from the cases without the balance holes. The instantaneous flow field prediction from the CFD near the cut water in the back clearance will be discussed in the next section.

The pressure distribution in the experiment and the CFD for the cases without the balance holes shows that near the center in Figure C 23, Figure C 24, Figure C 35, Figure C 36, Figure C 47, and Figure C 48 the area covered with low pressure increases as the back clearance increases, while high pressure zones at the outer rim covers almost the same area for every back clearance cases. The difference in the area covered with low pressure zones between the case with the 0.91 mm back clearance and the case with the 1.87 mm back clearance is much smaller than that between the 1.87 mm back clearance case and the 3.17 mm back clearance. This is why there is a abrupt decrease in axial thrust as the back clearance increases from 1.87mm to 3.17mm (Figure C 15 and Figure C 17).

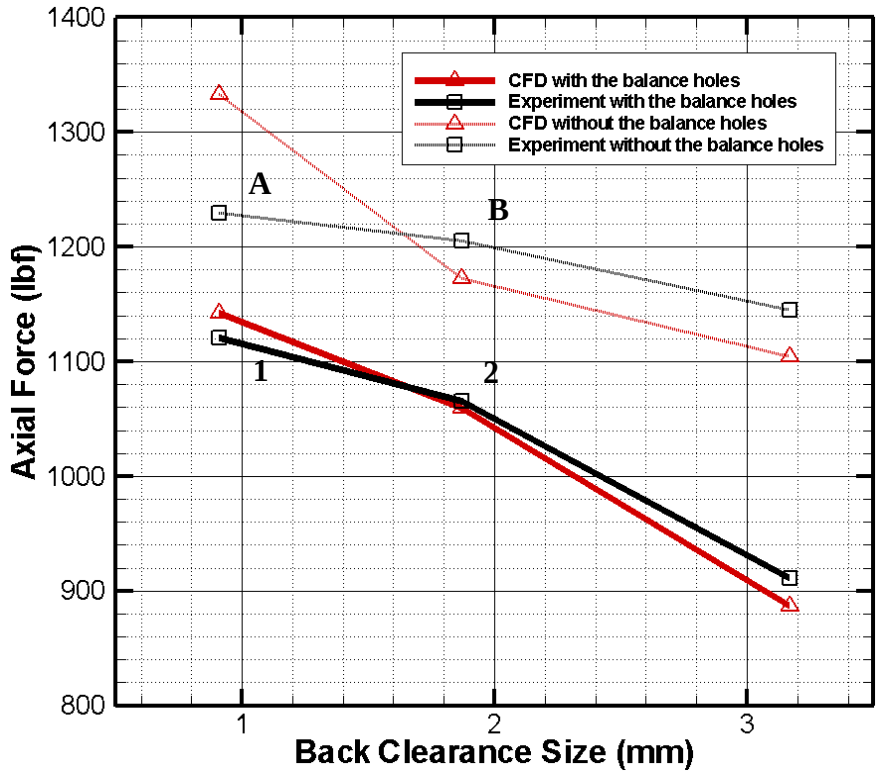

Figure 16 The rate of decrease in axial thrust in terms of the back clearance sizes at the design flow condition

This trend also holds for the cases with the balance holes. The experimental data shows that the rate of decrease of axial thrust in terms of the back clearance size change is the same for both the case with the balance holes (from '1' to '2' in Figure 16) and the case without the balance holes (from 'A' to 'B' in Figure 16), while the CFD predicts that the case without the balance holes is more sensitive to the change of the size of the back clearance size (larger drop of axial thrust with the same change in the back clearance size).

5 Other Forces Predictions (Appendix C)

This part will discuss about the forces acting on the impeller such as moments about X- and Y- axis and the actual axial force obtained using the entire computational grid in the impeller. The forces are calculated by integrating the scalar product of pressure and the normal vector to the surface over the impeller. The moments are calculated by integrating the cross-product of the forces on the impeller and the position vector to the point at which the force is applied.

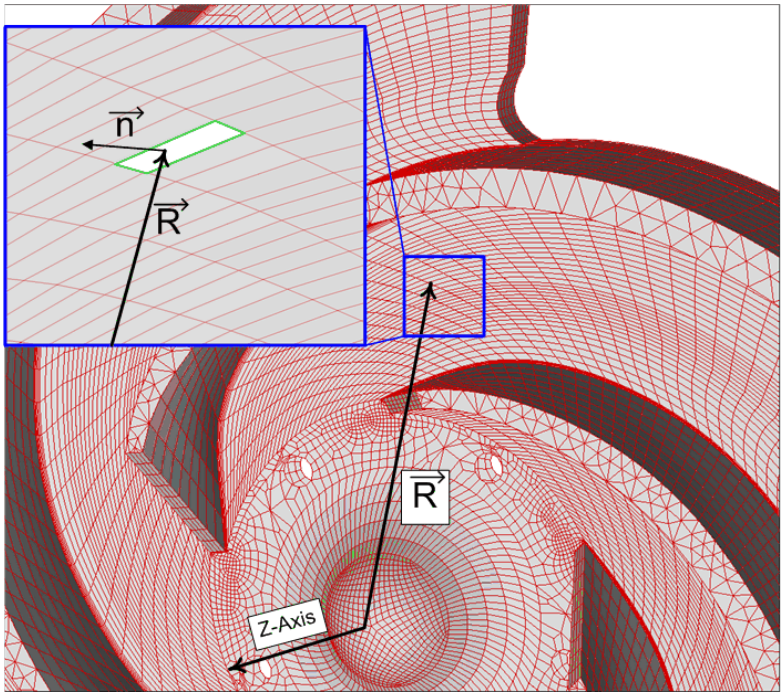

Figure 17 The element for calculating the forces and the moments acting on the impeller from the CFD

$$\vec{F} = \int p\vec{n}dA$$

$$\vec{M} = \int p\vec{n} \times \vec{R}dA$$

where $\vec{n}$ is a normal vector to the element surface (shown in green rectangle in Figure 17), $\vec{R}$ is position vector to the center of the element surface, and p is pressure acting on the element. The method of calculating the forces and the moments will provide one the exact loads exerting on the impeller.

Figures C 55 and C 60 show the moments and the forces acting on the impeller as functions of the flow coefficient, Q_s. Along with the CFD predictions, the experimental data from Hossain's work are shown.

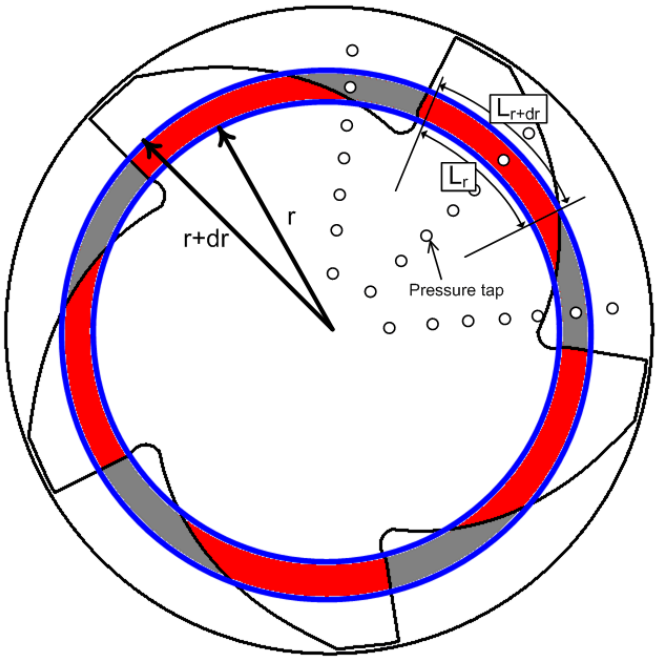

Figure 18 Hossain's methodology for taking the cutaway portion into calculating moment acting on the impeller

He calculated moments using the pressure distribution on the housing then, using the differential area (dA in following equation), he performed integrations over the front and the back housing to calculate moment.

$$dA = \frac{(L_r + L_{r+dr})}{2} dr \cdot \frac{A_{dr} - A'_{dr}}{A_{dr}}$$

where L_r is the arc length of the ring for a pressure tap at r, L_{r+dr} is the arc length of the ring for a pressure tap at r+dr, A_{dr} is the area of annulus at r (red and grey area combined in Figure 18Figure 18), and A'_{dr} is the cutaway area of the annulus at r (grey area in Figure 18)

His "steady-state" averaging did not accommodate phase averaging which enables one to designate the pressure tap whether it is placed on the cutaway portion or on the impeller back face. Hosssain used a methodology that was the time averaged pressure data on an azimuthal position at certain radial position was integrated over the segment of the annulus area. The effect of the cutaway can only be described by the area ratio, $\frac{A_{dr} - A'_{dr}}{A_{dr}}$. However, this way of calculating moment and force seems to over-predict the magnitude as shown in Figures C 55 and C 60. Figures C 55 and C 56 show the moments for the cases without balance holes. The conventional knowledge dictates that, as the flow rate approaches the optimum condition (Q_s = 0.0406), the pressure loading in each impeller passage is supposed to be equal. Hossain's data does not show that trait. However, due to the effect of the cutwater, there should be slight pressure

asymmetry existing at the azimuthal position of 56 degrees. Because the position of the cutwater not being at 45 degrees at which the moments about X- and Y- axis are the same, a higher moment is induced about the Y-axis due to a longer moment arm (r_x) for Y-moment (Figure 19).

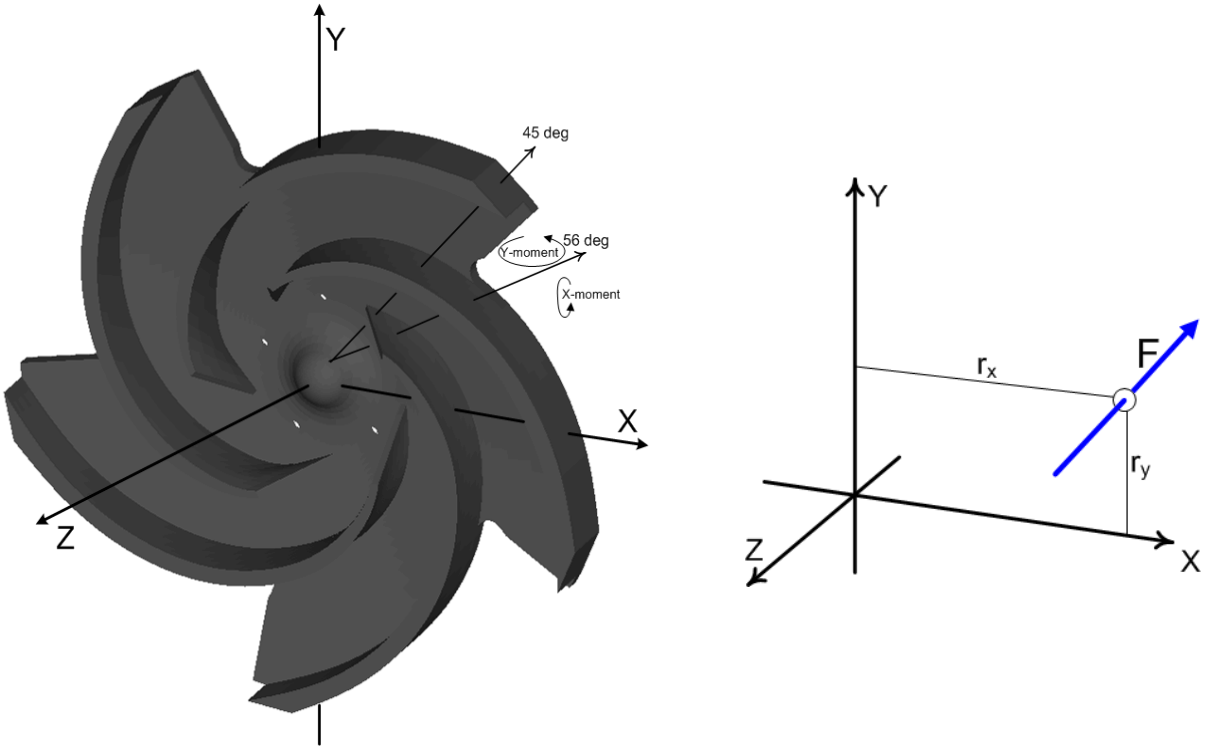

Figure 19 Moments due to the force acting at 56 degree (F is force due to pressure asymmetry on the impeller passages at the optimum operating condition).

This effect can clearly be seen in Figures C 55, C 56, C 57, and C 58 in that all the cases with different back clearance approach to zero moment, but the magnitudes have none-zero values. In the other flow rate conditions, for either case with or without balance holes, the Y-moment is larger than the X-moment, and the Y-Moment shows almost no changes as the flow rate changes.

Figures C 59 and C 60 show the axial forces acting on the impeller. The difference between the figures with which were discussed and the Figures C 59 and C 60 is that the later is from the direct integration of force on the impeller. As shown in the results from the experiments, the CFD simulation predicts a decrease in the axial force as the axial clearance increases. Moreover, the effect of the back clearance in the change of the axial clearance seems to be greater than the effect shown from the experimental data.

In summary, the overall axial thrust was reduced by 18% for the cases without balance holes and by 28% with balance holes by increasing the back clearance size. Having balance holes reduced the axial thrust by 29% for 3.17mm back clearance case. Given the fact that most of the industrial pumps run continuously for days or months, the longevity of the bearing can be extended because the axial loading can be reduced by maximum 30% by having larger clearance and balance holes. The torsion on the impeller shaft is also reduced by 2% by having larger clearance.

6 Unsteady Data (Appendix D)

This section presents pressure spectrum comparisons for the three back clearance cases with and without balance holes, and three flow rates. The comparison between the CFD and the experiment of the unsteady data for the case with the back clearance size of 1.87 mm without the balance holes was already discussed in the previous section. Figure D 1 to Figure D 18 show comparisons of pressure fluctuations at two points. These points are at the cut water (30 degrees azimuthal position) and the

housing (-30 degrees azimuthal position). The former is labeled as “tongue”, and the later is called “volute”.

The overall trend shown in the experimental results is that pressure peak at the normalized frequency of 1 at the tongue position is higher in amplitude than that at the volute position regardless the operating condition. As the flow rate increases, the overall amplitude of the pressure at the blade passing frequency also increases. The case with balance holes induces higher pressure fluctuation amplitude than that without balance holes. The CFD prediction of the first harmonic agrees well with the experimental data. However, while experimental data shows the peak at the running frequency (1/5 of normalized frequency: the rotational speed of the impeller), CFD prediction shows only the peaks at the blade passing frequency and its harmonics. It is believed that this is due to the vibration from the rotor, and CFD analysis did not take this into account. CFD also predicts the increasing amplitude of the pressure at the blade passing frequency as the flow rate increases. The increased pressure peaks on the case with balance holes also can be found on the CFD prediction. One common trait on the CFD prediction is that the pressure spectrum from the CFD agrees well with measurements on the cases without balance holes regardless of the size of back clearance. The CFD under predicts the amplitude of the pressure peak at the blade passing frequency in the cases with balance holes.

Since the CFD prediction of the flow field near the tip and the region near the bottom plate are in good agreement with experiment, further study of the flow field using CFD prediction is vindicated.

B CFD Flow Field Study Inside the Back Clearance

This section will discuss the complicated flow field around the impeller. The flow inside the back clearance behaves in the same manner which Soong et al (2003). have witnessed in their experiments. Their qualitative experiment showed a complex flow pattern inside the gap such as global recirculation throughout the gap and small vortices in vicinity of the gap outlet. The gap between the disks in their experiment was either shrouded partially at the periphery or opened to the external air. The flow behind the impeller with no cutaway sections, behaves in a similar way as Andersson et al. (2006) have shown in their LES prediction. The addition of cutaways on the impeller greatly alters the flow field. Especially where the flow from the impeller passage mixes with the flow inside the back clearance, the flow field becomes a highly complicated, 3-D unsteady flow. There are distinct flow patterns among the cases with different back clearance sizes. Balance holes also create a complex flow inside the back clearance. Gan et al. (1995) measured the tangential and the radial velocity inside the gap flow between the rotating disk and the stationary disk using an LDA system. In their quantitative experiment, the velocity components data for different Reynolds number and different configurations of the shroud at the radial outlet of the gap (either open or shrouded) showed two kinds of flow patterns which are described by Batchelor (1951) and Stewartson (1953). The shape of the shroud from their experiment was different than that of Soong et al., and their work did not consider the size of the gap.

Owen et al. (1989) suggested that the transition from the laminar flow to the turbulent flow occurred at the local Reynolds number ($\mathrm{Re}_r = \frac{\Omega r^2}{\nu}$) of 3 x10^5 inside the

gap flow between the rotating disks. In this study, the local Reynolds number at the radius where the balance holes are is about $3x10^5$. The flow is laminar in the region inside this radial position which covers a relatively small area compared to entire area of the back face of the impeller. Ergo, the assumption that the flow in most of the region is turbulent flow and the usage of turbulent model inside the back clearance is justified. The cases with balance holes show a much different flow pattern than the flow between the solid disks on which other workers have performed their research. The flow near the balance hole has higher velocity than that from the disk gap flow and the flow is definitely turbulent. Thereby, the necessity of defining different criteria for the transition arises in those cases.

The velocity components (radial and tangential velocity) presented in this study will be in the form of non-dimensional numbers, and the pressure data will be in the form of head (m).

Velocities: $\beta_r = \frac{V_r}{r\Omega}$ and $\beta_\theta = \frac{V_\theta}{r\Omega}$

Pressure: $H_p = \frac{P}{\gamma}$, where γ = specific weight, ρg .

1 The Cases without Balance Holes

a) Velocity Field

Conventional knowledge dictates the notion that, for a given flow with fixed total pressure, flow through a narrower passage has higher velocity than that through a wider passage according to conservation of mass. According to the Bernoulli equation

or the Euler equation the pressure increases as the velocity decreases when total pressure is constant. Thus as the magnitude of velocity increases the pressure decreases according to the Bernoulli equation. This notion has been adapted by the engineers who work on clearance flows in turbomachinery (Thorne et al., Stepanoff, Kurokawa et al., Bayley et al., and etc.). From the works of Bayley et al., this notion seems to be valid for the flow inside the clearance according to their experiment regarding the measurement of the pressure and the velocity distribution inside the gap flow between the rotating disks. Their results showed the trend that as the gap size increases, the pressure decreases at a given gap flow rate (constant total head and different velocities inside the gap). However, in their experiment, the gap size and the flow rate through the gap were controlled separately. They have found that, as the magnitude of the radial velocity increase, the pressure inside the gap also increase under a given gap size. This means that the pressure distribution is controlled by the total head supplied into the gap flow, not solely by the velocity or by the gap size. Their experiment setup was a through-flow coming from the periphery to the center eye exit, while the clearance flow in this work is mostly disk gap flow (Figure 20). The cases with the balance holes will be studied in the following section.

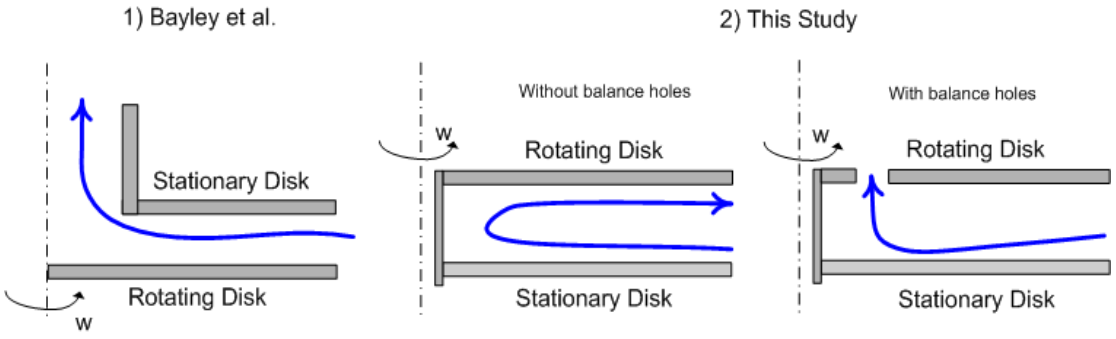

Figure 20 The schematic diagram of the gap flow for the work of Bayley et al. (1964) and for this study

In appendix E, plots of β_θ and β_r based upon the CFD results are shown. These data are the velocity distribution inside the back clearance encompassing from the radial center to the periphery of the impeller, which includes the cutaway section. The 3-dimensional velocity data and the pressure data (presented earlier) are averaged azimuthally and the velocity profile is presented at three radial positions which are thought to represent the velocity profile inside the back clearance. The first radial position is in the middle of the solid disk, the second position is where the cutaway section starts, and the third position is in the middle of the cutaway section (Figure 21). In the figures of β_r, the negative value represents the inward flow and the positive value represents the outward flow, and the z/s value of 1 is the surface of the impeller (rotating disk) and the z/s value of 0 is the housing surface (stationary disk).

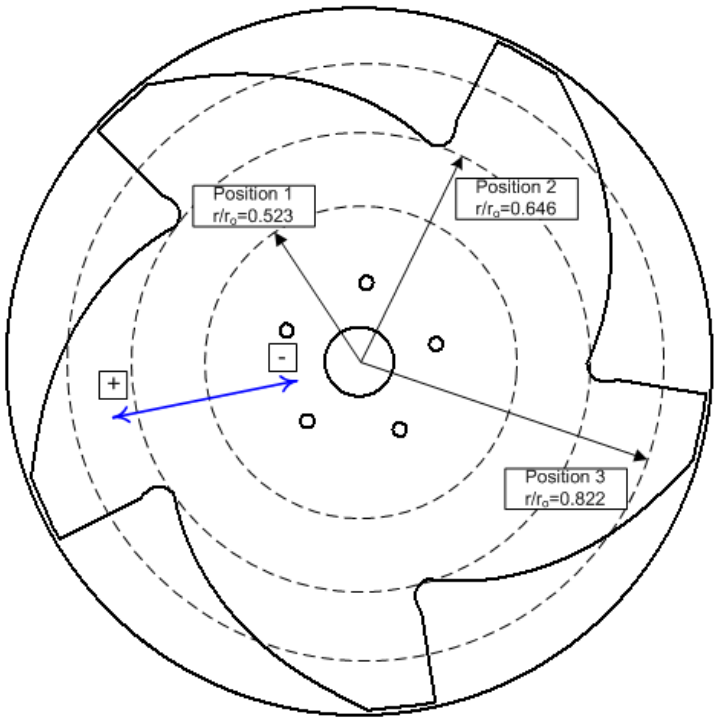

Figure 21 The schematic diagram of the positions for the velocity profile plots

Figure E 1 through Figure E 18 show the velocity profile for the impeller without balance holes. Figure E 1 through Figure E 9 (the plots of β_θ) show the gradual transition of the fluid speed from zero to the local rotation speed of the impeller. This trend indicates that the viscous drag force affects the region up to the stationary disk. However, one can clearly see the boundary layer near the rotating disk and the stationary disk, where the slopes of the velocity are the same and larger than that in the core section. This trend seems to be a mixture of what Bachelor and Stewartson have predicted. Bachelor predicted that, on the flow within the gap between one disk being stationary and the other being rotating, there will be a definite signature of a boundary layer on both disks and the core flow will rotate with the same angular velocity. As a

result, the radial inflow and the radial outflow will be limited inside the boundary layer and at higher Reynolds number these trend becomes more evident. Later, Stewartson proposed that the flow near the rotating disks will have the same trends as Bachelor predicted, but the flow near the stationary disk will be under little influence of the rotating disk, hence the profile of the velocity near the stationary disk will possess such a shape that it will satisfy the non-slip condition near the wall. Gan et al. claimed that the flow as Bachelor predicted can be found in the situation where the disk gap flow is surrounded by a periphery shroud which is utilized in their experiments, while the Stewartson-type flow can be found in the open gap flow. In the plots of β_θ, the velocity profile does not show that the core flow has the same tangential velocity as Bachelor (1951) predicted, but the Von Karman type boundary layer can be found on both the stationary and the rotating disks. The profile of β_θ at the core seems to agree what Stewartson (1953) predicted, and there is no non-zero β_r zone as he also predicted. In Figure 22 and Figure 23, above statement is summarized.

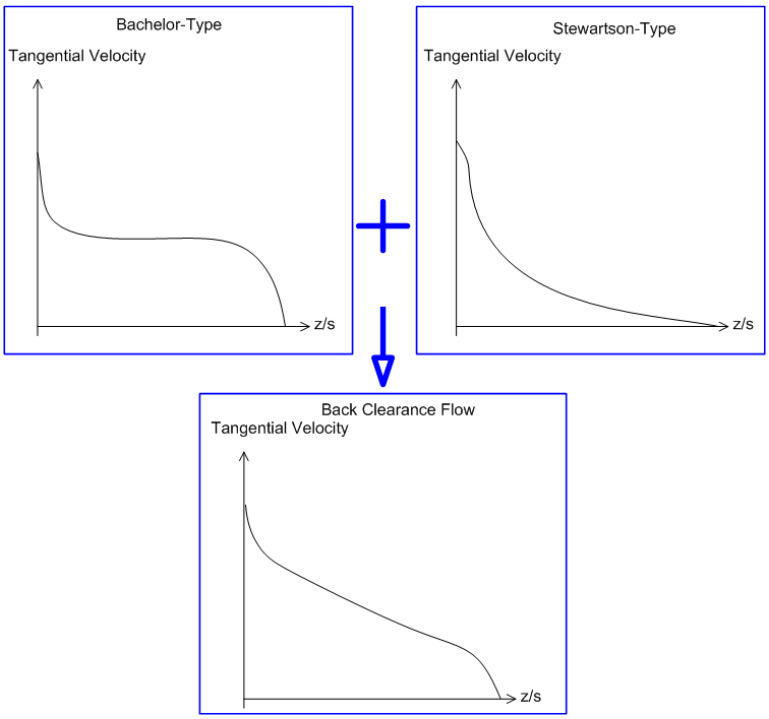

Figure 22 Tangential velocity profile trends

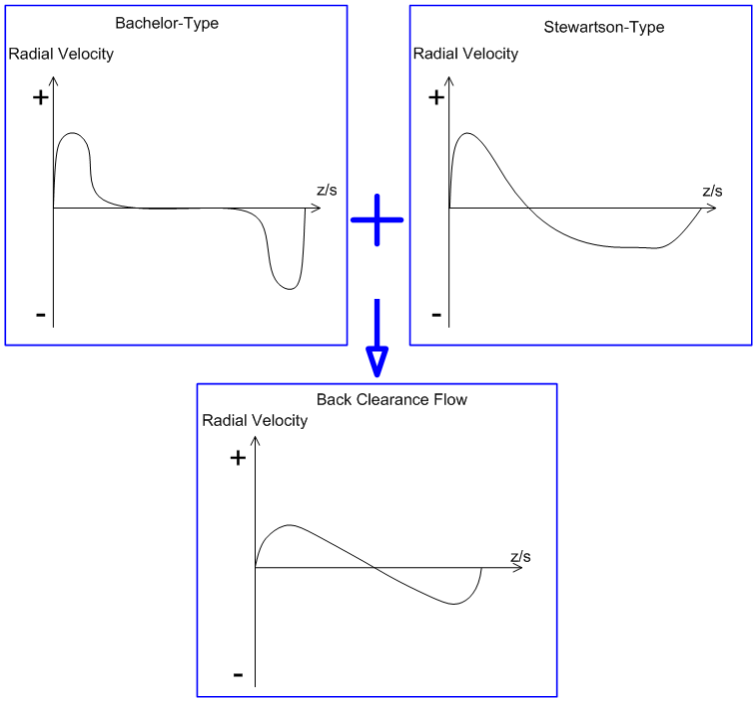

Figure 23 Radial velocity profile trends

In these plots, the same velocity profile can found in Andersson and Lygren's work which involved open disk gap flow. The reason why the velocity profiles have such shapes as shown in Figure 22 and Figure 23 can be attributed to the interference of the boundary layers on both the rotating disk and the stationary disk due to the smaller axial distance than the two boundary layer's heights combined. The plots of β_θ show that the magnitude of β_θ is reduced as the radial location approaches to the axis of rotation. This trend coincides with the experimental work of Gan et al. even though their work involved a non-dimensional gap size of 0.12 while the gap size in this work ranges from 0.005 to 0.018. While Gan et al. do not explain the reason for this relationship between β_θ and radial coordinate, this author suspects that the local Reynolds number plays a certain role in that relationship.

From Figure E 10 to Figure E 18, one can find that the magnitude of β_r increases as the back clearance size increases at the radial position of r/r_o=0.523 and r/r_o=0.646 where there is no cutaway section. At the cutaway section (the radial position of r/r_o=0.822), β_r increases in magnitude, and the shape of profile changes as the back clearance size increases. This effect of the back clearance size (gap size) can also be found in the narrow gap case data in Andersson and Lygren's work.

The plots for β_r show the important trait that the shape of the radial velocity profile does not change as the radial position changes in that the β_r profiles at both positions overlap. This means that the cutaway portions have almost no effect on the radial velocity profile and the leakage flow rate inside the solid disk gap does not change. However, in Figure E 16 though Figure E 18 which are the plots of the cases

with 3.17mm back clearance, the β_r profiles show that the transition of the profile from that at r/r_o=0.822 to that at r/r_o=0.523, and the profile at r/r_o=0.523 resembles that from Bachelor's prediction.

b) Pressure Field

As for the pressure distribution inside the back clearance, one thing that should be emphasized is that the static pressure inside the passage is directly propagated to the back clearance in vertical (axial) direction as the flow passes just above the start of the cutaway. Inside the radial position of the indentation (step at the end of the impeller face), the total pressure converts its whole magnitude into the static pressure since the velocity head inside the clearance is several orders of magnitude smaller than the pressure head. Outside the radial position of the indentation (the ears of the impeller), the total pressure distribution shows the equi-total pressure surface spread out below the ear of the impeller (Figure 24).

One of the causes that results in the difference in the pressure inside the back clearance for the different axial clearances is the differences in the supply total pressure or the static pressure from the impeller passage. Since the geometrical differences exist among three back clearance cases in the size of the axial clearance, and the impeller passages are the same for three cases, the total pressure developments through the passage are supposed to be the same. From the work of Plutecki et al., however, total head (total pressure head) decreases as the axial clearance increases for the semi-open impeller. Also, according to Gyulai et al., there is an optimum position for the impeller to produce the maximum head from the impeller, and the head decreases as the axial

position of the impeller moves away from the optimum position. Figure E 46 through Figure E 51, the instantaneous dynamic head (velocity head defined as $H_v = \frac{1}{2g}(V_x^2 + V_y^2 + V_z^2)$) distribution at the exit of the impeller is shown for different axial clearances and different flow rate.

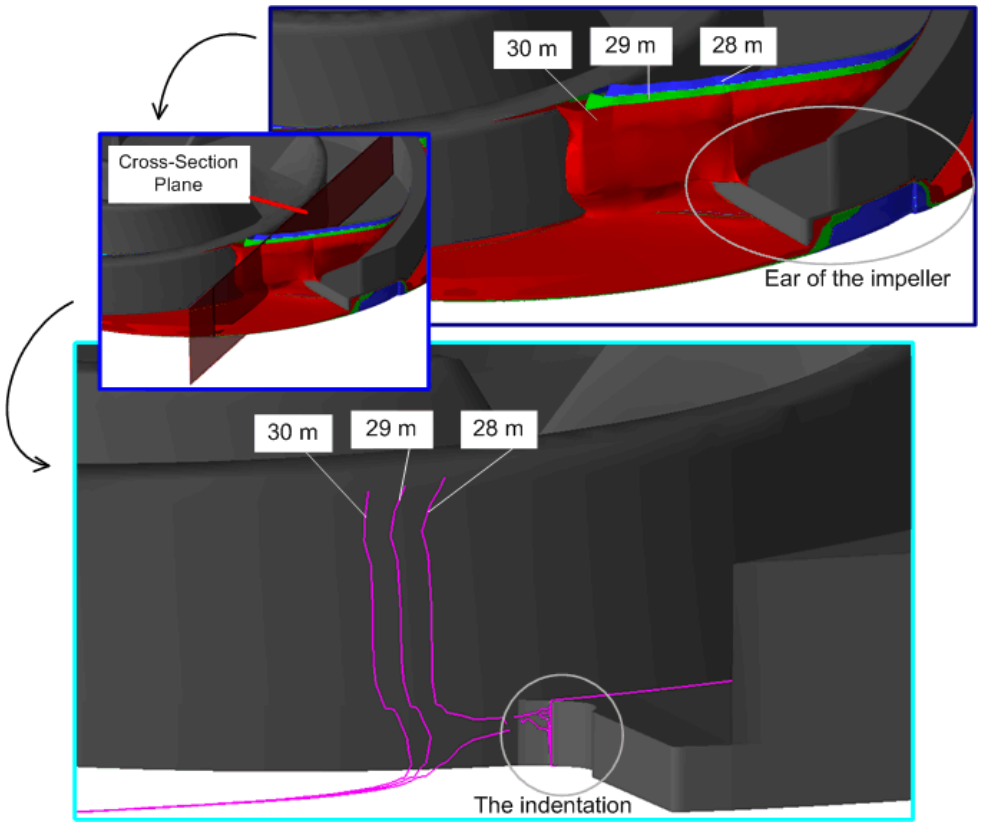

Figure 24 Total pressure propagation from the impeller passage to the back clearance (total pressure shown in head, m)

This clearly shows the axial position has a definite effect upon the flow field, and this effect is thought to cause the decrease in the total pressure head. From the position

where the back clearance flow is supplied with the impeller passage pressure, the pressure head decreases as the radial position approaches to the center of the impeller. This is due to rotation of the liquid in the clearance (Stepanoff, 1948). The relationship between the pressure decrease and the radial position can be explained by using following equation and Figure 25.

$$H_{EU} = \rho(UV_\theta - U_{in}V_{\theta,in}) \tag{10}$$

$$P_t = P_{t,in} + H_{EU} - L \tag{11}$$

$$V_\theta = W\cos\beta \tag{12}$$

$$V_m = W\sin\beta \tag{13}$$

$$\Delta(p + \frac{1}{2}\rho {V_m}^2 + \frac{1}{2}\rho {V_\theta}^2) = \Delta H_{EU} - L \tag{14}$$

$$\Delta(p + \frac{1}{2}\rho {V_m}^2 + \frac{1}{2}\rho {V_\theta}^2) = \rho\Delta\{U(U - W\cos\beta)\} - L \tag{15}$$

Since ${V_m}^2 = {W_m}^2$

$$\Delta(p + \frac{1}{2}\rho {W_m}^2 + \frac{1}{2}\rho {V_\theta}^2) = \rho\Delta\{U^2 - UW\cos\beta\} - L \tag{16}$$

And, using (12) and (13),

$$\Delta\left\{p + \frac{1}{2}\rho(W\cos\beta)^2 + \frac{1}{2}\rho(U - W\sin\beta)^2\right\} = \rho\Delta\{U^2 - UW\cos\beta\} - L \tag{17}$$

$$\Delta p = \frac{\rho}{2}\Delta\{2U^2 - 2UW\cos\beta - (W\cos\beta)^2 - (U - W\sin\beta)^2\} - L \tag{18}$$

$$\Delta p = \frac{\rho}{2}\Delta\{U^2 - W^2\} - L \tag{19}$$

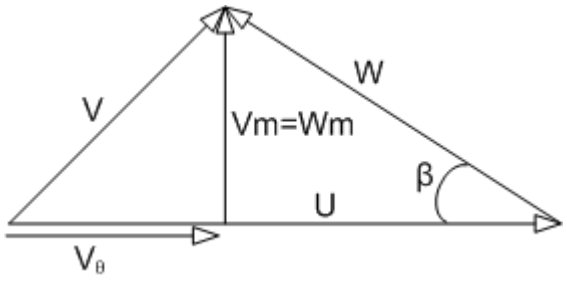

Figure 25 The velocity triangle at arbitrary position inside the back clearance

Equation (19) states that the static pressure drop is directly related to the local impeller velocity ($U = rw$) and the magnitude of the relative velocity. Because the magnitude of the relative velocity is an order of magnitude smaller than the local impeller velocity, one can deduce that the magnitude of right hand side of the equation (19) is dominated by the local impeller velocity terms. Thus, as the radial position goes from the periphery to the center of the impeller, the local impeller velocity reduces and the static pressure reduces.

As stated above, the static pressure at the back clearance is almost equal to that of the passage at the same radial position, and this impeller passage pressure is larger for the case with smaller back clearance. Figure E 36 through Figure E 39 show the pressure distribution in both the impeller passage and the back clearance at different flow rates. On the graphs, the cutaway section is located from about r/r_o=0.7 and beyond. The plots for back clearance flow are generated by averaging 3-D velocity-pressure data azimuthally and extracting the data from the core of the back clearance. The impeller passage flow plot is from averaging the 5 middle of the impeller passages (Figure 26). Due to averaging process, the local picture of the axial pressure propagation is lost. This is why the pressure head from the impeller passage and the

back clearance does not overlap each other at r/r_o=0.7. However, in Figure E 40 through Figure E 42 the cross-sections of the impeller passage show that the pressure from the impeller passage is directly propagated to the back clearance.

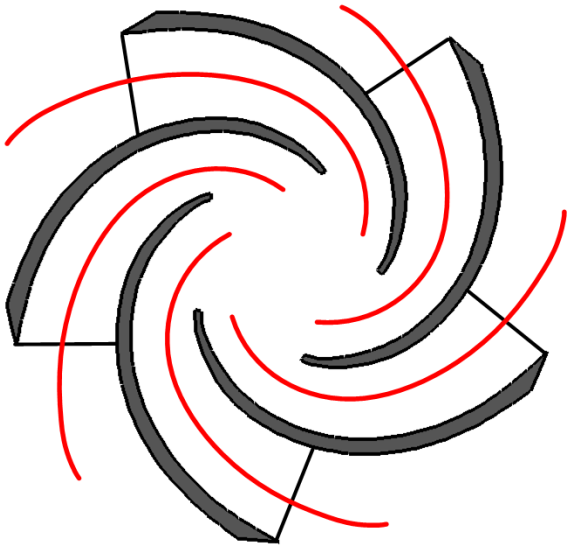

Figure 26 The position where the cross-sectional picture of the impeller is taken

Figure E 36 through Figure E 39 clearly shows that the pressure head for the smallest back clearance case in the impeller passage is the highest and this highest head is the cause of the highest head in the back clearance.

Another factor that causes the pressure differences inside the clearance among the cases with different back clearances is the differences in the velocity magnitude inside the back clearance, which is, as shown in the previous part, as the back clearance decreases the magnitude of the velocity also decreases. As Soong et al. (2003) had shown in their experiment, the smaller gap acts as a blockage to the radially incoming leakage flow and slows it down, while the larger gap facilitates easier introduction of

the leakage flow into the back clearance. Due to this blockage effect of the small clearance, the conversion of the pressure head into the velocity can not be facilitated as easily as the case with larger clearance.

2 The Cases with Balance Holes

a) Velocity Field

As mentioned in a previous section, the balance holes reduce the axial thrust by by-passing the flow from the periphery of the impeller to the inlet of the impeller. In contrast to the solid impeller where the flow with high head supplied from the exit of the impeller stays inside the clearance only to be reduced in magnitude by the rotation of the fluid. For the cases with the balance holes, the balance holes play important roles in reducing the axial thrust by consuming high pressure head to provide the through flow. The exact flow field inside the back clearance with the balance holes has not been, to this author's knowledge, revealed. Only the pressure distribution data which is averaged azimuthally are available from the works of Thorne (1973), Trout (1962), Kurokawa (1994), and Matsui (2007). While the flow inside the back clearance without the balance holes shows one large re-circulation zone due to the centrifugal effect on the rotating wall, the flow with the balance holes shows a through flow without the re-circulation. The centrifugal force used to create the radial outward flow for a closed impeller is overwhelmed by the pressure gradient between the pressure at the exit of the impeller and the inlet of the impeller (Figure 27) for the impeller with balance hole.

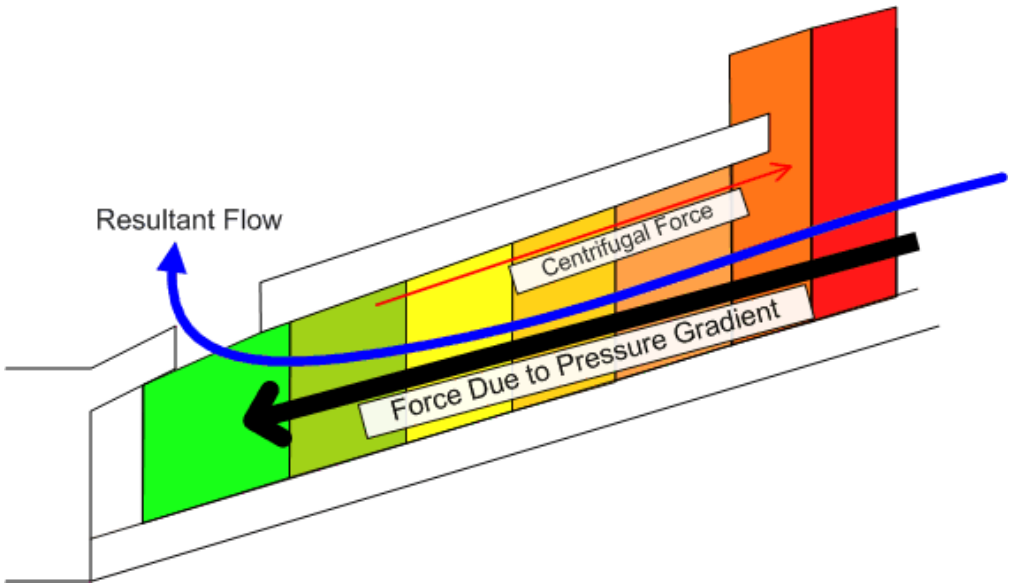

Figure 27 The schematic diagram of the forces inside the back clearance to induce the through flow inside the back clearance

From Figure E 19 to Figure E 27, non-dimensional tangential velocity plots are shown. The cases with balance holes show that the tangential velocity profiles and its magnitude for three radial positions are similar. At r/r_o=0.822, the tangential velocity profile reveals that the magnitude is similar to that without the balance holes. The thickness of the boundary layer is larger on the stationary disk than that on the rotating side. This trait shows that the influence of the balance holes cease to exists on the ears of the impeller.

If the plots of the tangential velocity profiles for both the cases (with and without the balance holes) are overlapped, one can clearly see that the thickness of the boundary layer on the rotating disk in the cases with balance holes is much smaller than that in the cases without the balance holes (Figure 28). This is due to the fact that the fluid present with no balance holes has a larger residence time in the back

clearance, allowing the rotating impeller the ability to impart more tangential momentum to the fluid resulting in a thicker boundary layer for the tangential velocity.

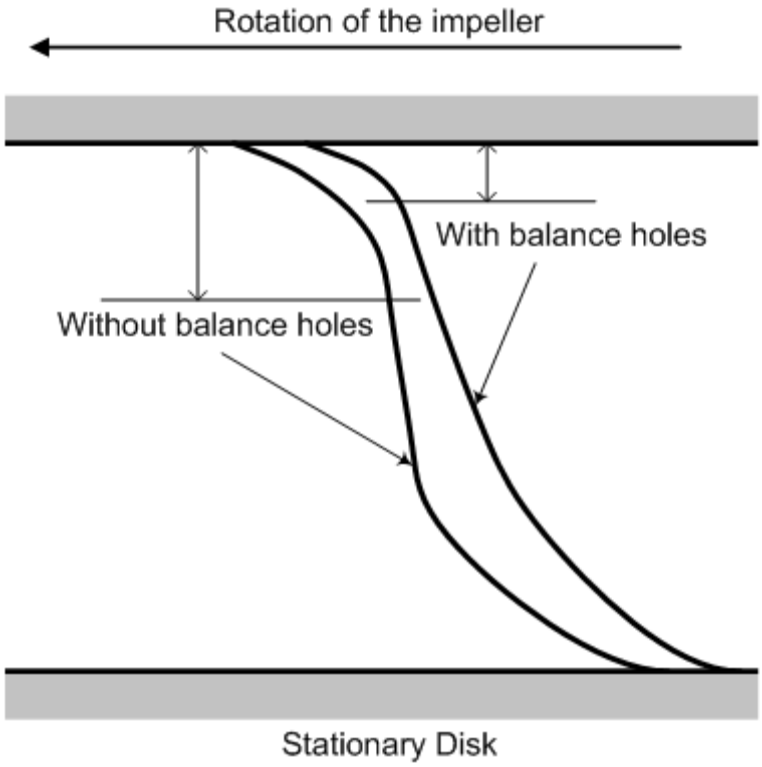

Figure 28 The differences in the tangential velocity profile inside the back clearance

The cases with a 3.17 mm back clearance (Figure E 25 through Figure E 27) show the definite trait that can be seen in the Bachelor's work (Figure 22) which involved the disk gap flow with shroud. The core (z/s=0.4 through z/s=0.85) rotates with same angular velocity and non-dimensional tangential velocity of 0.8, which is a typical behavior of the forced-vortex flow.

From Figure E 28 to Figure E 36, the plots of the non-dimensional radial velocity are shown. Due to the global re-circulation inside the back clearance (from the exit of

the impeller to the balance holes), the symmetric velocity profiles that can be found in Figure E 10 through Figure E 18 are no longer present. The radial velocity has an overall negative sign which represents the flow toward the center of the impeller, and, due to the centrifugal effect on the rotating disk, the velocity profile shows a much smaller radial velocity magnitude on the rotating disk than at other axial locations. All the cases with balance holes show that the magnitude of the radial velocity increases as radial position approaches to the center of the impeller. On the cases with a back clearance size of 3.17mm (Figure E 34 through Figure E 36), for a fixed balance hole size results in the balance hole restricting the flow instead of the clearance area. Hence, the radial inward velocity is decreased with increased clearance. Due to relatively large gap size (larger fluid volume in the gap), the radial inward mainstream which has limited momentum could not overcome the centrifugal force on the rotating side and the radial flow reveres its direction on the rotating disk side. In other words, part of the radial inflow passes through the balance holes into the impeller eye while the rest flows radially outward along the back side of the impeller.

b) Pressure Field

Figure E 40 through Figure E 42 shows the static pressure head in the impeller passage and the back clearance. The pressure heads inside the impeller passage with the balance holes show almost no difference to that without the balance holes. However, the effect of balance hole on the pressure inside the back clearance is clearly seen. The global re-circulation shown in Figure 15 generates a pressure gradient from the head at the impeller exit to the head at the inlet of the impeller. Theoretically, the

head inside the back clearance should approach the head at the pump inlet as the radial position approaches to zero. However, due to the finite number of the balance holes and the radial position of the balance holes not being at the center of the impeller, this pressure relief inside the back clearance can only happen on the location limited to the vicinity of the balance holes. Moreover, the flow inside the large back clearance find its way to the balance holes with less secondary flow (swirl inside the balance holes), and causes a more effective pressure relief. This is why the pressure head for the case with 3.17mm back clearance shows the lowest value at the balance holes. In other cases (0.91mm and 1.87mm back clearance) where the smaller gap restrict the flow to the balance holes, there are sudden decreases in the pressure head at the radial position of 0.24 where the center of the balance hole is located, then the pressure head does not decrease further as the radial position approaches to the center of the impeller.

The difference in the pressure head for different back clearance sizes is caused by the same effect explained in the previous section. The lower pressure head developed in the case with large back clearance is propagated to the back clearance vertically, and generates lower pressure overall inside the back clearance, while the high pressure head in the case with small back clearance generates high back pressure. Added to this effect, as shown in the previous part, the magnitude of the through-velocity inside the large back clearance possesses high values, which convert more pressure energy into kinetic energy than the cases with smaller back clearance (smaller velocity magnitude).

c) Flow through Balance Hole

In this part, the empirical equation for calculating the leakage flow through the balance hole will be presented. Usually the leakage flow rate through the balance holes is used in calculating the loss and the effectiveness of the balance holes. However, because it is hard to measure the precise flow rate through the balance hole due to the nature of the rotating impeller, the common practice is to perform a leakage estimation as carried out by using the pressure difference between the inlet and the outlet of the balance holes and the rotating pipe flow or the orifice equation (Hossain (2002) and Kurokawa et al. (1994)).

In Figure 29, a comparison is made between the leakage flow rate prediction using CFD and the formula from the work of Kurokawa et al., which is

$$Q_b = (\pi r_o^2)\sqrt{2\Delta P_b / \rho}\ .$$

The formula did not take into account of the effect of the back clearance size nor the effect of the impeller rotation.

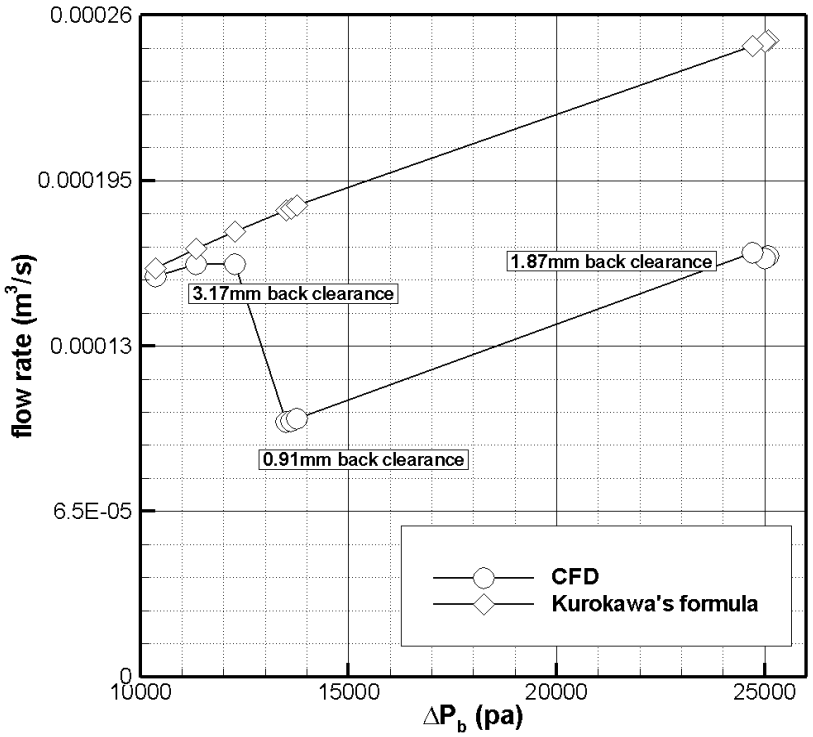

Figure 29 The leakage flow rate prediction from the CFD and the formula of Kurokawa et al.

Figure 29 clearly shows the discrepancy between Kurokawa's equation and the CFD prediction which facilitates the effects of the back clearance size. It appears that the CFD prediction for the case with the 3.17mm back clearance produces results that most agree with Kurokawa's prediction, however, with different back clearance sizes, the prediction using Kurokawa's equation results are much difference than the CFD prediction. However, one thing to be emphasized from the work of Kurokawa et al. is that the rate at which the flow rate increases with increasing ΔP_b is almost the same as that from the CFD predication. This trend can be found in the results for the cases with the 0.91mm back clearance and the 1.87mm back clearance. Ergo, by adding the effect of the back clearance into the equation that utilizes the same concept that Kurokawa et

al. used, more precise predictions of the leakage flow rate through the balance holes can be achieved.

To create the non-dimensional empirical equation, the parameters that affect the leakage flow rate should be addressed. This author made an assumption that following parameters will have the largest effects on the flow rate.

Ω : Angular velocity of the impeller (rad/sec)

d_b : The diameter of the balance hole (m)

s : The axial clearance (m)

ΔP_b : The pressure drop between the inlet and the outlet of the balance hole (pa)

r_o : The radius of the impeller (m)

γ : Specific weight of the fluid (kg/m·s^2)

One can use the Buckingham pi theorem to create the non-dimensional grouping, but this author utilized the non-dimensional parameters that are commonly used in the pump researches.

The first parameter is the specific flow which is defined as

$Q_{s,b} = \dfrac{Q_b}{\Omega r_o^3}$, where Q_b is the leakage flow rate through the balance hole. This parameter takes into account of the effect of the rotational speed of the impeller.

The second parameter is the gap ratio which is defined as

$E = \dfrac{s}{r_o}$, which contains the effect of the back clearance size.

The last parameter is the head coefficient for the pressure drop between the inlet and the outlet of the balance hole, and defined as

$$\mathrm{X} = \frac{\Delta P}{d_b \gamma}.$$

These three parameters will be related in the following manner.

$Q_{s,b} = A_1 \cdot E^{A_2} \mathrm{X}^{A_3}$, where A_1, A_2, and A_3 are the constants.

Using a curve fitting software (Tablecurve 3D), the three constants are calculated, and the empirical equation for the specific flow, $Q_{s,b}$ in terms of the gap ratio, E and the head coefficient, X is obtained

$$Q_{s,b} = 3.8E^{0.422}\mathrm{X}^{0.318} \text{ or } \frac{Q_b}{\Omega d_b^3} = 3.8\left(\frac{s}{r_o}\right)^{0.422}\left(\frac{\Delta P}{d_b \gamma}\right)^{0.318}$$

The flow rate through the balance holes is

$$Q_b = 3.8\left(\Omega r_o^3\right)\left(\frac{s}{r_o}\right)^{0.422}\left(\frac{\Delta P}{d_b \gamma}\right)^{0.318}.$$

Figure 30 shows the 3-d plot of the flow coefficient $Q_{s,b}$ in term of X and E along with the CFD data for every operating condition dealt in this work. As one can see from the plot, the pressure drop coefficient, X, alone can not predict the precise leakage flow rate, but, with the gap ratio E, the function can now compensate for the back clearance size effect.

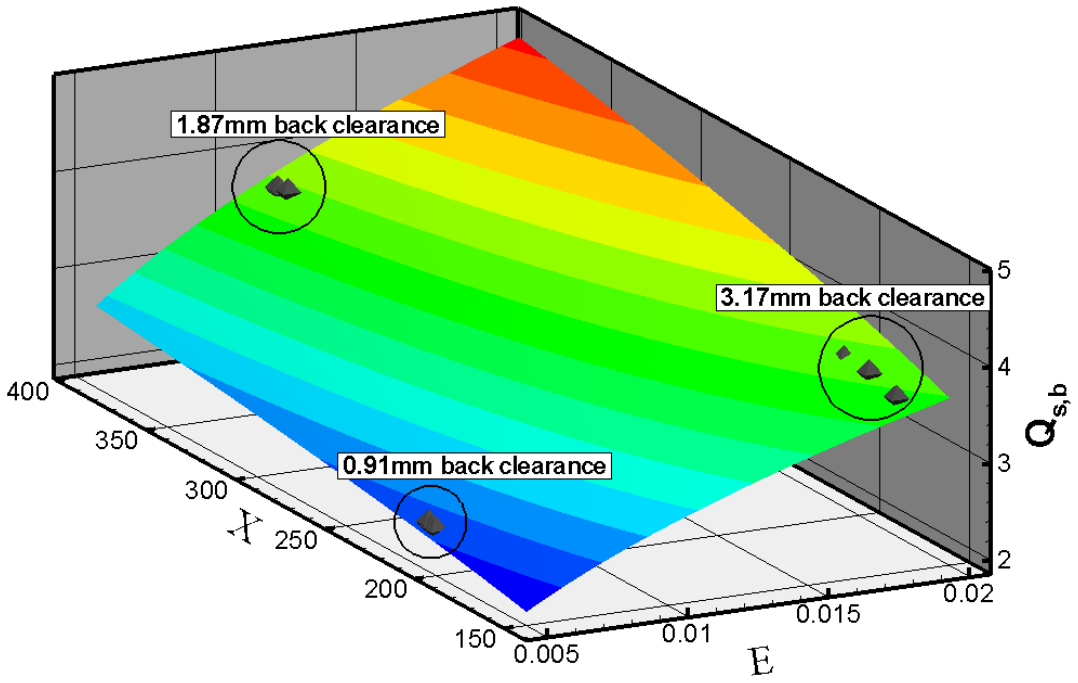

Figure 30 The 3-d plot of the curve-fit function of Qb

V CONCLUSION AND RECOMMENDATIONS FOR FUTURE WORK

The CFD simulations on the centrifugal pump with a semi-open impeller are performed. The CFD model is validated using the LDA data of the flow inside the passage, the performance data, the unsteady pressure fluctuations, the pressure distribution on the housing, and the axial loading on the impeller. The CFD model showed excellent agreement with the experimental data for both the steady-state data and the unsteady data. 3-D unsteady simulation of the pump revealed the complicate nature of the back clearance flow interacting with the impeller passage flow via the cutaway section. Moreover the flow through the balance hole was able to be simulated. The 3-D simulation could provide the forces and the moment acting on the impeller, which was conventionally calculated by using the pressure data from the housing and the integration using the integral surface of dA based on Hossain's work.

The conventional knowledge of the way of reducing the axial thrust by having smaller axial clearance is not found to be the case for the pump with a semi-open impeller with cutaway sections. The pressure inside the impeller passage is smaller for the pump with larger axial clearance, which reduces the axial loading of the impeller. The velocity head inside the back clearance becomes larger with larger back clearance, which converts pressure head into velocity head and further reduces pressure head.

Based on the CFD model which is already validated, the empirical model of the leakage flow rate through the balance hole is established. This leakage model includes not only the pressure drop across the inlet and the outlet of the balance hole, but also the rotational speed and the size of the back clearance.

This work simulated the complicate back clearance flow and the flow through the cutaway section based on the LDA data and many global parameters such as head and efficiency. Although the CFD model is validated against available experimental data, since no experimental data for the back clearance flow was available, the prediction of the back clearance flow could not be directly validated. The LDA data or the PIV data which can provide information on the flow filed inside the back clearance can validate the back clearance flow prediction.

Simple pressure probe located above and below the balance hole can provide the differential pressure by which one can calculated the leakage flow through the balance hole. The LDA data which is taken from either the inlet or the outlet will be able to provide the axial velocity through the balance hole and the leakage flow rate, which can validate the empirical model suggested in this work.

REFERENCES

Andersson, H. I. and Lygren, M., 2006, Les of Open Rotor-Stator Flow, International Journal of Heat and Fluid Flow, 27, 551-557

Batchelor, G. K., 1951, Note on a Class of Solutions of the Navier-Stokes Equations Representing Steady Rotationally-Symmetric Flow, Quarterly Journal of Mechanics Applied Mathatics, 4, 29-41

Bayley, F. J. and Conway, L., 1964, Fluid Friction and Leakage between a Stationary and Rotating Disc, Journal of Mechanical Engineering Science, 6, 164-172

Benra, F. K. and Dohmen, H. J., 2004, Theoretical and Experimental Investigation on the Flow Induced Vibrations of a Centrifugal Pump, Proceedings of the Biennial International Pipeline Conference, Calgary, Alberta., Canada, 39-46

Berchane, N. S., 2002, Experimental Evaluation of the Flow inside and Open Faced Impeller, M.S. Thesis, Texas A&M University

Bolleter, U., 1988, On Blade Passage Tones of Centrifugal Pumps, Vibrations, 4, 8-13

Brkich, A., 1946, How Axial Thrust Is Balanced in Single-State Centrifugal Pumps, Power, 90, 16-18

Byskov, R. K., Jacobsen, C. B. and Pedersen, N., 2003, Flow in a Centrifugal Pump Impeller at Design and Off-Design Conditions - Part 2: Large Eddy Simulations, Journal of Fluids Engineering, Transactions of the ASME, 125, 73-83

Cao, S. L., Goulas, A., Yakinthos, K., Wu, Y. L., Tsukamoto, H. and Deliporanides, G., 1998, Numerical Simulation of Three-Dimensional Turbulent Flow in a Centrifugal Pump Impeller, Proceedings of the International Conference on Pumps and Fans, ICPF, Tsinghua, China, 411-418

Chu, S. D., R; Katz, J., 1995a, Relationship between Unsteady Flow, Pressure Fluctuation, and Noise in a Centrifugal Pump-Part A: Use of PDV Data to Compute the Pressure Field, Journal of Fluid Engineering, 117, 24-29

Chu, S. D., R; Katz, J., 1995b, Relationship between Unsteady Flow, Pressure Fluctuation, and Noise in a Centrifugal Pump-Part B: Effects of Blade-Tongue Interactions, Journal of Fluid Engineering, 117, 30-35

Dean, J. R. C. and Senoo, Y., 1960, Rotating Wakes in Vaneless Diffusers, Journal of Basic Engineering Series D, Transactions of the ASME, 82, 563-574

Dong, R., Chu, S. and Katz, J., 1992a, Quantitative Visualization of the Flow within the Volute of a Centrifugal Pump. Part A: Technique, Journal of Fluids Engineering, Transactions of the ASME, 114, 390-395

Dong, R., Chu, S. and Katz, J., 1992b, Quantitative Visualization of the Flow within the Volute of a Centrifugal Pump. Part B: Results and Analysis, Journal of Fluids Engineering, Transactions of the ASME, 114, 396-403

Gan, X. P. and MacGregor, S. A., 1995, Experimental Study of the Flow in the Cavity between Rotating Disks, Experimental Thermal and Fluid Science, 10, 379

Gonzalez, J., Fernandez, J., Blanco, E. and Santolaria, C., 2002, Numerical Simulation of the Dynamic Effects Due to Impeller-Volute Interaction in a Centrifugal Pump, Journal of Fluids Engineering, Transactions of the ASME, 124, 348-355

Gonzalez, J. and Santolaria, C., 2006, Unsteady Flow Structure and Global Variables in a Centrifugal Pump, Journal of Fluids Engineering, Transactions of the ASME, 128, 937-946

Guelich, J. F., 1999, Impact of Three-Dimensional Phenomena on the Design of Rotodynamic Pumps, Proceedings of the Institution of Mechanical Engineers, Part C: Journal of Mechanical Engineering Science, 213, 59-70

Gyulai, F. A., V.; Popoviciu, M., 1975, Researches Regarding Axial Hydraulic Thrust at Centrifugal Pumps, Journal of Applied Mechanics, Transactions of the ASME, 1, 379-387

Hossain, S., 2000, Effect of Back Clearance and Balance Hole upon Centrifugal Pump Performance, M.S. Thesis, Texas A&M University

Kubota, Y., Suzuki, T., Tomita, H., Nagafugi, T. and Okamura, C., 1983, Vibration of Rotating Bladed Disc Excited by Stationary Distributed Forces, Bulletin of the JSME, 26, 1952-1957

Kurokawa, J., Kamijo, K. and Shimura, T., 1994, Axial Thrust Behavior in Lox-Pump of Rocket Engine, Journal of Propulsion and Power, 10, 244-250

Langthjem, M. A. and Olhoff, N., 2004a, A Numerical Study of Flow-Induced Noise in a Two-Dimensional Centrifugal Pump. Part 1: Hydrodynamics, Journal of Fluids and Structures, 19, 349-368

Langthjem, M. A. and Olhoff, N., 2004b, A Numerical Study of Flow-Induced Noise in a Two-Dimensional Centrifugal Pump. Part 2. Hydroacoustics, Journal of Fluids and Structures, 18, 369-386

Matsui, J., Kurokawa, J. and Ito, Y., 2007, Estimation of an Axial Thrust of Centrifugal Pumps and Pump, Transactions of the Japan Society of Mechanical Engineers, Part B, 73, 1663-1669

Murakami, M., Kikuyama, K. and Asakura, E., 1980, Velocity and Pressure Distributions in the Impeller Passages of Centrifugal Pumps, Journal of Fluids Engineering, Transactions of the ASME, 102, 420-426

Owen, J. M., and Rogers, R. H., 1989, Flow and Heat Transfer in Rotating-Disc Systems, Research Studies Press, New York

Pavesi, G., Ardizzon, G. and Cavazzini, G., 2005, Unsteady Flow Field and Noise Generation in a Centrifugal Pump Impeller with a Vaneless Diffuser, Proceedings of 2005 ASME Fluids Engineering Division Summer Meeting, FEDSM2005, Houston, Texas, United States, 1486-1493

Pedersen, N., Larsen, P. S. and Jacobsen, C. B., 2003, Flow in a Centrifugal Pump Impeller at Design and Off-Design Conditions - Part 1: Particle Image Velocimetry (PIV) and Laser Doppler Velocimetry (LDV) Measurements, Journal of Fluids Engineering, Transactions of the ASME, 125, 61-72

Plutecki, J. and Wajda, A., 1975, Influence of an Axial Clearance between a Semi-Open Impeller and a Casing on Pump Parameters, by Example of H1-150 Pump, Proceedings of Conference on Fluid Machine, 5th, Proceeding, Budapest, Hungary, 833-845

Polhemus, J. H. and Healy, J., 1929, Dredge-Pump Pressures and Thrust Loads, American Society of Mechanical Engineers, Transactions of Hydraulics, 51, 33-40

Rzentkowski, G., 1996, Generation and Control of Pressure Pulsations Emitted from Centrifugal Pumps: A Review, Proceedings of the 1996 ASME Pressure Vessels and Piping Conference, Montreal, Canada, 439-454

Soong, C.-Y., Wu, C.-C., Liu, T.-P. and Liu, T.-P., 2003, Flow Structure between Two Co-Axial Disks Rotating Independently, Experimental Thermal and Fluid Science, 27, 295-311

Stepanoff, A. J., 1932, Leakage Loss and Axial Thrust in Centrifugal Pumps, American Society of Mechanical Engineers, Transactions of Hydraulics, 54, 65-103

Stepanoff, A. J., 1948, Centrifugal and Axial Flow Pumps, John Wiley & Sons, Inc., New York

Stewartson, K., 1953, On the Flow between Two Rotating Coaxial Disks, Proceedings of the Cambridge Philosophical Society, 49, 333-341

Thorne, E. W. a. B., J. R., 1973, Axial Thrust in Semi-Open Impellers, Proceedings of the Process Pumps Conference, IMechE, Durham, UK, 9-15

Trout, R. G., 1962, Axial Thrust in Centrifugal Pumps, Proceedings of American Society of Mechanical Engineers, 8

Yedidiah, S., 2006a, Application of CFD to the Design of Centrifugal Pumps, Proceedings of 2006 ASME Joint U.S.-European Fluids Engineering Summer Meeting, FEDSM 2006, Miami, Florida, United States, 6

Yedidiah, S., 2006b, Translating Equations into Their Physical Meaning, as an Effective Tool of Engineering, Proceedings of ASME Fluids Engineering Division Summer Meeting 2006, FEDSM2006, Miami, Florida, United States, 201-208

APPENDIX A

CFD GRID INDEPENDENCE STUDY AND VALIDATION OF SELECTION OF THE BOUNDARY CONDITION

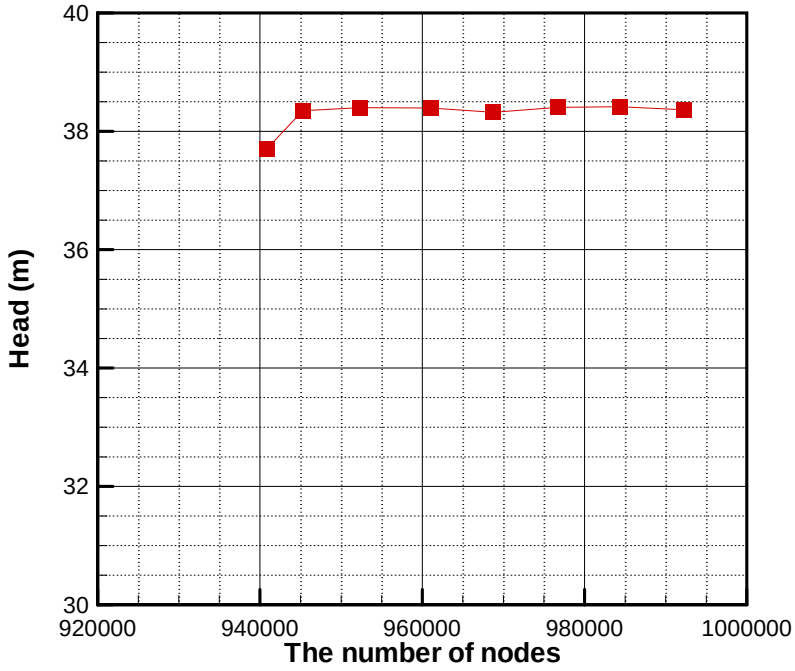

Figure A 1 Change of head in terms of the number of nodes

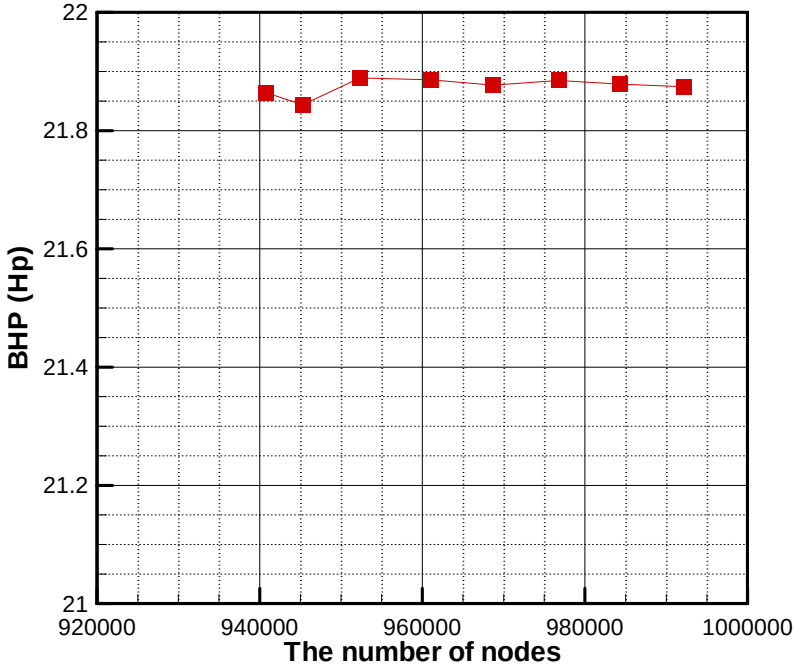

Figure A 2 Change of BHP in terms of the number of nodes

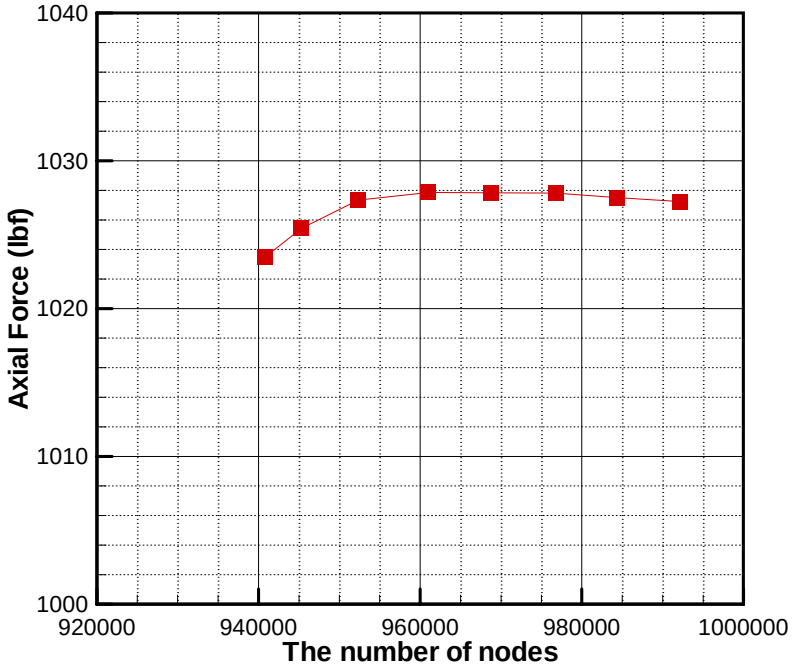

Figure A 3 Change of the axial force in terms of the number of nodes

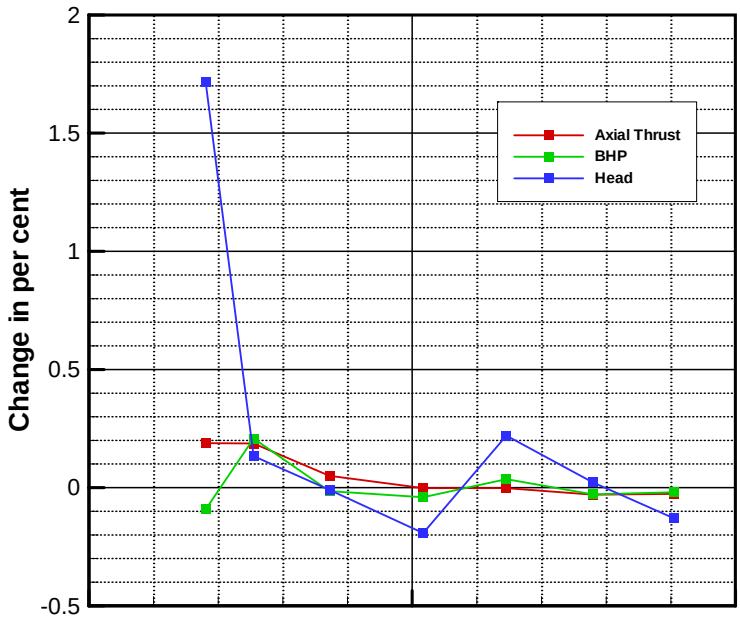

Figure A 4 Changes of variables in terms of the number of nodes

Table A 1 The summary of the grid adaptation (the shaded rows represent the increase or the decrease from the previous row)

Adaptation Step	The Number of Nodes	Target Cells	Maximum Curvature (Pa/m)	Thresholds for Adaptation (Pa/m)	Target Zones	Axial Thrust (lbf)	BHP (Hp)	Head(m)
1	940826		64.8		All	1023.5	21.8640	37.7000
		169		50		+0.187964	-0.09249	+1.718342
2	945280		57.3		All	1025.424	21.84378	38.34782
		404		445		+0.186835	+0.20773	+0.133251
3	952322		44.78156		All	1027.34	21.88916	38.39891
		605		33		+0.050287	-0.01482	-0.00936
4	961023		41.87128		All	1027.856	21.88591	38.39532
		765		29		-0.00231	-0.04043	-0.19218
5	968747		34.31147		All	1027.833	21.87706	38.32153
		639		27		-0.00169	+0.035846	+0.220226
6	976757		21.4		All	1027.815	21.8849	38.40593
		724		17		-0.02968	-0.02842	+0.022744
7	984334		21.9		All	1027.51	21.87869	38.41466
		631		13		-0.02642	-0.01975	-0.1304
8	992199		22.3		All	1027.239	21.87437	38.36457

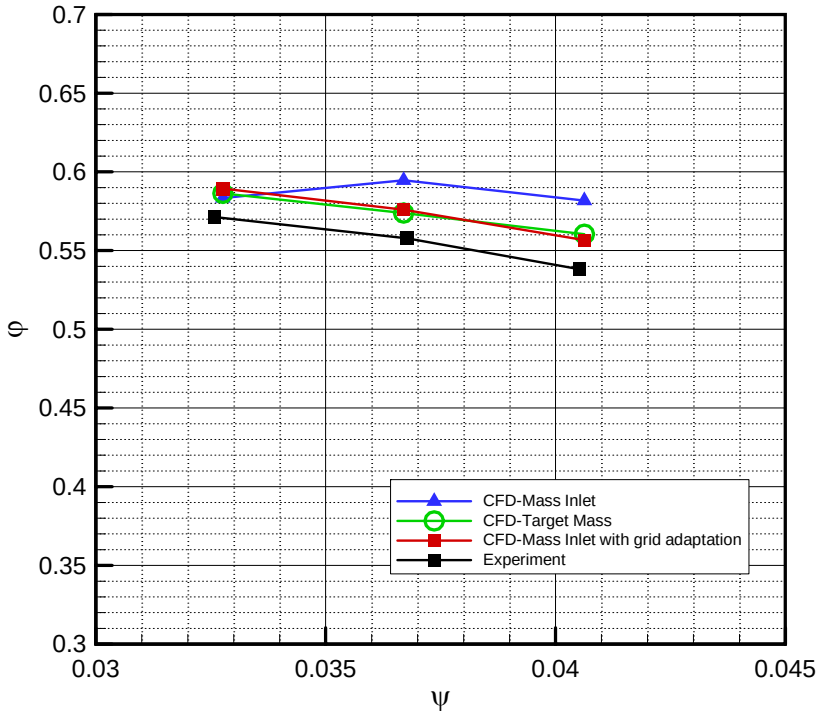

Figure A 5 Performance predictions of the pump with 0.91 mm clearance without balance holes using different boundary conditions

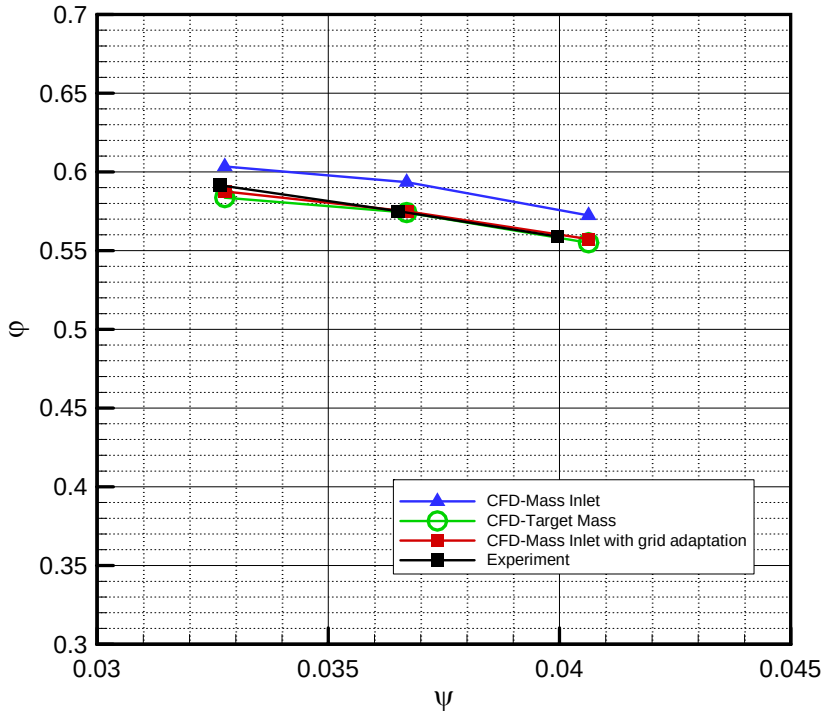

Figure A 6 Performance predictions of the pump with 0.91 mm clearance with balance holes using different boundary conditions

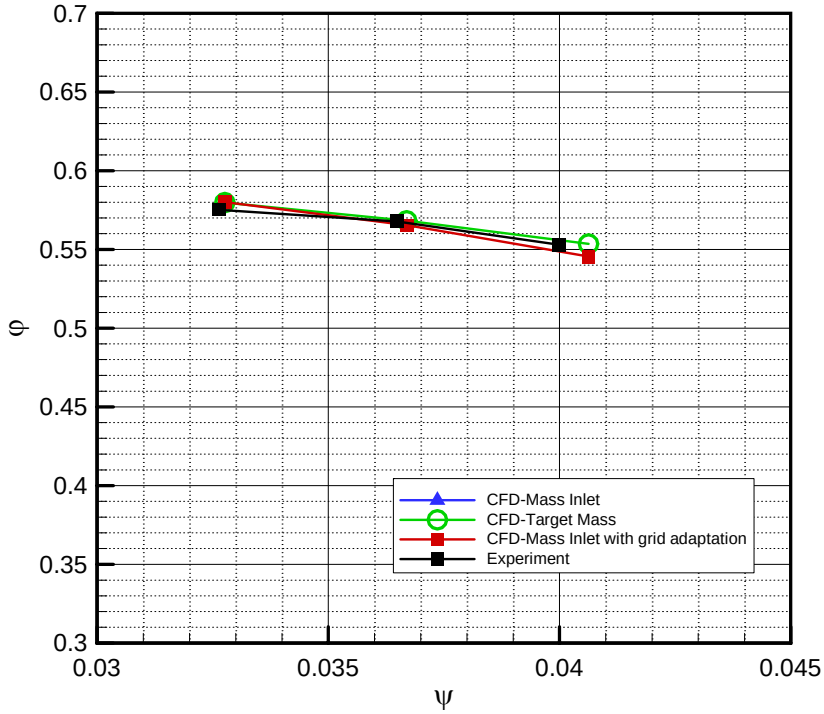

Figure A 7 Performance predictions of the pump with 1.87 mm clearance without balance holes using different boundary conditions

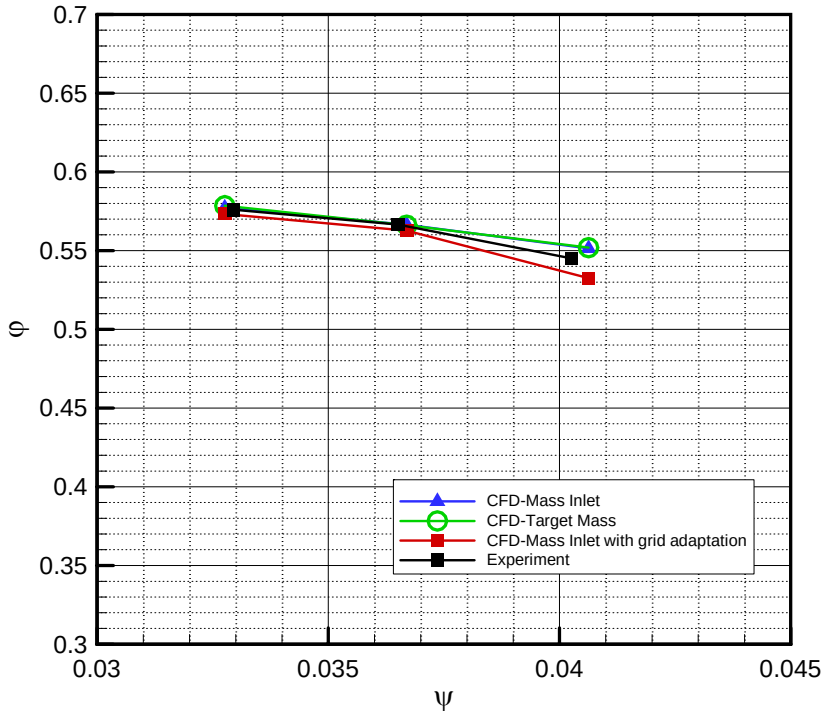

Figure A 8 Performance predictions of the pump with 1.87 mm clearance with balance holes using different boundary conditions

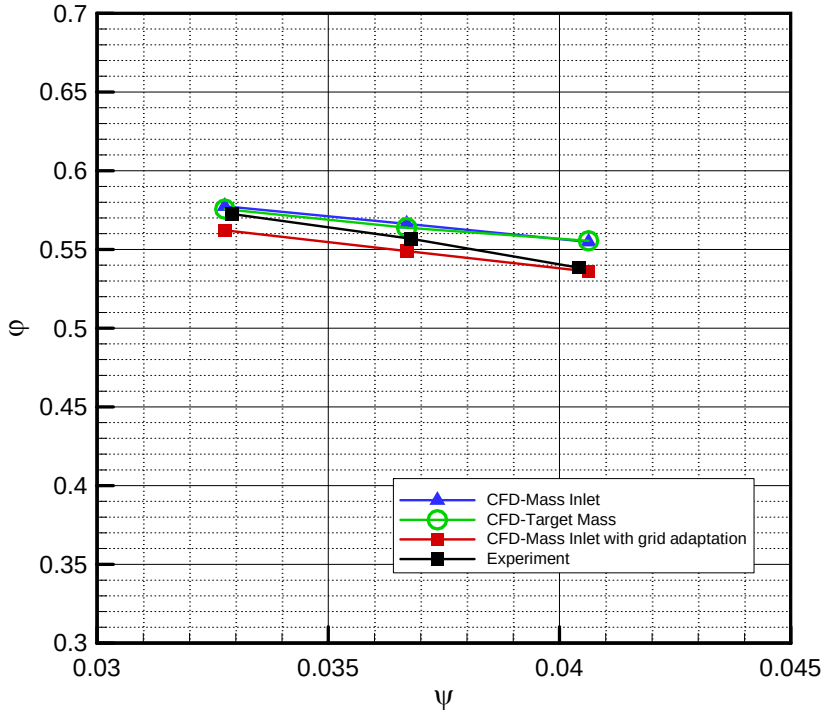

Figure A 9 Performance predictions of the pump with 3.17 mm clearance without balance holes using different boundary conditions

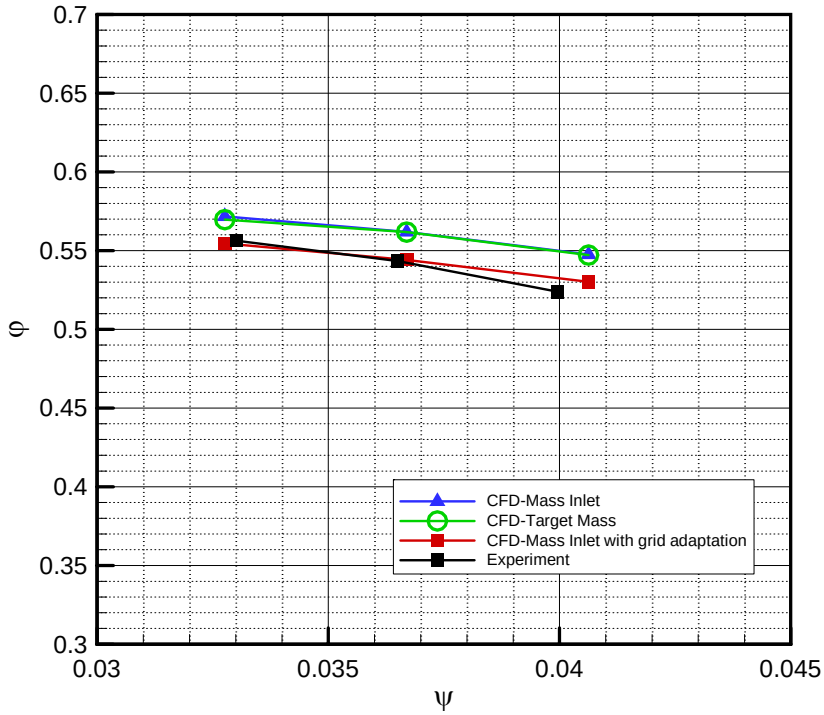

Figure A 10 Performance predictions of the pump with 3.17 mm clearance with balance holes using different boundary conditions

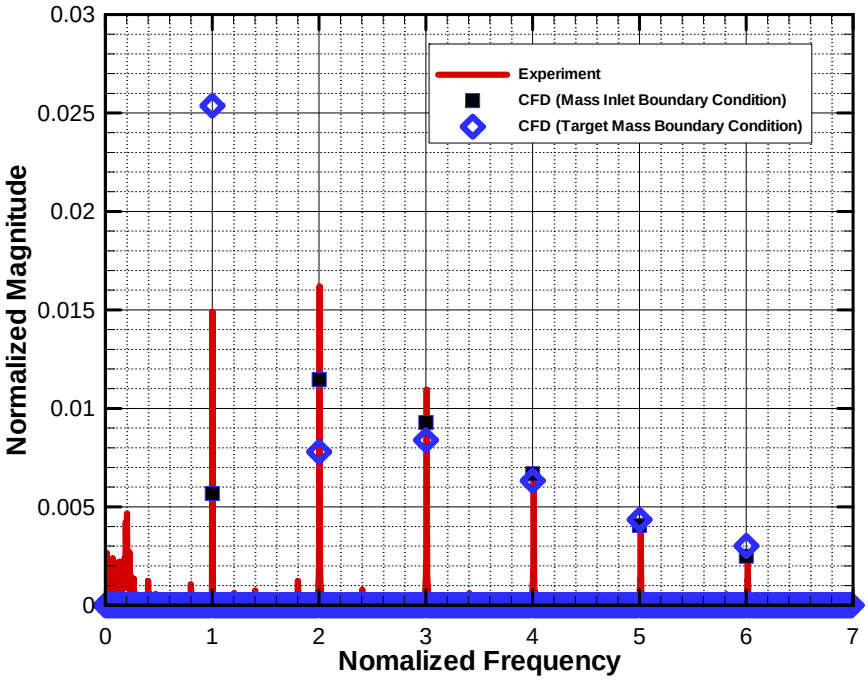

Figure A 11 Unsteady pressure spectrum of the pump with 1.87mm back clearance and no back clearance on the 30 degree azimuthal position at 31lit/sec flow rate

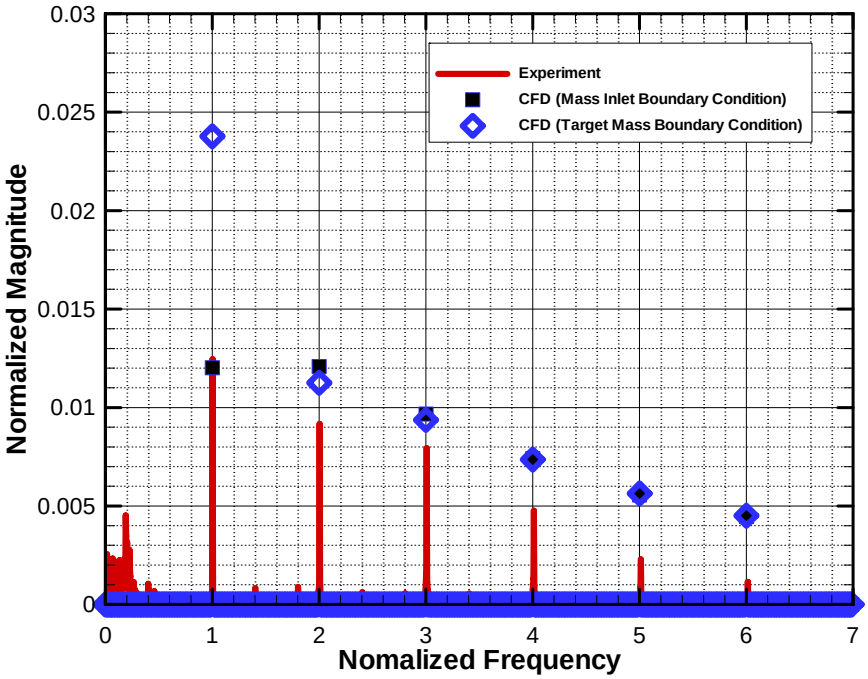

Figure A 12 Unsteady pressure spectrum of the pump with 1.87mm back clearance and no back clearance on the 110 degree azimuthal position at 31lit/sec flow rate

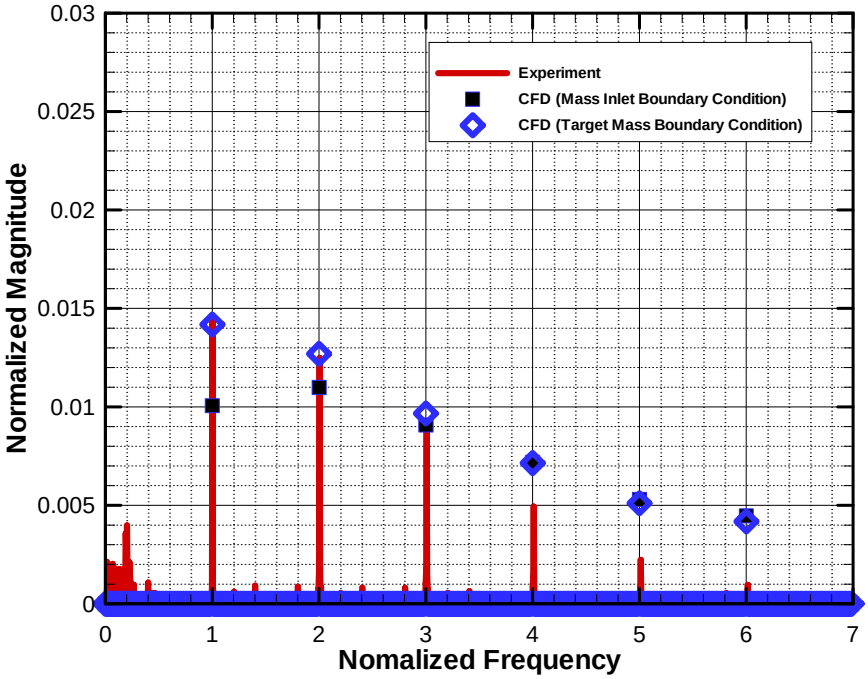

Figure A 13 Unsteady pressure spectrum of the pump with 1.87mm back clearance and no back clearance on the 180 degree azimuthal position at 31lit/sec flow rate

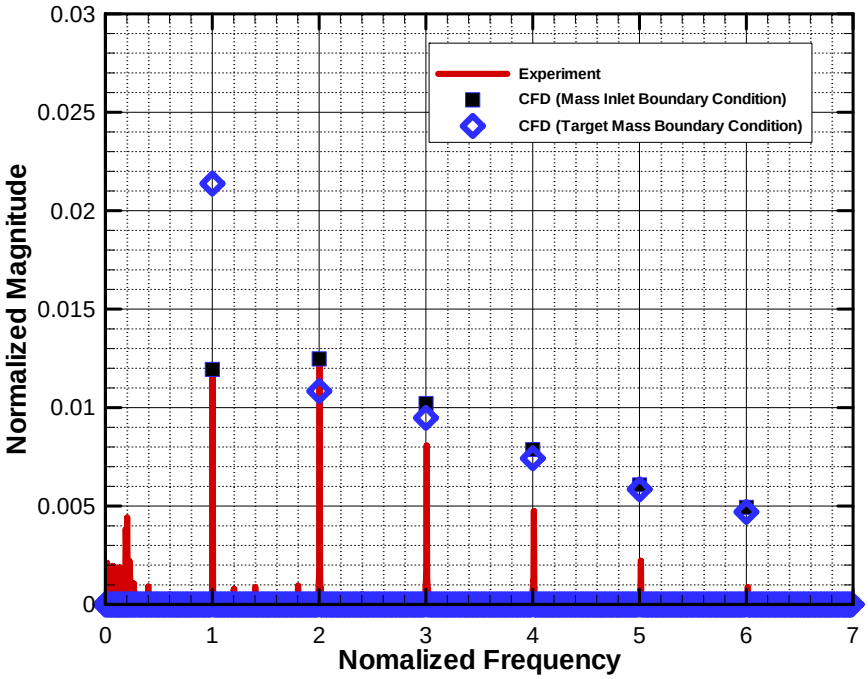

Figure A 14 Unsteady pressure spectrum of the pump with 1.87mm back clearance and no back clearance on the 250 degree azimuthal position at 31lit/sec flow rate

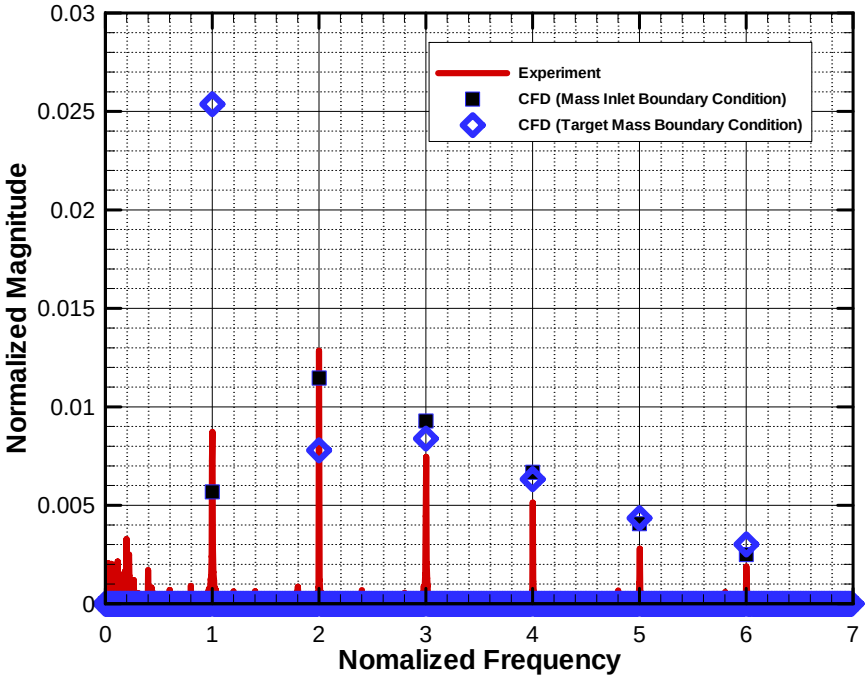

Figure A 15 Unsteady pressure spectrum of the pump with 1.87mm back clearance and no back clearance on the 30 degree azimuthal position at 28lit/sec flow rate

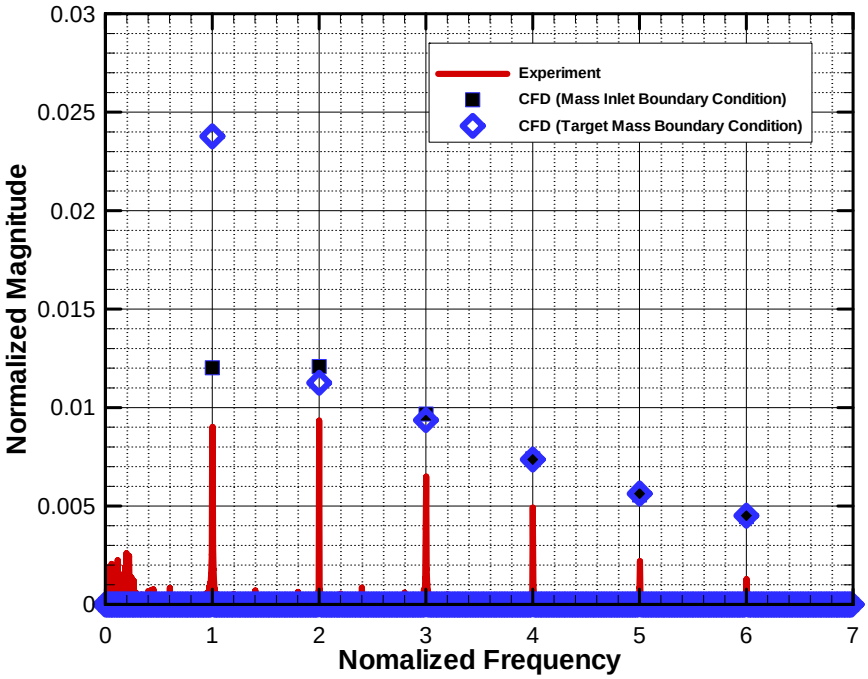

Figure A 16 Unsteady pressure spectrum of the pump with 1.87mm back clearance and no back clearance on the 110 degree azimuthal position at 28lit/sec flow rate

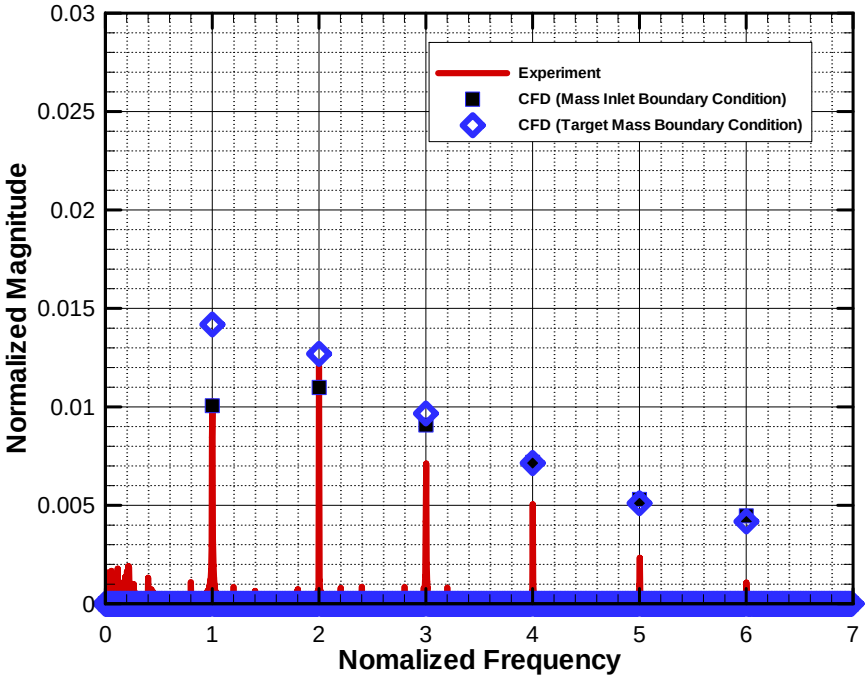

Figure A 17 Unsteady pressure spectrum of the pump with 1.87mm back clearance and no back clearance on the 180 degree azimuthal position at 28lit/sec flow rate

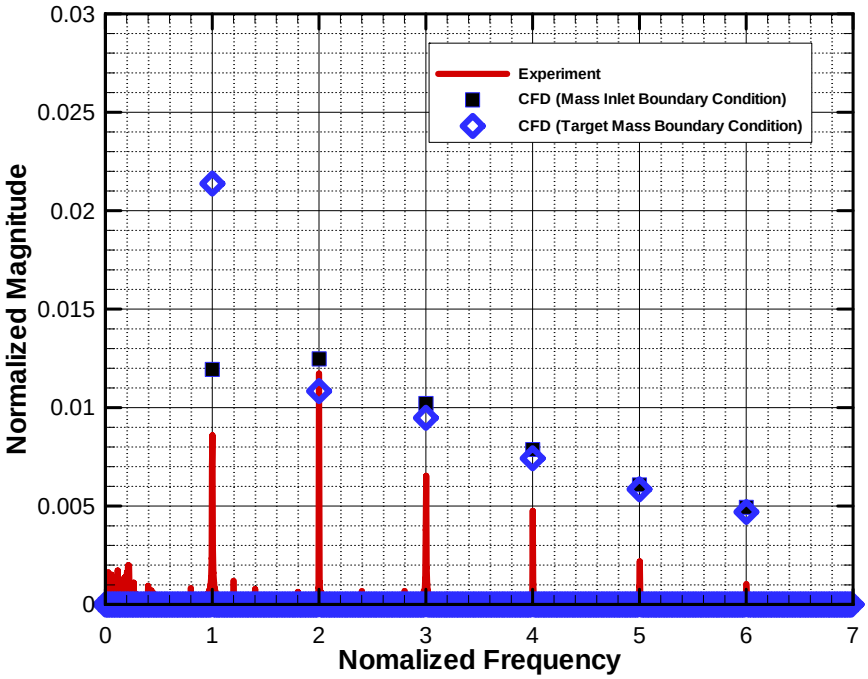

Figure A 18 Unsteady pressure spectrum of the pump with 1.87mm back clearance and no back clearance on the 250 degree azimuthal position at 28lit/sec flow rate

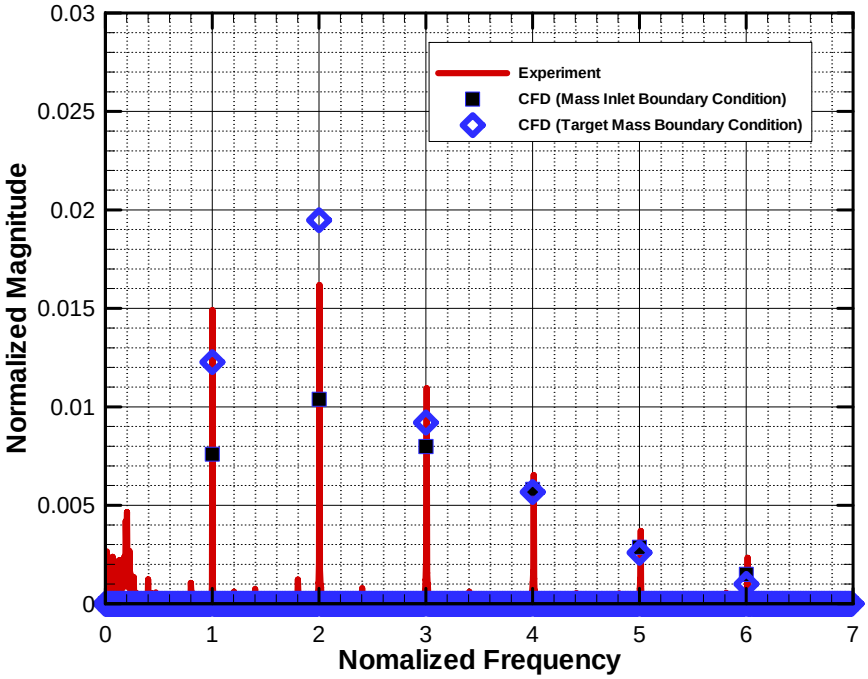

Figure A 19 Unsteady pressure spectrum of the pump with 1.87mm back clearance and no back clearance on the 30 degree azimuthal position at 25lit/sec flow rate

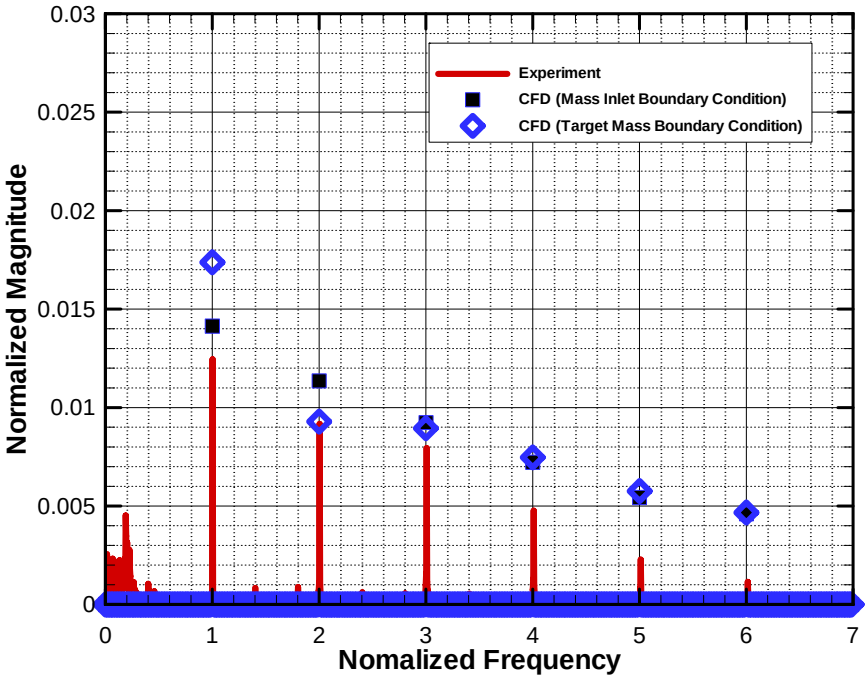

Figure A 20 Unsteady pressure spectrum of the pump with 1.87mm back clearance and no back clearance on the 110 degree azimuthal position at 25lit/sec flow rate

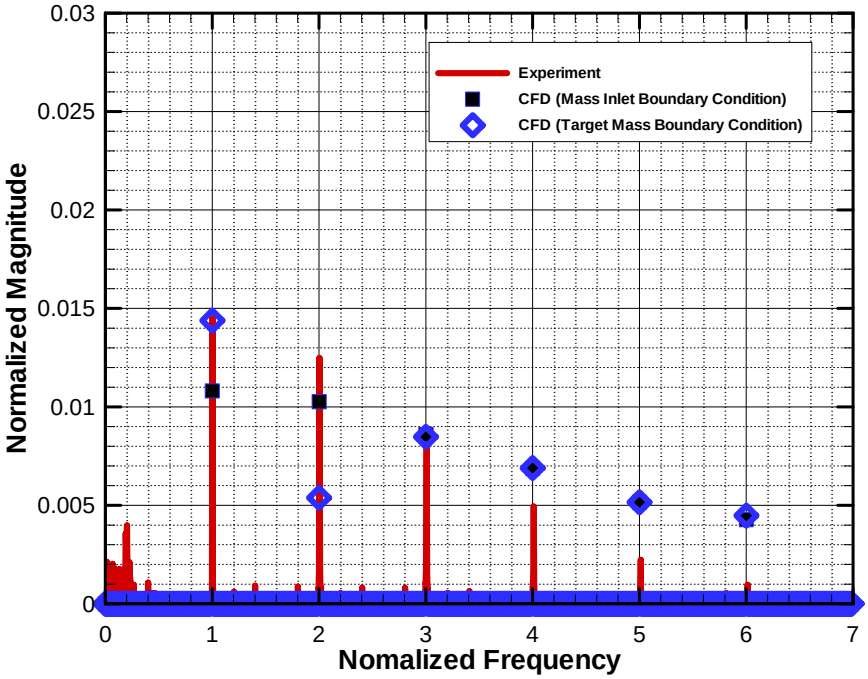

Figure A 21 Unsteady pressure spectrum of the pump with 1.87mm back clearance and no back clearance on the 180 degree azimuthal position at 25lit/sec flow rate

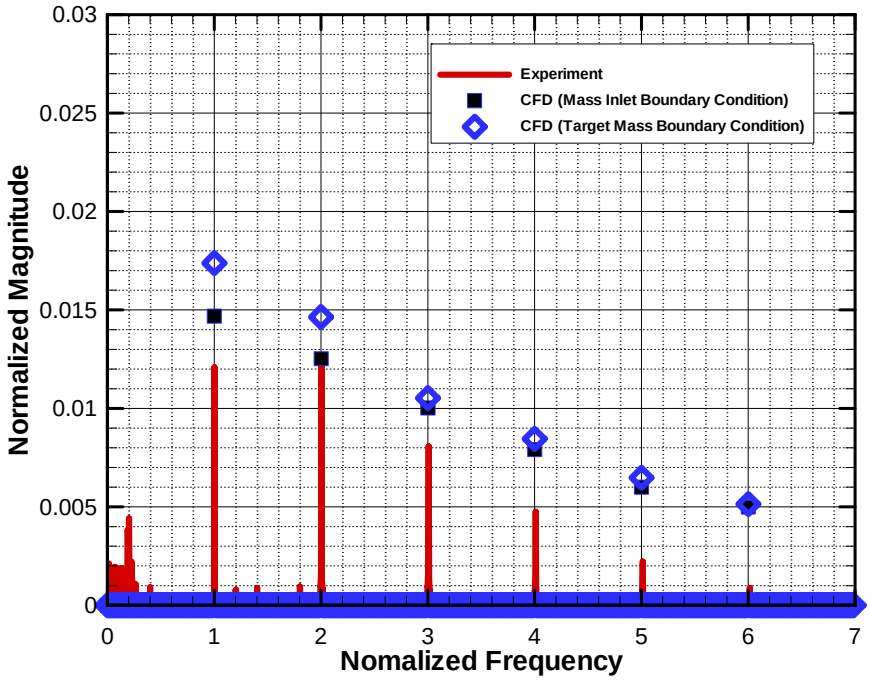

Figure A 22 Unsteady pressure spectrum of the pump with 1.87mm back clearance and no back clearance on the 250 degree azimuthal position at 25lit/sec flow rate

Table A 2 Zone ID and its description used in y* plots

Zone ID	Corresponding part of the pump
1	Pressure side blade surface
2	Suction side blade surface
3	Top side blade surface
4	Back surface of the housing
5	Front surface of the housing (Part 1)
6	Front surface of the housing (Part 2)
7	Back surface of the impeller
8	Front surface of the impeller
9	Front surface of the impeller before the passage

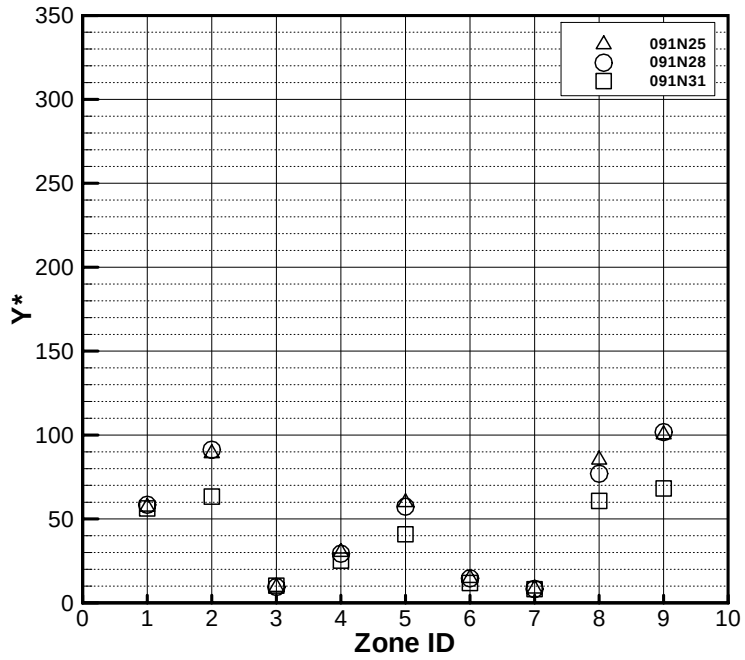

Figure A 23 y* distribution among the zones of the pump with 0.91 mm back clearance without the balance holes

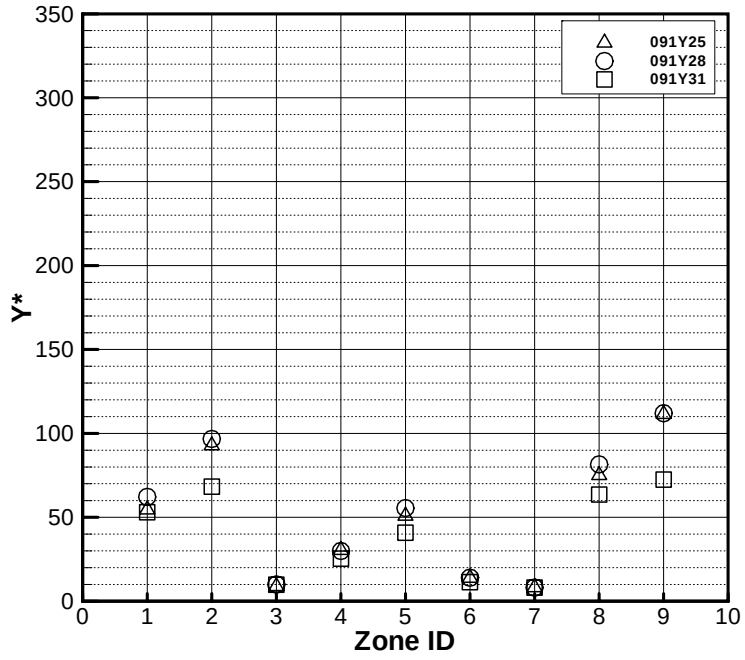

Figure A 24 y* distribution among the zones of the pump with 0.91 mm back clearance with the balance holes

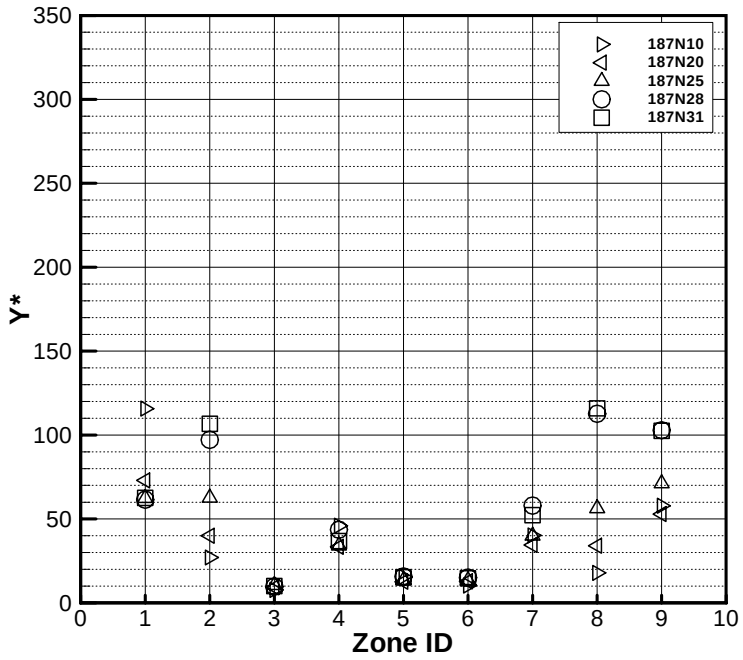

Figure A 25 y* distribution among the zones of the pump with 1.87 mm back clearance without the balance holes

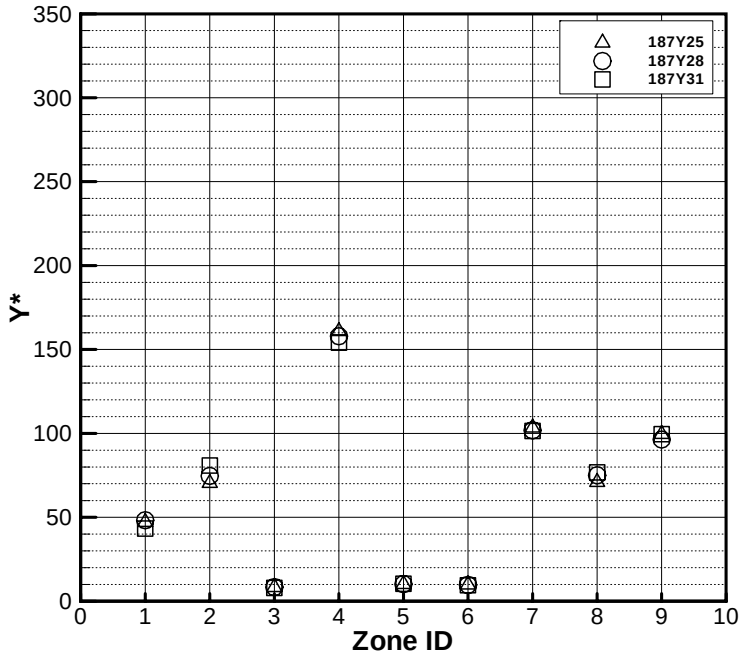

Figure A 26 y* distribution among the zones of the pump with 1.87 mm back clearance with the balance holes

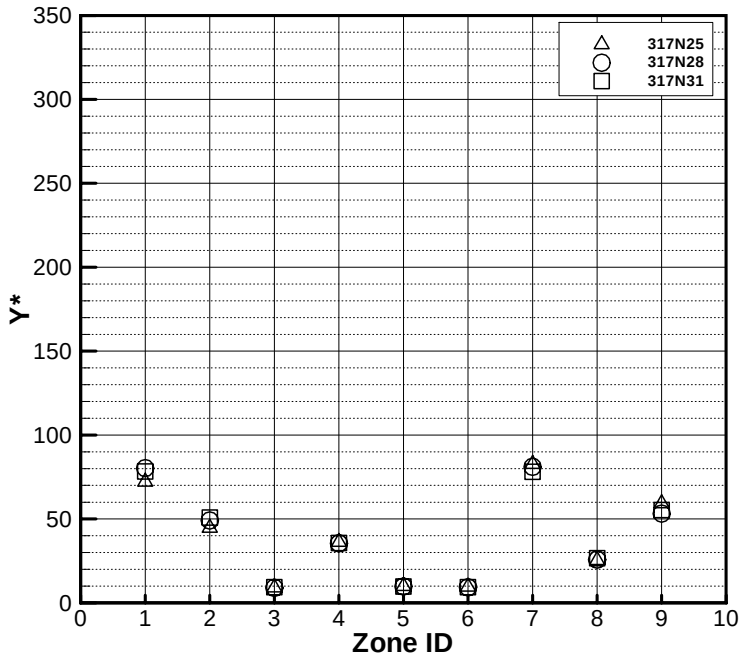

Figure A 27 y* distribution among the zones of the pump with 3.17 mm back clearance without the balance holes

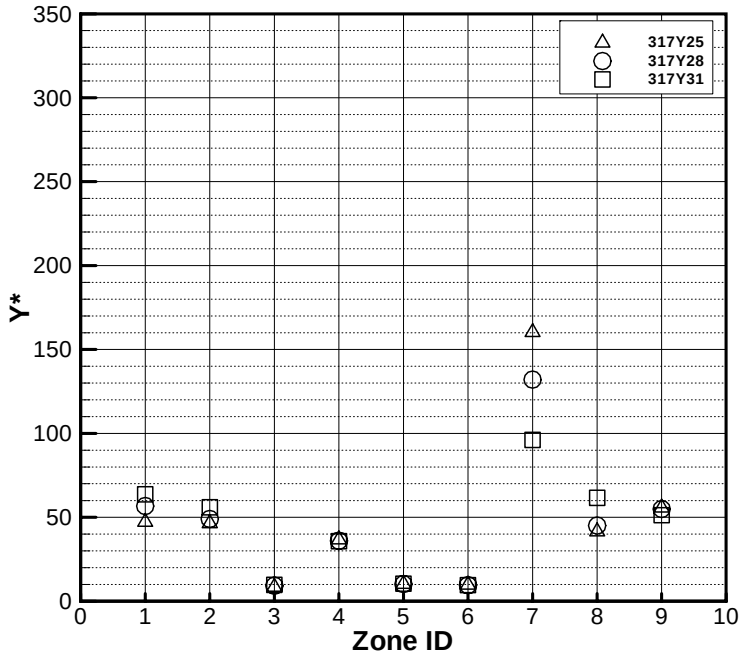

Figure A 28 y* distribution among the zones of the pump with 3.17 mm back clearance without the balance holes

APPENDIX B

LDA MEASUREMENTS AND CFD PREDICTIONS

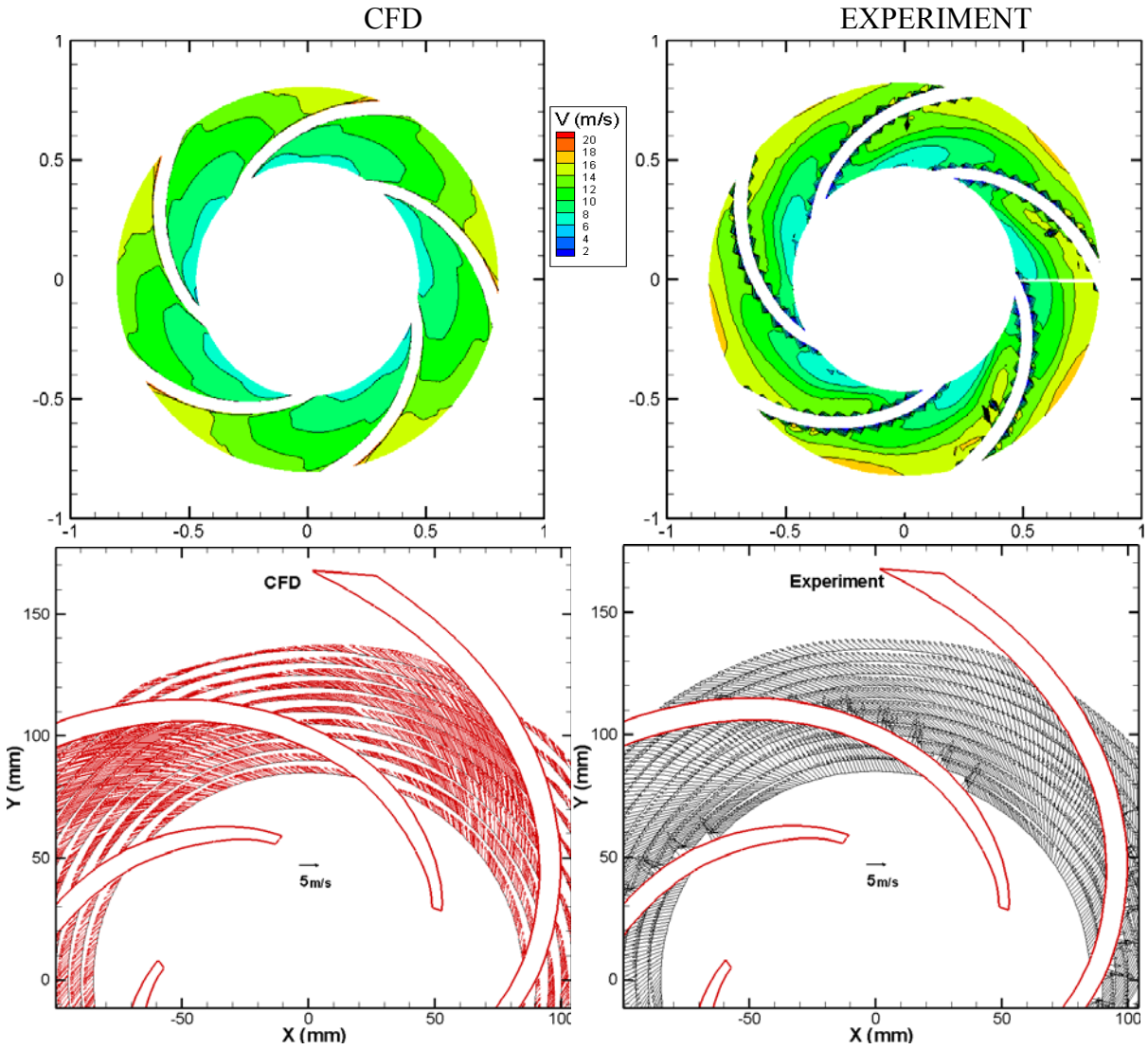

Figure B 1 The comparison between the LDA data and the CFD prediction at the flow rate: 31 lit/sec, Window A, z/h = 0.47

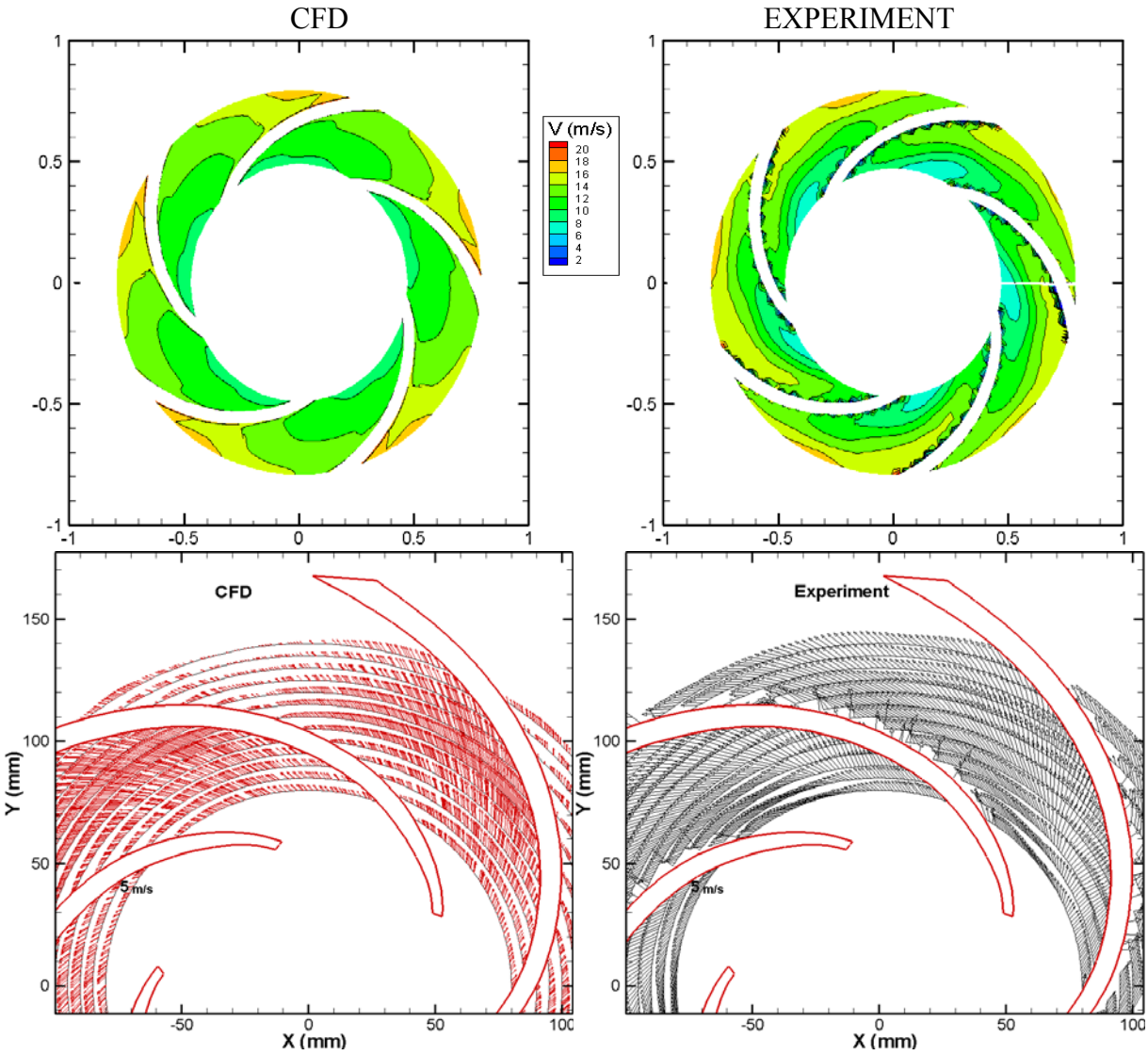

Figure B 2 The comparison between the LDA data and the CFD prediction at the flow rate: 31 lit/sec, Window B, z/h = 0.47

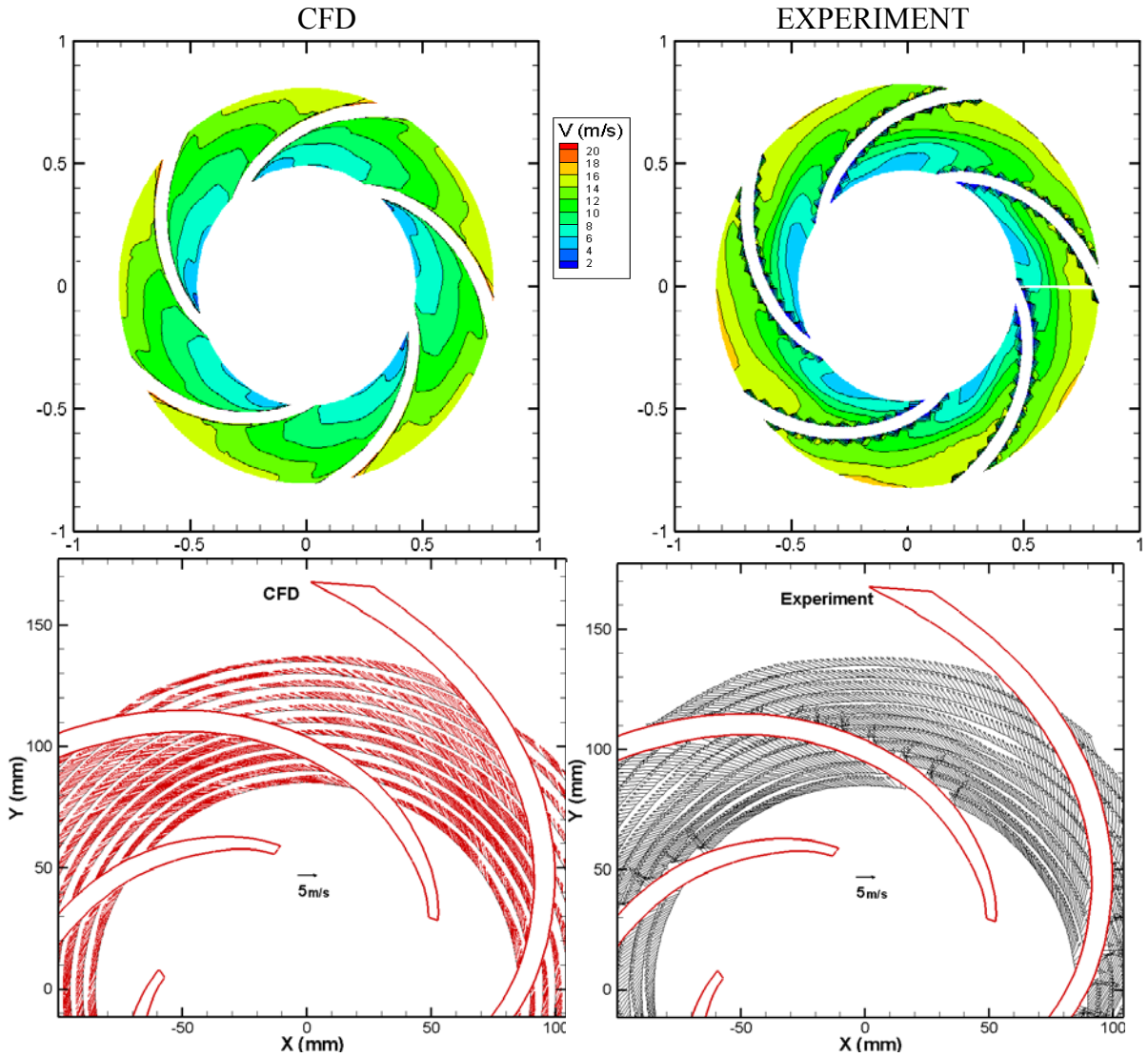

Figure B 3 The comparison between the LDA data and the CFD prediction at the flow rate: 31 lit/sec, Window A, z/h = 0.66

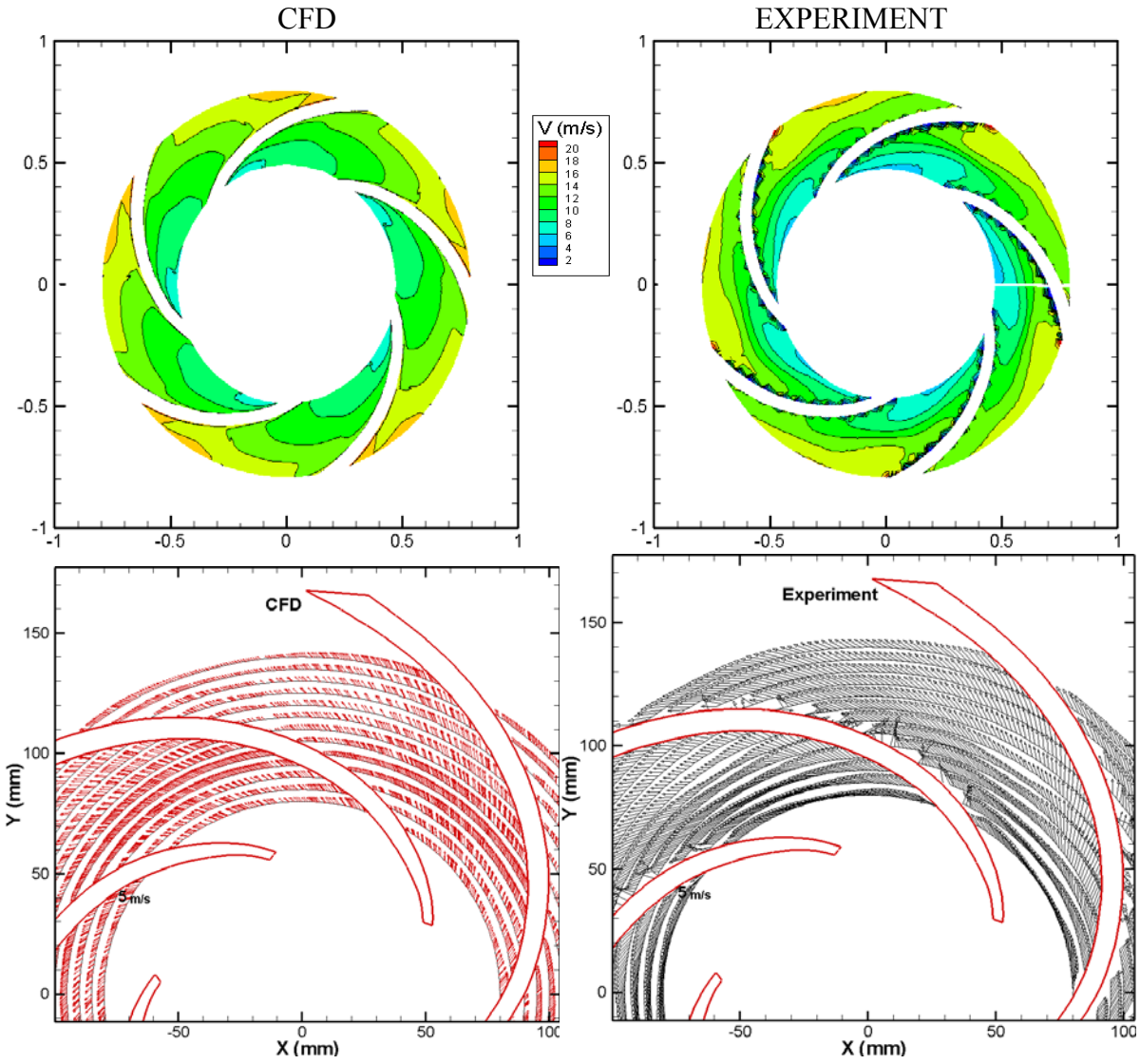

Figure B 4 The comparison between the LDA data and the CFD prediction at the flow rate: 31 lit/sec, Window B, z/h = 0.66

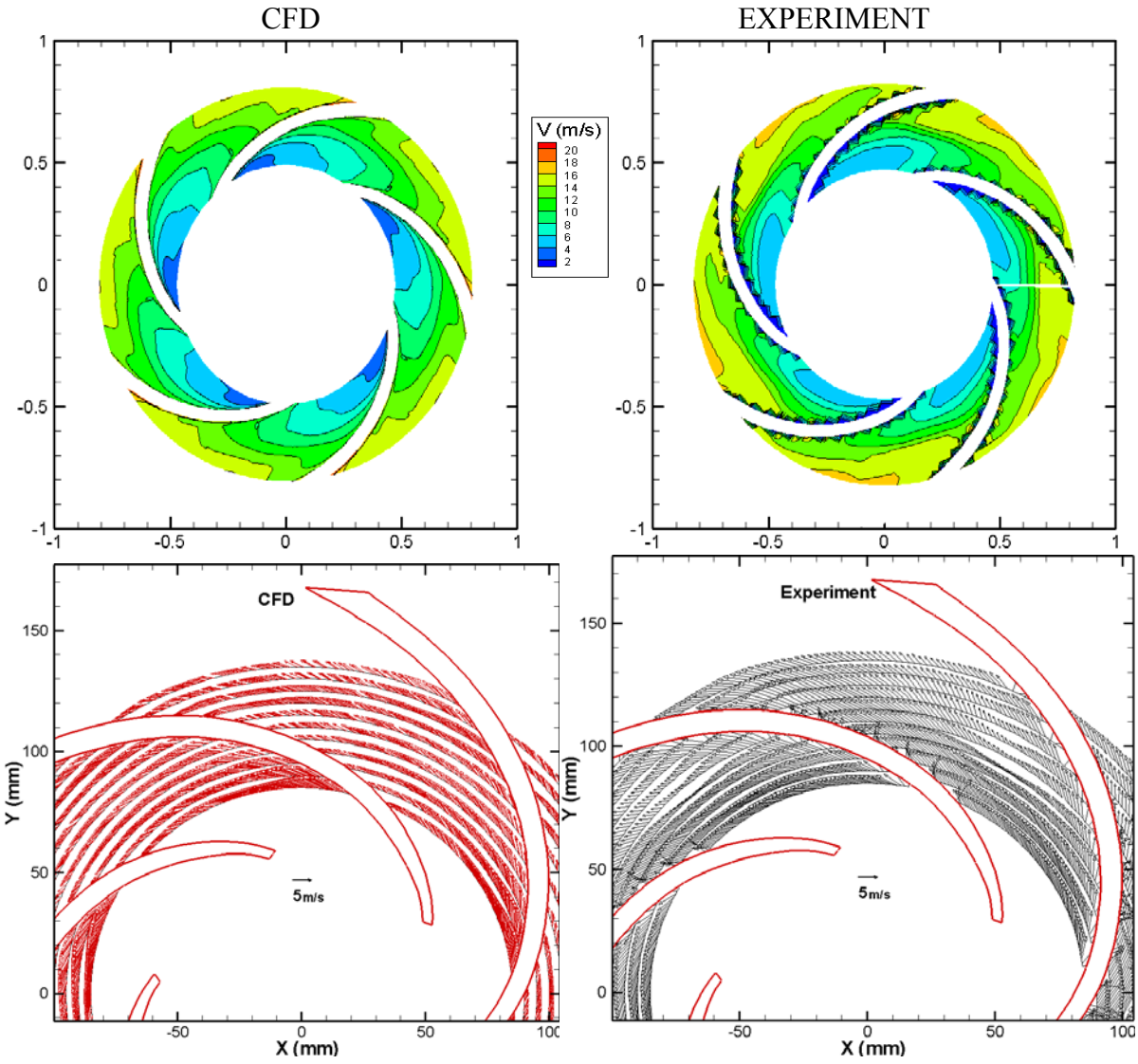

Figure B 5 The comparison between the LDA data and the CFD prediction at the flow rate: 31 lit/sec, Window A, z/h = 0.87

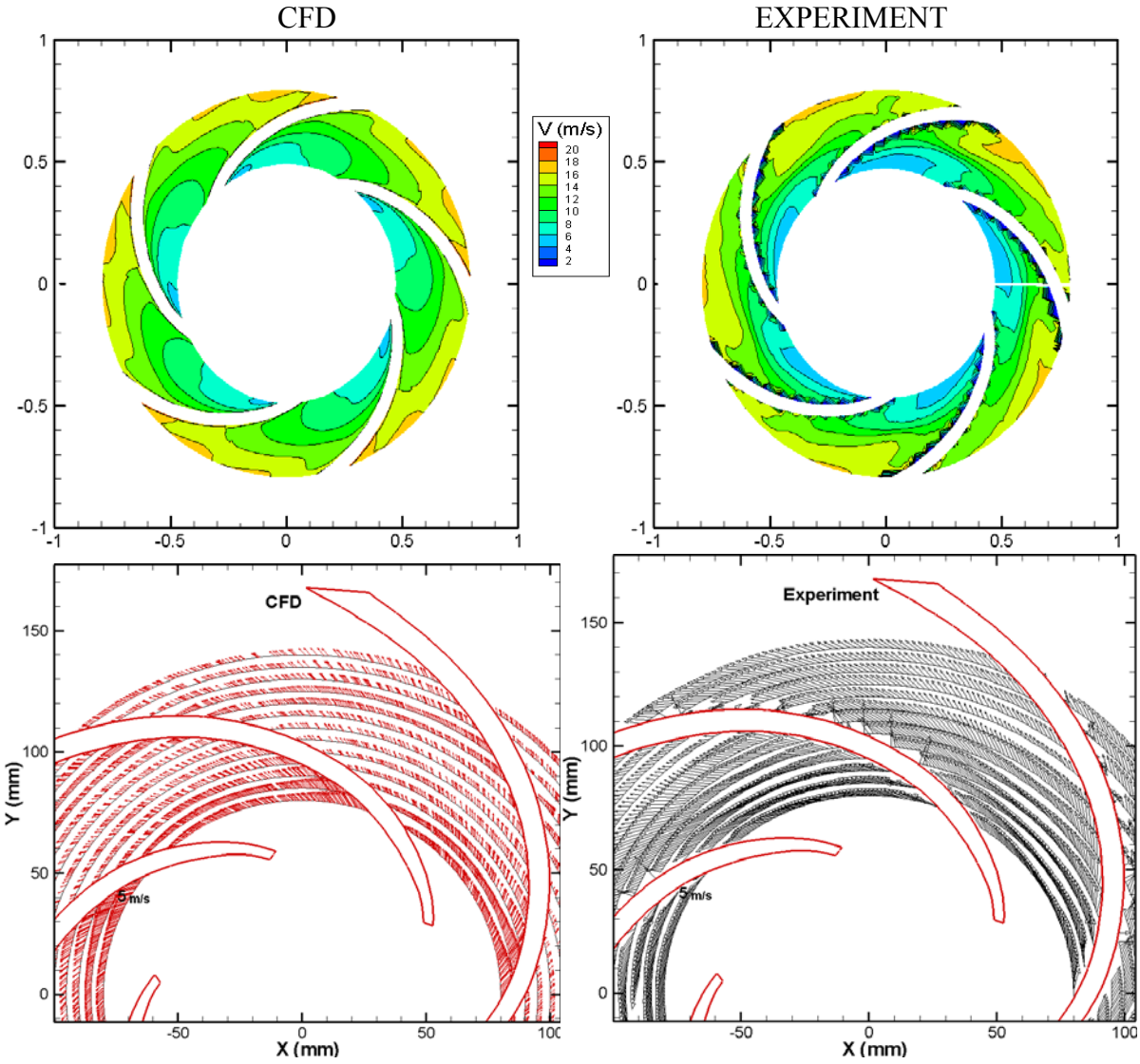

Figure B 6 The comparison between the LDA data and the CFD prediction at the flow rate: 31 lit/sec, Window B, z/h = 0.87

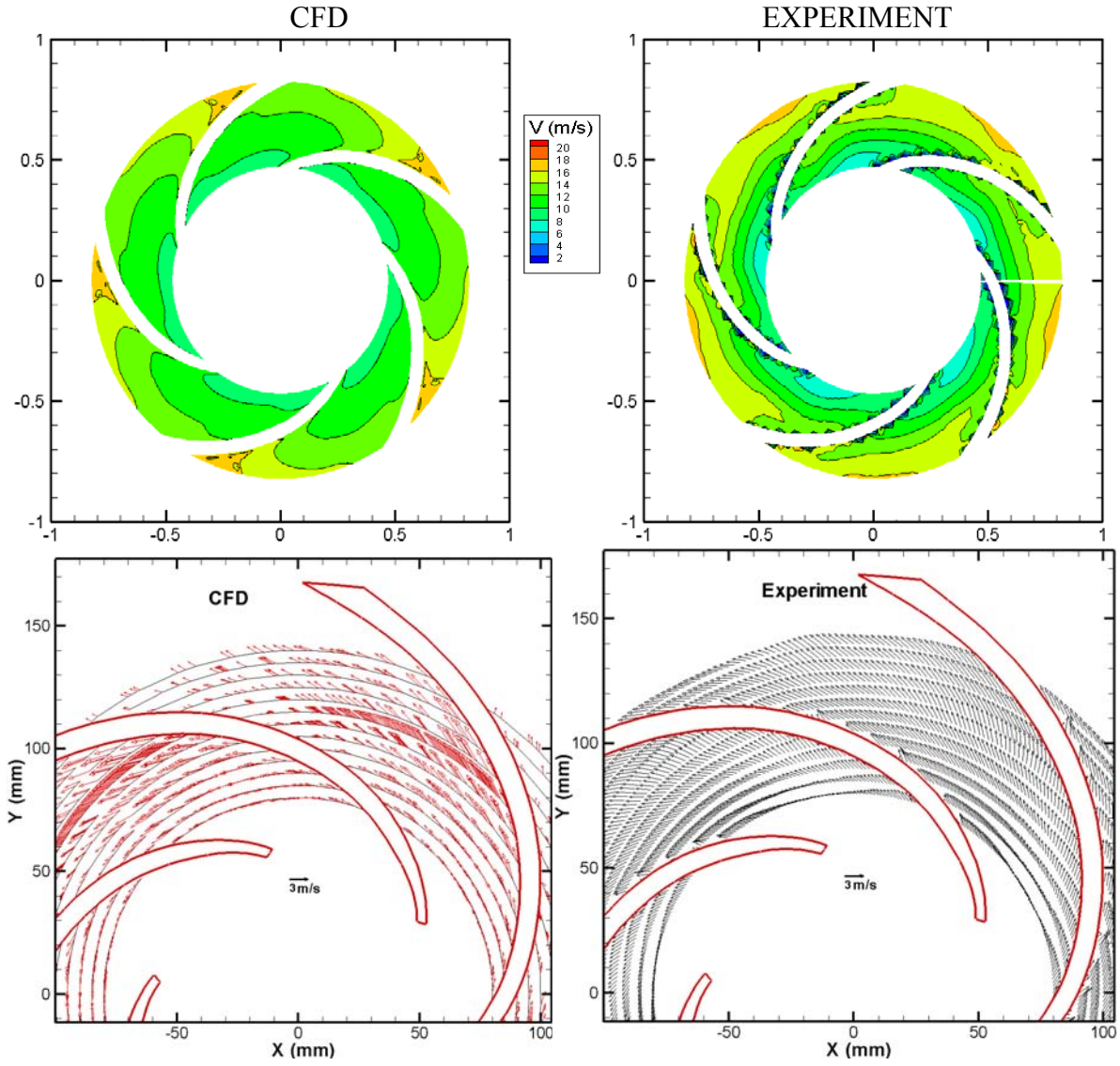

Figure B 7 The comparison between the LDA data and the CFD prediction at the flow rate: 20 lit/sec, Window A, z/h = 0.47

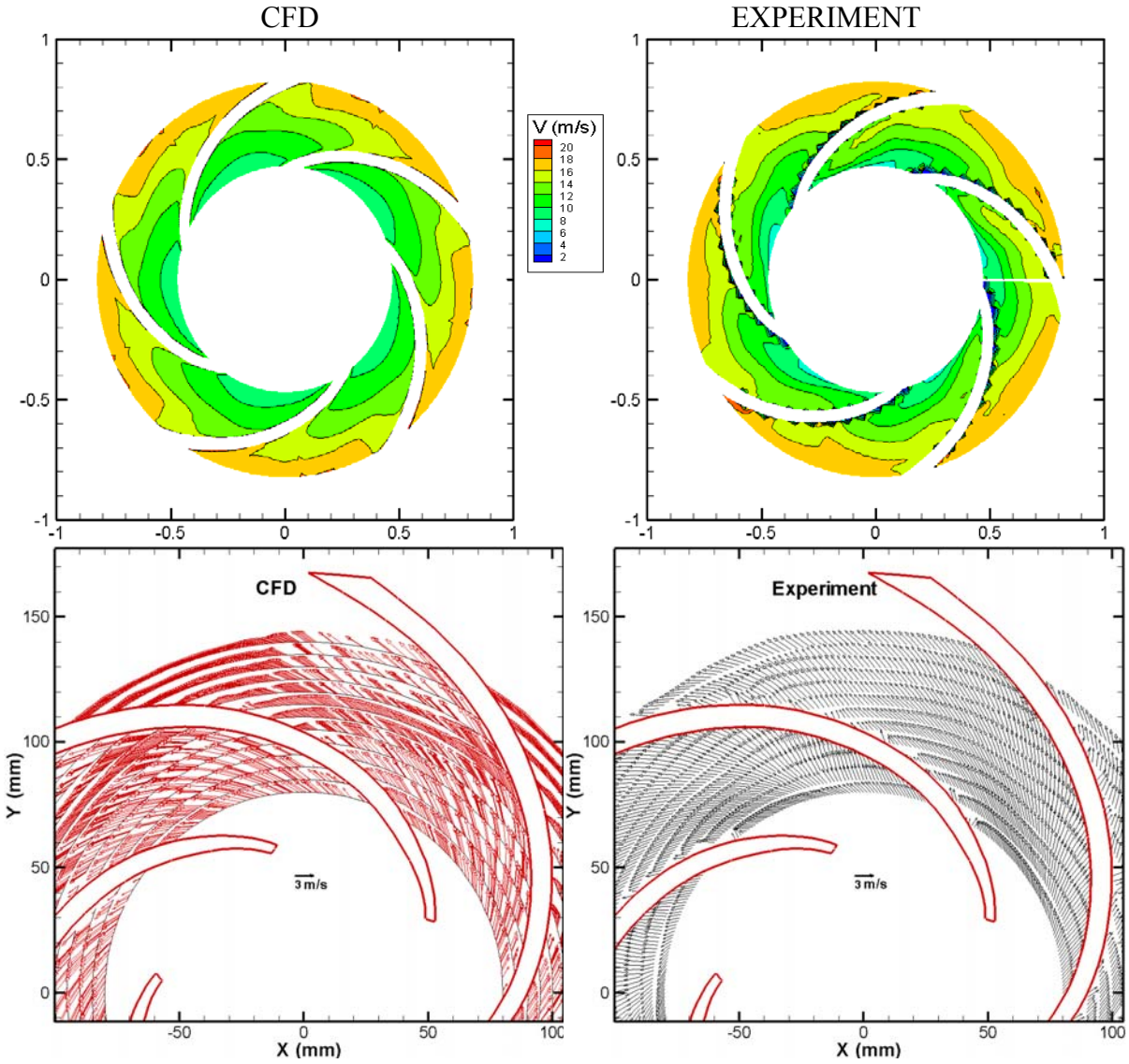

Figure B 8 The comparison between the LDA data and the CFD prediction at the flow rate: 20 lit/sec, Window B, z/h = 0.47

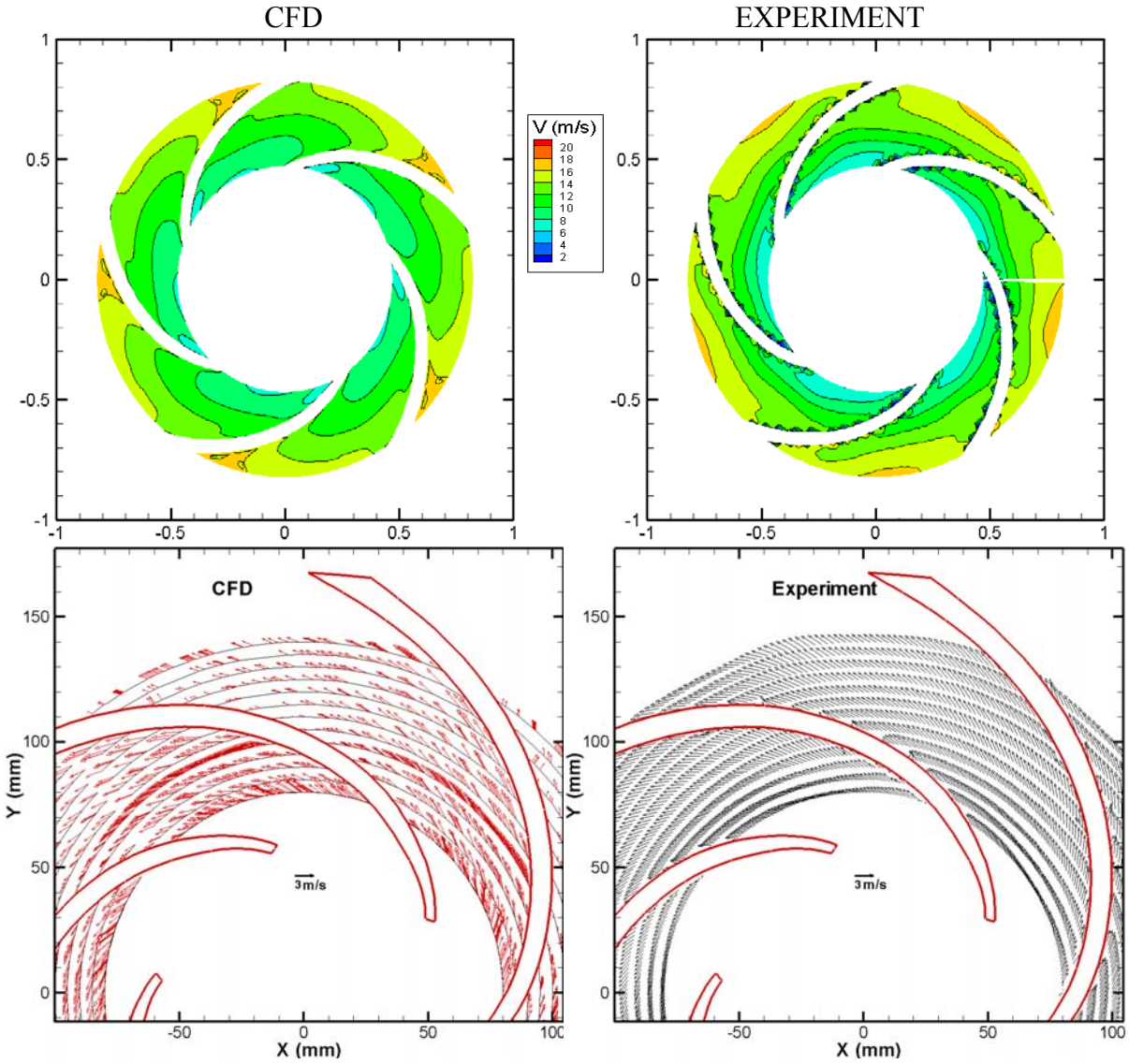

Figure B 9 The comparison between the LDA data and the CFD prediction at the flow rate: 20 lit/sec, Window A, z/h = 0.66

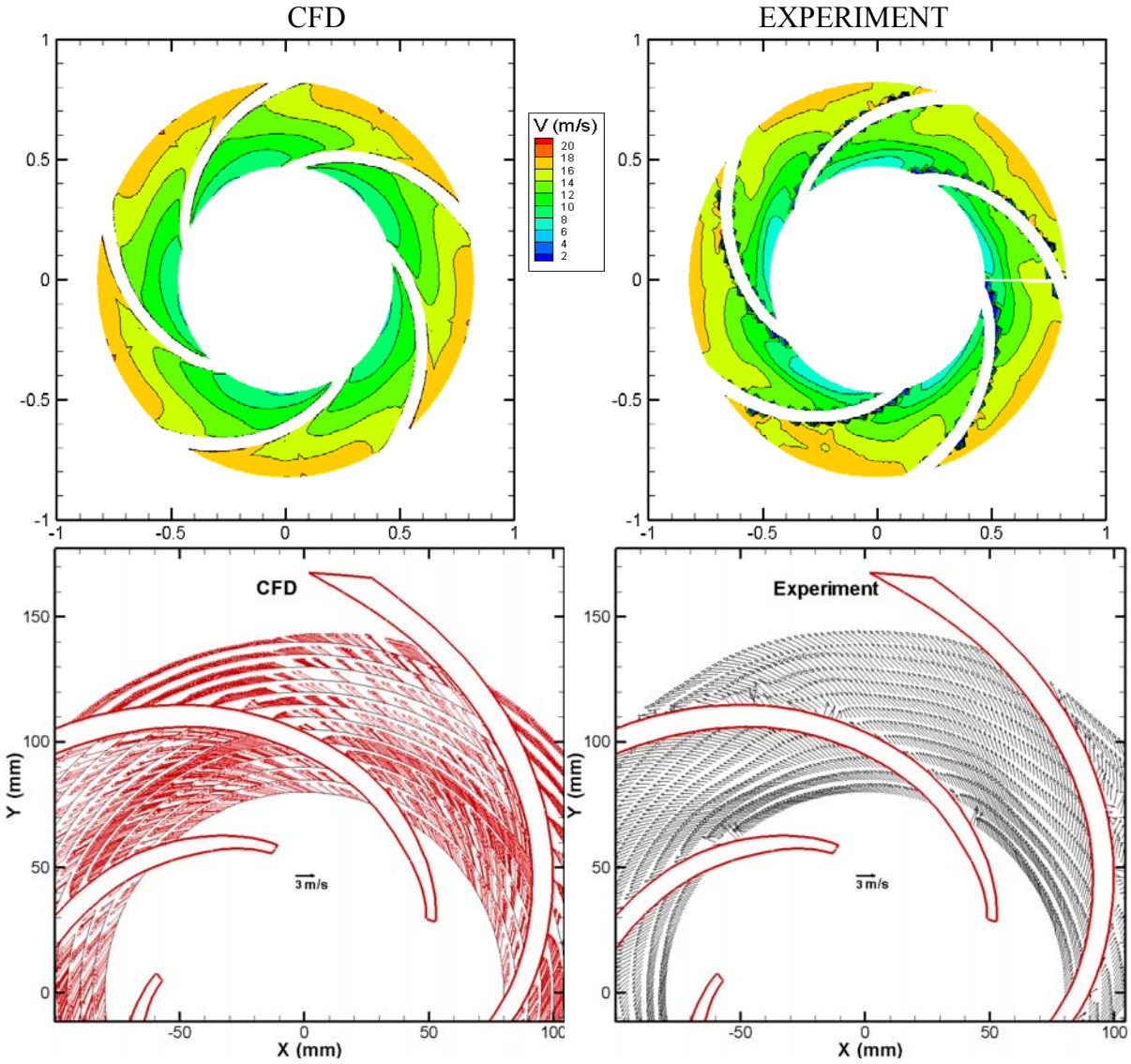

Figure B 10 The comparison between the LDA data and the CFD prediction at the flow rate: 20 lit/sec, Window B, z/h = 0.66

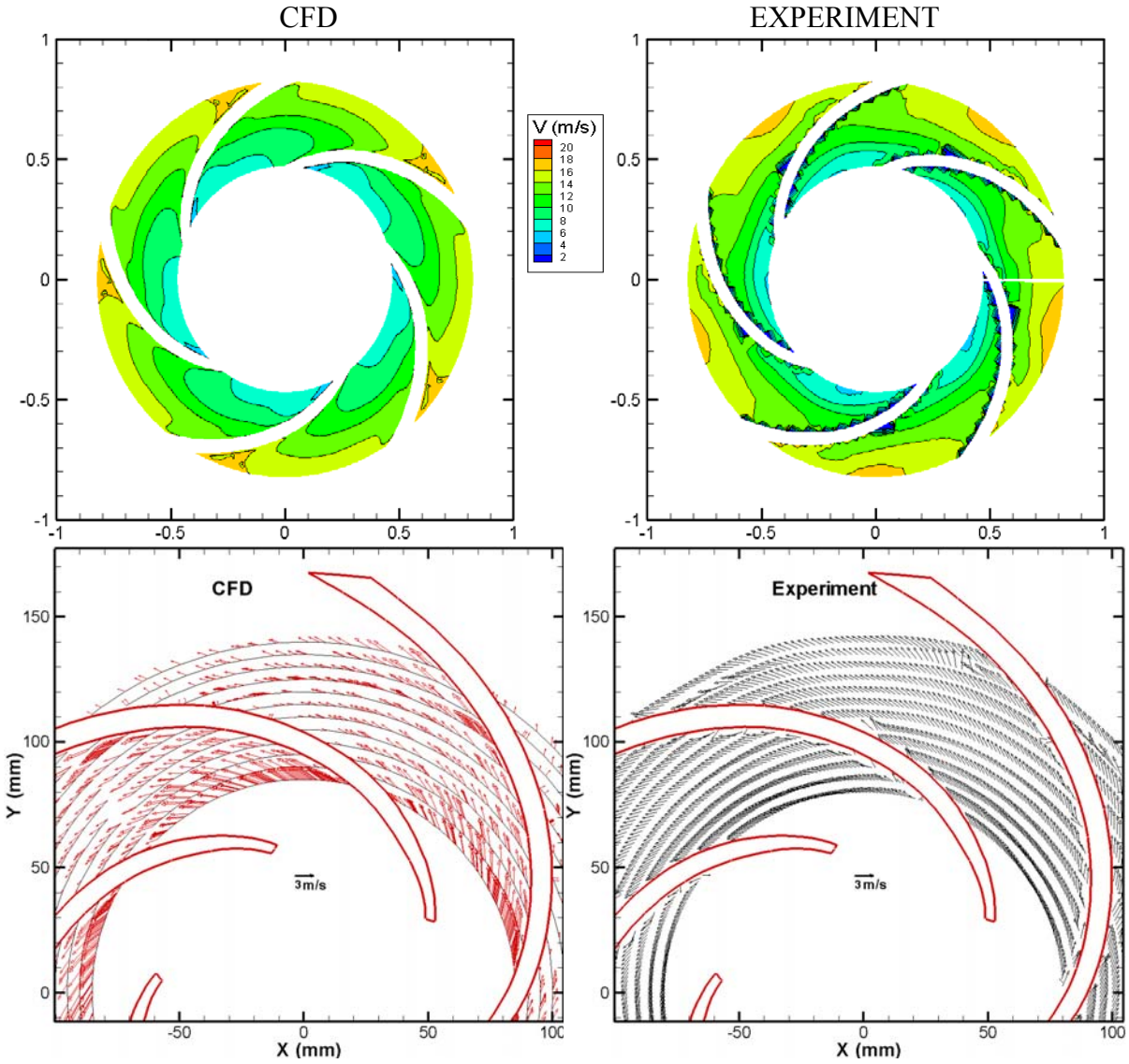

Figure B 11 The comparison between the LDA data and the CFD prediction at the flow rate: 20 lit/sec, Window A, z/h = 0.87

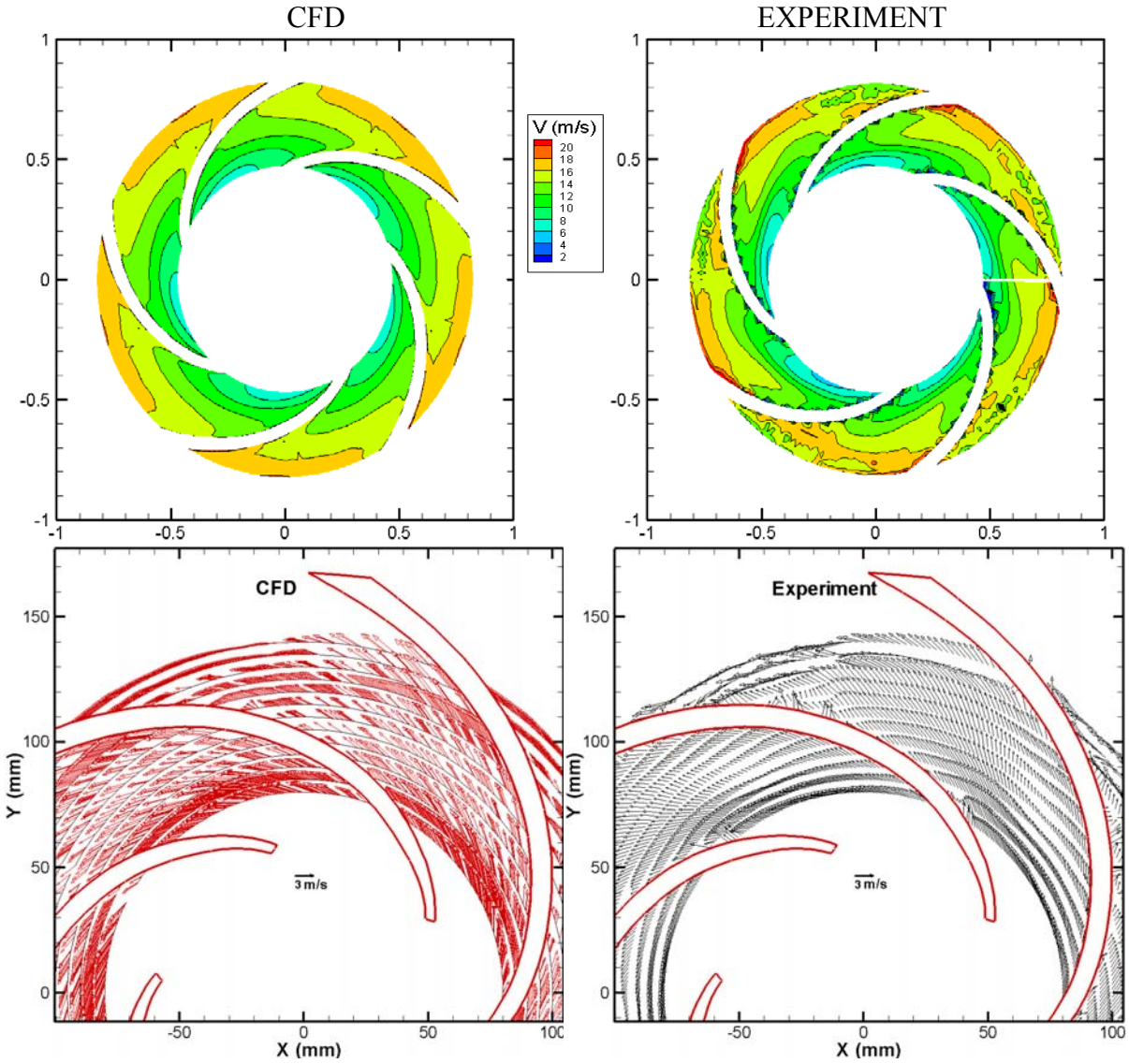

Figure B 12 The comparison between the LDA data and the CFD prediction at the flow rate: 20 lit/sec, Window B, z/h = 0.87

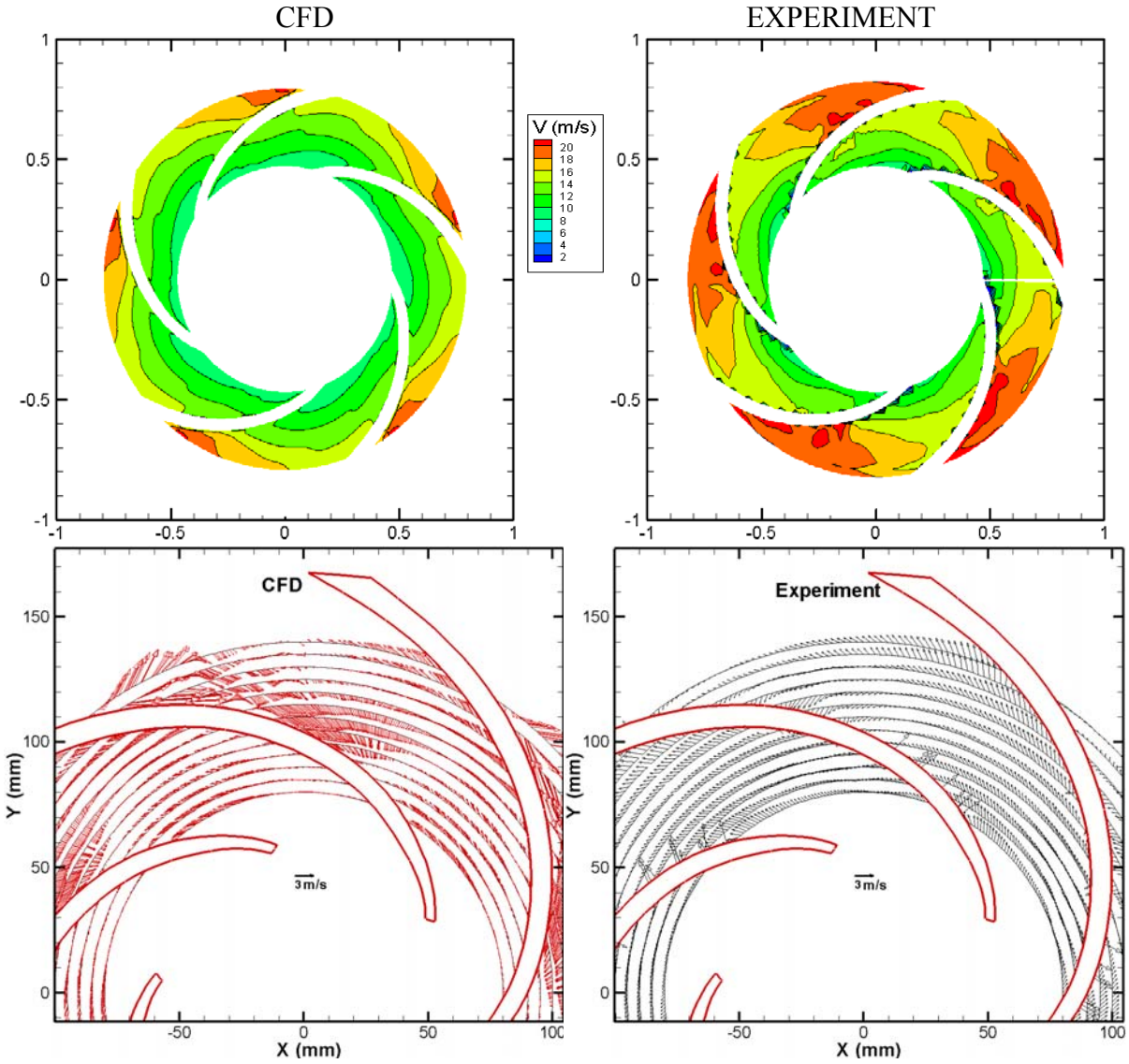

Figure B 13 The comparison between the LDA data and the CFD prediction at the flow rate: 10 lit/sec, Window A, z/h = 0.47

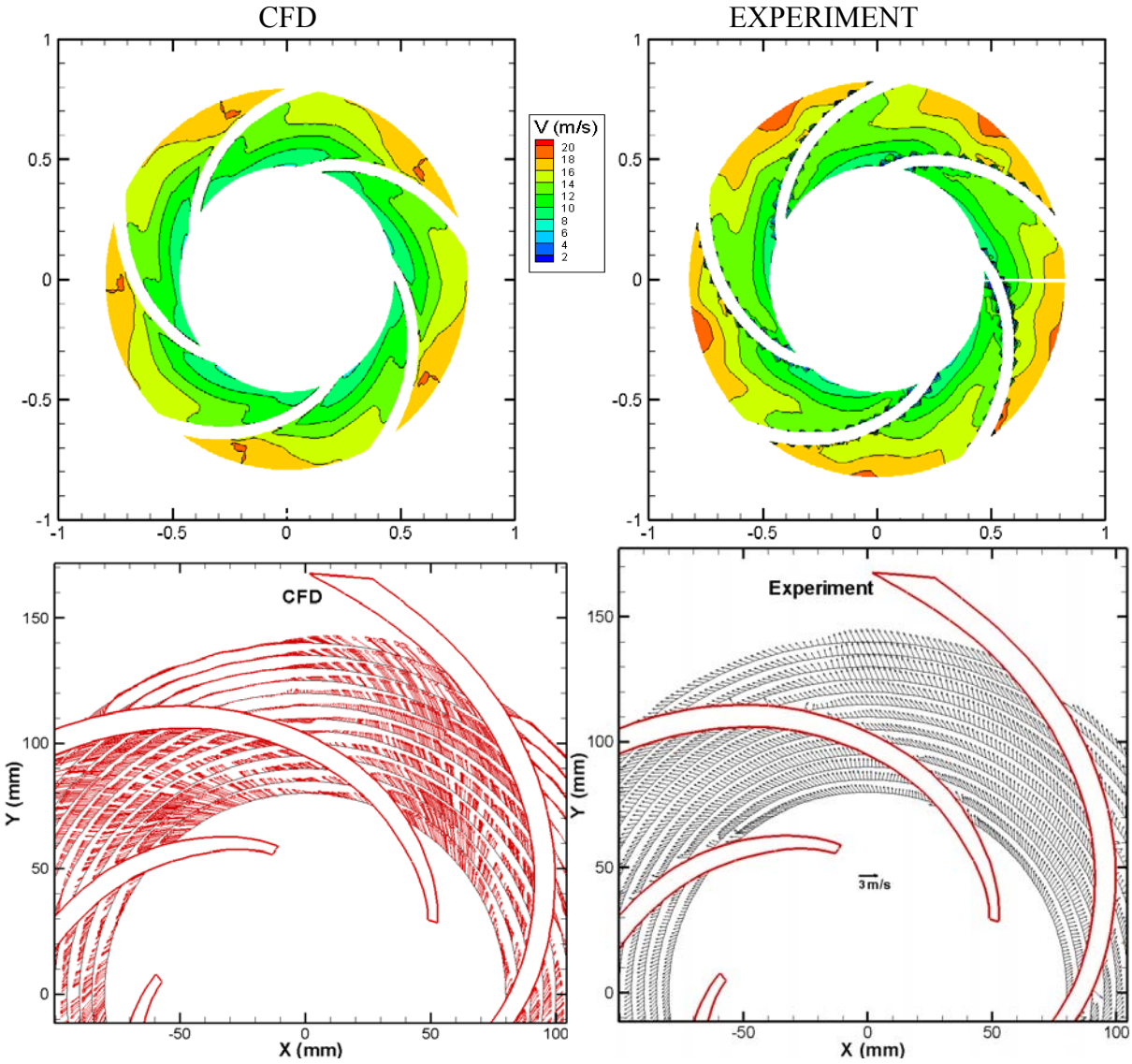

Figure B 14 The comparison between the LDA data and the CFD prediction at the flow rate: 10 lit/sec, Window B, z/h = 0.47

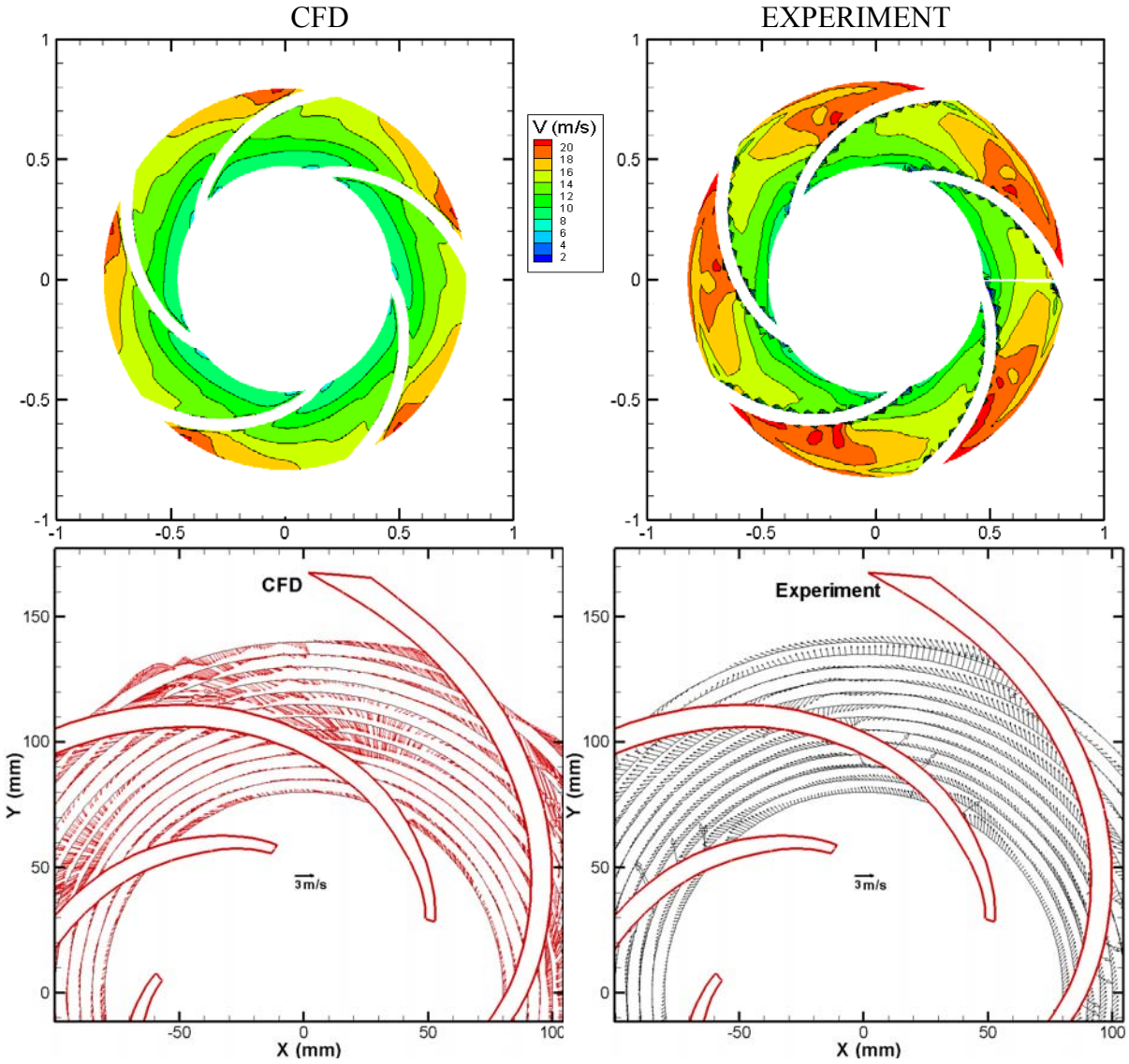

Figure B 15 The comparison between the LDA data and the CFD prediction at the flow rate: 10 lit/sec, Window A, z/h = 0.66

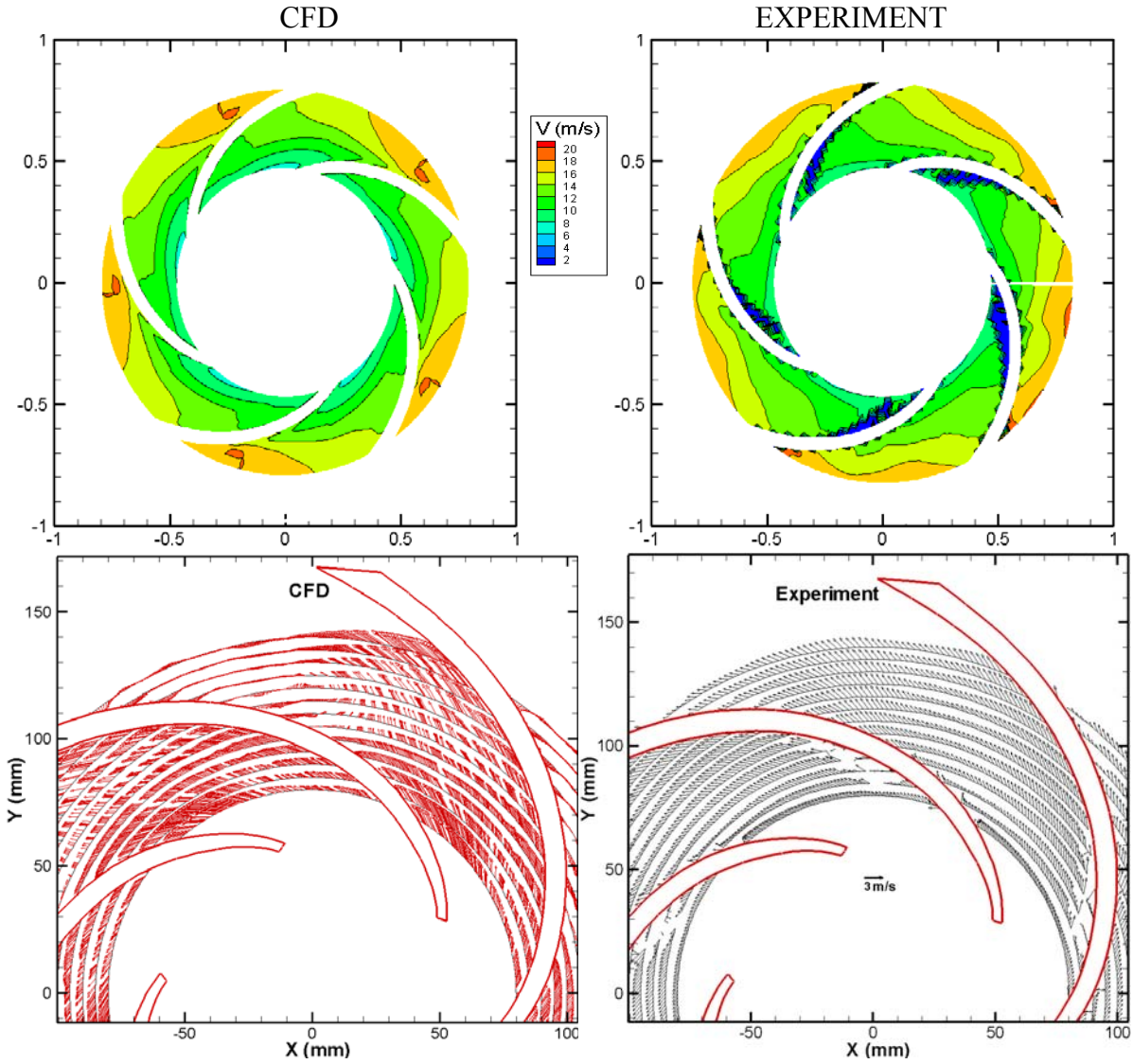

Figure B 16 The comparison between the LDA data and the CFD prediction at the flow rate: 10 lit/sec, Window B, z/h = 0.66

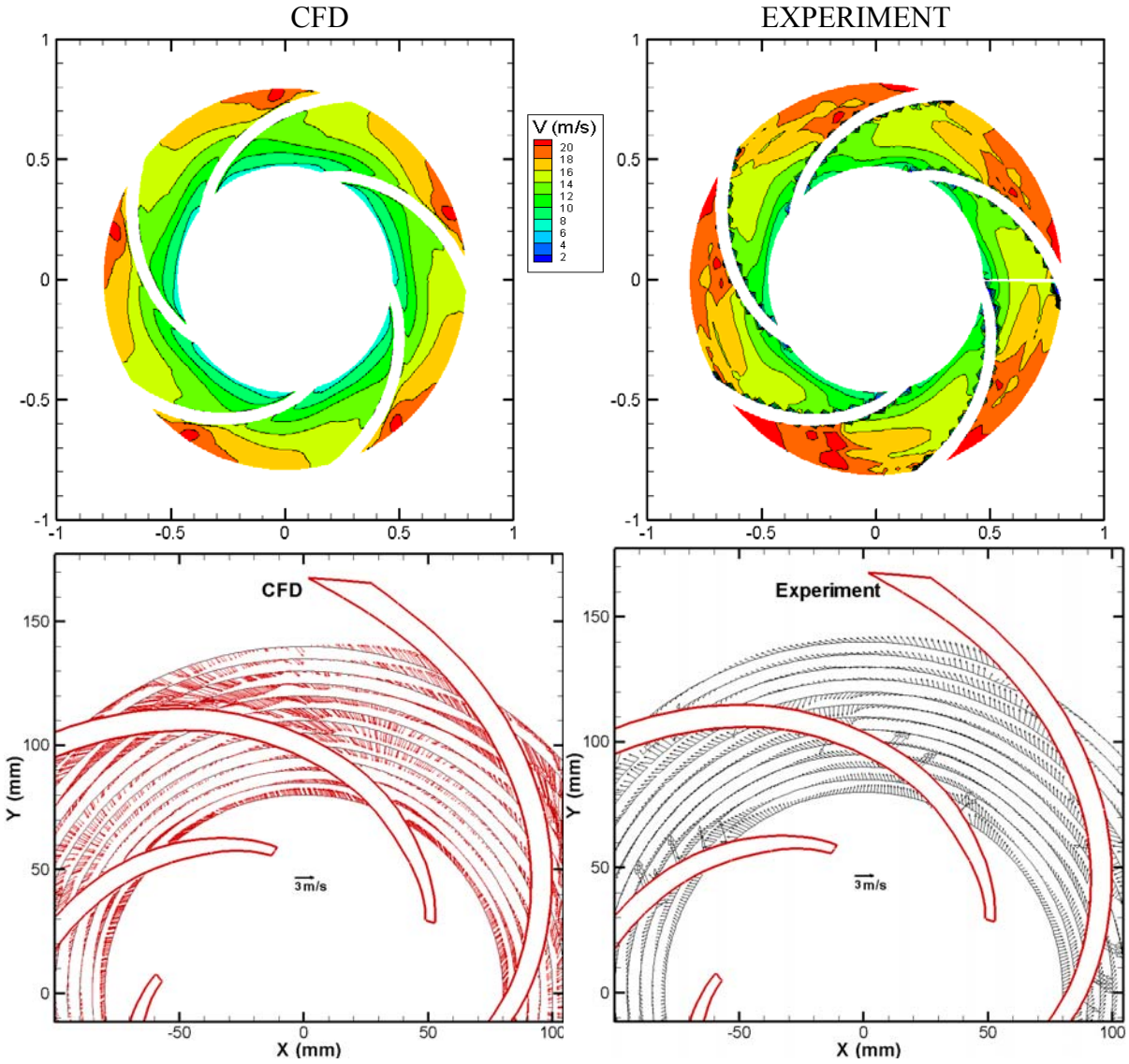

Figure B 17 The comparison between the LDA data and the CFD prediction at the flow rate: 10 lit/sec, Window A, z/h = 0.87

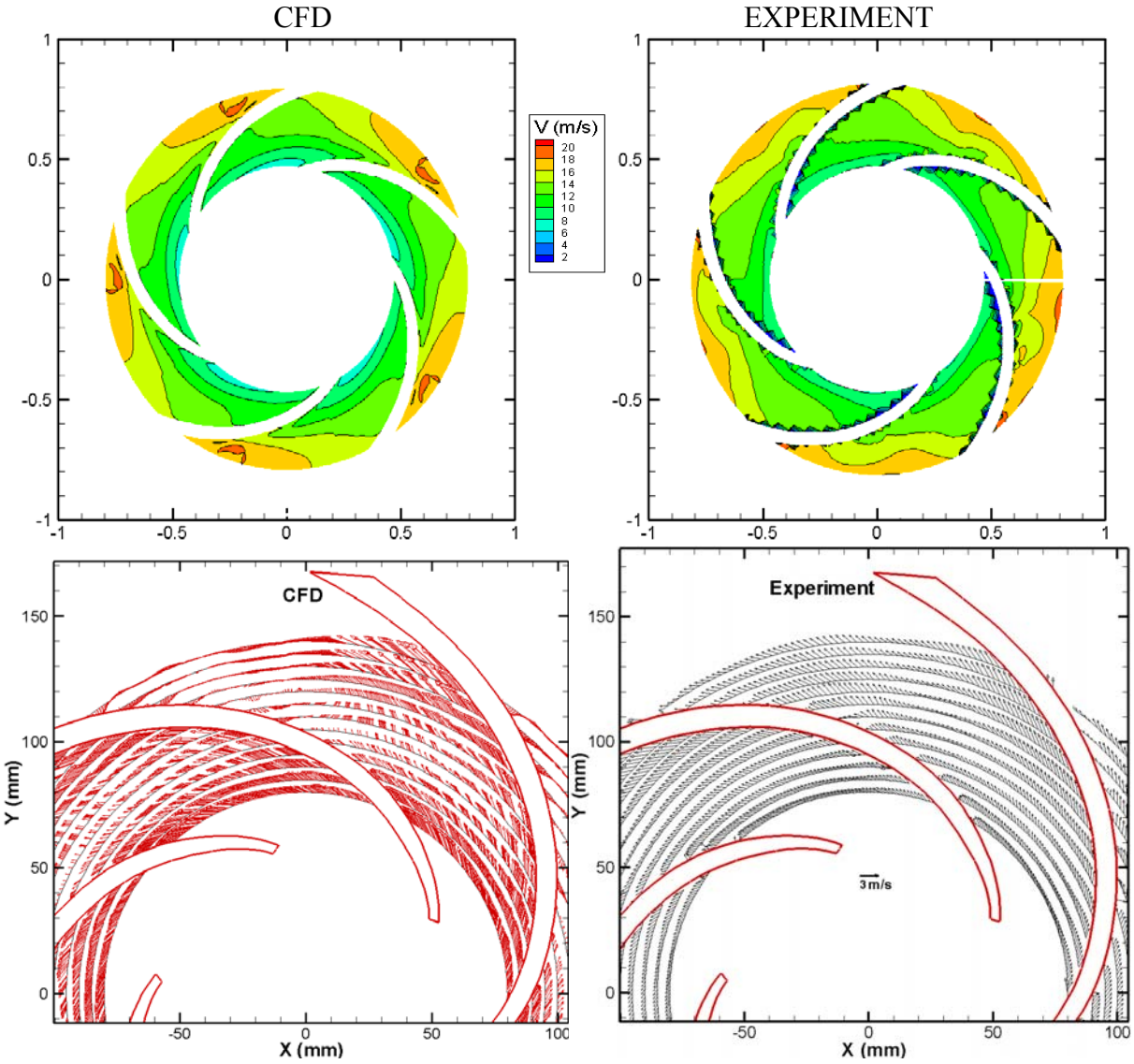

Figure B 18 The comparison between the LDA data and the CFD prediction at the flow rate: 10 lit/sec, Window B, z/h = 0.87

APPENDIX C

PERFORMANCE PLOTS AND AXIAL THRUST PREDICTION

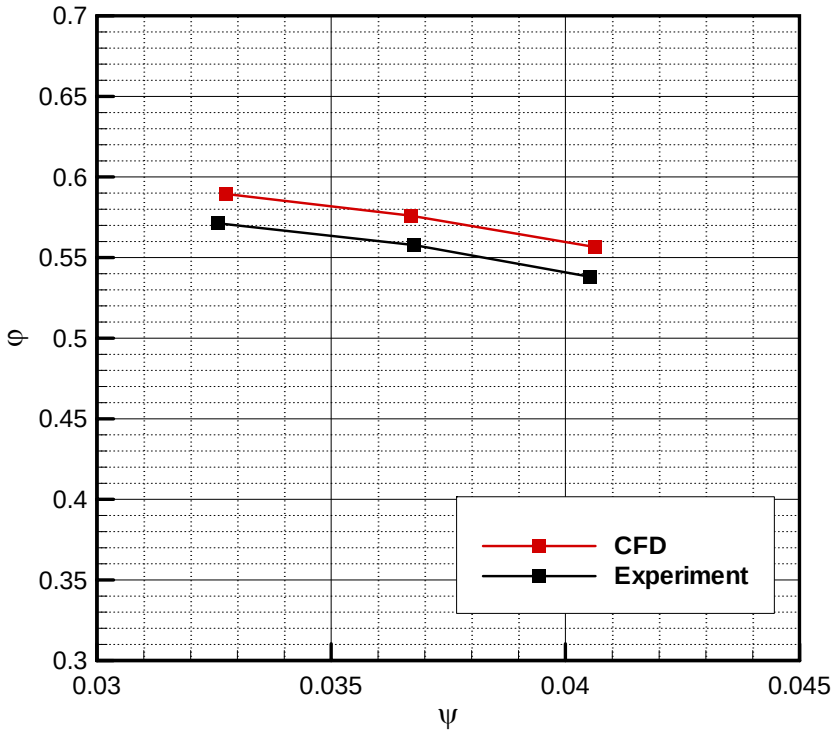

Figure C 1 Performance plot of 0.91mm clearance without balance holes

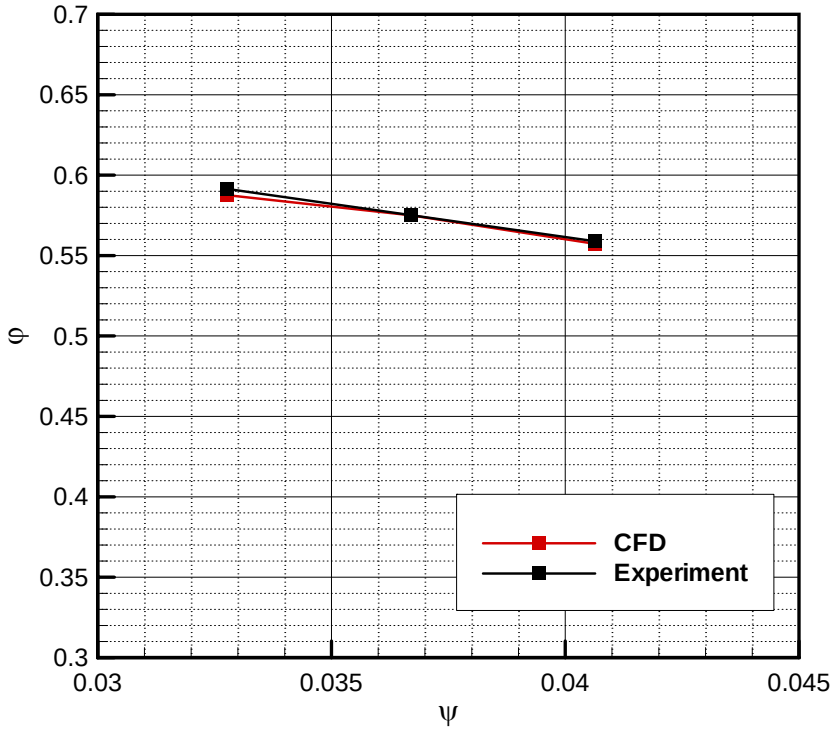

Figure C 2 Performance plot of 0.91mm clearance with balance holes

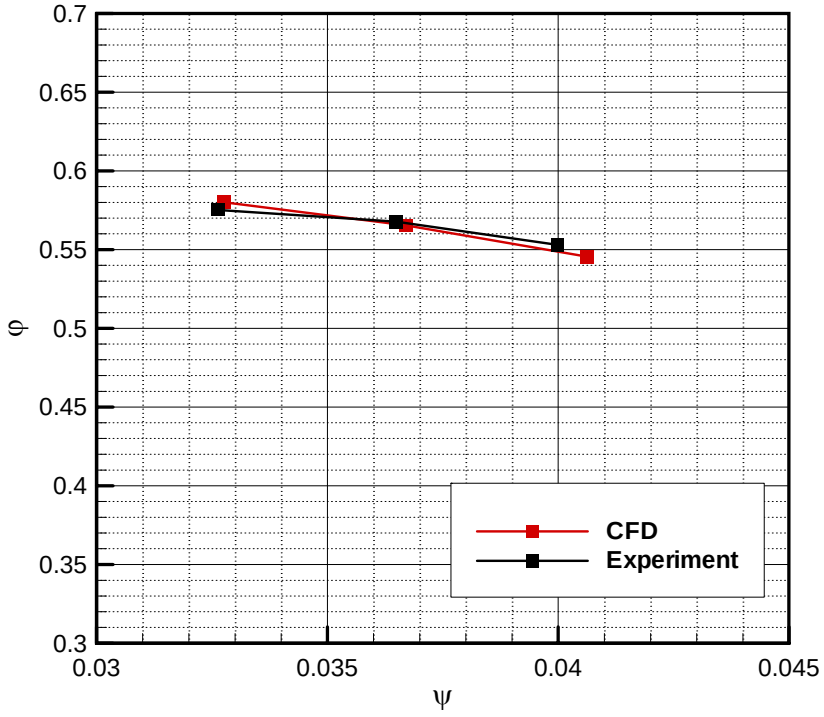

Figure C 3 Performance plot of 1.87mm clearance without balance holes

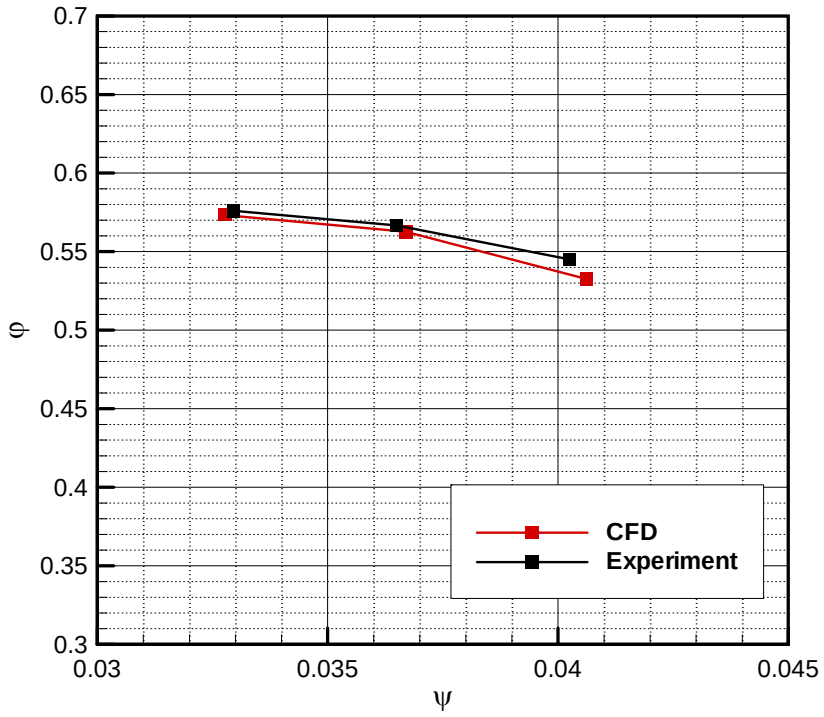

Figure C 4 Performance plot of 1.87mm clearance with balance holes

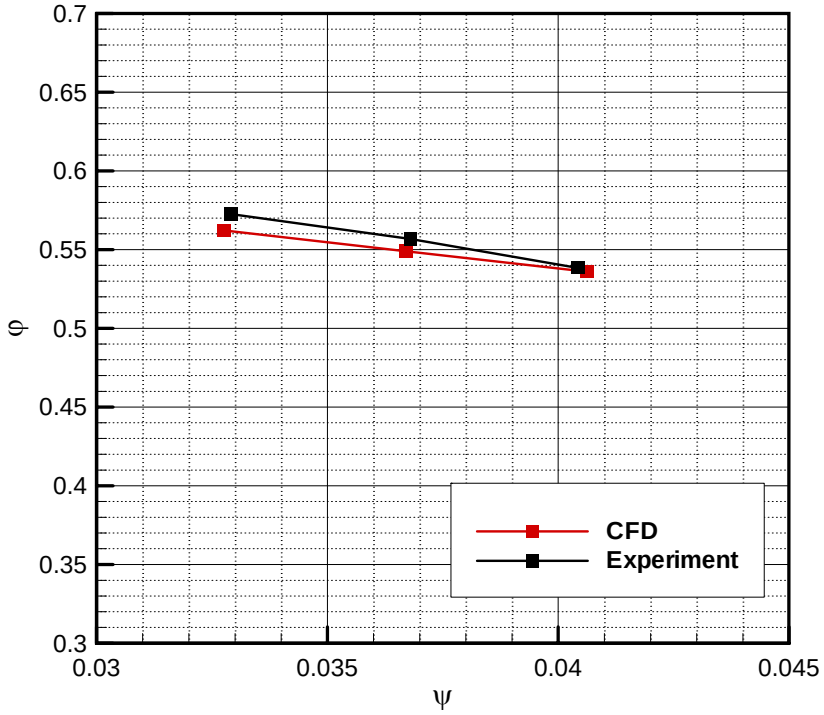

Figure C 5 Performance plot of 3.17mm clearance without balance holes

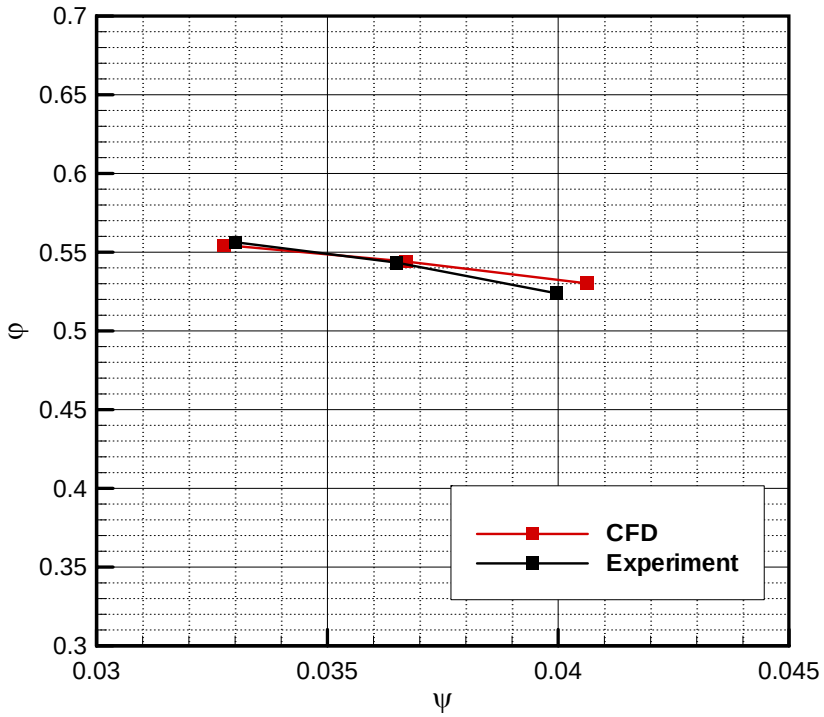

Figure C 6 Performance plot of 3.17mm clearance with balance holes

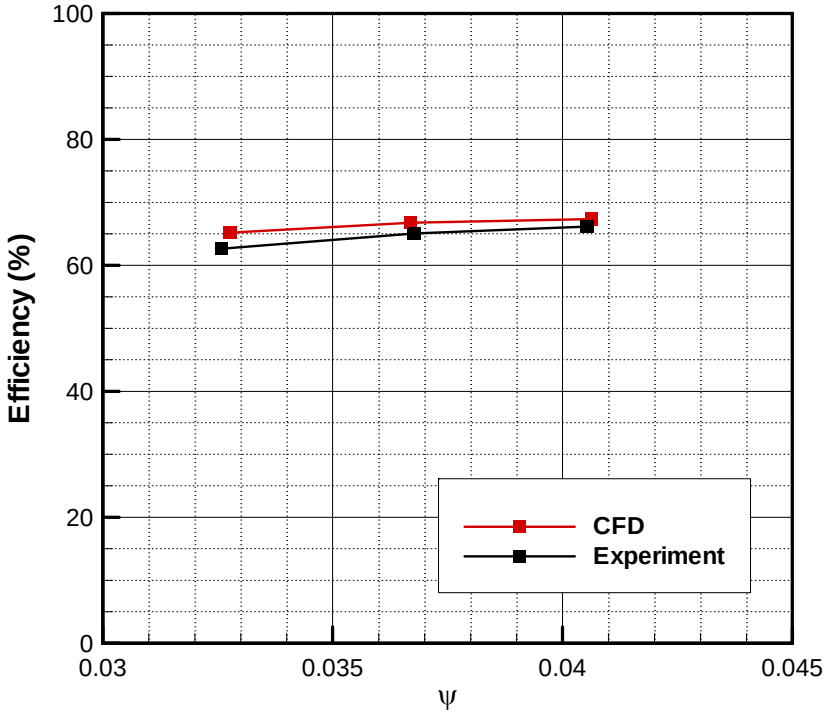

Figure C 7 Efficiency curve of 0.91mm clearance without balance holes

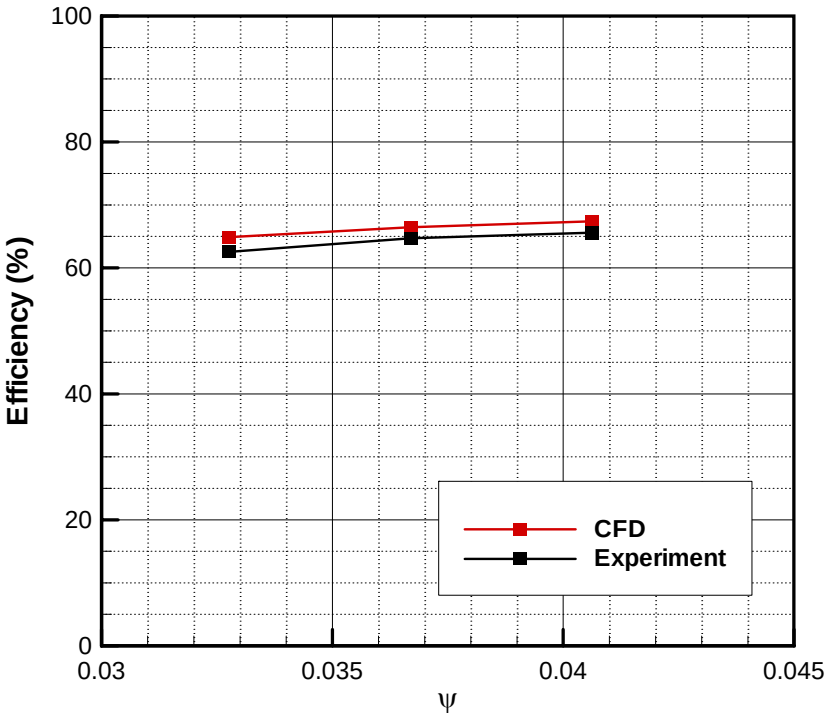

Figure C 8 Efficiency curve of 0.91mm clearance with balance holes

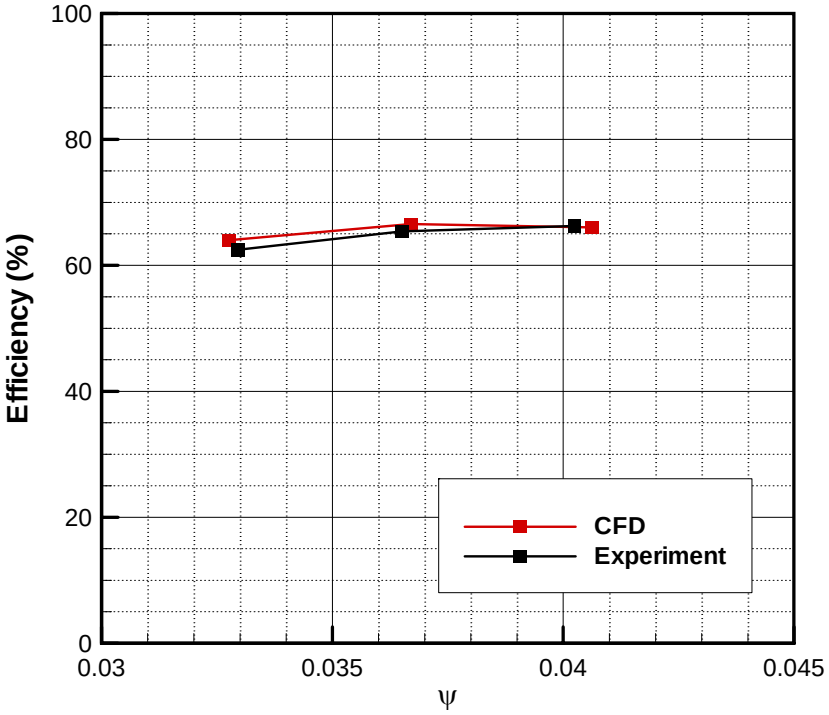

Figure C 9 Efficiency curve of 1.87mm clearance without balance holes

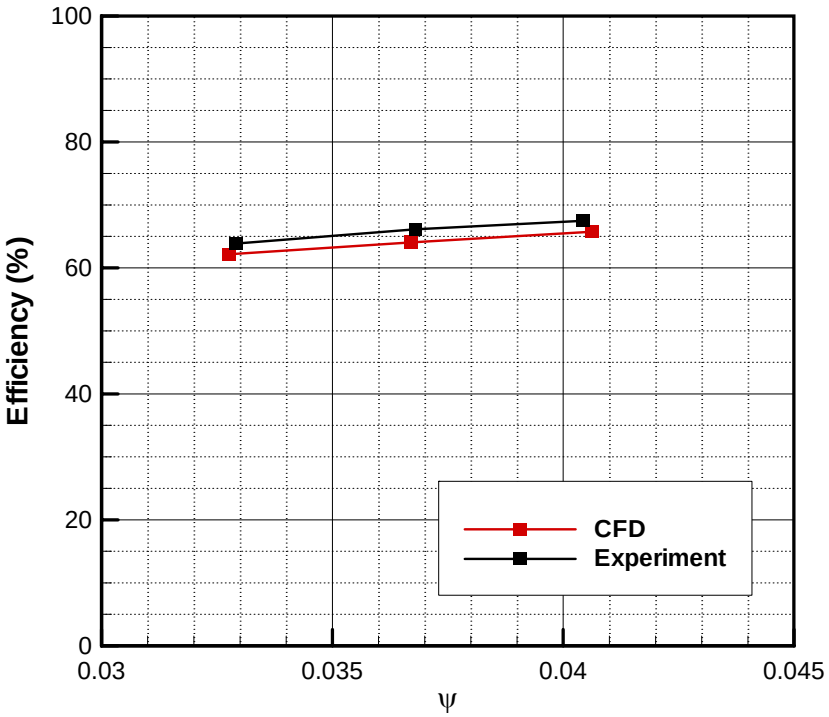

Figure C 10 Efficiency curve of 1.87mm clearance with balance holes

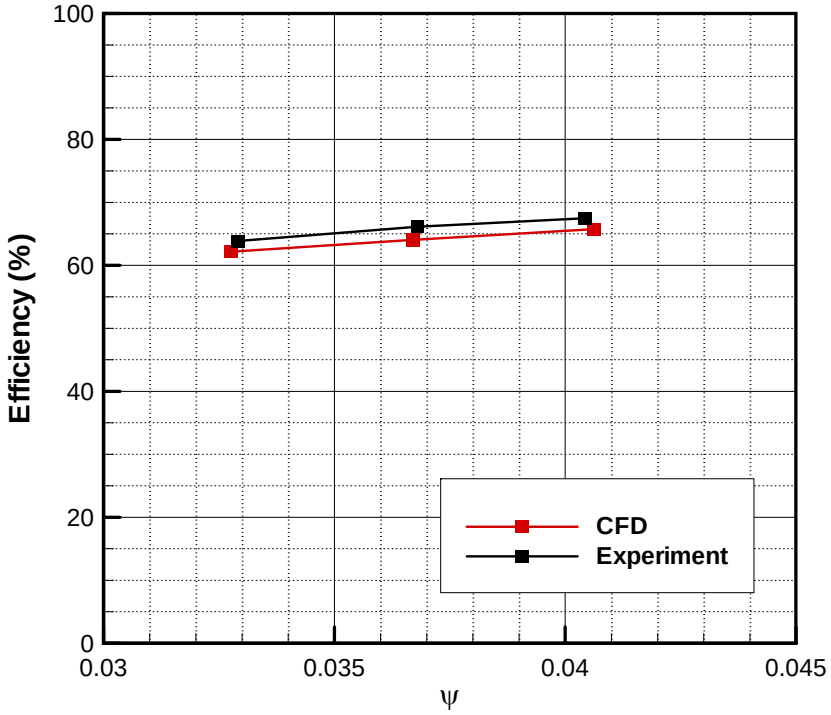

Figure C 11 Efficiency curve of 3.17mm clearance without balance holes

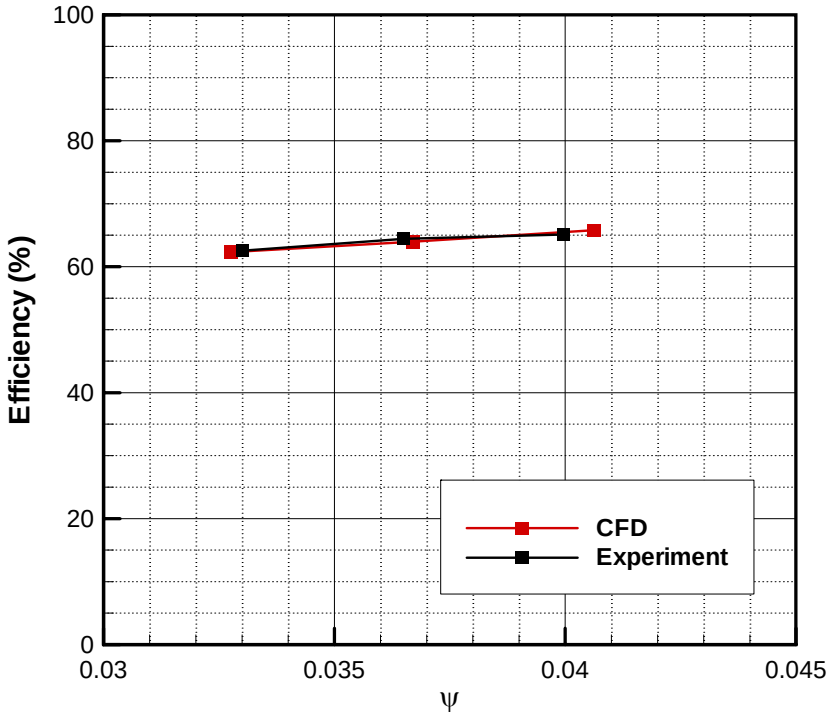

Figure C 12 Efficiency curve of 3.17mm clearance with balance holes

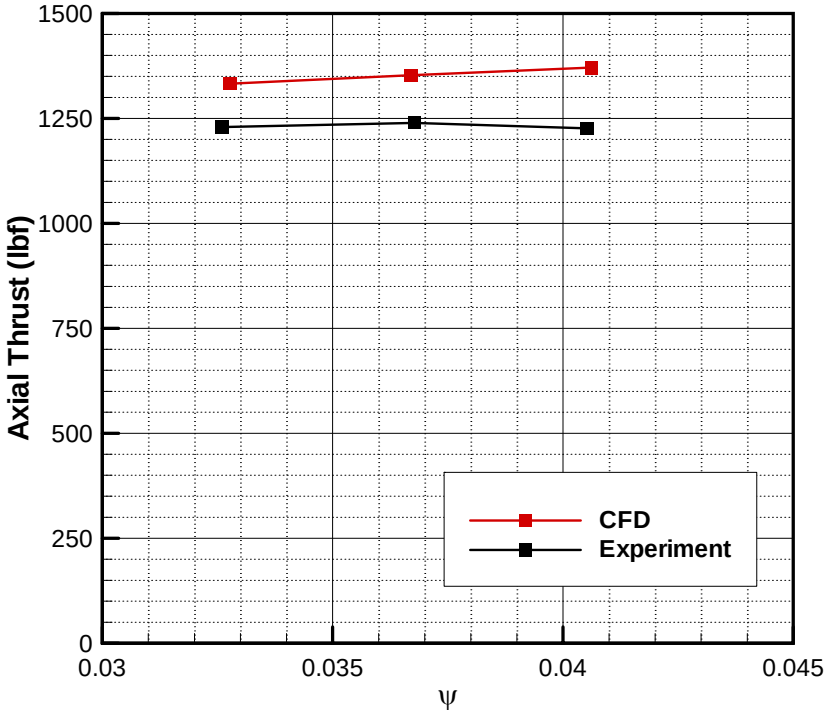

Figure C 13 Axial thrust of 0.91mm clearance without balance holes

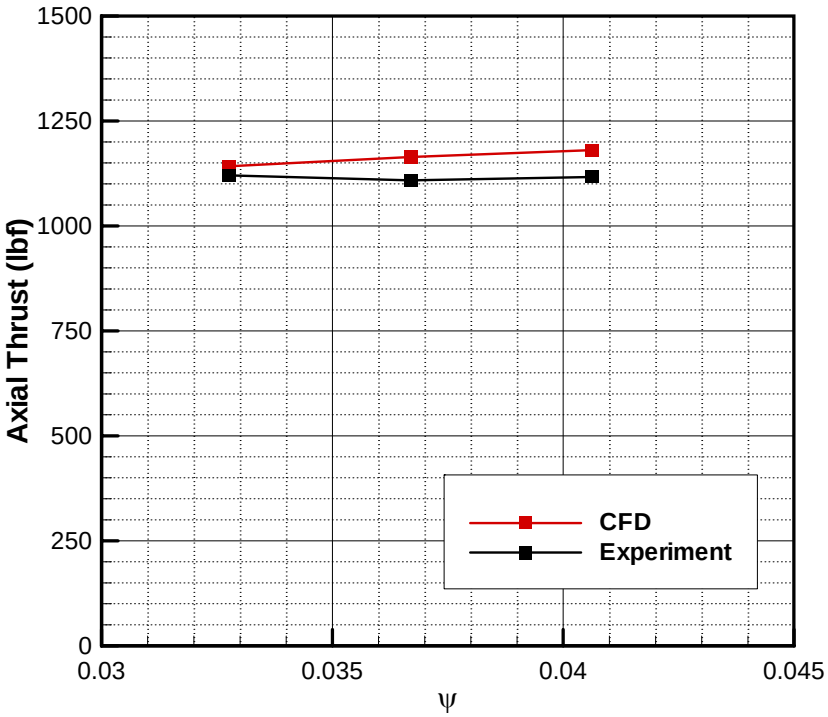

Figure C 14 Axial thrust of 0.91mm clearance with balance holes

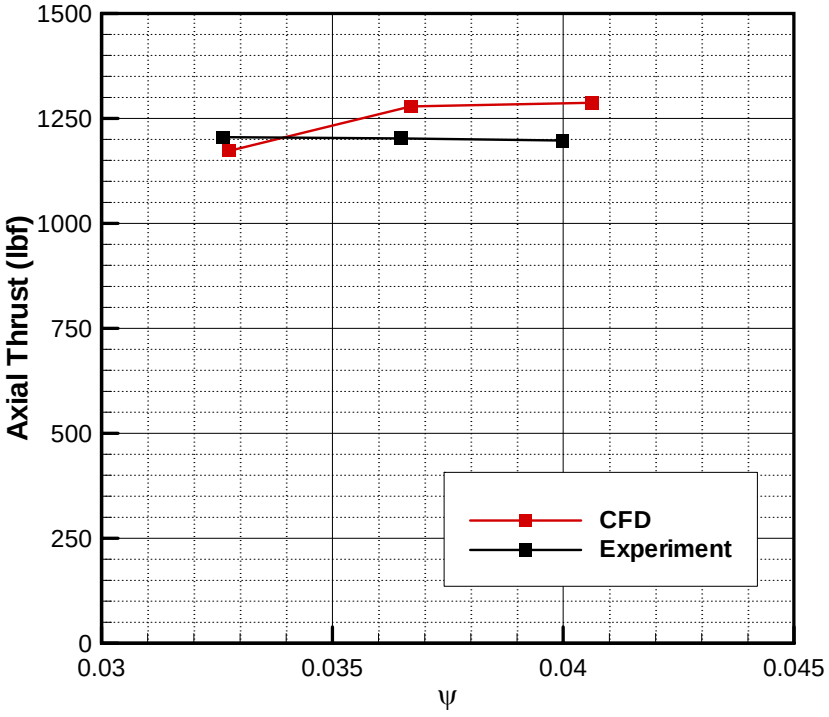

Figure C 15 Axial thrust of 1.87mm clearance without balance holes

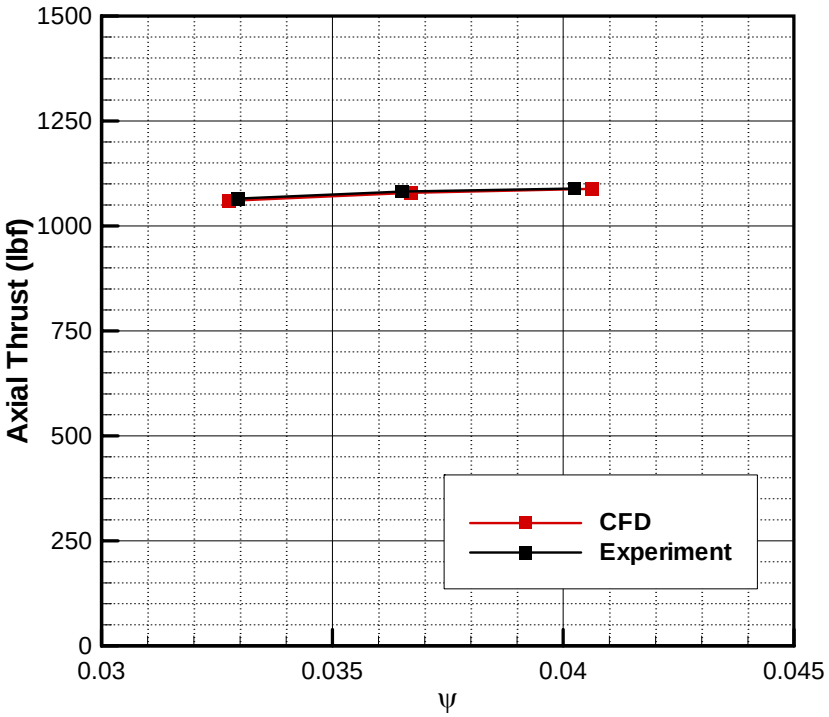

Figure C 16 Axial thrust of 1.87mm clearance with balance holes

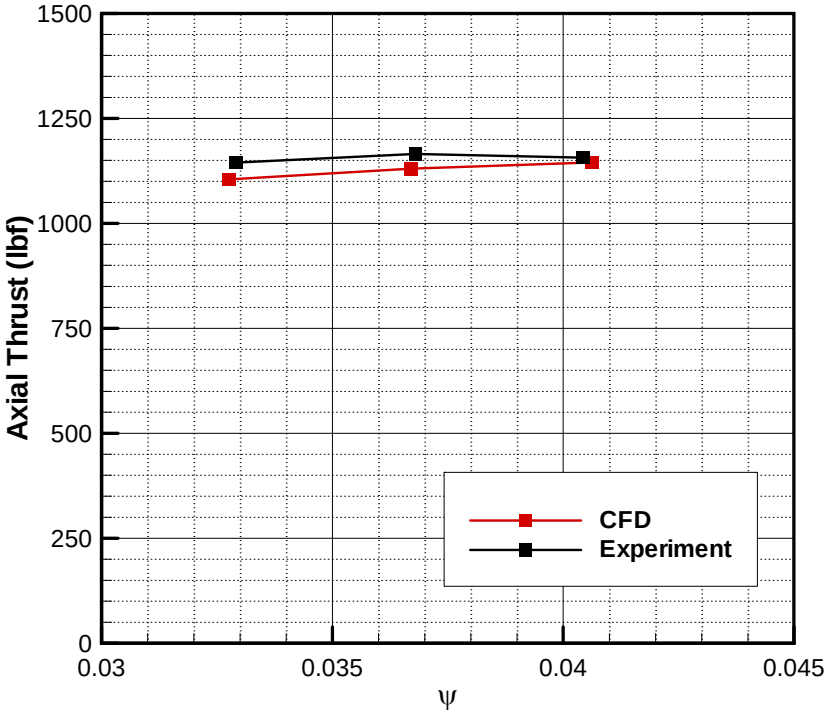

Figure C 17 Axial thrust of 3.17mm clearance without balance holes

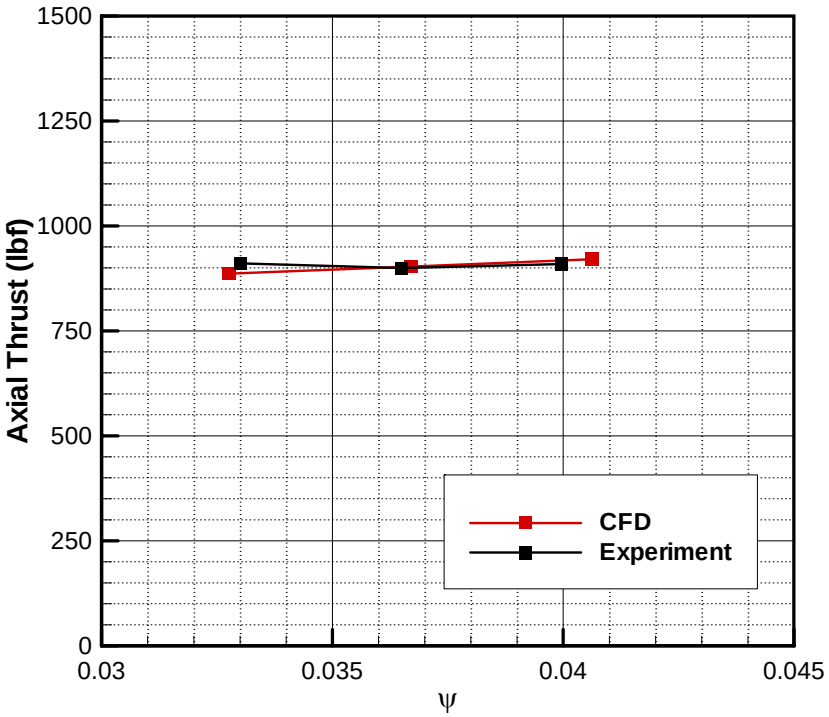

Figure C 18 Axial thrust of 3.17mm clearance with balance holes

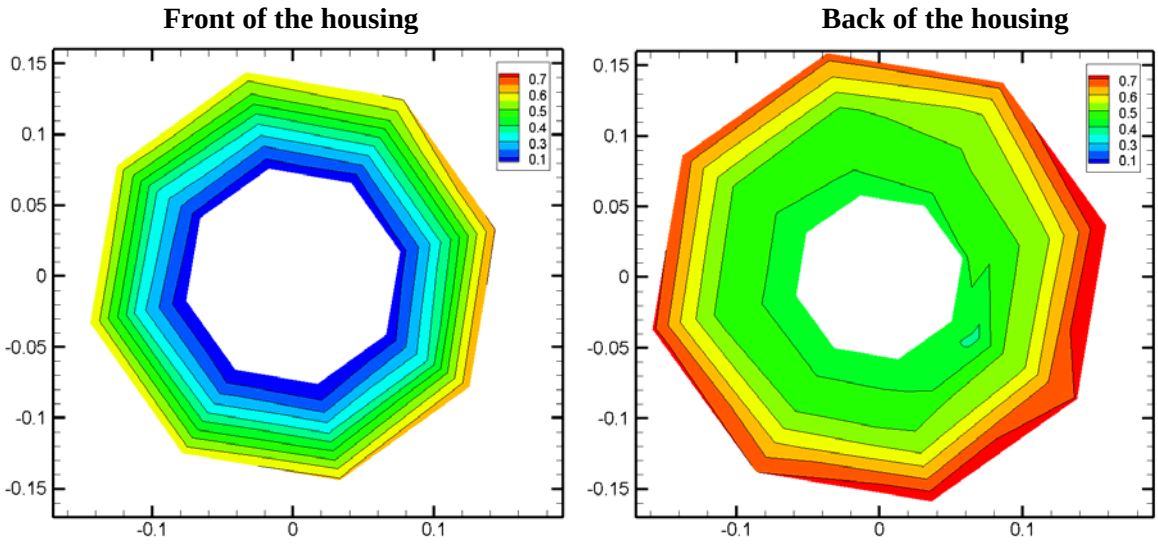

Figure C 19 Normalized pressure distribution of the pump with 0.91mm clearance without balance hole at 25 lit/sec flow rate from experiment by Hossain

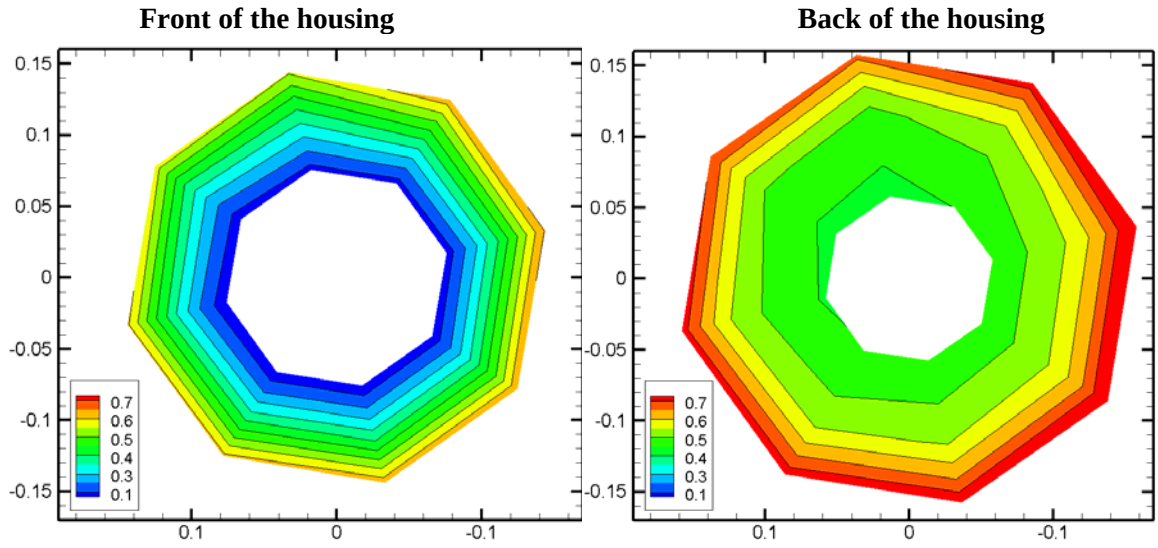

Figure C 20 Normalized pressure distribution of the pump with 0.91mm clearance without balance hole at 25 lit/sec flow rate from CFD

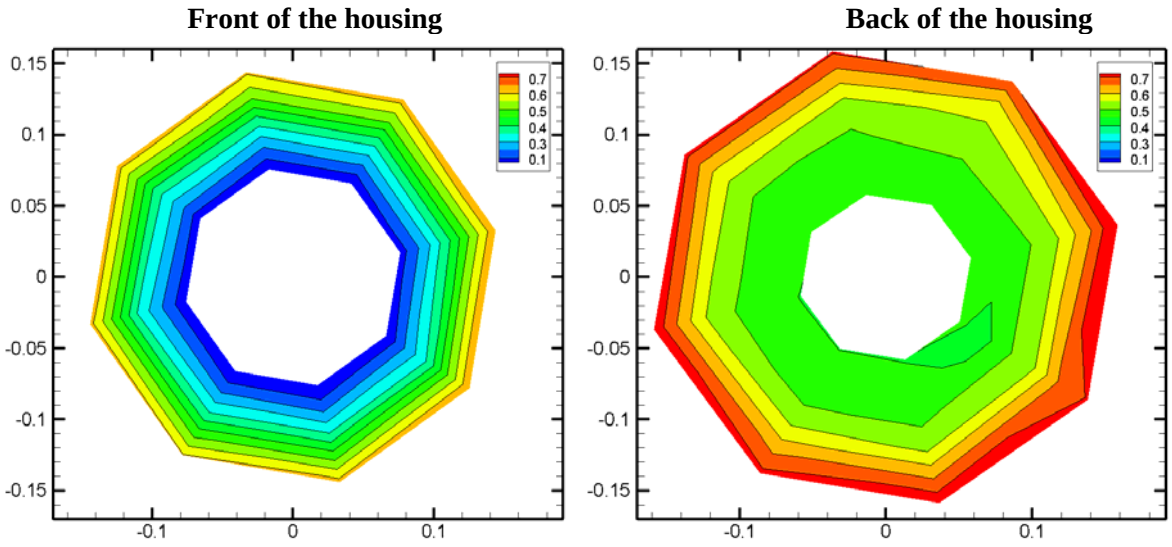

Figure C 21 Normalized pressure distribution of the pump with 0.91mm clearance without balance hole at 28 lit/sec flow rate from experiment by Hossain

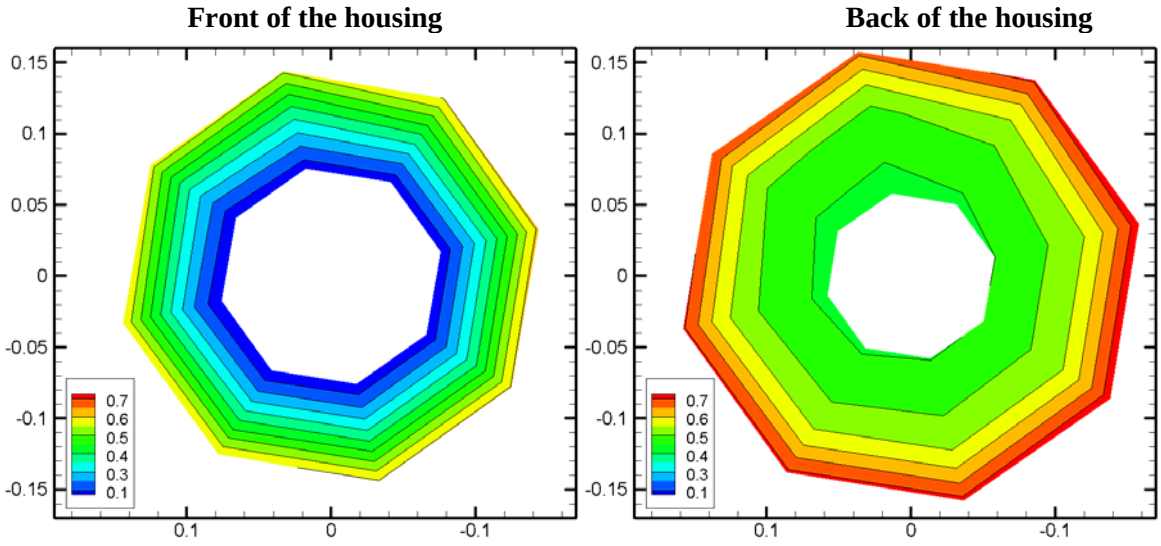

Figure C 22 Normalized pressure distribution of the pump with 0.91mm clearance without balance hole at 28 lit/sec flow rate from CFD

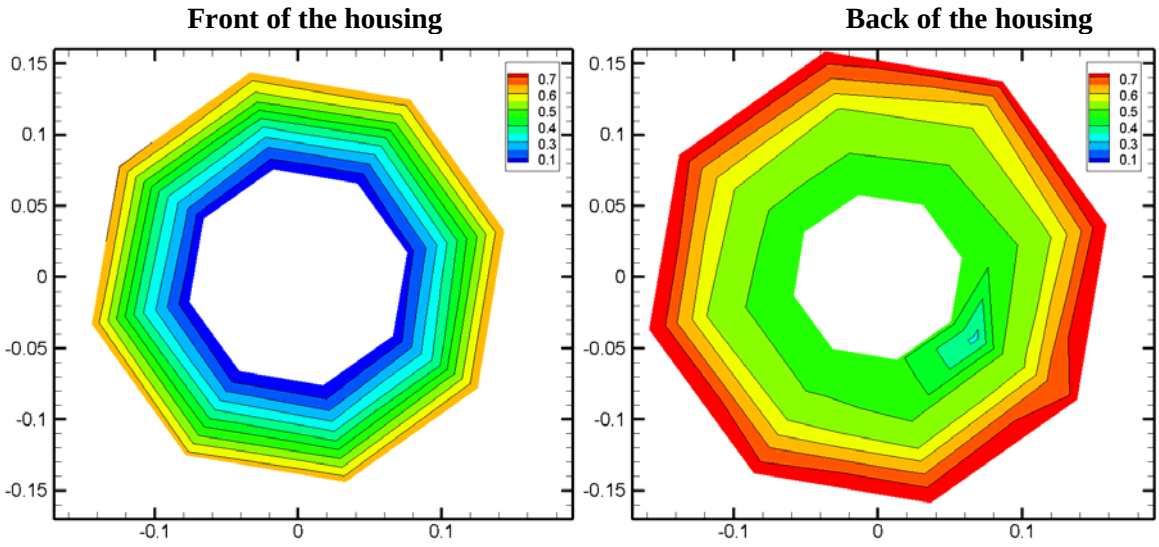

Figure C 23 Normalized pressure distribution of the pump with 0.91mm clearance without balance hole at 31 lit/sec flow rate from experiment by Hossain

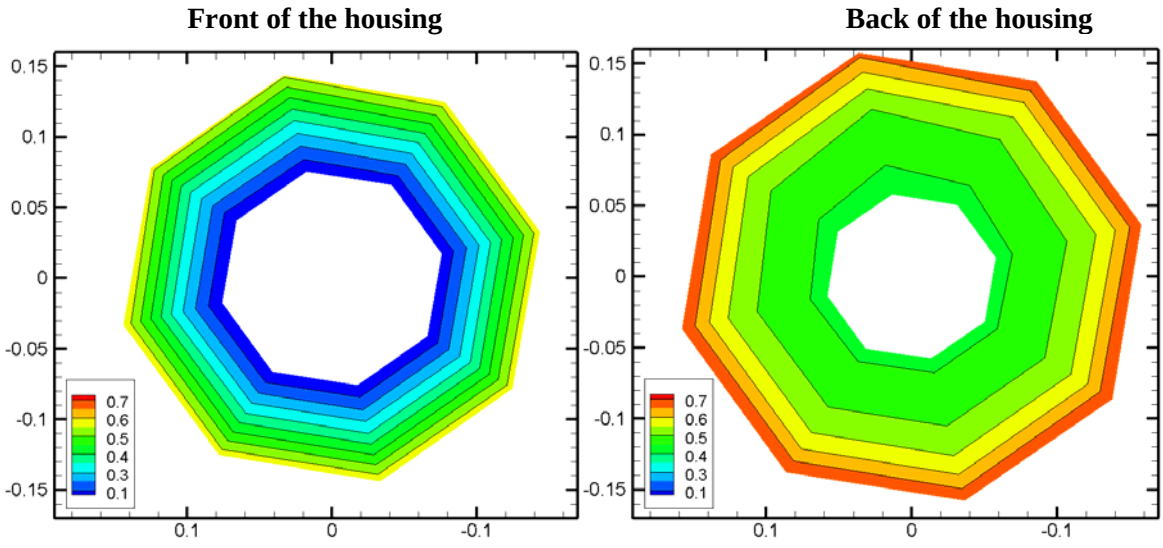

Figure C 24 Normalized pressure distribution of the pump with 0.91mm clearance without balance hole at 31 lit/sec flow rate from CFD

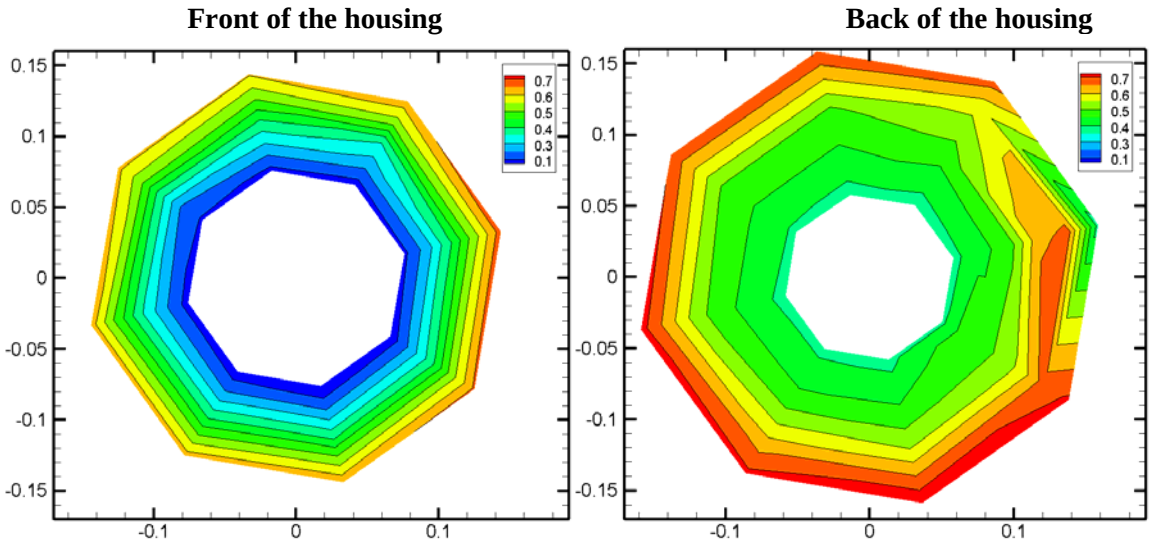

Figure C 25 Normalized pressure distribution of the pump with 0.91mm clearance with balance hole at 25 lit/sec flow rate from experiment by Hossain

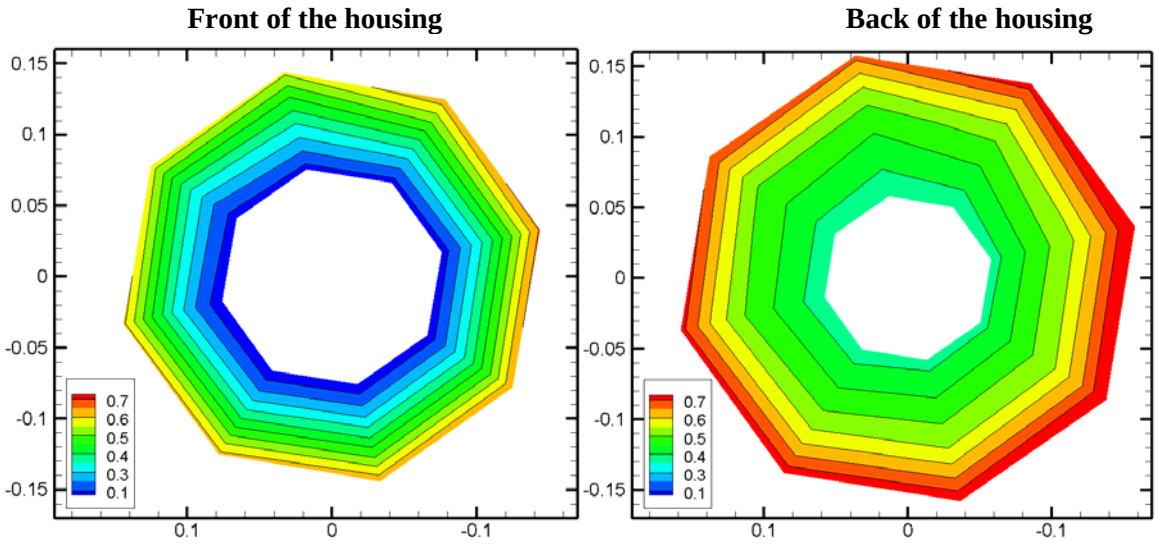

Figure C 26 Normalized pressure distribution of the pump with 0.91mm clearance with balance hole at 25 lit/sec flow rate from CFD

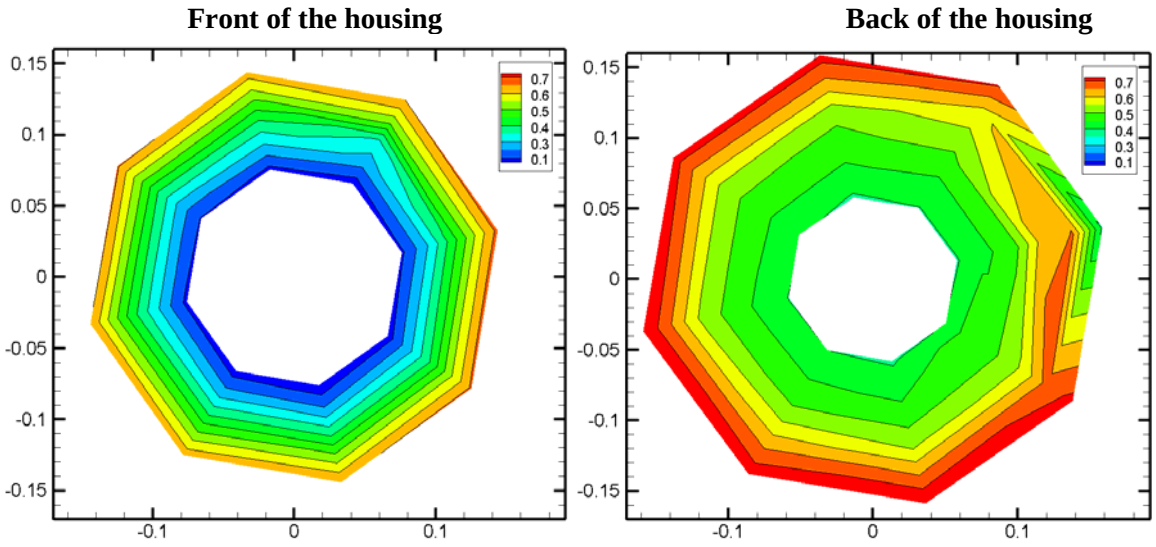

Figure C 27 Normalized pressure distribution of the pump with 0.91mm clearance with balance hole at 28 lit/sec flow rate from experiment by Hossain

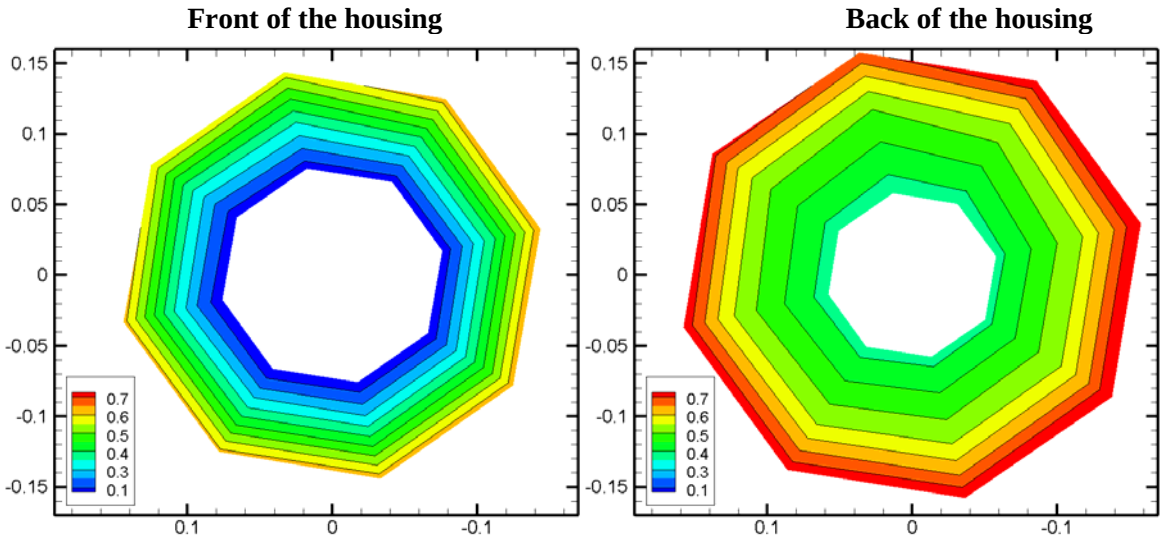

Figure C 28 Normalized pressure distribution of the pump with 0.91mm clearance with balance hole at 28 lit/sec flow rate from CFD

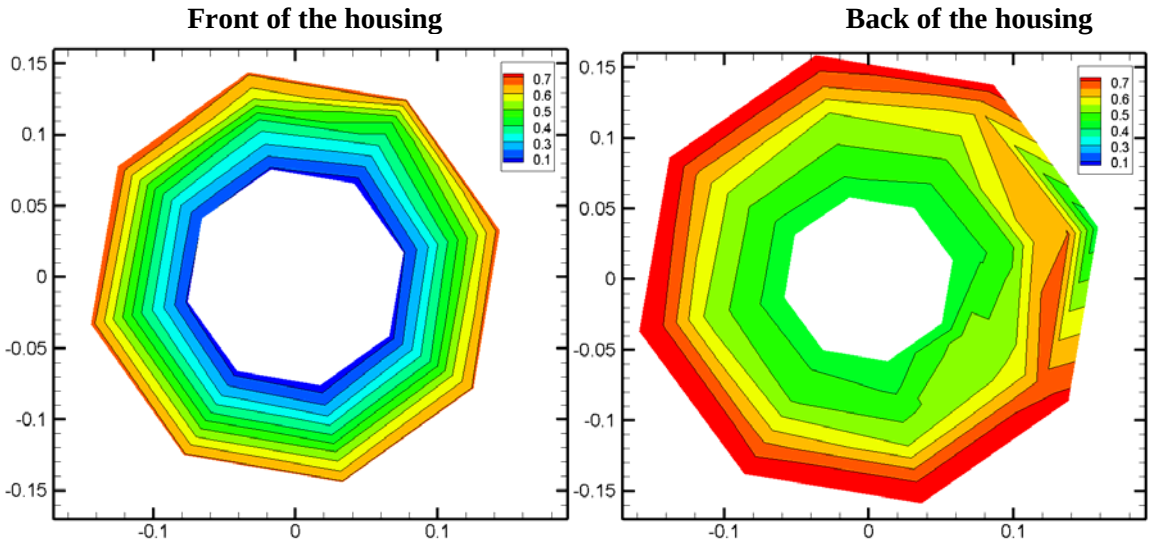

Figure C 29 Normalized pressure distribution of the pump with 0.91mm clearance with balance hole at 31 lit/sec flow rate from experiment by Hossain

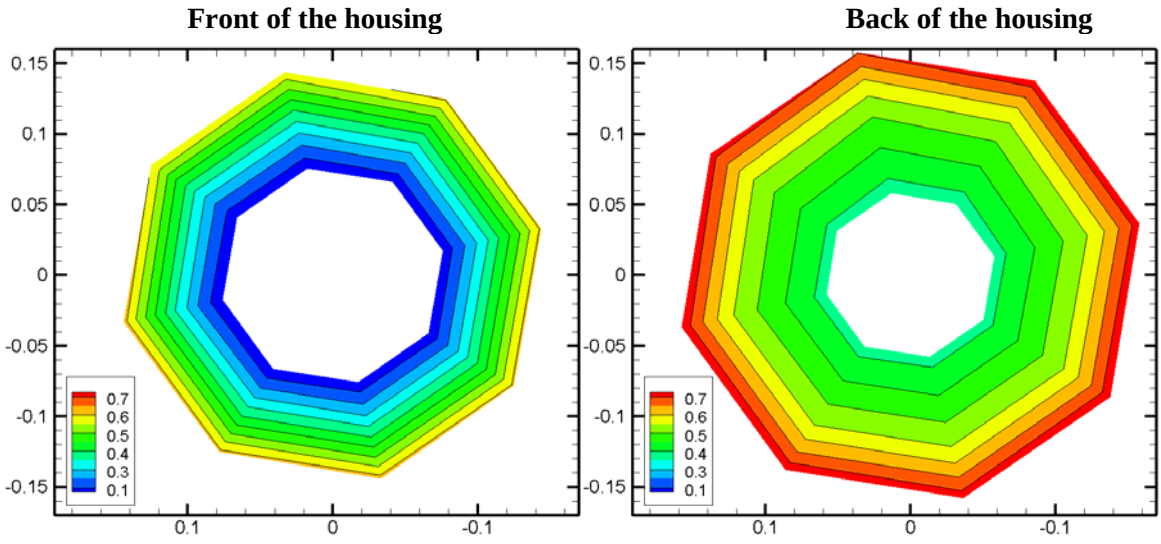

Figure C 30 Normalized pressure distribution of the pump with 0.91mm clearance with balance hole at 31 lit/sec flow rate from CFD

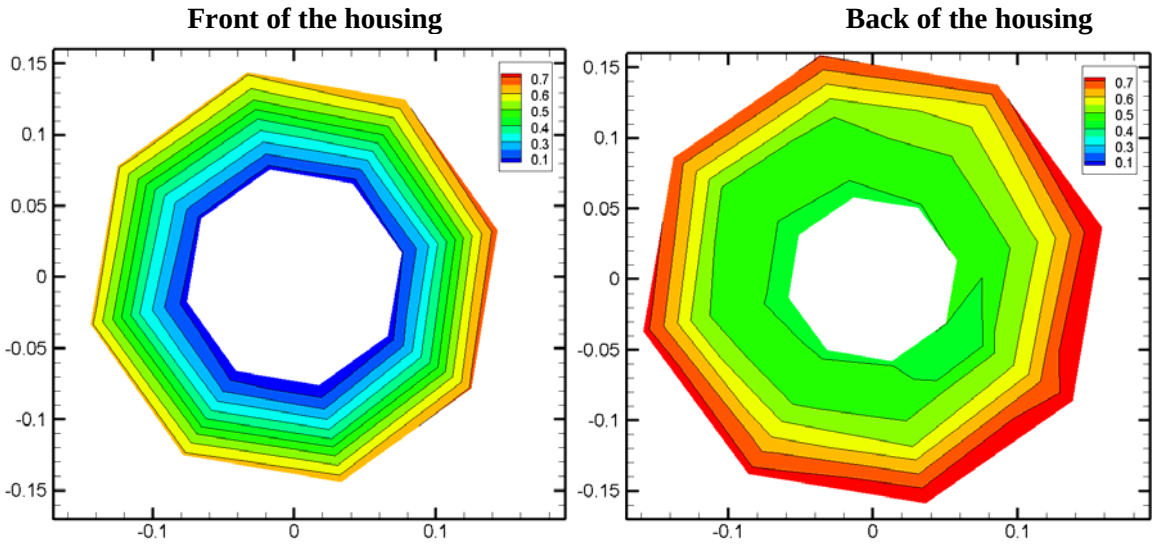

Figure C 31 Normalized pressure distribution of the pump with 1.87mm clearance without balance hole at 25 lit/sec flow rate from experiment by Hossain

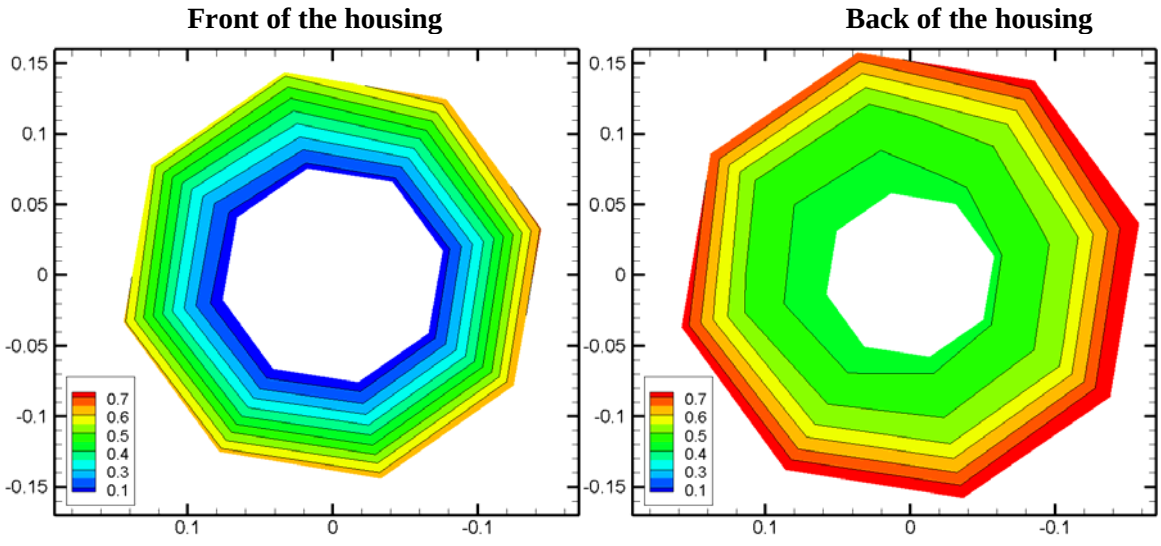

Figure C 32 Normalized pressure distribution of the pump with 1.87mm clearance without balance hole at 25 lit/sec flow rate from CFD

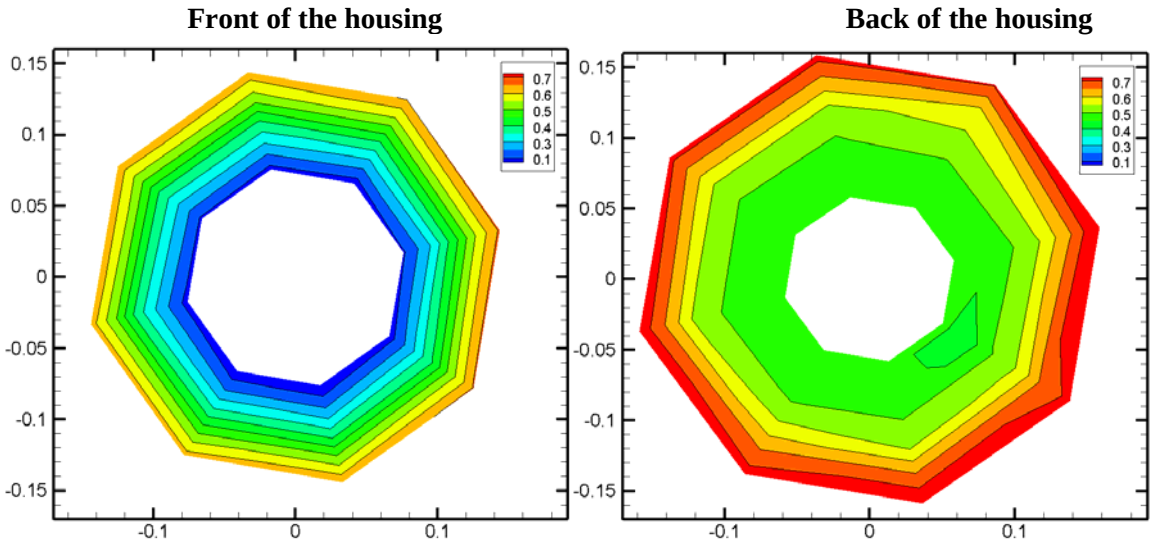

Figure C 33 Normalized pressure distribution of the pump with 1.87mm clearance without balance hole at 28 lit/sec flow rate from experiment by Hossain

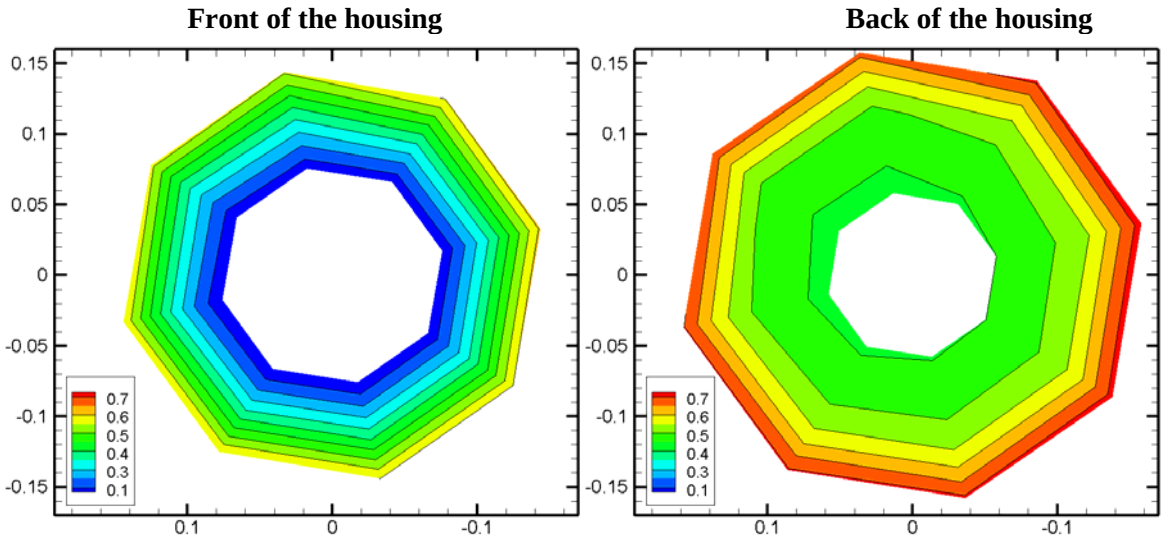

Figure C 34 Normalized pressure distribution of the pump with 1.87mm clearance without balance hole at 28 lit/sec flow rate from CFD

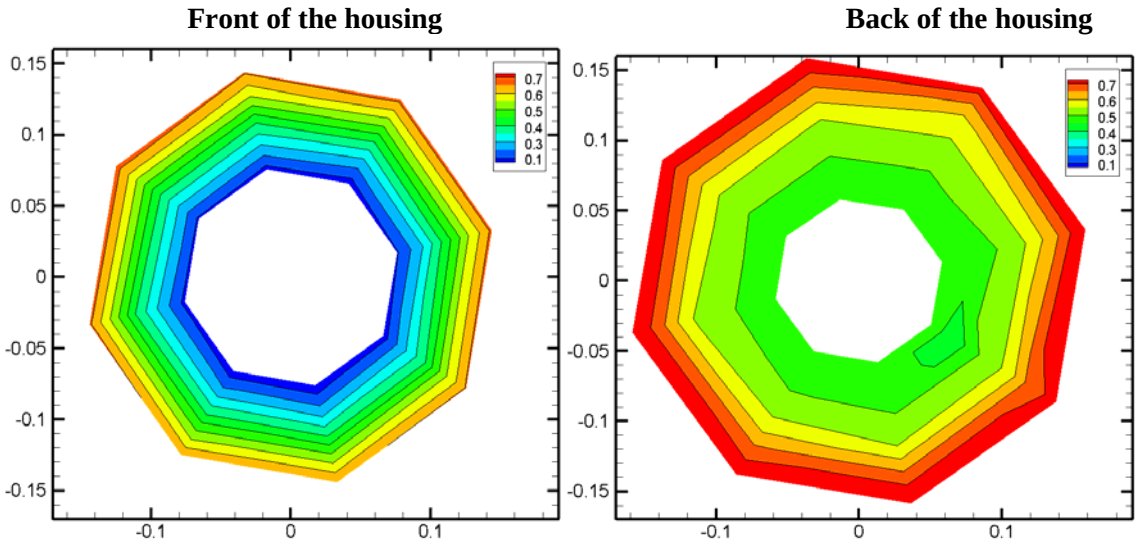

Figure C 35 Normalized pressure distribution of the pump with 1.87mm clearance without balance hole at 31 lit/sec flow rate from experiment by Hossain

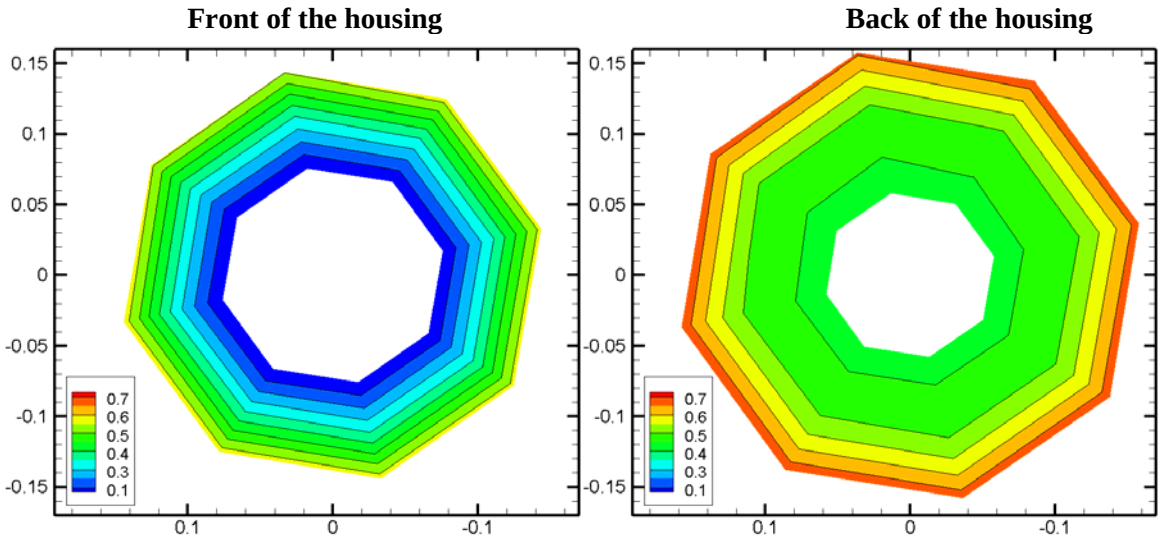

Figure C 36 Normalized pressure distribution of the pump with 1.87mm clearance without balance hole at 31 lit/sec flow rate from CFD

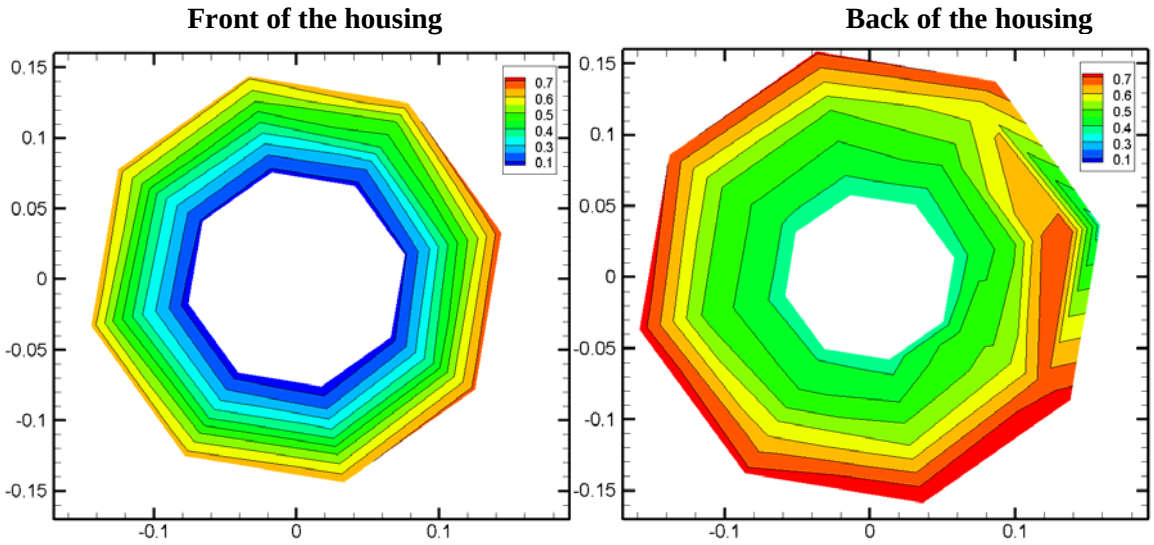

Figure C 37 Normalized pressure distribution of the pump with 1.87mm clearance with balance hole at 25 lit/sec flow rate from experiment by Hossain

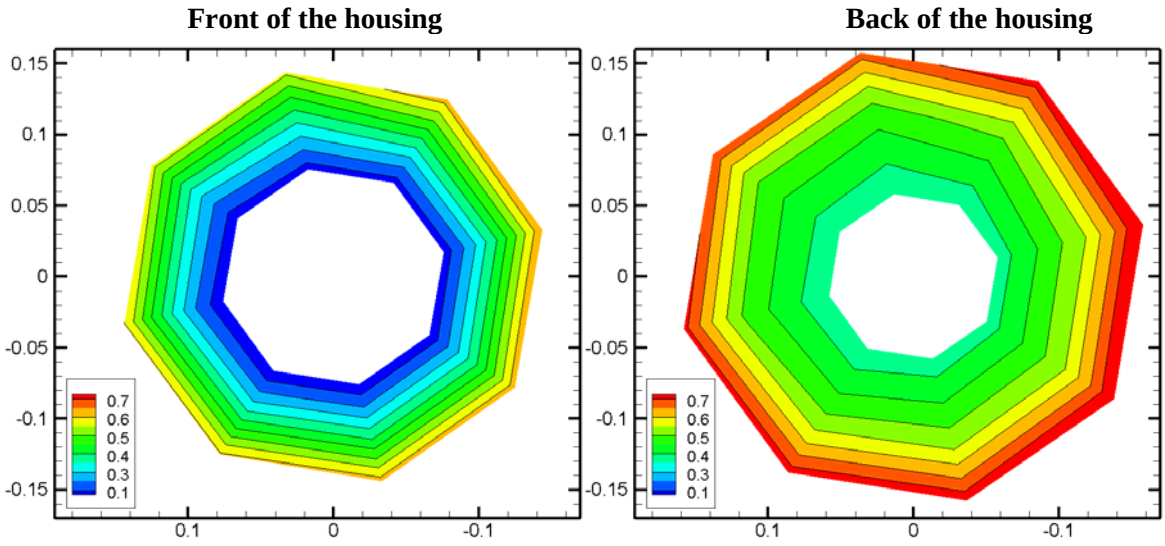

Figure C 38 Normalized pressure distribution of the pump with 1.87mm clearance with balance hole at 25 lit/sec flow rate from CFD

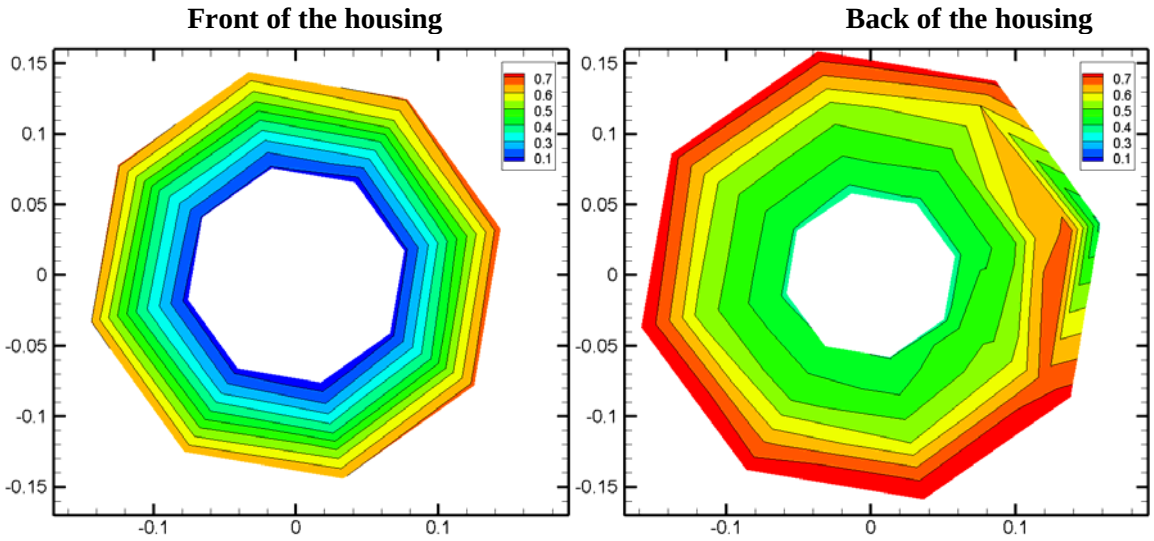

Figure C 39 Normalized pressure distribution of the pump with 1.87mm clearance with balance hole at 28 lit/sec flow rate from experiment by Hossain

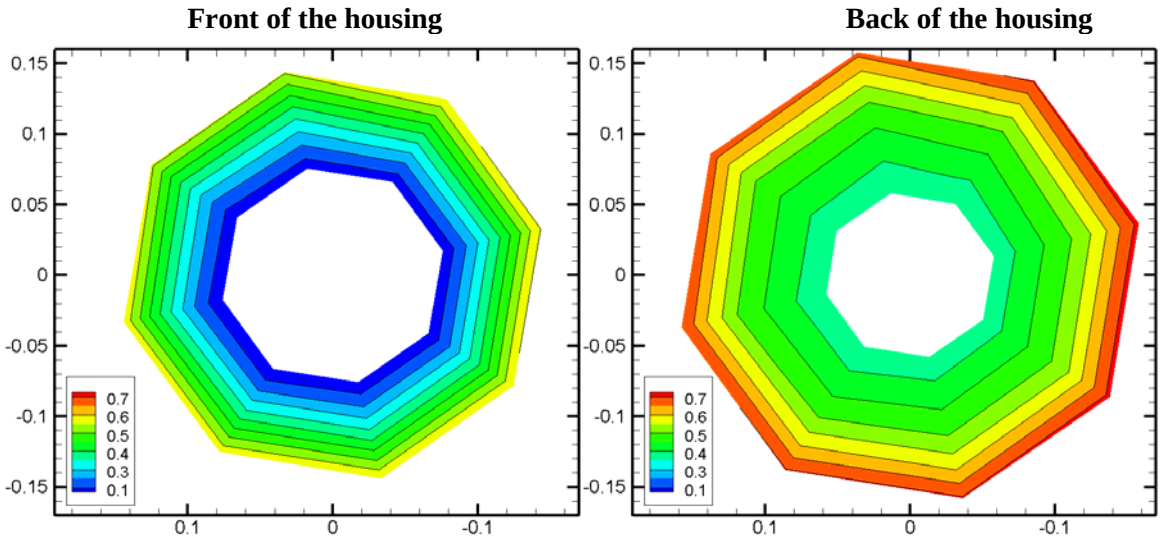

Figure C 40 Normalized pressure distribution of the pump with 1.87mm clearance with balance hole at 28 lit/sec flow rate from CFD

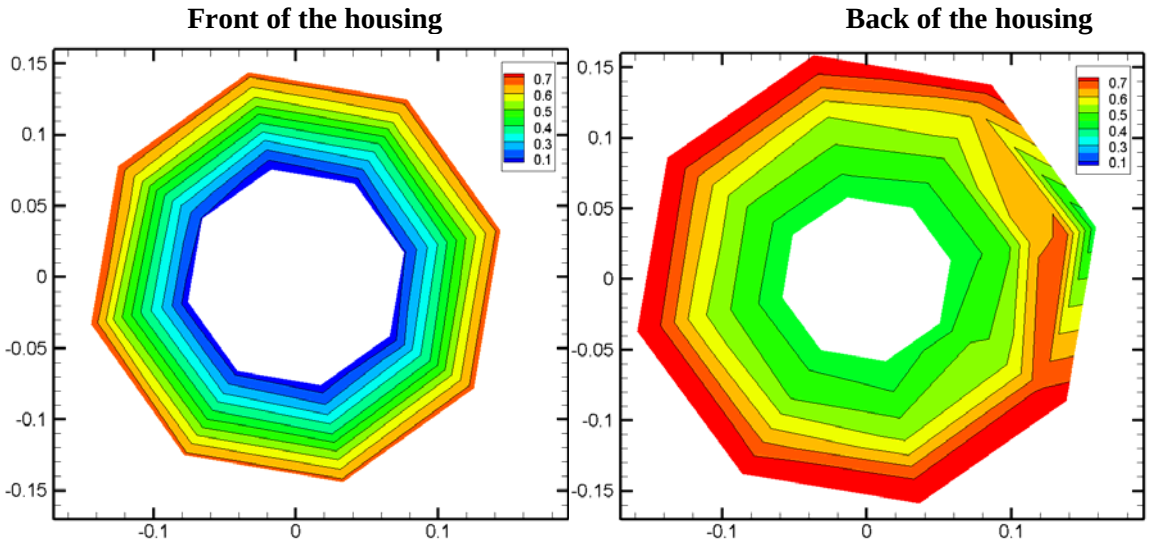

Figure C 41 Normalized pressure distribution of the pump with 1.87mm clearance with balance hole at 31 lit/sec flow rate from experiment by Hossain

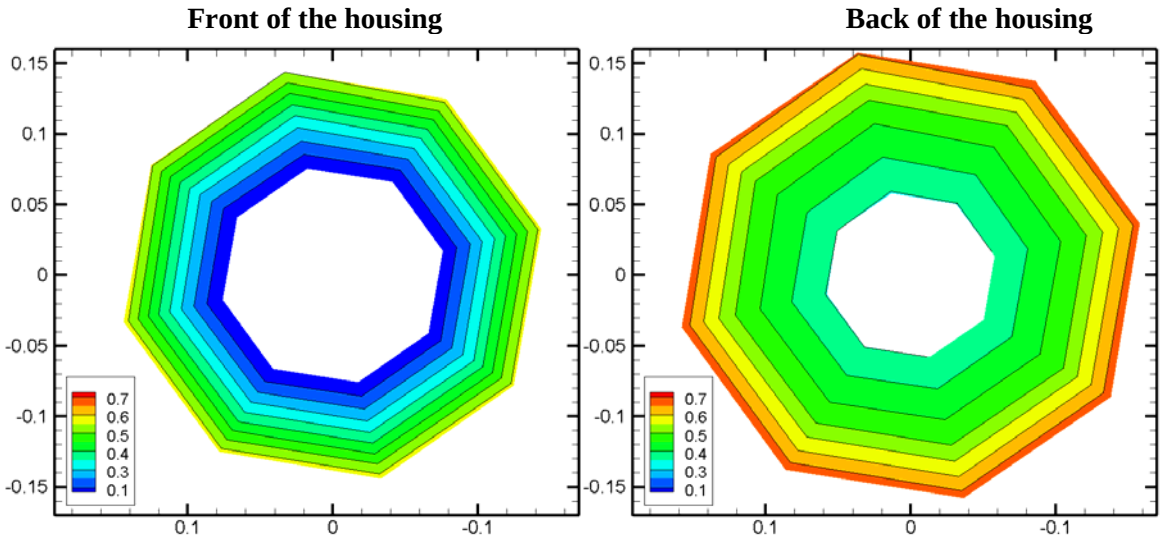

Figure C 42 Normalized pressure distribution of the pump with 1.87mm clearance with balance hole at 31 lit/sec flow rate from CFD

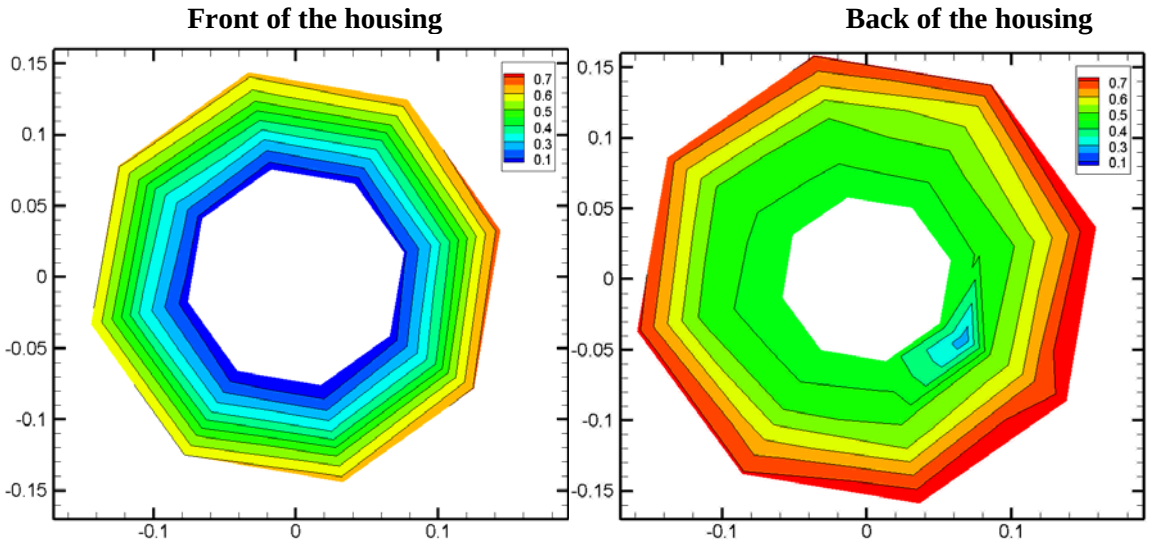

Figure C 43 Normalized pressure distribution of the pump with 3.17mm clearance without balance hole at 25 lit/sec flow rate from experiment by Hossain

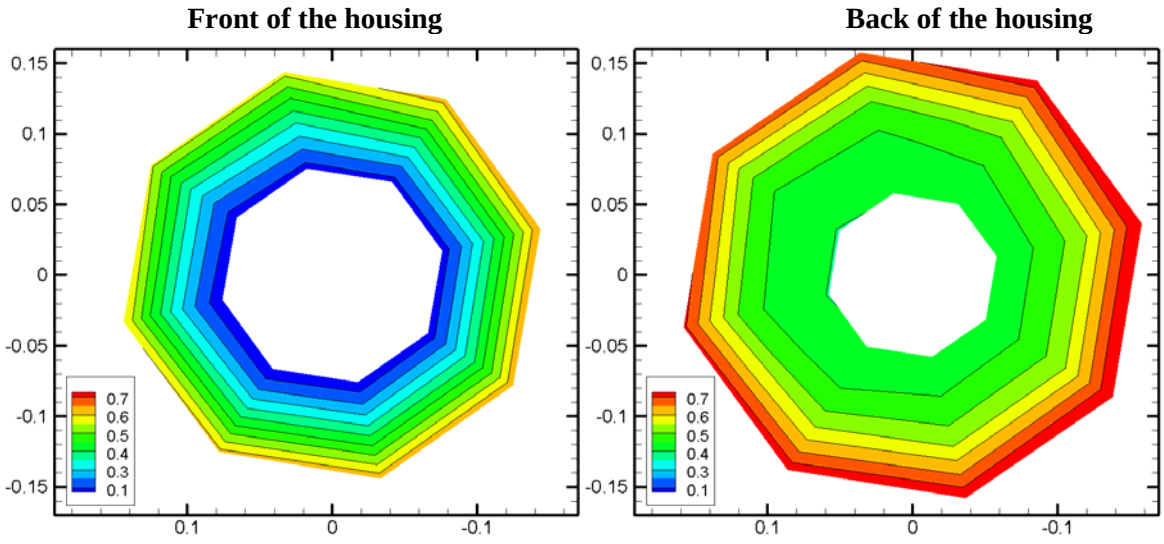

Figure C 44 Normalized pressure distribution of the pump with 3.17mm clearance without balance hole at 25 lit/sec flow rate from CFD

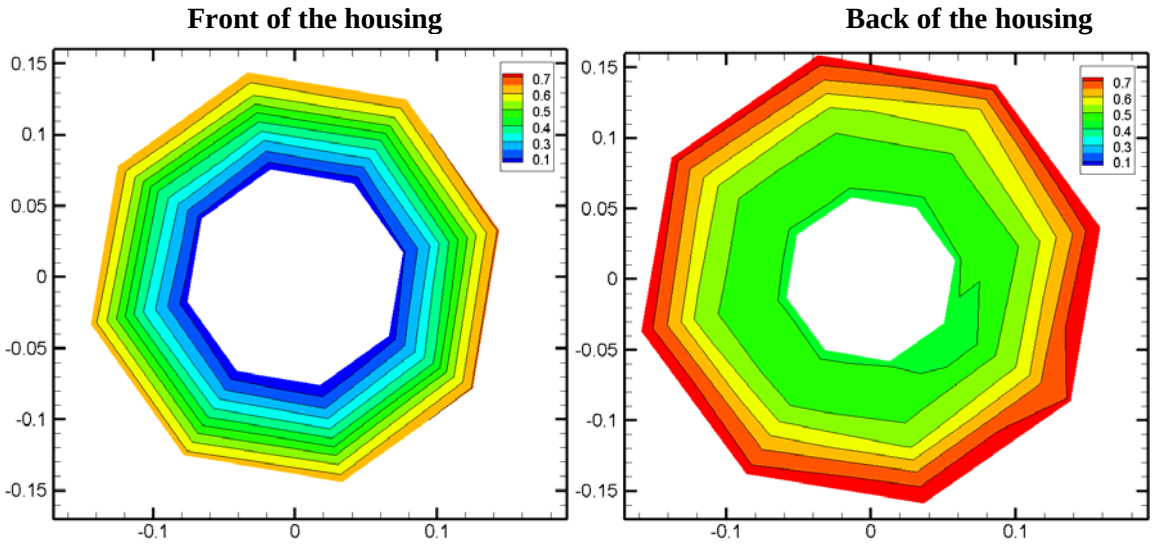

Figure C 45 Normalized pressure distribution of the pump with 3.17mm clearance without balance hole at 28 lit/sec flow rate from experiment by Hossain

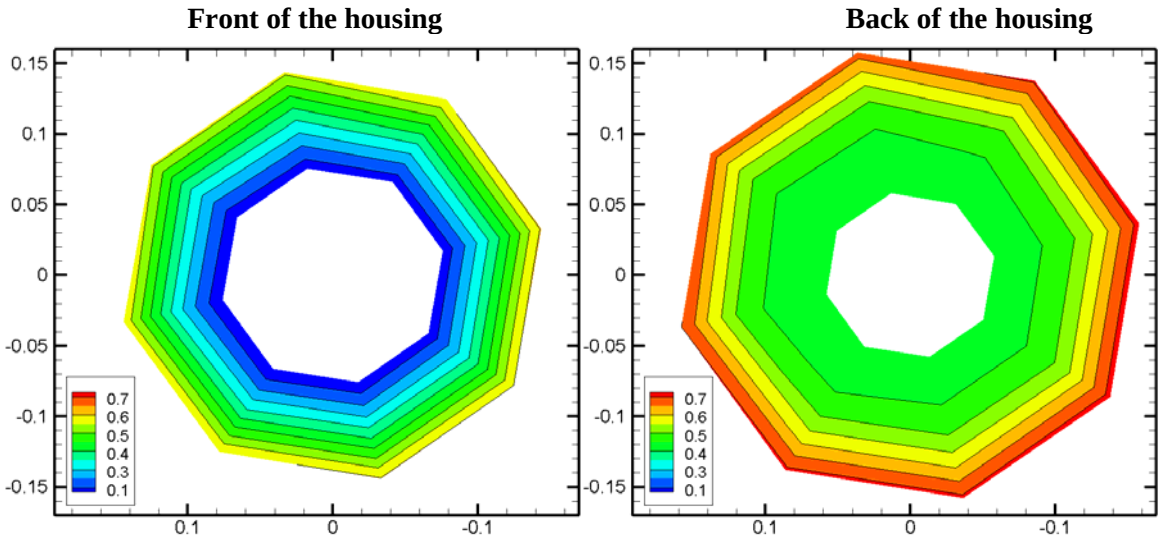

Figure C 46 Normalized pressure distribution of the pump with 3.17mm clearance without balance hole at 28 lit/sec flow rate from CFD

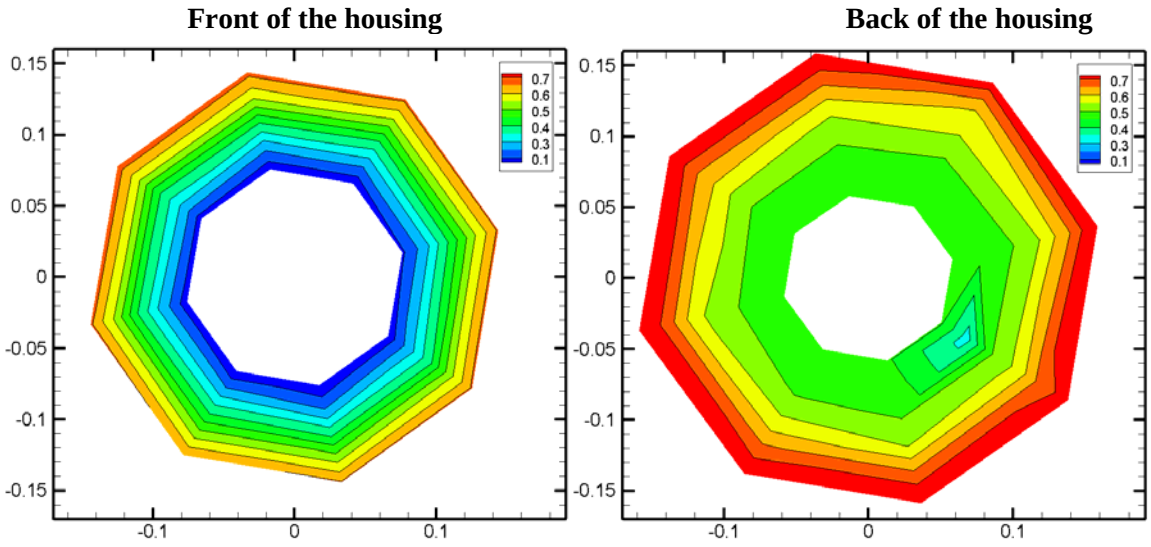

Figure C 47 Normalized pressure distribution of the pump with 3.17mm clearance without balance hole at 31 lit/sec flow rate from experiment by Hossain

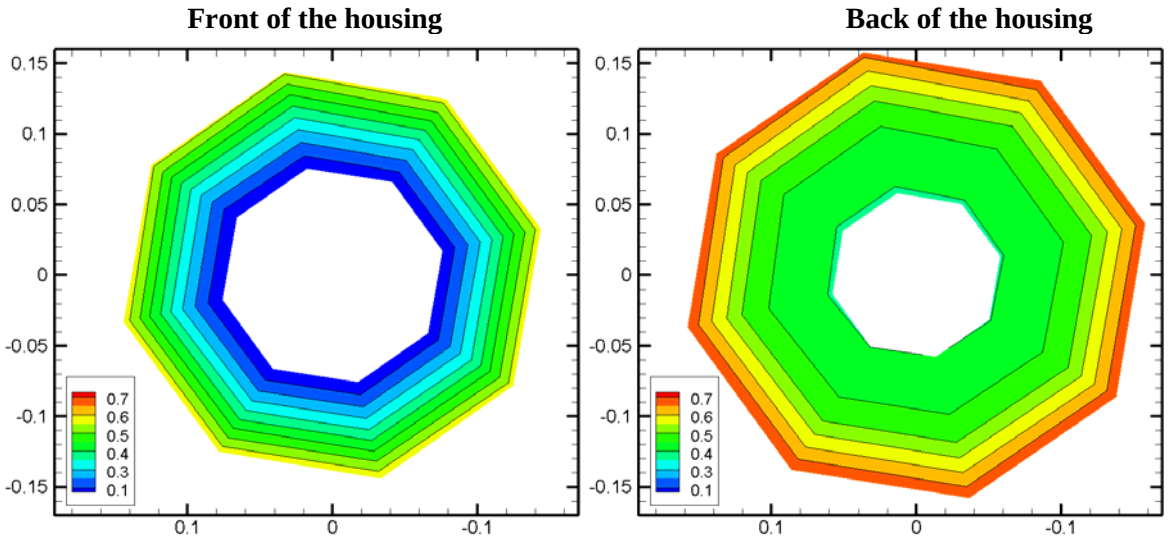

Figure C 48 Normalized pressure distribution of the pump with 3.17mm clearance without balance hole at 31 lit/sec flow rate from CFD

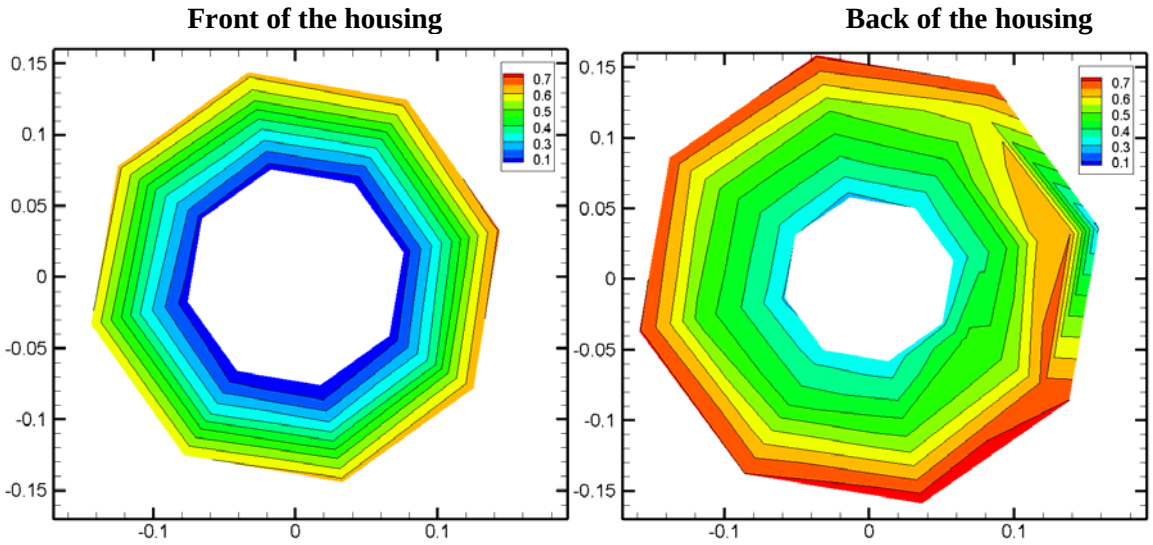

Figure C 49 Normalized pressure distribution of the pump with 3.17mm clearance with balance hole at 25 lit/sec flow rate from experiment by Hossain

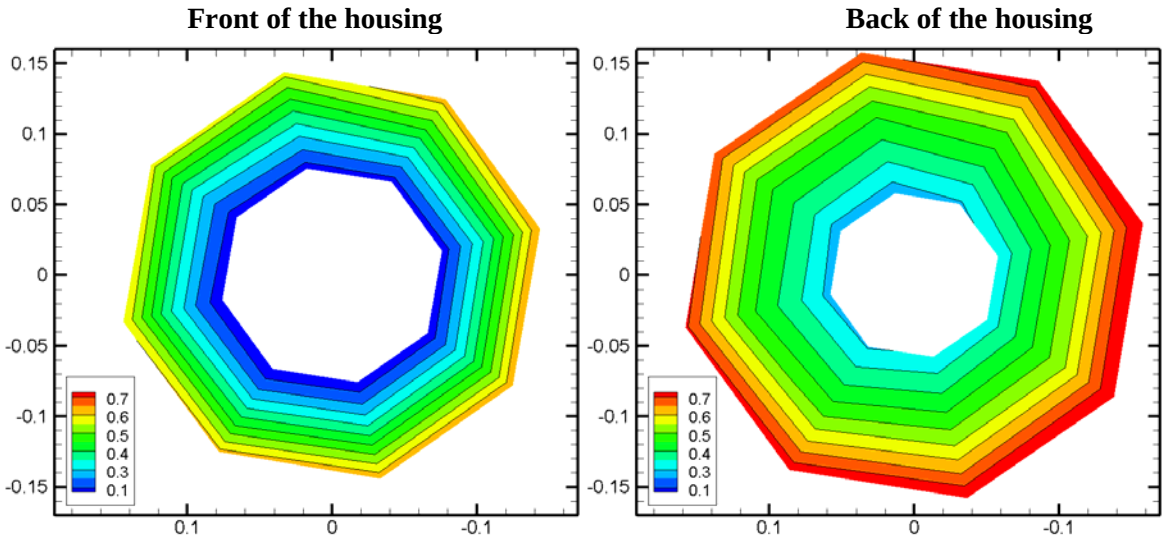

Figure C 50 Normalized pressure distribution of the pump with 3.17mm clearance with balance hole at 25 lit/sec flow rate from CFD

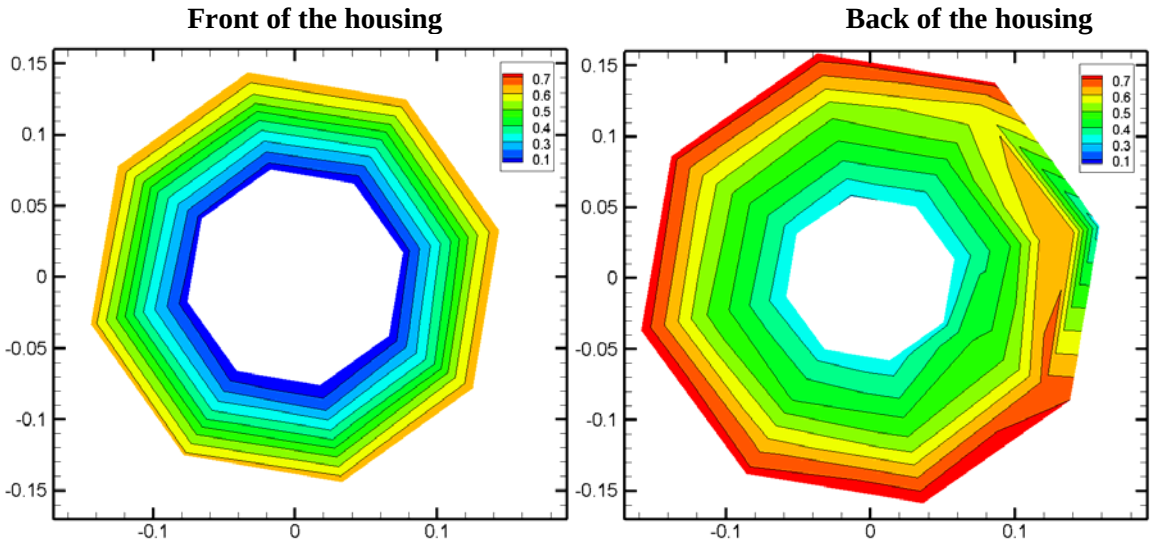

Figure C 51 Normalized pressure distribution of the pump with 3.17mm clearance with balance hole at 28 lit/sec flow rate from experiment by Hossain

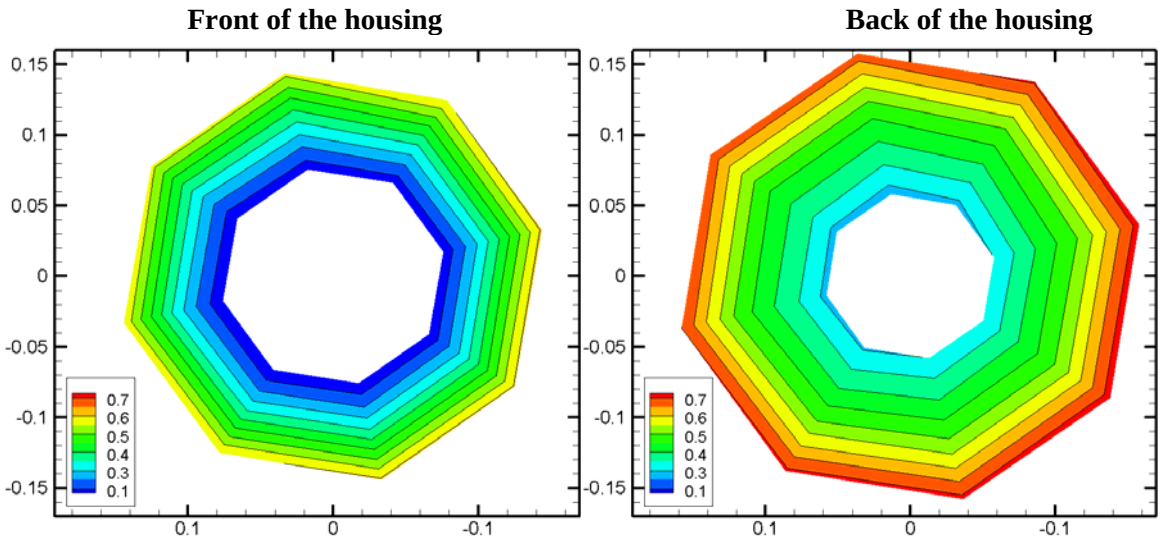

Figure C 52 Normalized pressure distribution of the pump with 3.17mm clearance with balance hole at 28 lit/sec flow rate from CFD

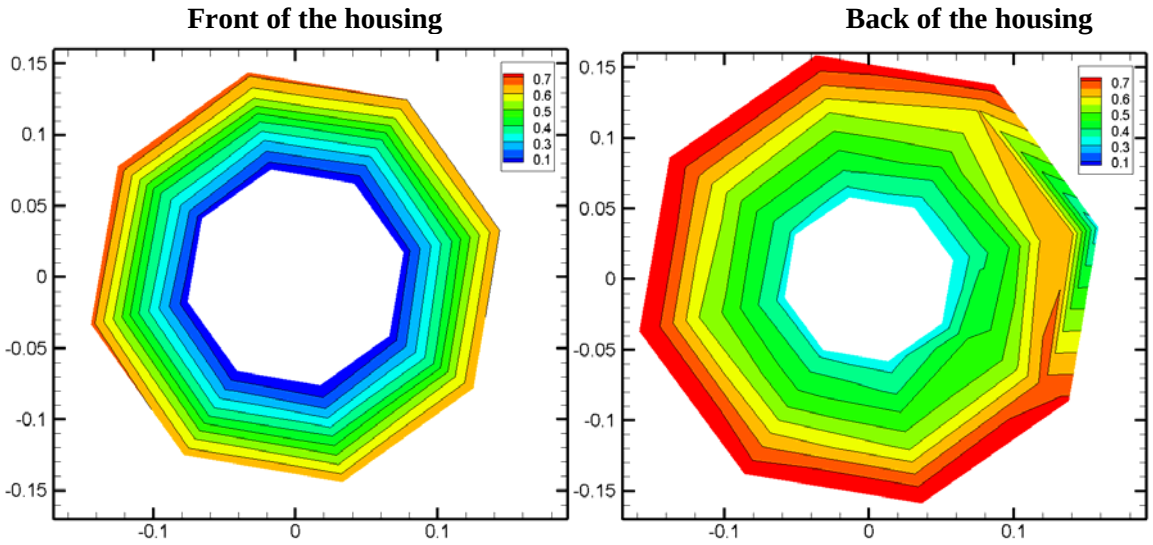

Figure C 53 Normalized pressure distribution of the pump with 3.17mm clearance with balance hole at 31 lit/sec flow rate from experiment by Hossain

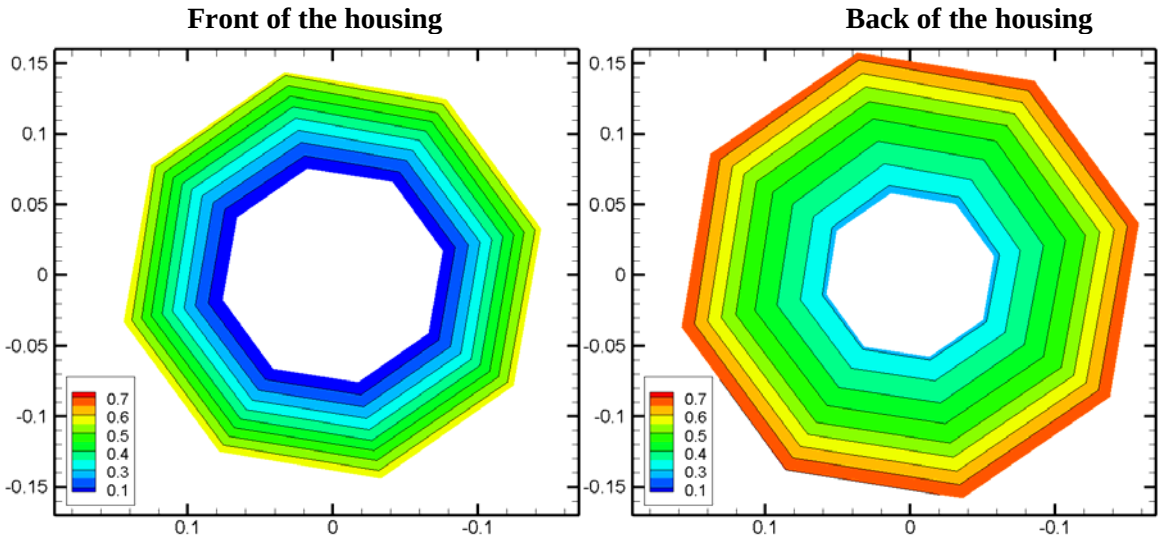

Figure C 54 Normalized pressure distribution of the pump with 3.17mm clearance with balance hole at 31 lit/sec flow rate from CFD

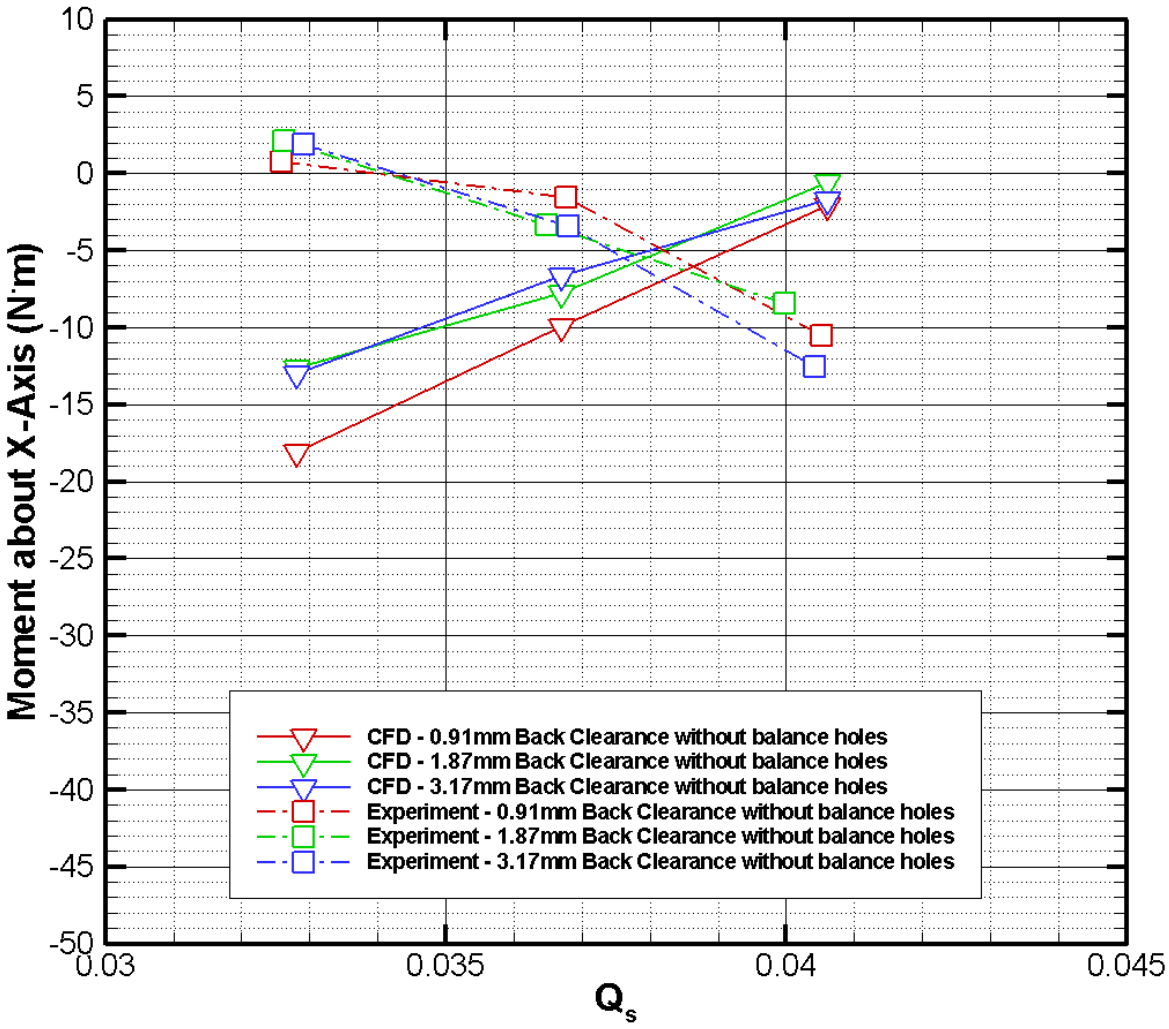

Figure C 55 The plot of moment about X-axis for the cases without balance holes

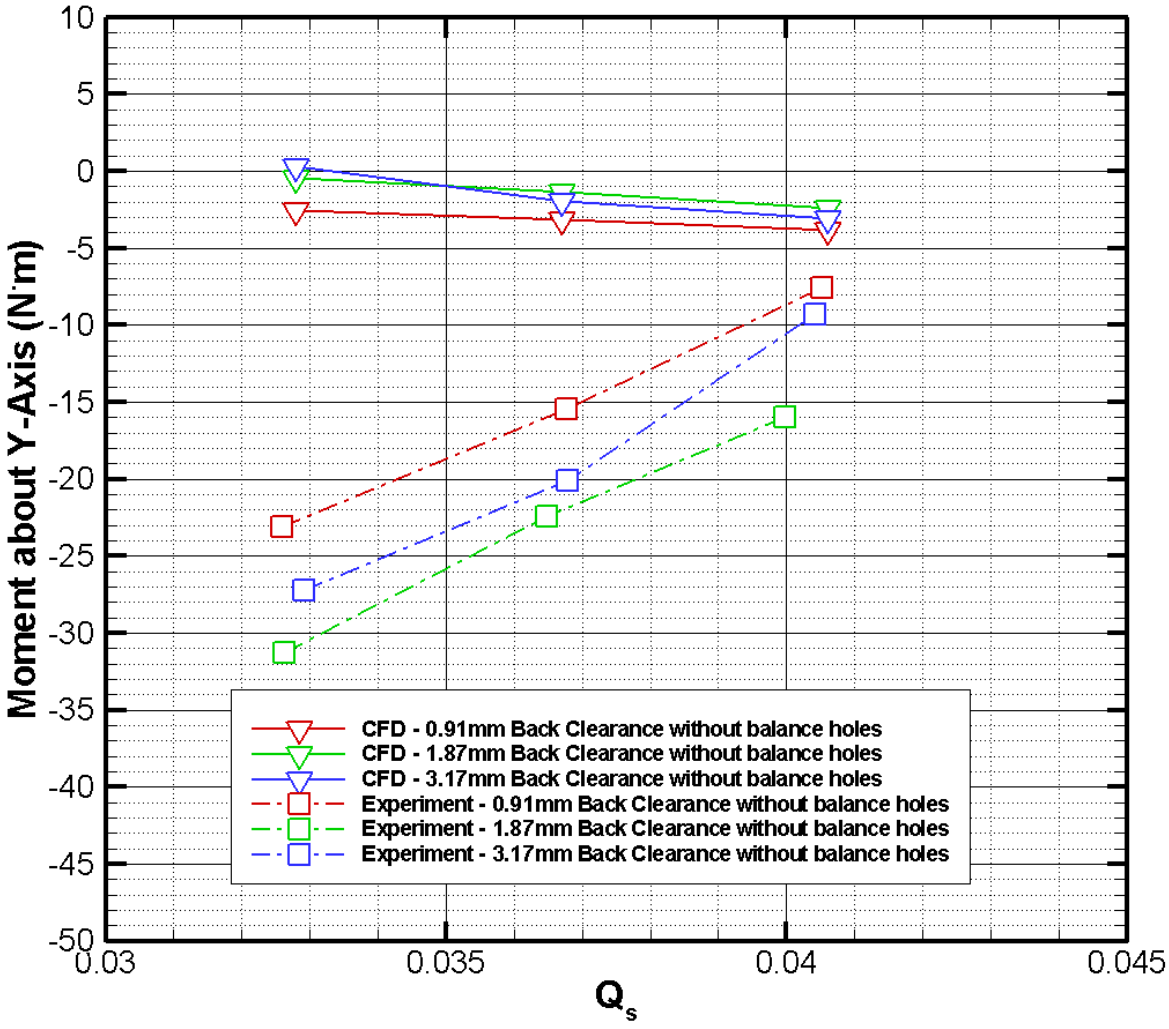

Figure C 56 The plot of moment about Y-axis for the cases without balance holes

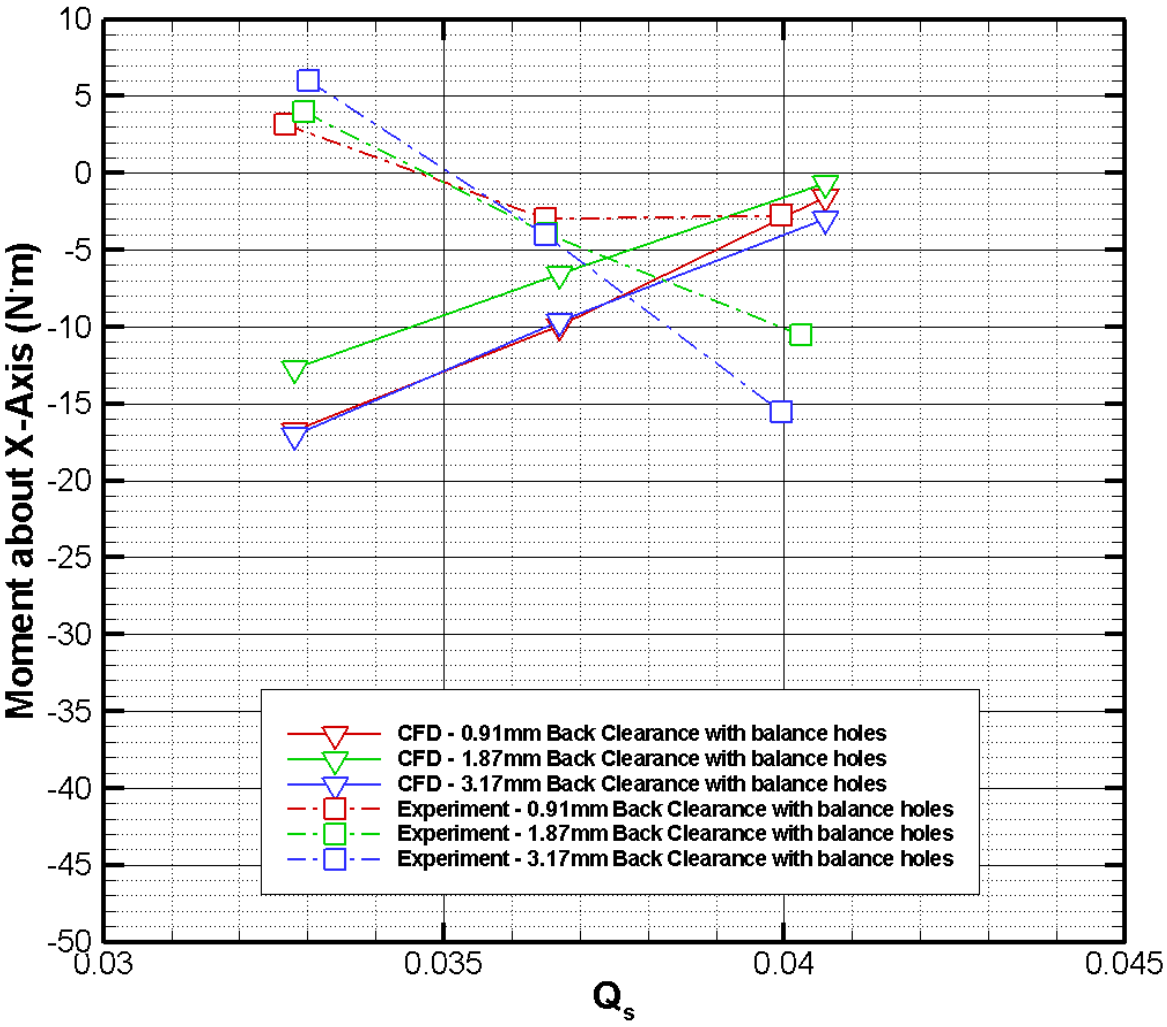

Figure C 57 The plot of moment about X-axis for the cases with balance holes

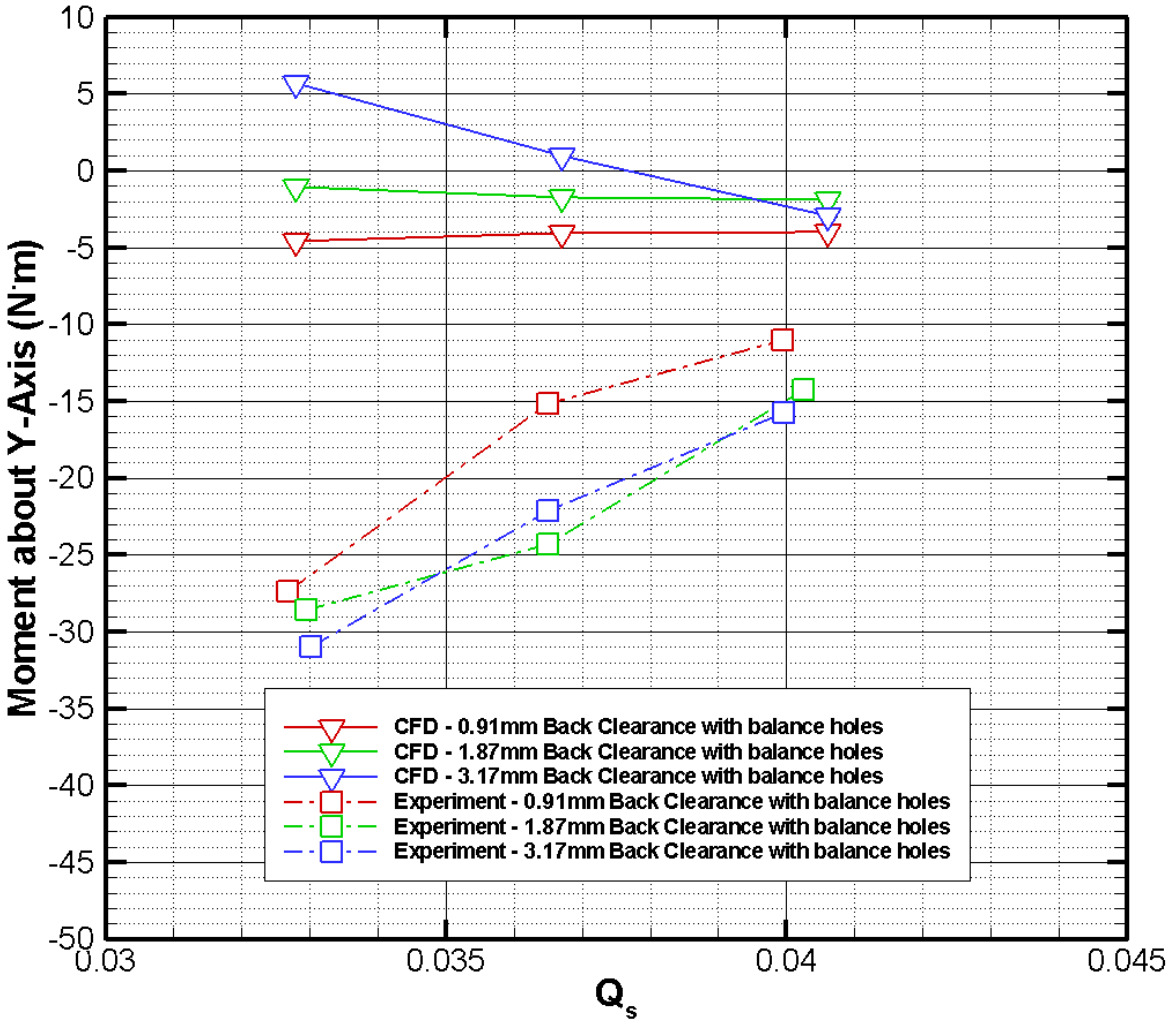

Figure C 58 The plot of moment about Y-axis for the cases with balance holes

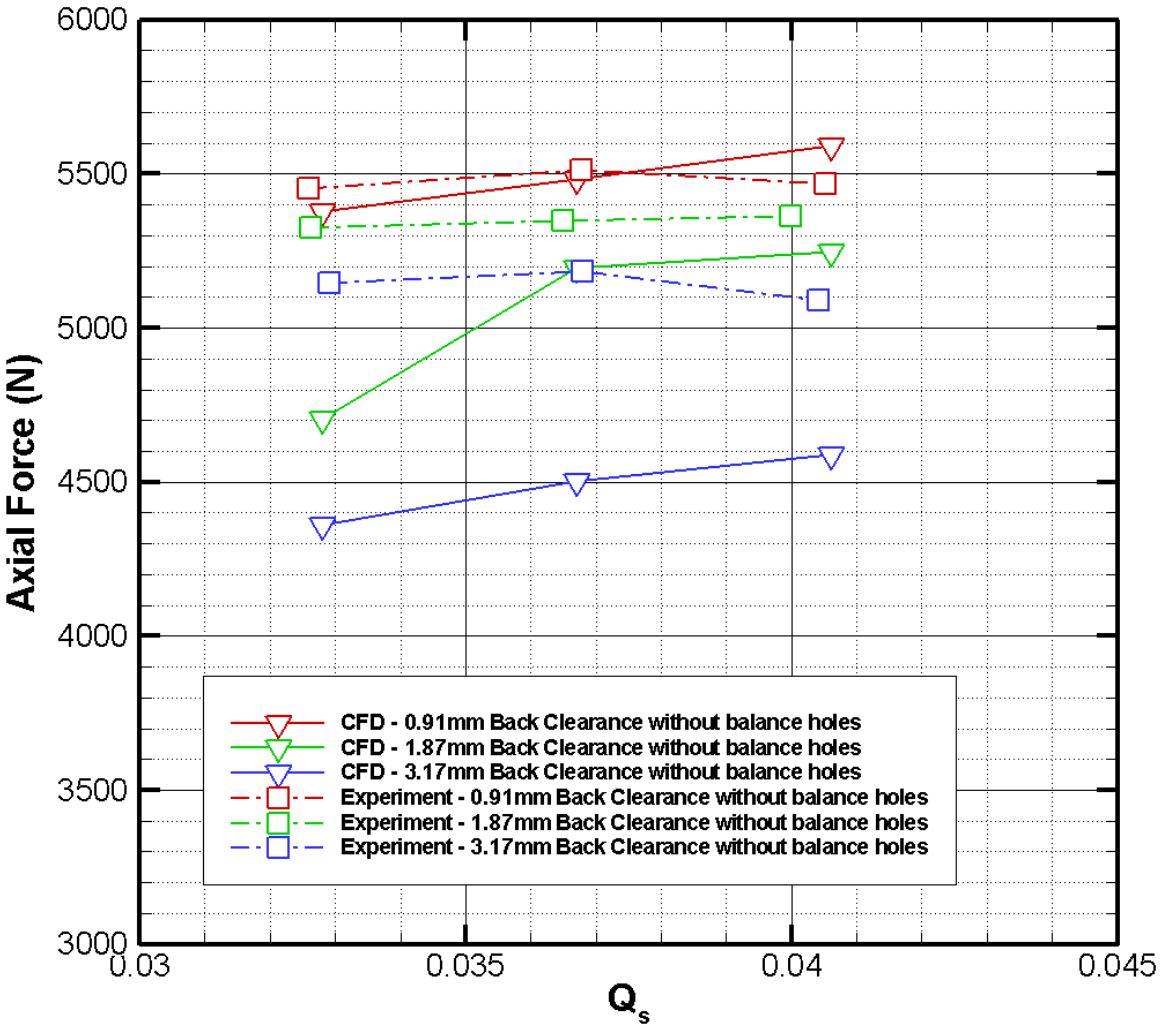

Figure C 59 The plot of axial thrust for the cases without balance holes

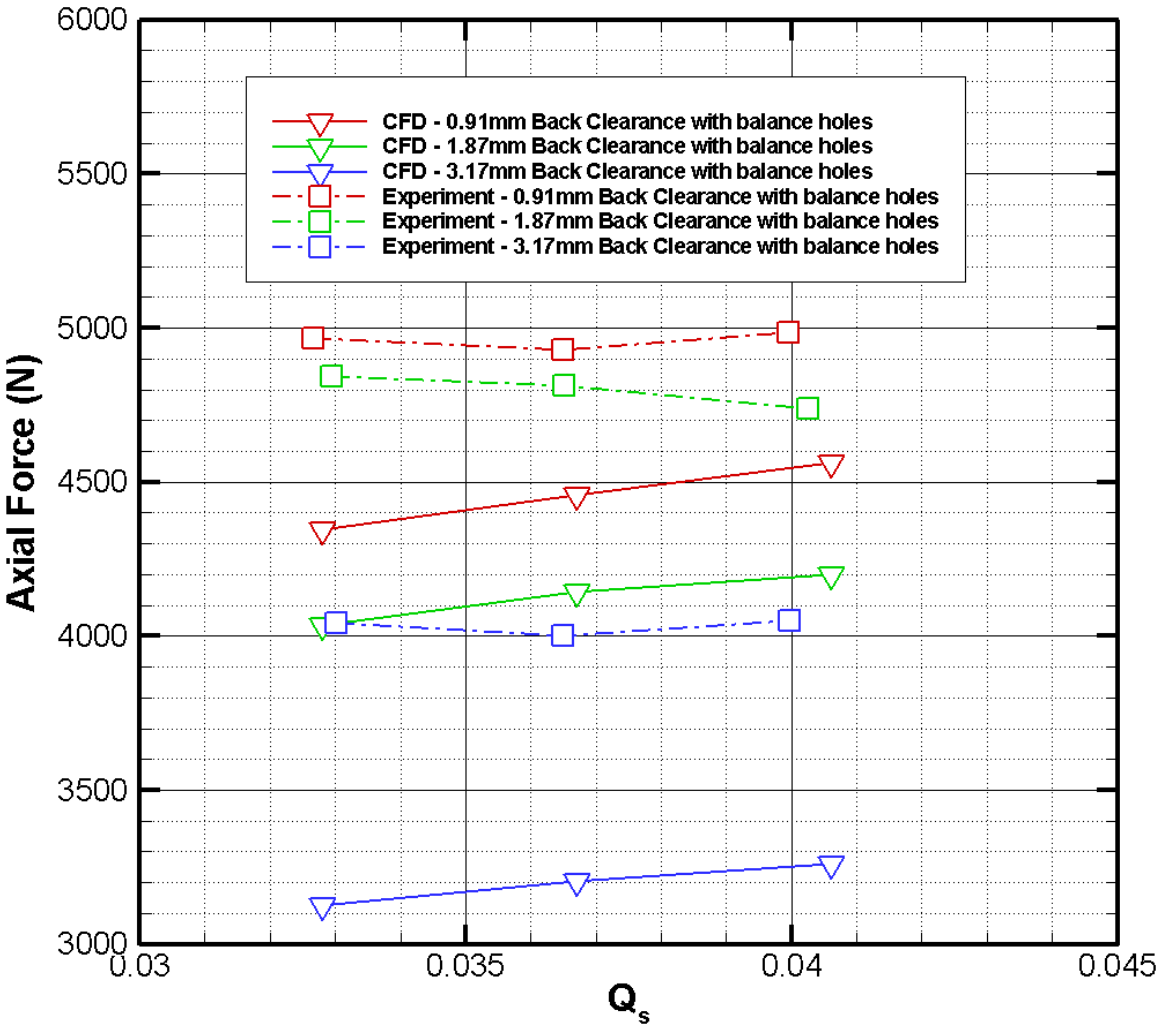

Figure C 60 The plot of axial thrust for the cases without balance holes

APPENDIX D

UNSTEADY DATA VALIDATIONS

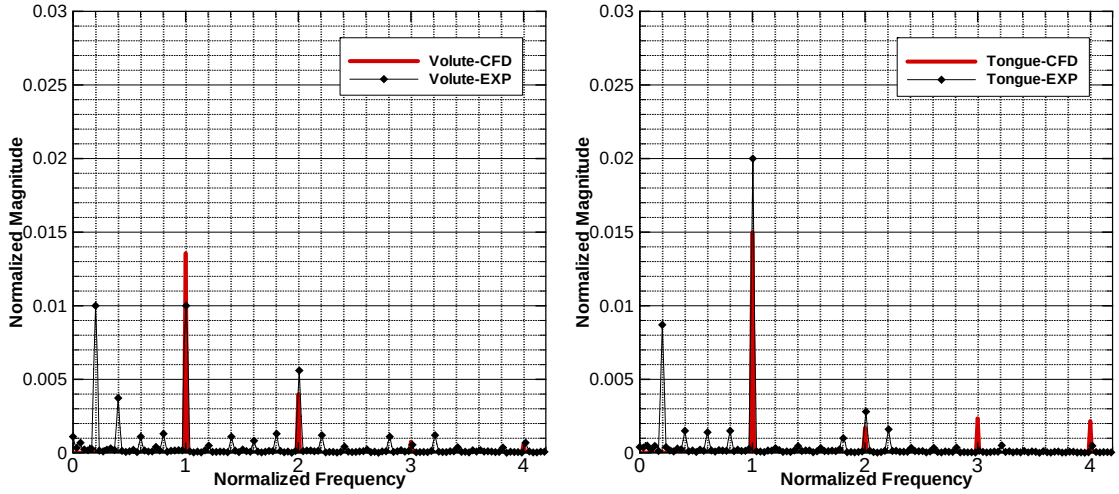

Figure D 1 Pressure spectrum of the pump with 0.91mm back clearance without balance holes at Q=25 lit/sec

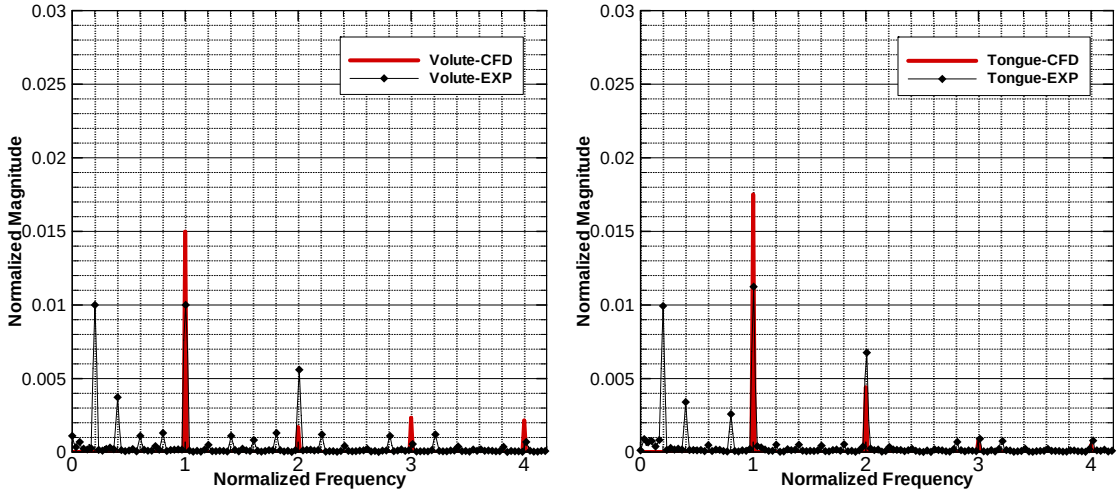

Figure D 2 Pressure spectrum of the pump with 0.91mm back clearance without balance holes at Q=28 lit/sec

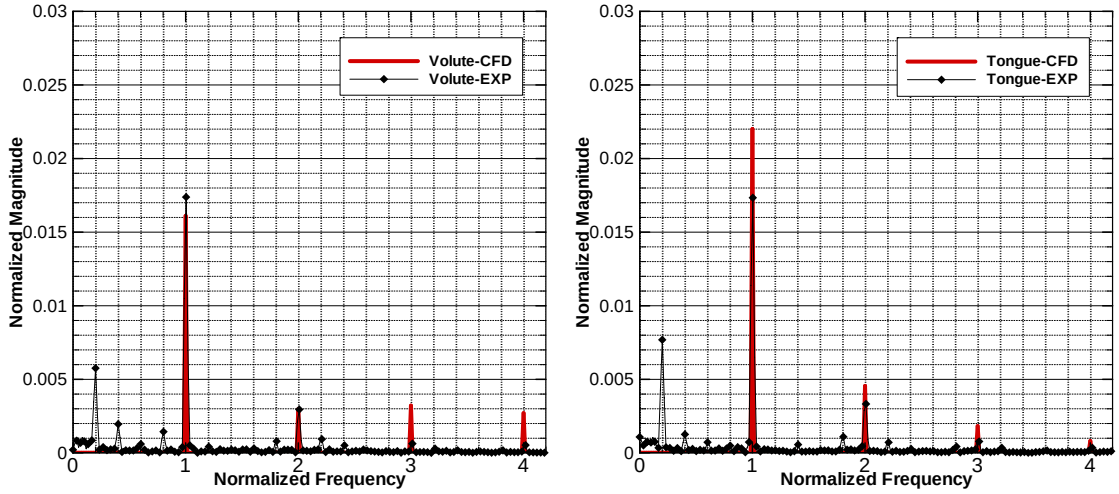

Figure D 3 Pressure spectrum of the pump with 0.91mm back clearance without balance holes at Q=31 lit/sec

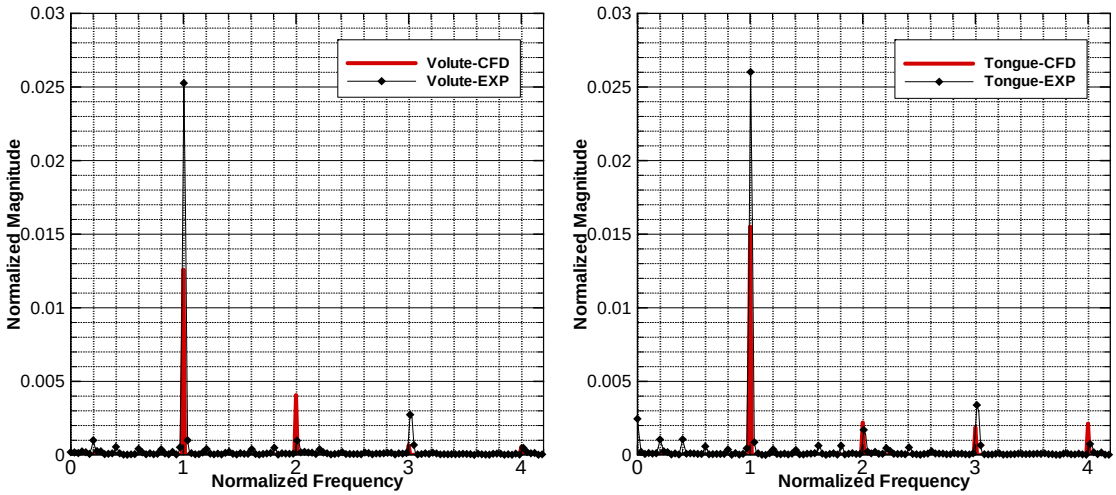

Figure D 4 Pressure spectrum of the pump with 0.91mm back clearance with balance holes at Q=25 lit/sec flow

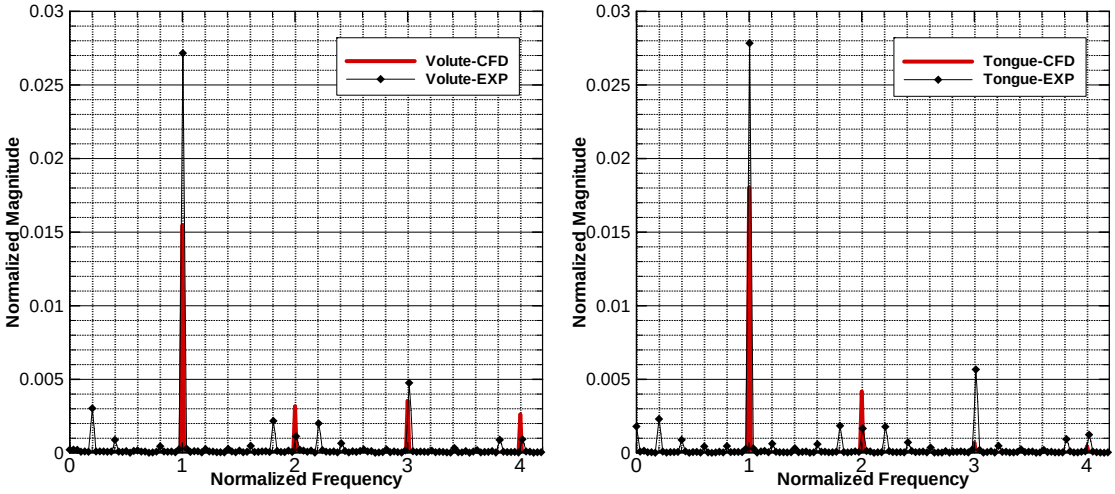

Figure D 5 Pressure spectrum of the pump with 0.91mm back clearance with balance holes at Q=28 lit/sec flow

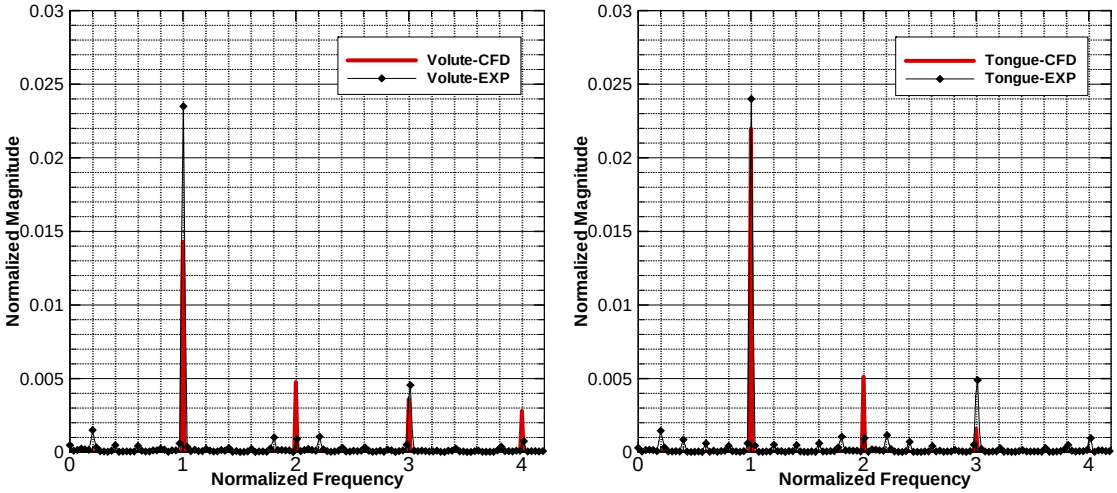

Figure D 6 Pressure spectrum of the pump with 0.91mm back clearance with balance holes at Q=31 lit/sec flow

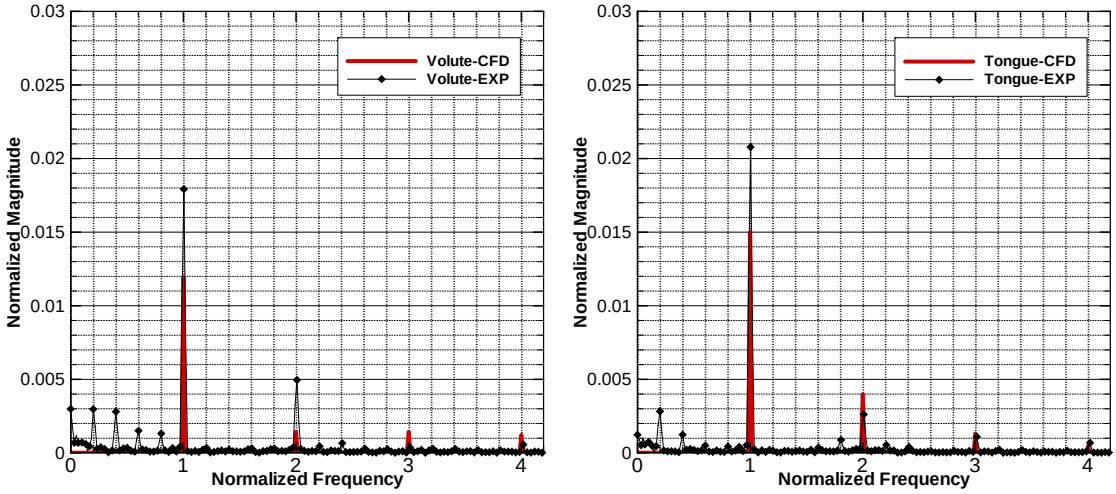

Figure D 7 Pressure spectrum of the pump with 1.87mm back clearance without balance holes at Q=25 lit/sec

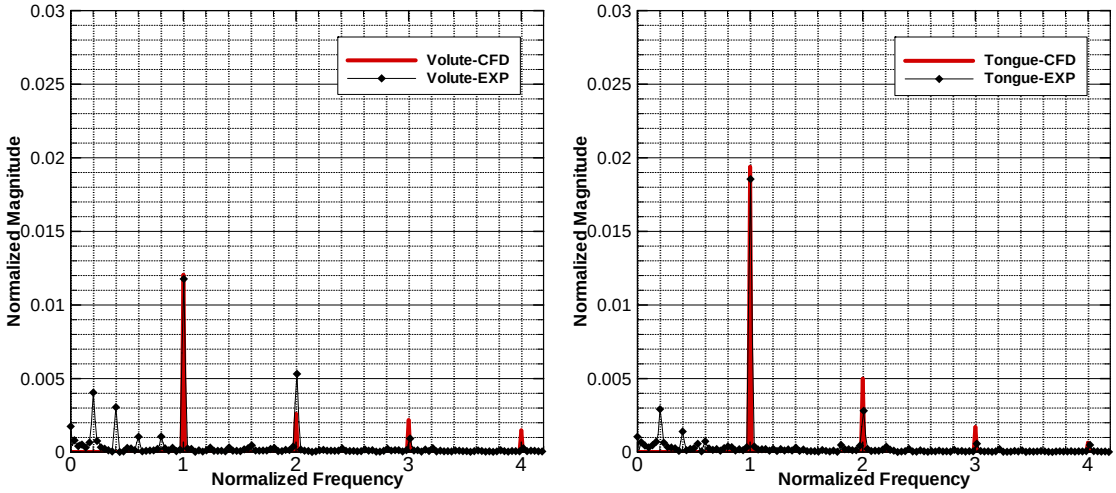

Figure D 8 Pressure spectrum of the pump with 1.87mm back clearance without balance holes at Q=28 lit/sec

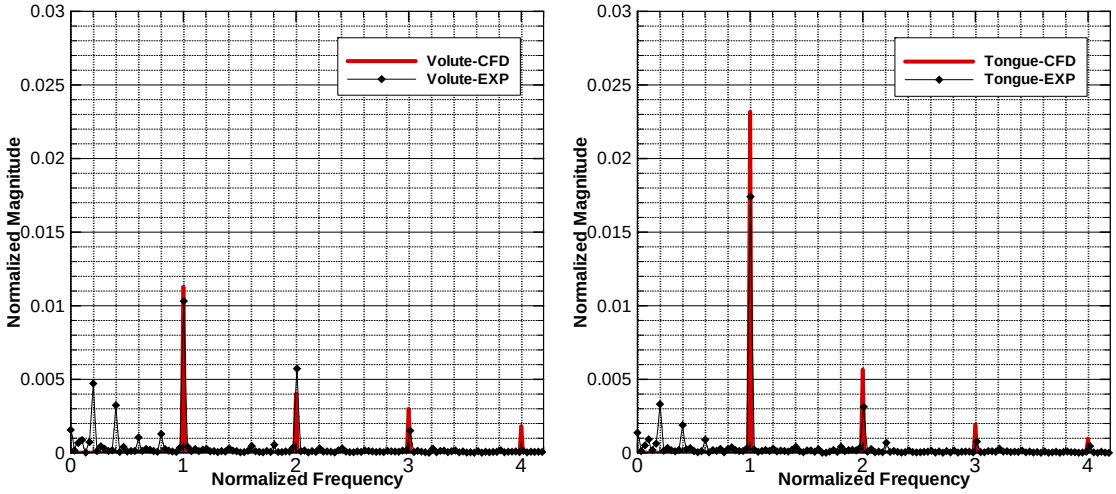

Figure D 9 Pressure spectrum of the pump with 1.87mm back clearance without balance holes at Q=31 lit/sec

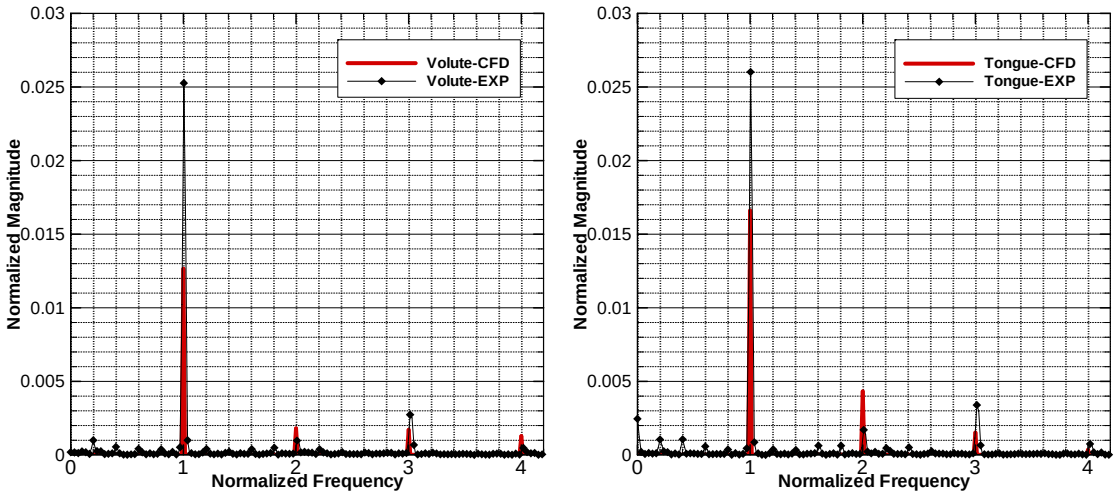

Figure D 10 Pressure spectrum of the pump with 1.87mm back clearance with balance holes at Q=25 lit/sec

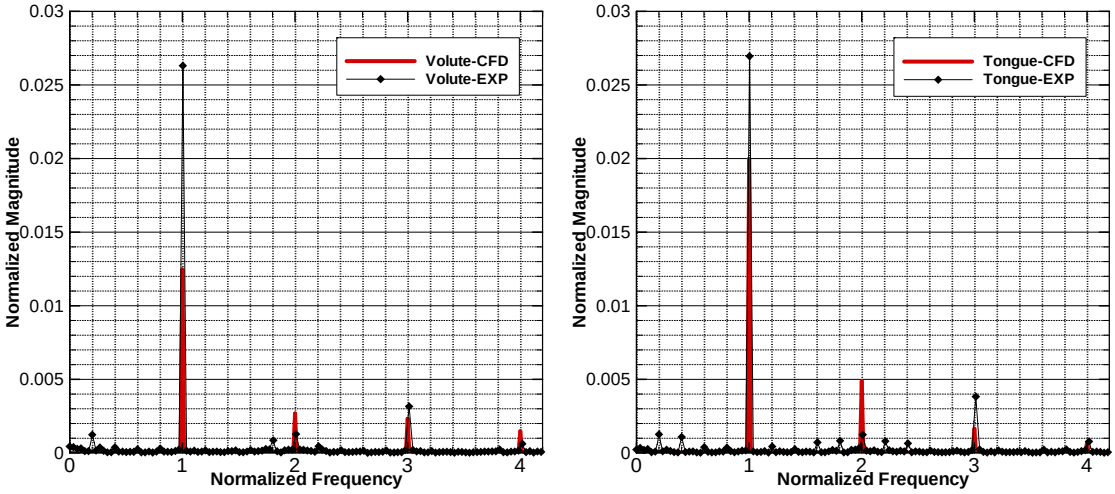

Figure D 11 Pressure spectrum of the pump with 1.87mm back clearance with balance holes at Q=28 lit/sec

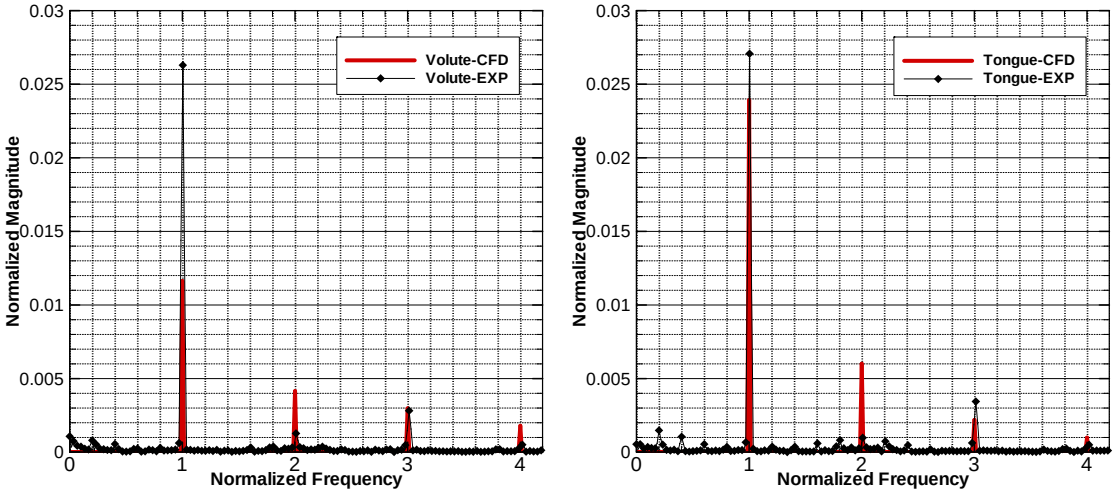

Figure D 12 Pressure spectrum of the pump with 1.87mm back clearance with balance holes at Q=31 lit/sec

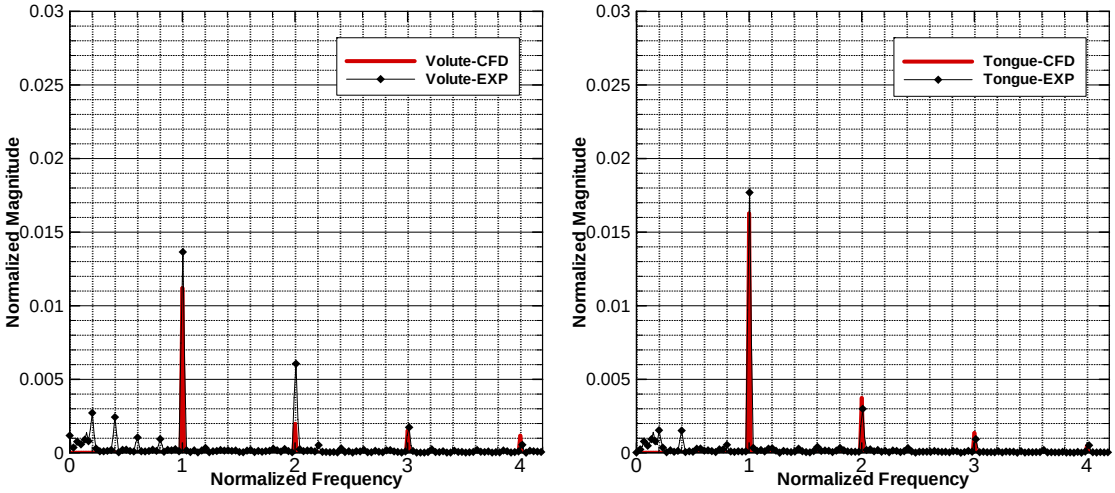

Figure D 13 Pressure spectrum of the pump with 3.17mm back clearance without balance holes at Q=25 lit/sec

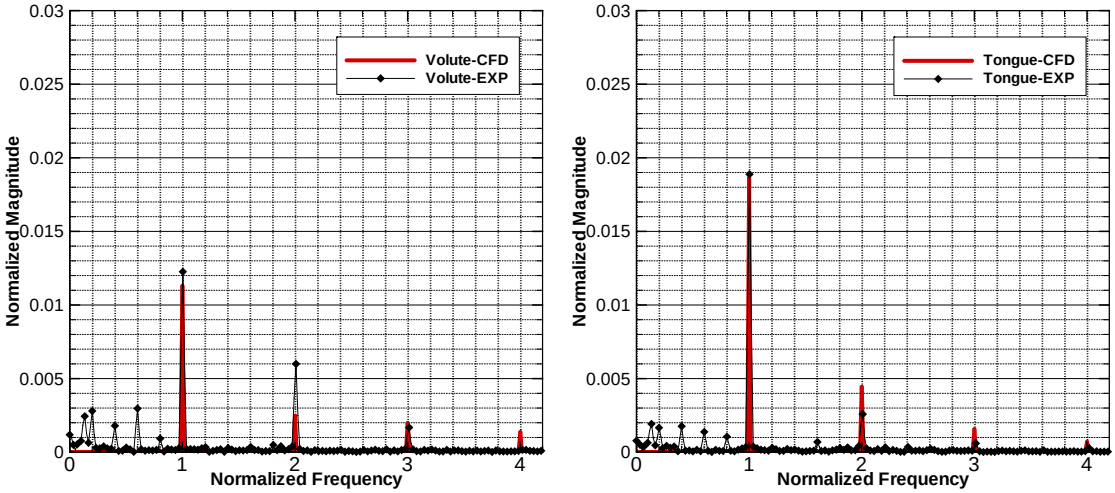

Figure D 14 Pressure spectrum of the pump with 3.17mm back clearance without balance holes at Q=28 lit/sec

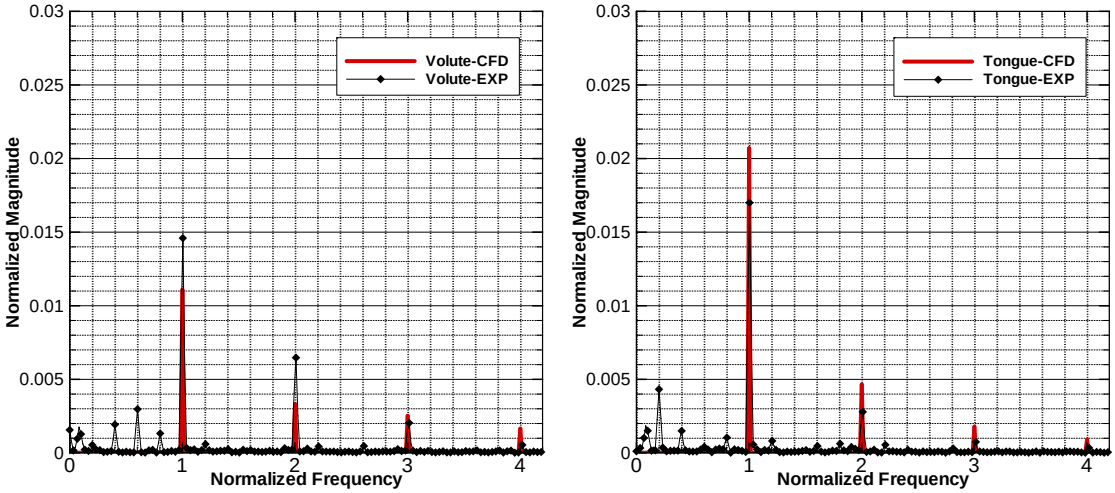

Figure D 15 Pressure spectrum of the pump with 3.17mm back clearance without balance holes at Q=31 lit/sec

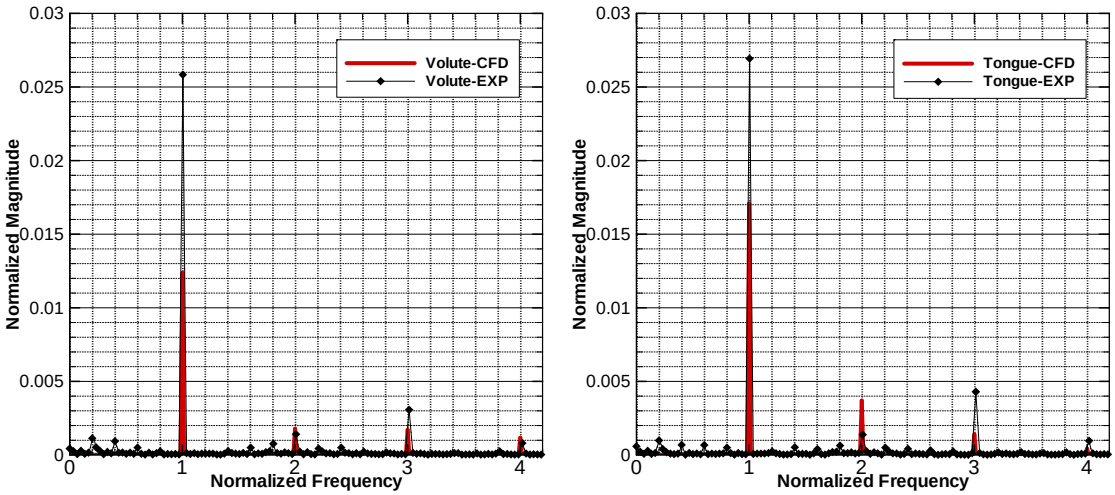

Figure D 16 Pressure spectrum of the pump with 3.17mm back clearance with balance holes at Q=25 lit/sec

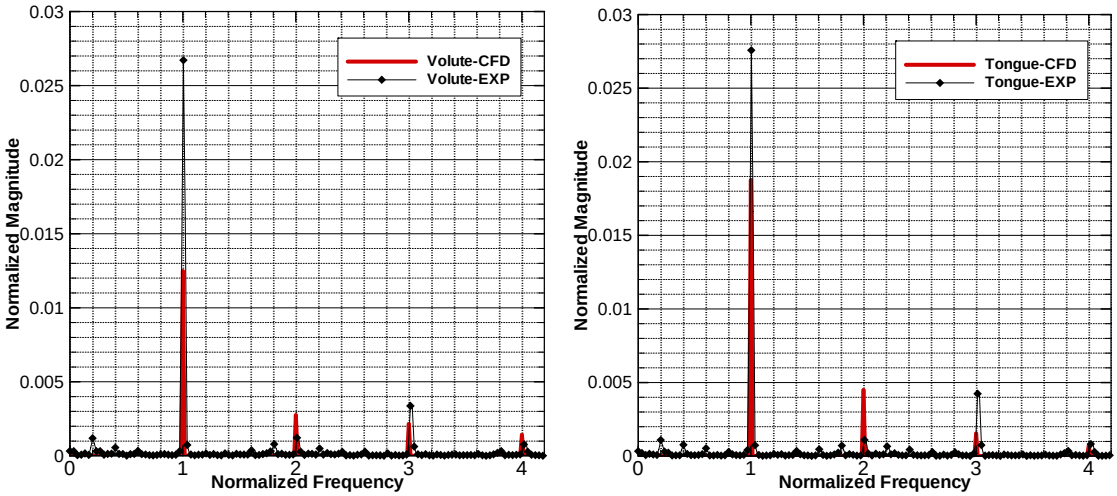

Figure D 17 Pressure spectrum of the pump with 3.17mm back clearance with balance holes at Q=28 lit/sec

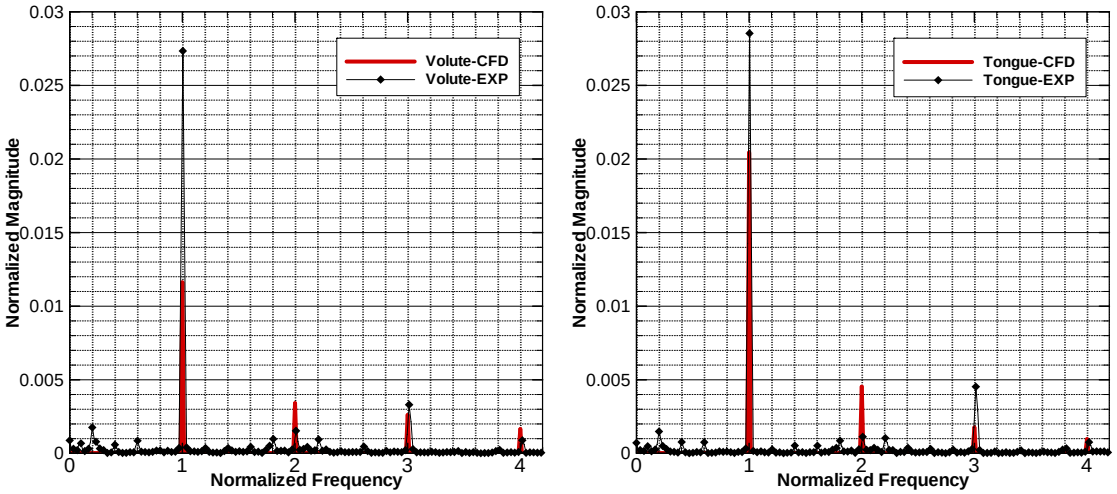

Figure D 18 Pressure spectrum of the pump with 3.17mm back clearance with balance holes at Q=31 lit/sec

APPENDIX E

BACK CLEARANCE FLOW FIELD

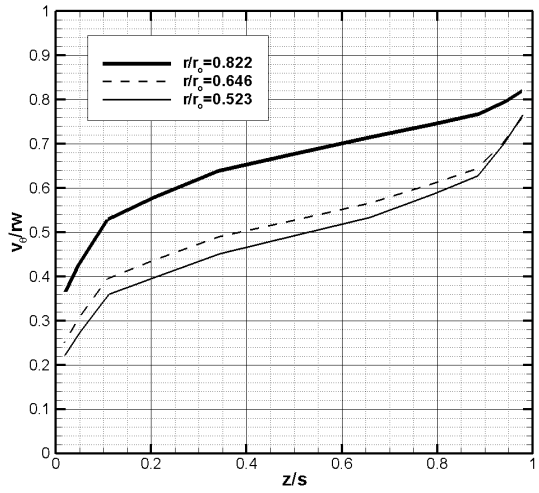

Figure E 1 β_θ plot of the case w/ 0.91mm back clearance at 25 liter/sec flow rate w/o balance holes

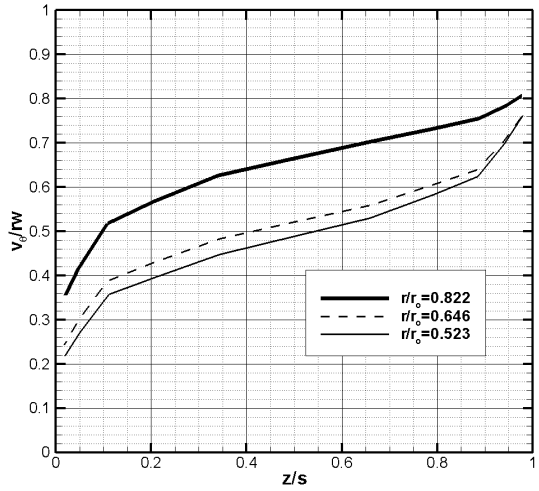

Figure E 2 β_θ plot of the case w/ 0.91mm back clearance at 28 liter/sec flow rate w/o balance holes

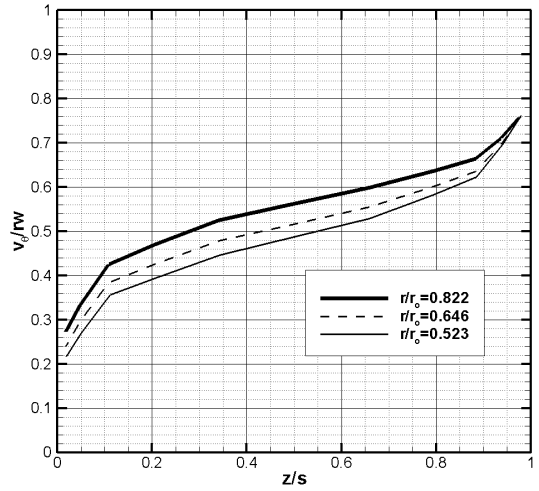

Figure E 3 β_θ plot of the case w/ 0.91mm back clearance at 31 liter/sec flow rate w/o balance holes

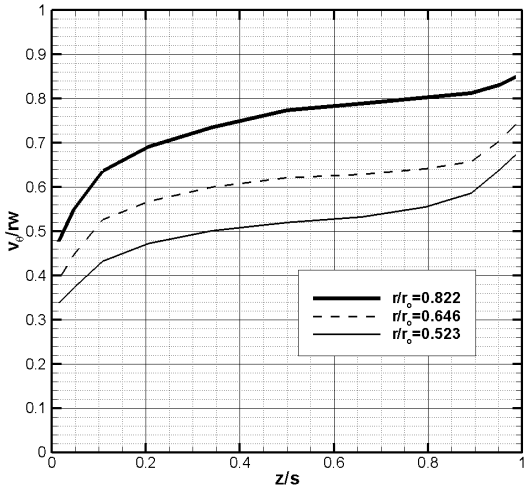

Figure E 4 β_θ plot of the case w/ 1.87mm back clearance at 25 liter/sec flow rate w/o balance holes

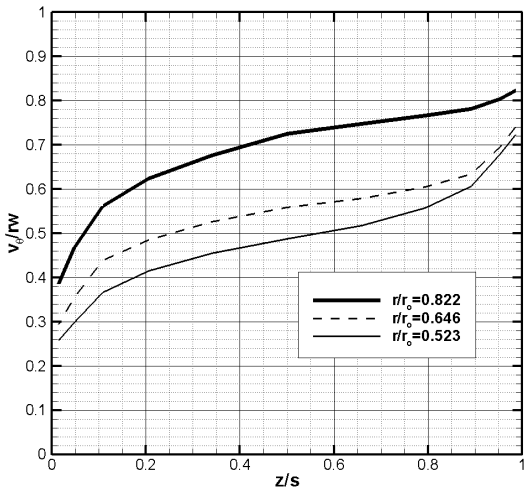

Figure E 5 β_θ plot of the case w/ 1.87mm back clearance at 28 liter/sec flow rate w/o balance holes

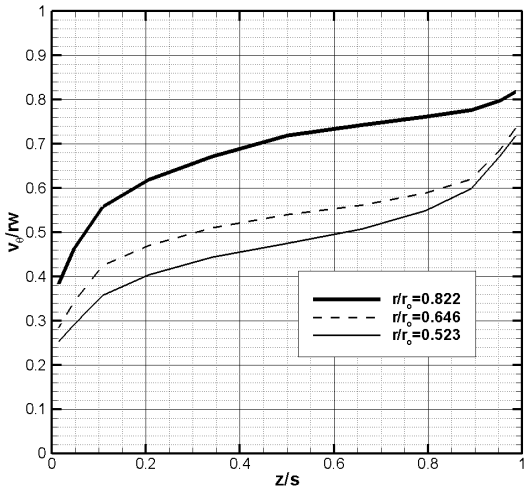

Figure E 6 β_θ plot of the case w/ 1.87mm back clearance at 31 liter/sec flow rate w/o balance holes

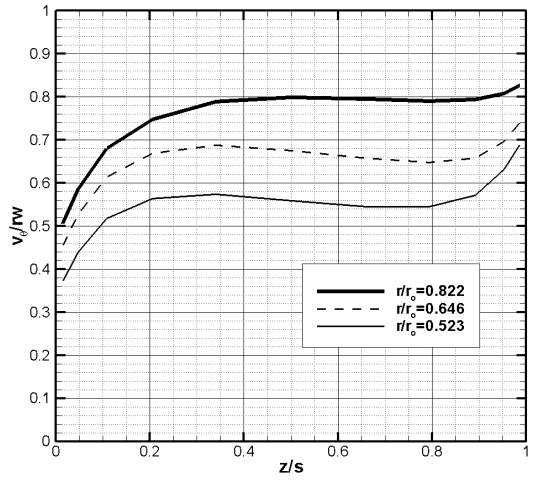

Figure E 7 β_θ plot of the case w/ 3.17mm back clearance at 25 liter/sec flow rate w/o balance holes

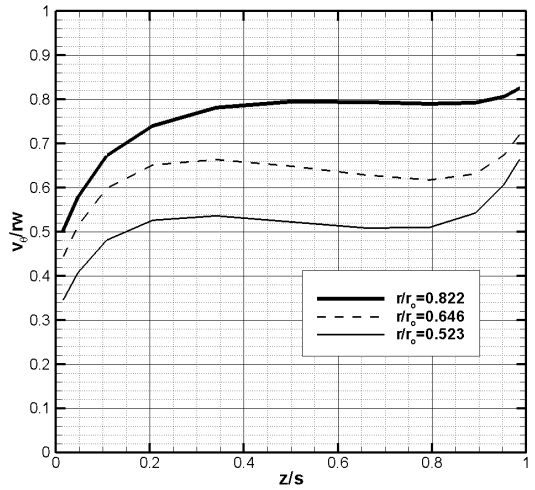

Figure E 8 β_θ plot of the case w/ 3.17mm back clearance at 28 liter/sec flow rate w/o balance holes

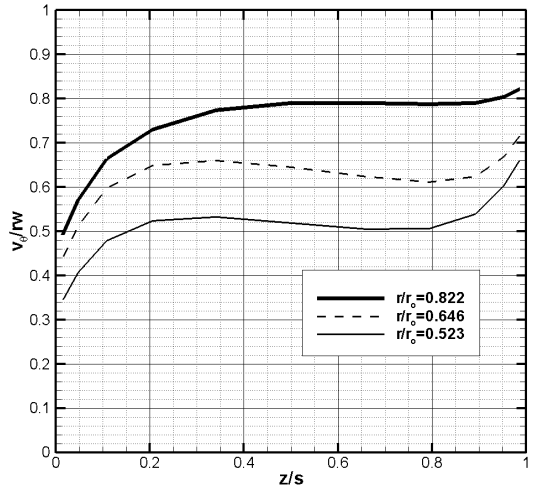

Figure E 9 β_θ plot of the case w/ 3.17mm back clearance at 31 liter/sec flow rate w/o balance holes

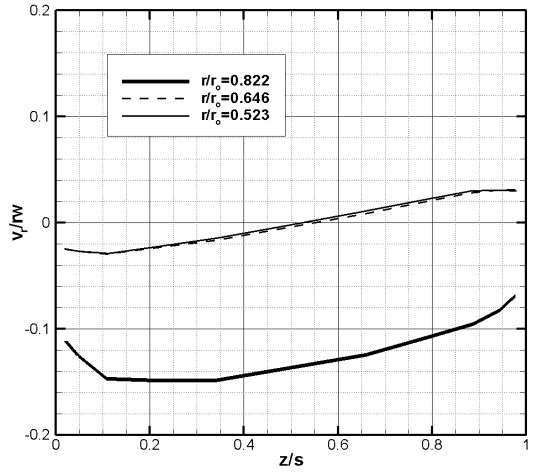

Figure E 10 β_r plot of the case w/ 0.91mm back clearance at 25 liter/sec flow rate w/o balance holes

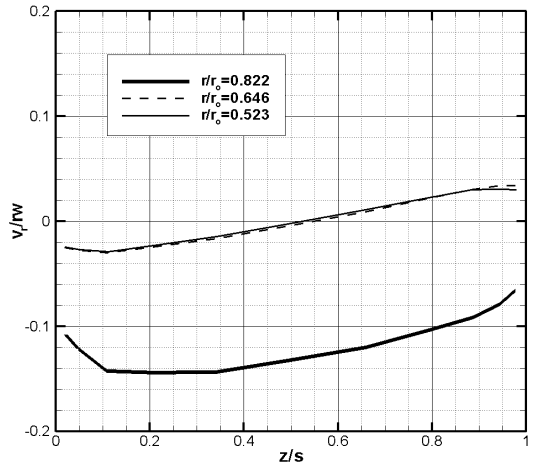

Figure E 11 β_r plot of the case w/ 0.91mm back clearance at 28 liter/sec flow rate w/o balance holes

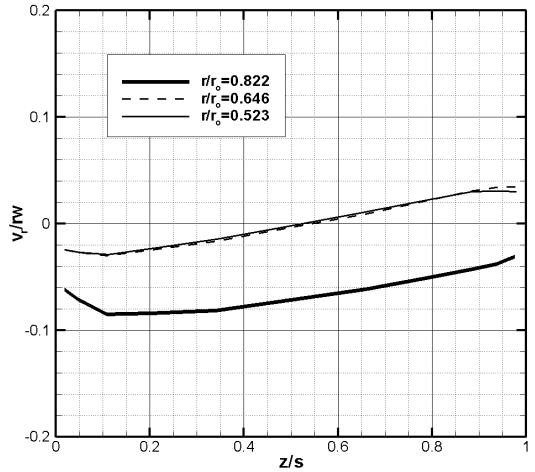

Figure E 12 β_r plot of the case w/ 0.91mm back clearance at 31 liter/sec flow rate w/o balance holes

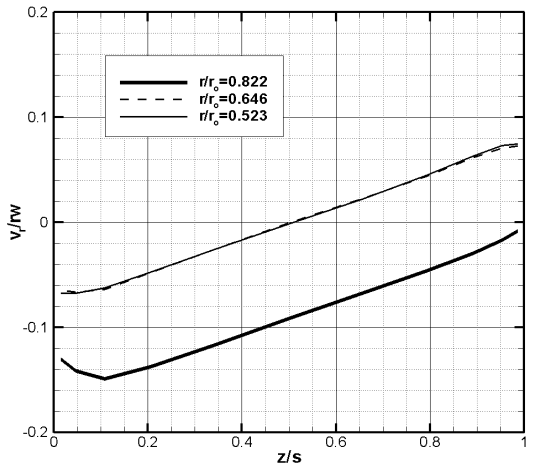

Figure E 13 β_r plot of the case w/ 1.87mm back clearance at 25 liter/sec flow rate w/o balance holes

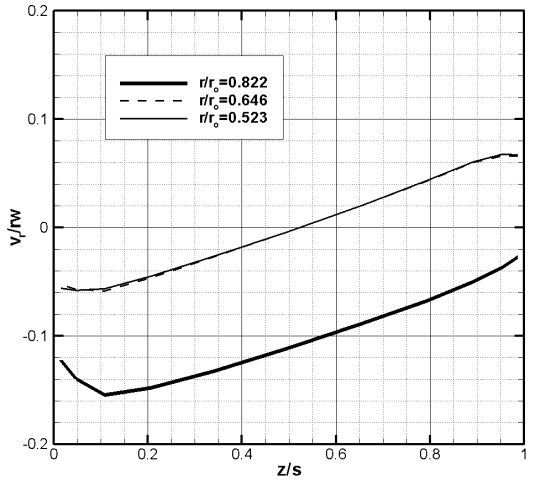

Figure E 14 β_r plot of the case w/ 1.87mm back clearance at 28 liter/sec flow rate w/o balance holes

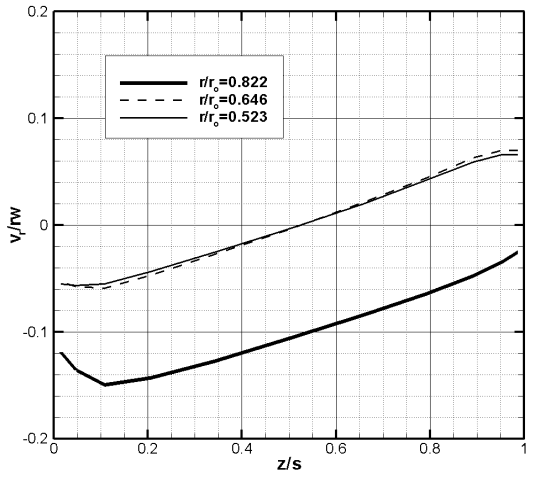

Figure E 15 β_r plot of the case w/ 1.87mm back clearance at 31 liter/sec flow rate w/o balance holes

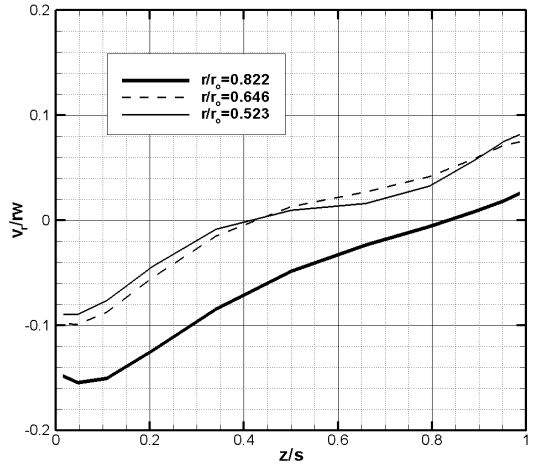

Figure E 16 β_r plot of the case w/ 3.17mm back clearance at 25 liter/sec flow rate w/o balance holes

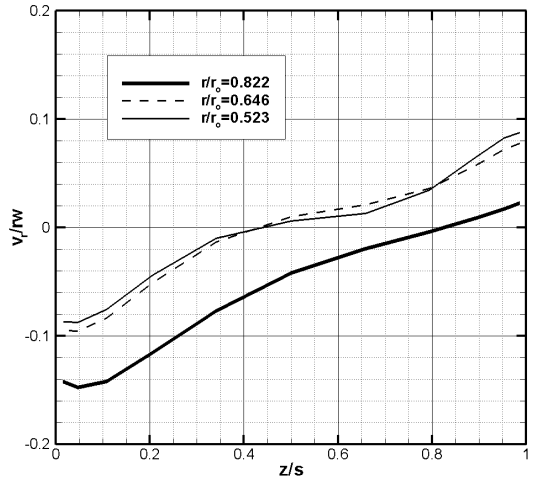

Figure E 17 β_r plot of the case w/ 3.17mm back clearance at 28 liter/sec flow rate w/o balance holes

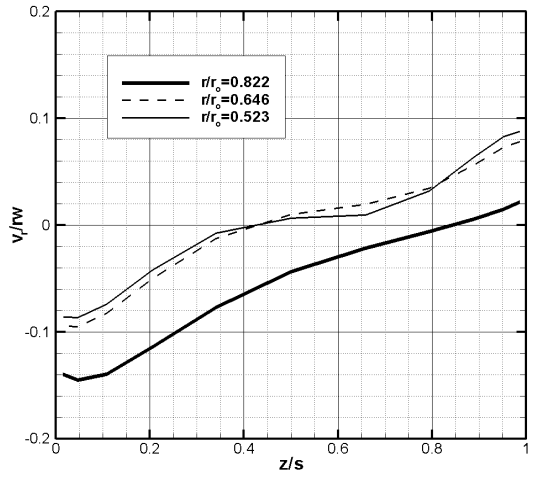

Figure E 18 β_r plot of the case w/ 3.17mm back clearance at 31 liter/sec flow rate w/o balance holes

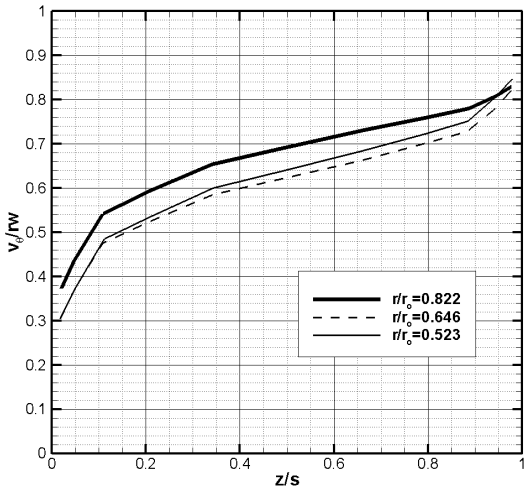

Figure E 19 β_θ plot of the case w/ 0.91mm back clearance at 25 liter/sec flow rate w/ balance holes

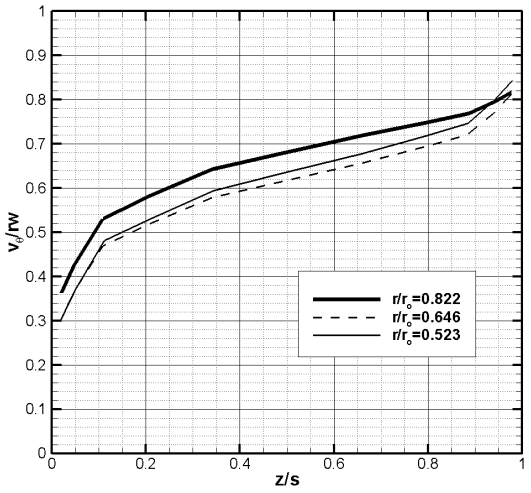

Figure E 20 β_θ plot of the case w/ 0.91mm back clearance at 28 liter/sec flow rate w/ balance holes

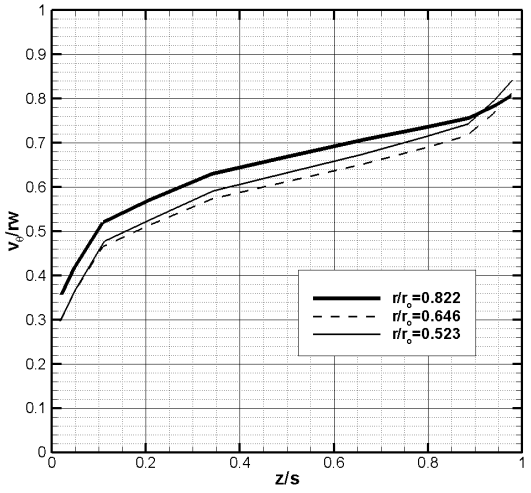

Figure E 21 β_θ plot of the case w/ 0.91mm back clearance at 31 liter/sec flow rate w/ balance holes

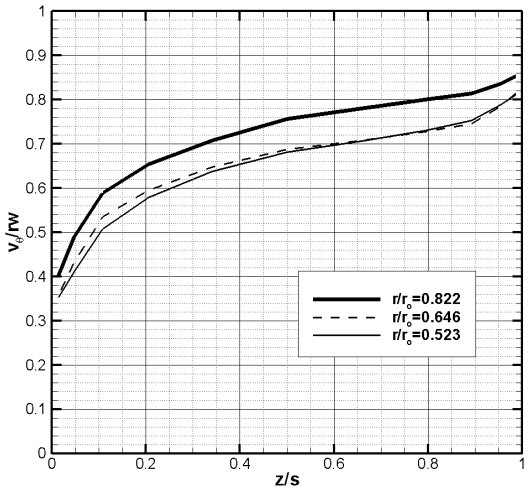

Figure E 22 β_θ plot of the case w/ 1.87mm back clearance at 25 liter/sec flow rate w/ balance holes

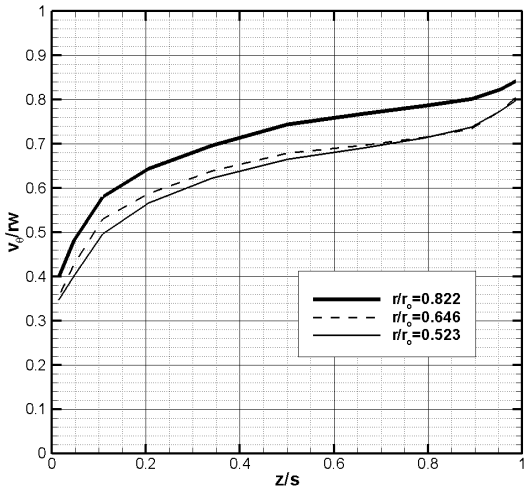

Figure E 23 β_θ plot of the case w/ 1.87mm back clearance at 28 liter/sec flow rate w/ balance holes

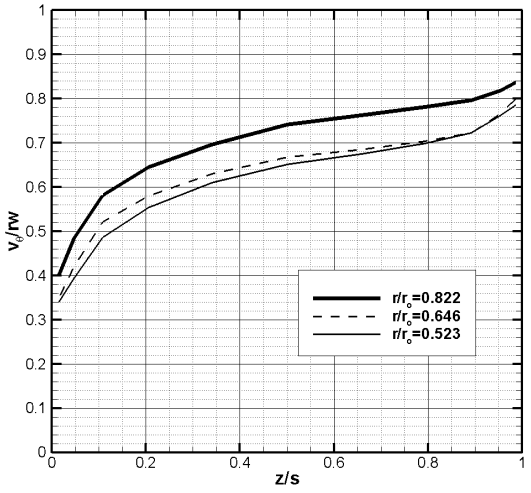

Figure E 24 β_θ plot of the case w/ 1.87mm back clearance at 31 liter/sec flow rate w/ balance holes

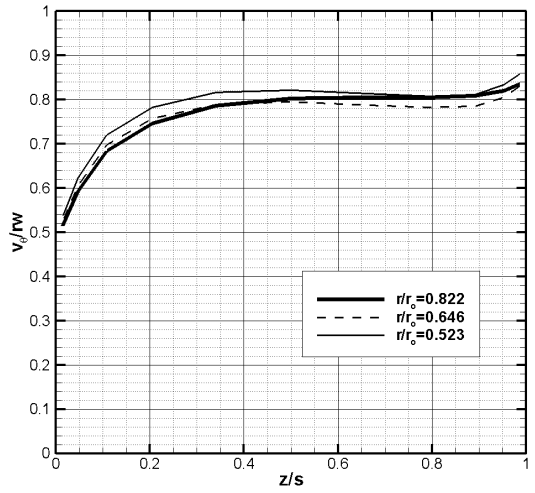

Figure E 25 β_θ plot of the case w/ 3.17mm back clearance at 25 liter/sec flow rate w/ balance holes

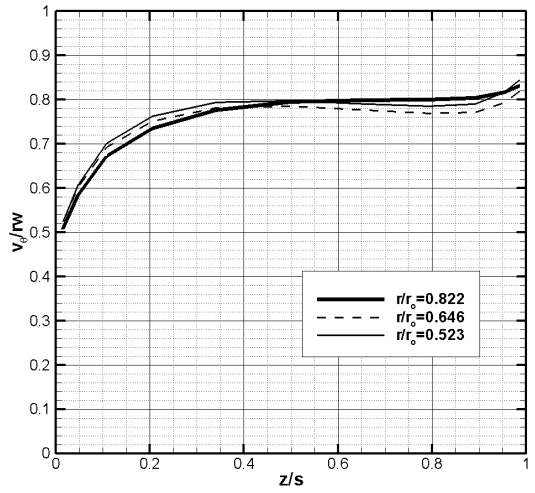

Figure E 26 β_θ plot of the case w/ 3.17mm back clearance at 28 liter/sec flow rate w/ balance holes

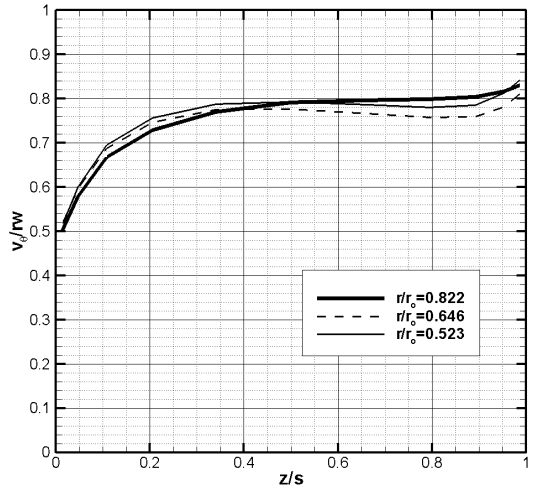

Figure E 27 β_θ plot of the case w/ 3.17mm back clearance at 31 liter/sec flow rate w/ balance holes

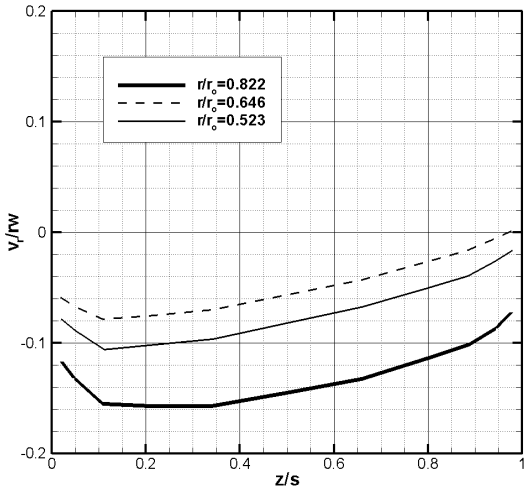

Figure E 28 β_r plot of the case w/ 0.91mm back clearance at 25 liter/sec flow rate w/ balance holes

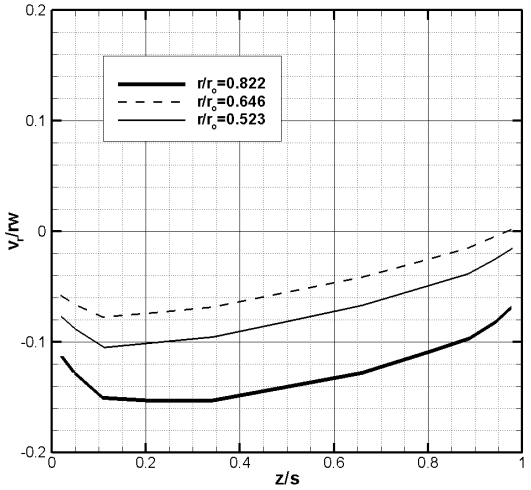

Figure E 29 β_r plot of the case w/ 0.91mm back clearance at 28 liter/sec flow rate w/ balance holes

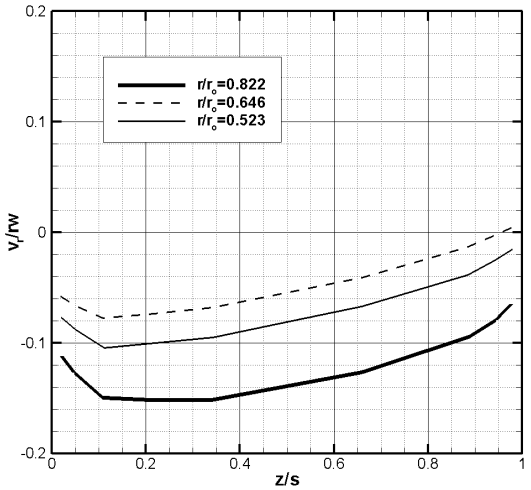

Figure E 30 β_r plot of the case w/ 0.91mm back clearance at 31 liter/sec flow rate w/ balance holes

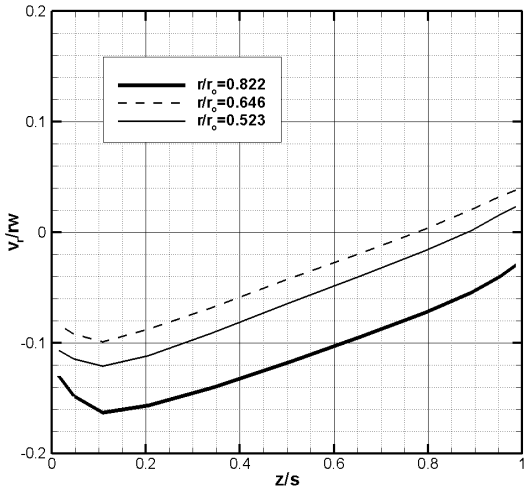

Figure E 31 β_r plot of the case w/ 1.87mm back clearance at 25 liter/sec flow rate w/ balance holes

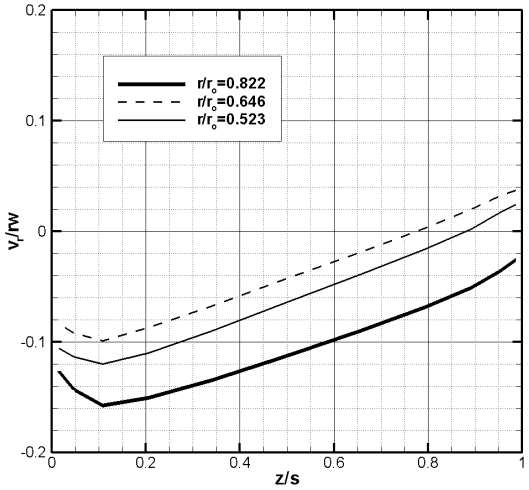

Figure E 32 β_r plot of the case w/ 1.87mm back clearance at 28 liter/sec flow rate w/ balance holes

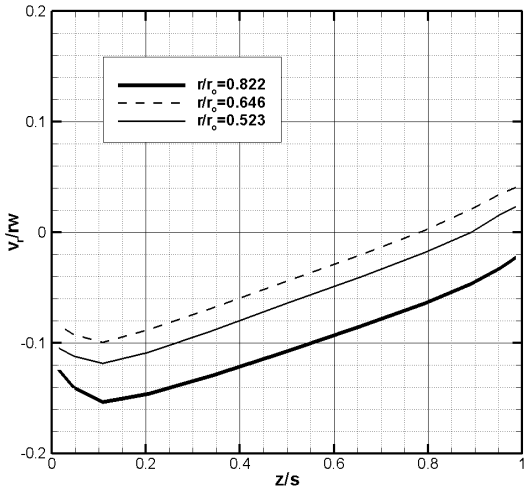

Figure E 33 β_r plot of the case w/ 1.87mm back clearance at 31 liter/sec flow rate w/ balance holes

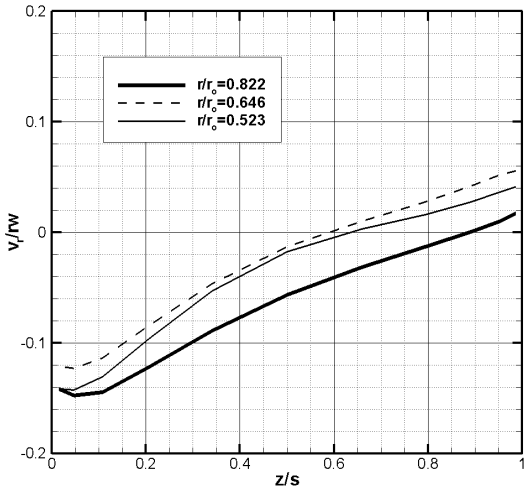

Figure E 34 β_r plot of the case w/ 3.17mm back clearance at 25 liter/sec flow rate w/ balance holes

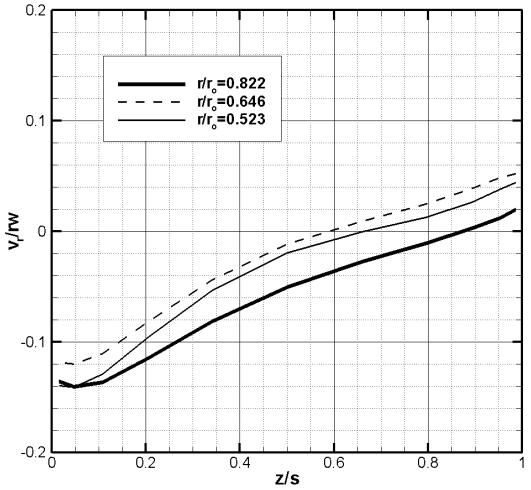

Figure E 35 β_r plot of the case w/ 3.17mm back clearance at 28 liter/sec flow rate w/ balance holes

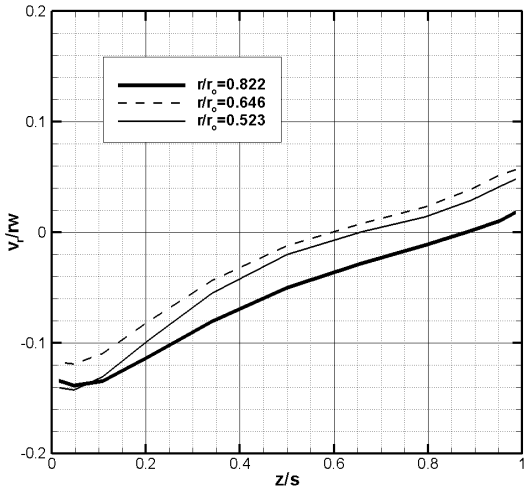

Figure E 36 β_r plot of the case w/ 3.17mm back clearance at 31 liter/sec flow rate w/ balance holes

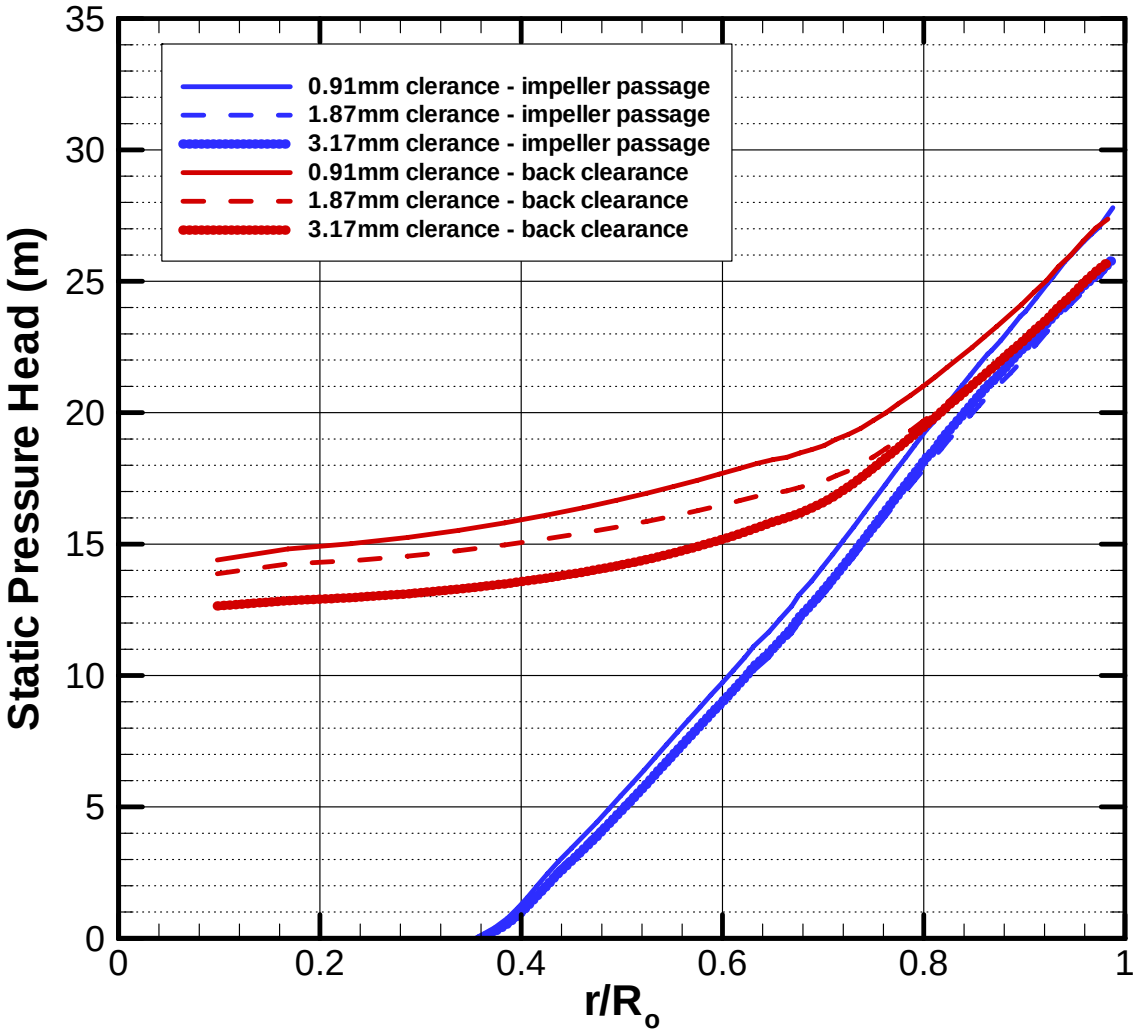

Figure E 37 The static pressure head distribution of the cases without balance holes at 31 liter/sec flow rate

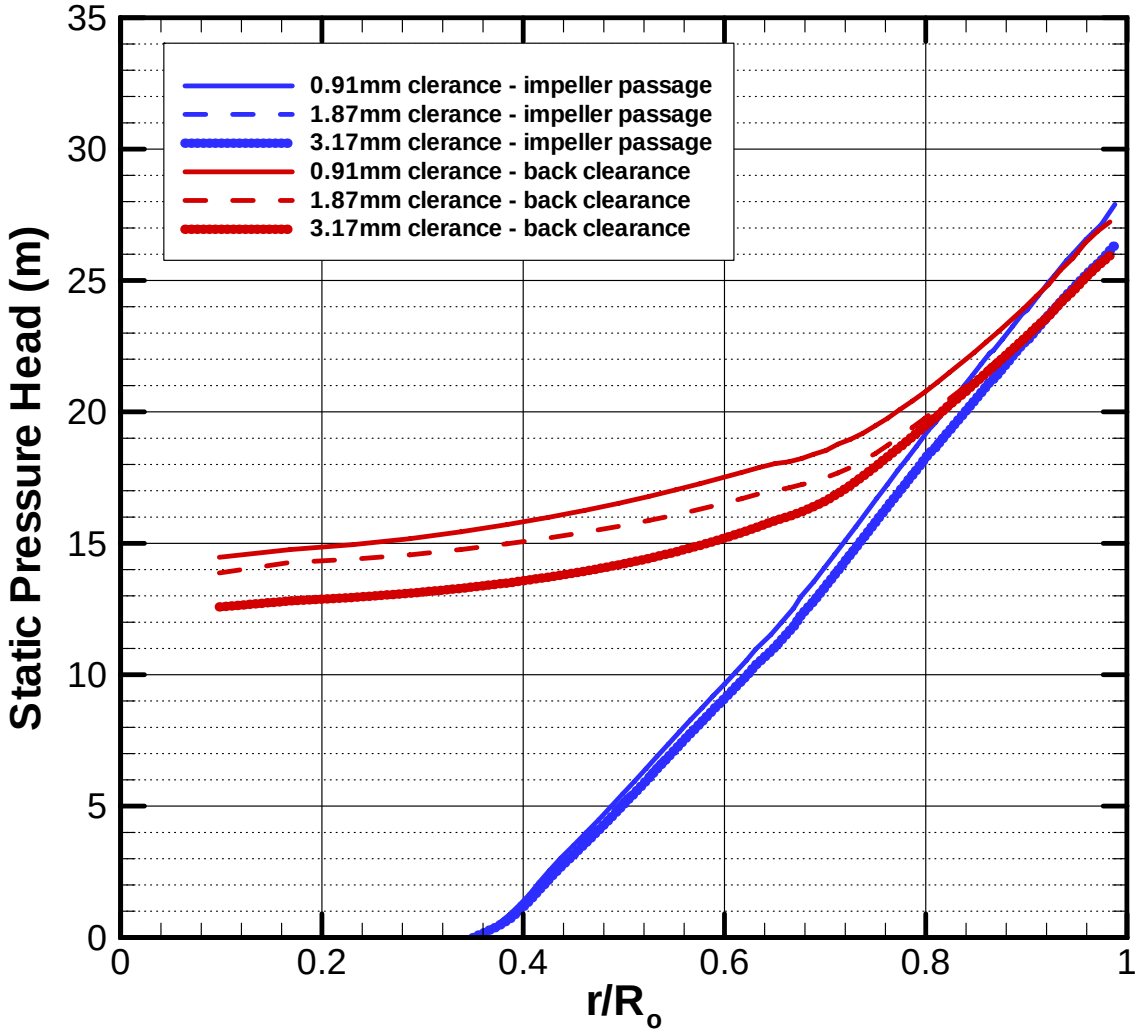

Figure E 38 The static pressure head distribution of the cases without balance holes at 28 liter/sec flow rate

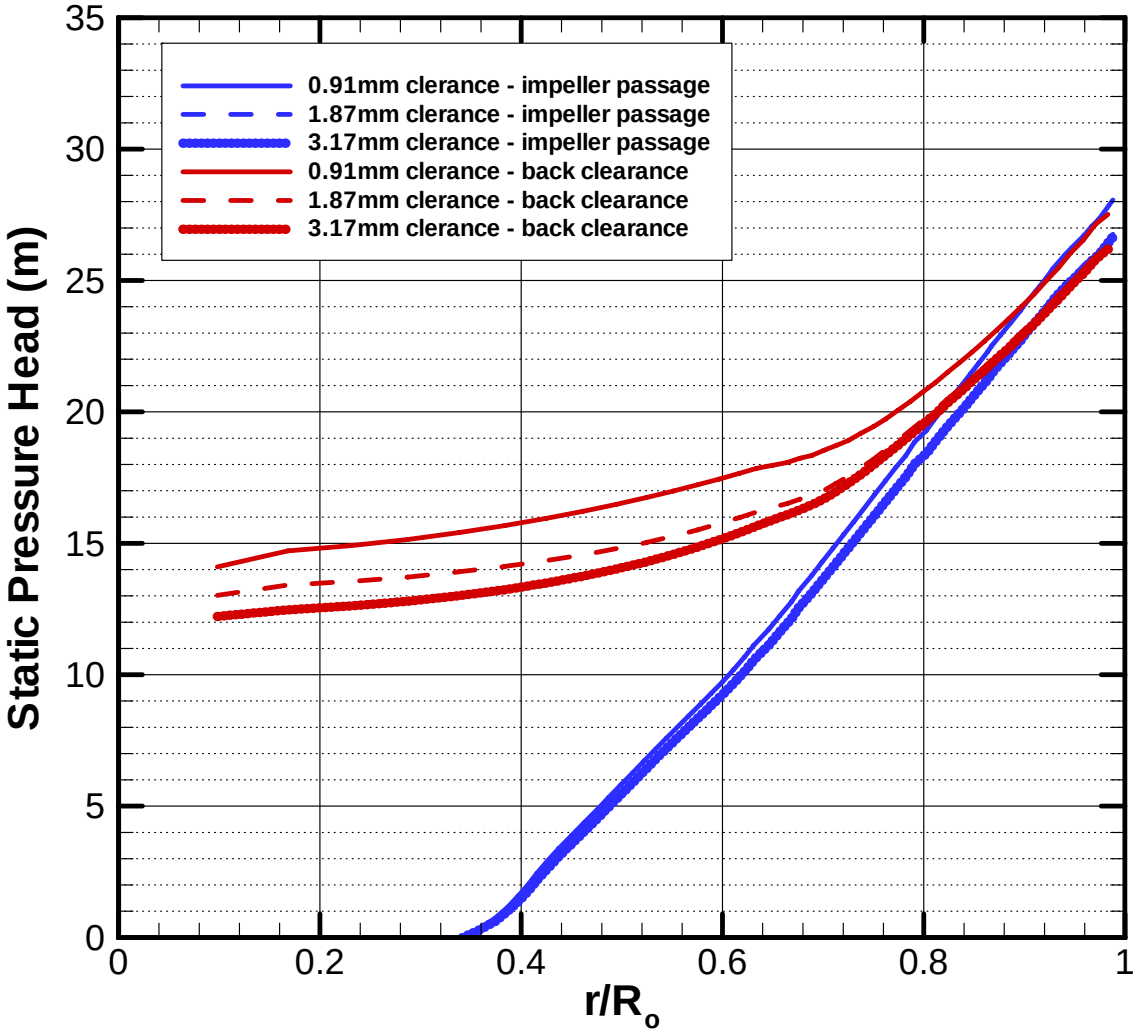

Figure E 39 The static pressure head distribution of the cases without balance holes at 25 liter/sec flow rate

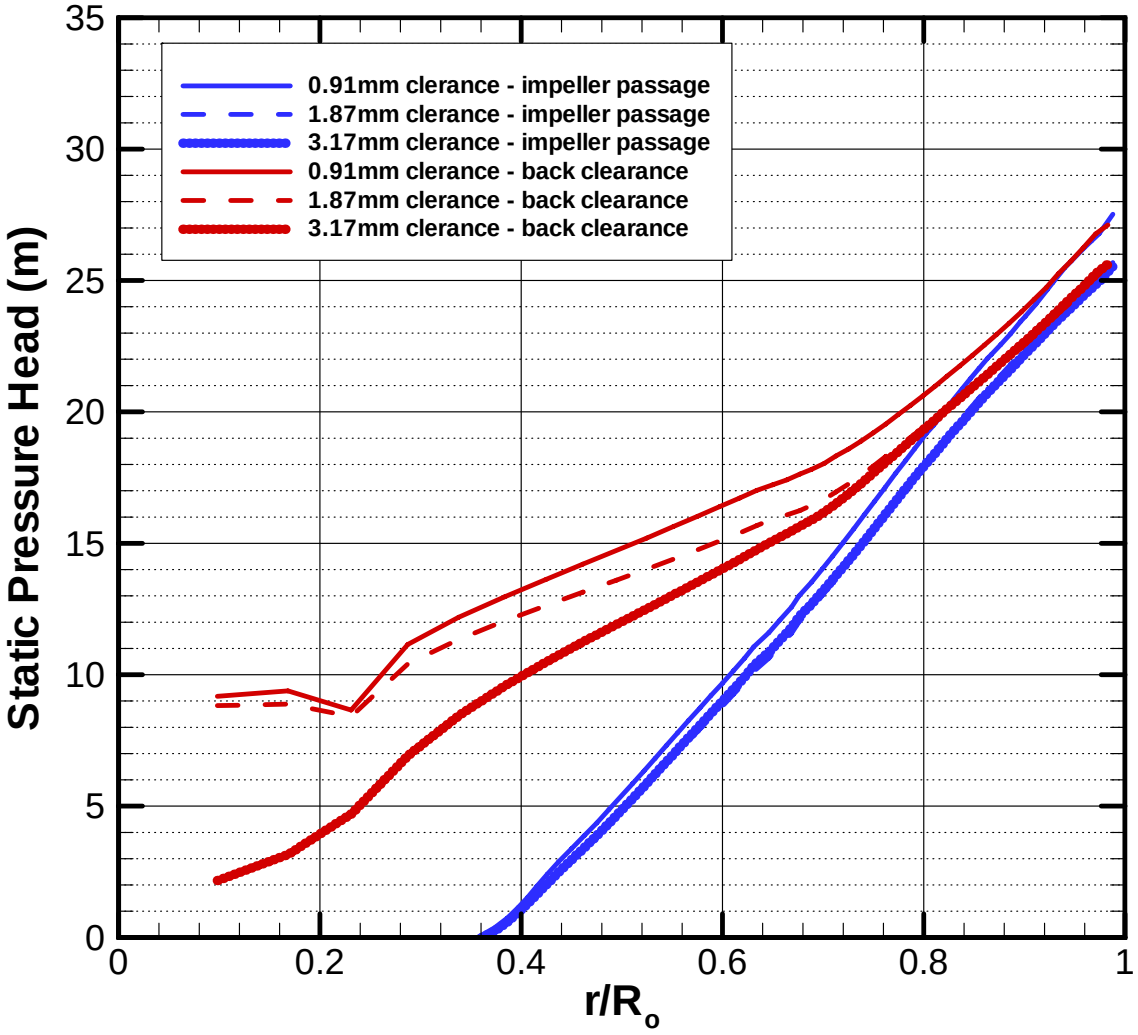

Figure E 40 The static pressure head distribution of the cases with balance holes at 31 liter/sec flow rate

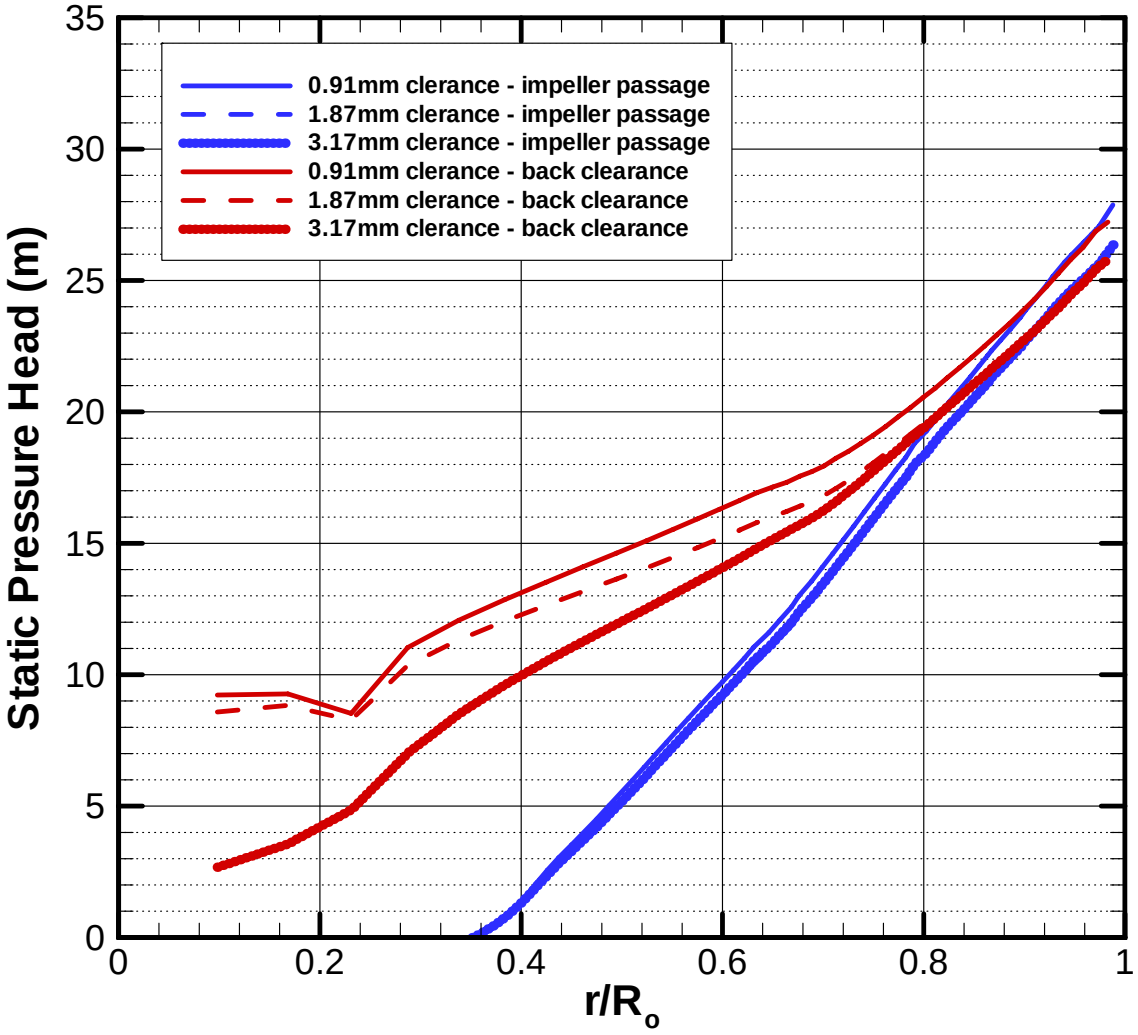

Figure E 41 The static pressure head distribution of the cases with balance holes at 28 liter/sec flow rate

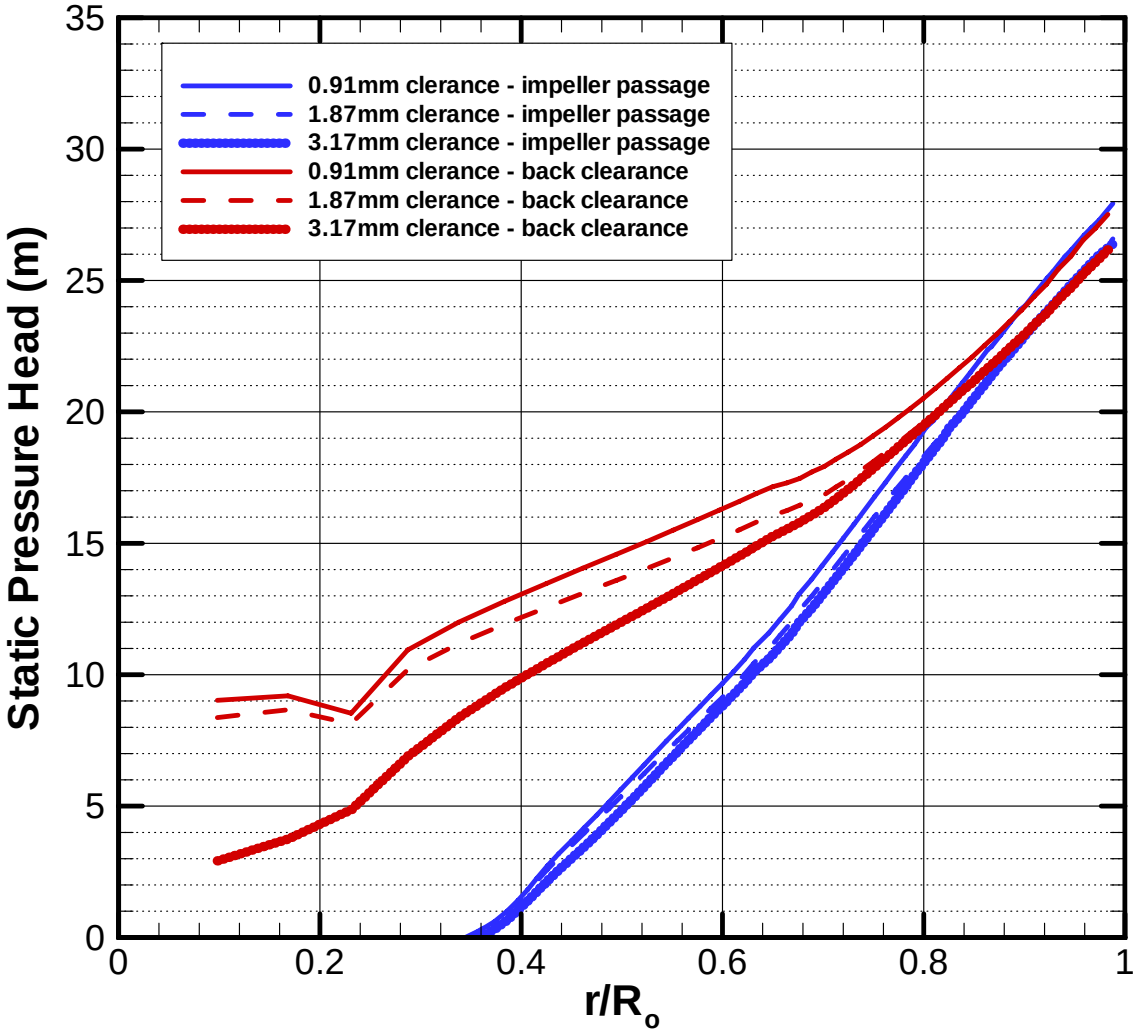

Figure E 42 The static pressure head distribution of the cases with balance holes at 25 liter/sec flow rate

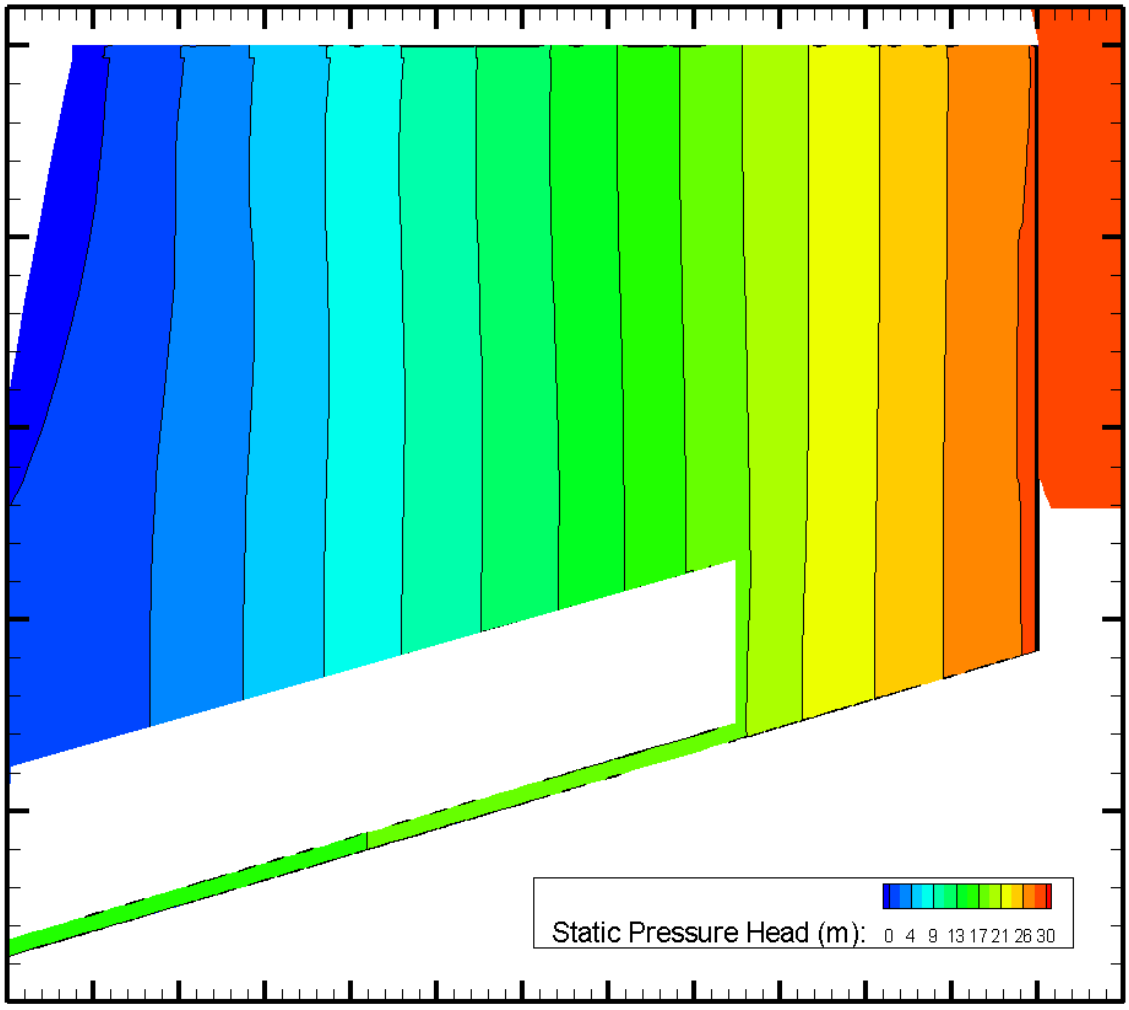

Figure E 43 Static pressure head contour plot of the cross-section of the impeller with 0.91mm back clearance at 31 liter/sec flow rate

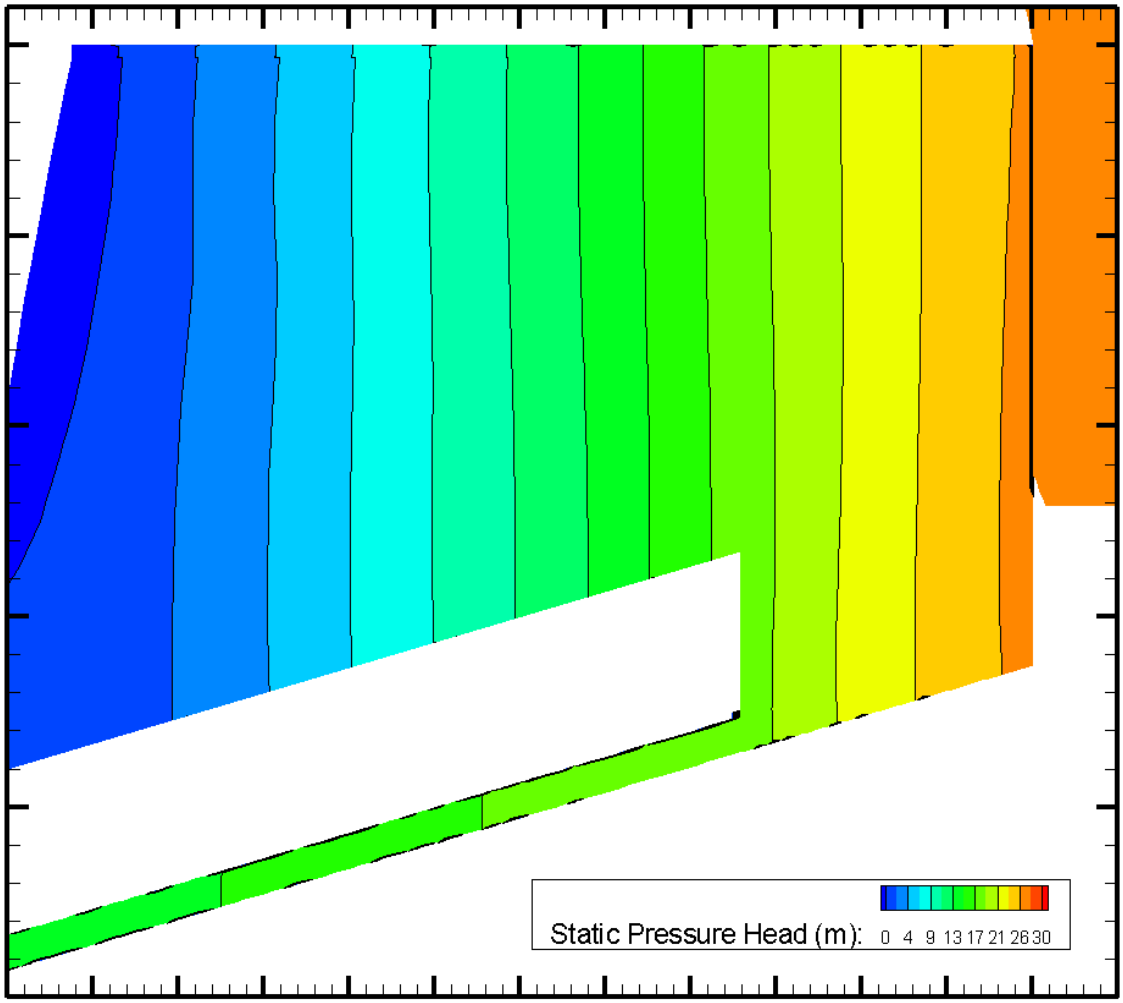

Figure E 44 Static pressure head contour plot of the cross-section of the impeller with 1.87mm back clearance at 31 liter/sec flow rate

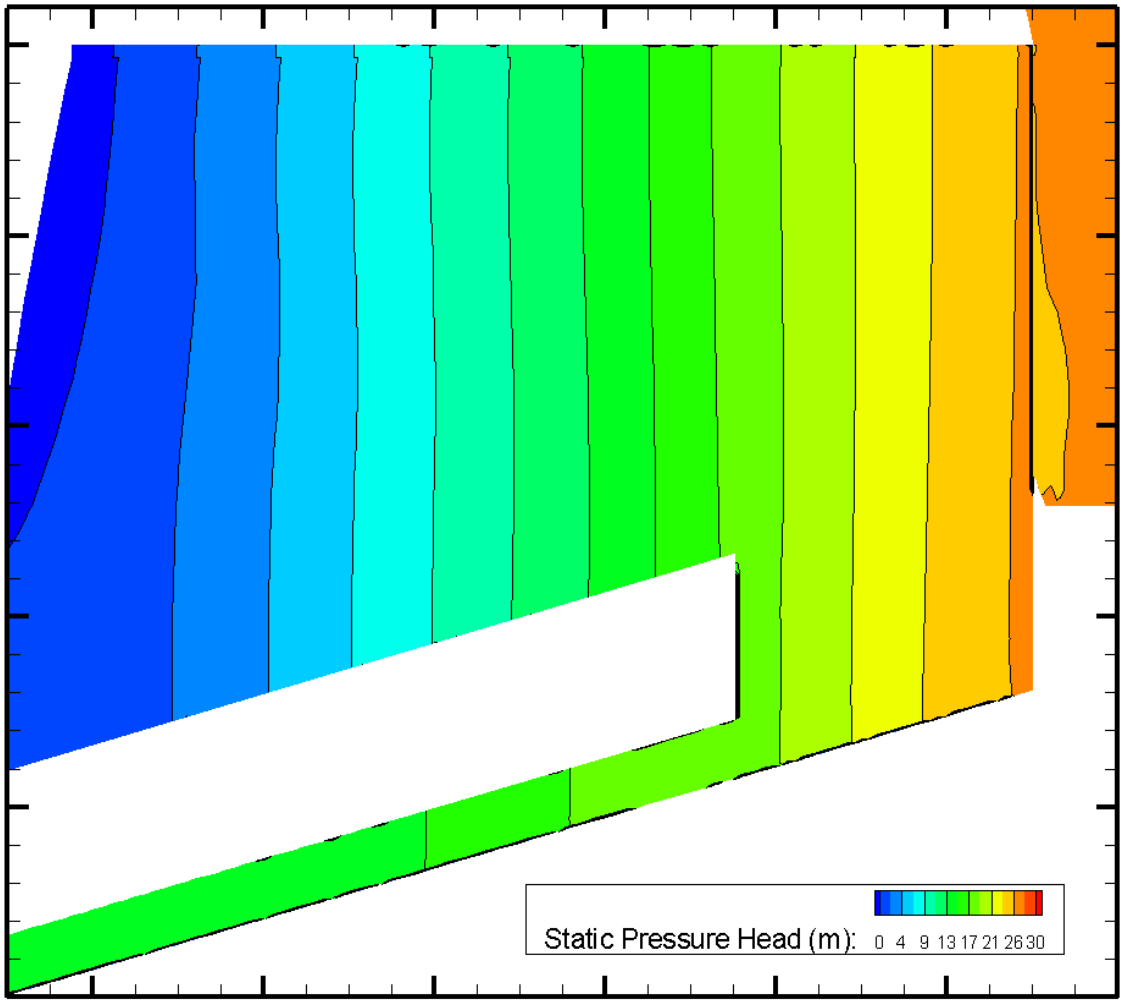

Figure E 45 Static pressure head contour plot of the cross-section of the impeller with 3.17mm back clearance at 31 liter/sec flow rate.00

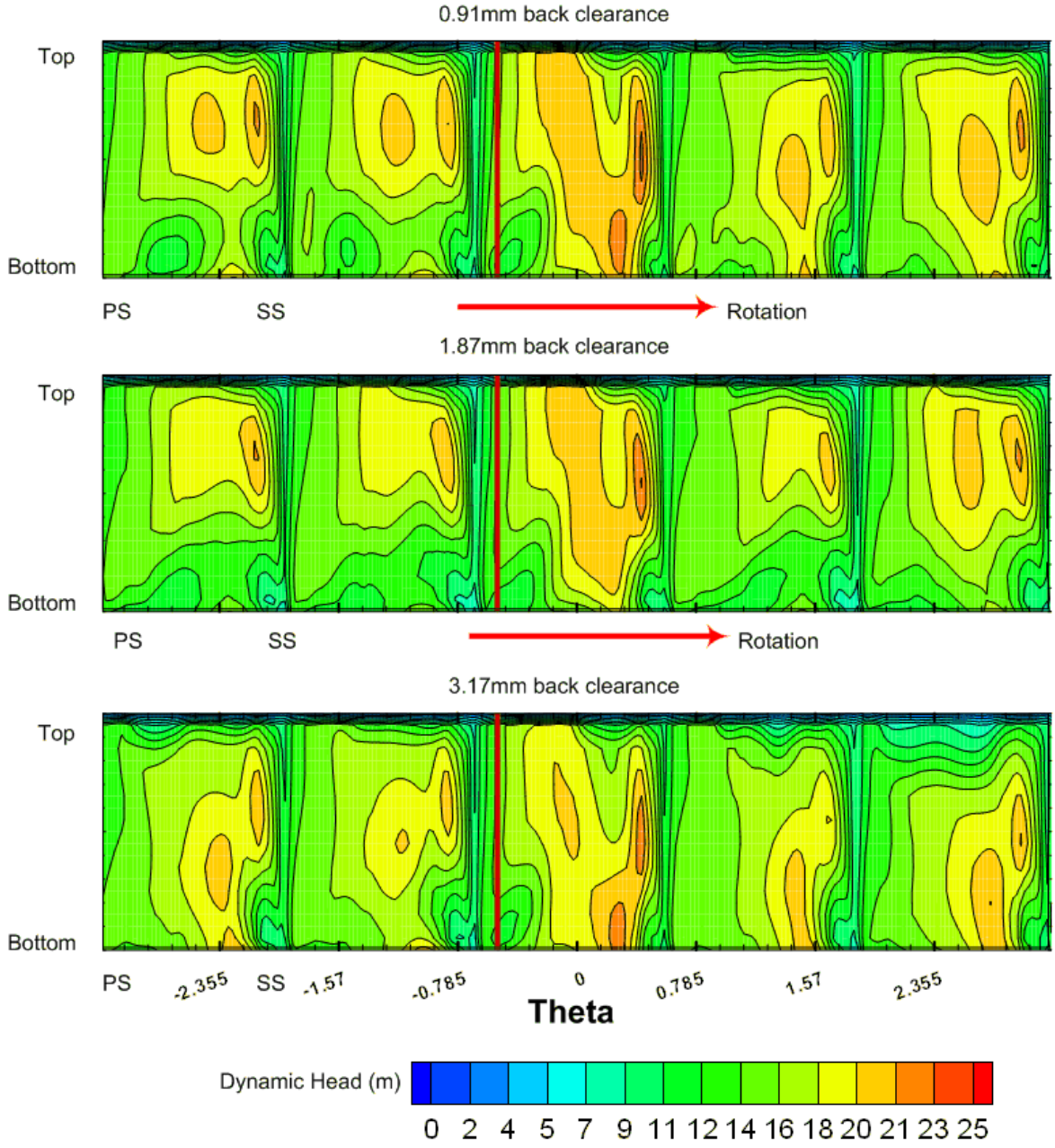

Figure E 46 The contour plots of dynamic head at the exit of the impeller without the balance holes at 31 liter/sec

(Note: Red vertical line is the location where the cutwater is located)

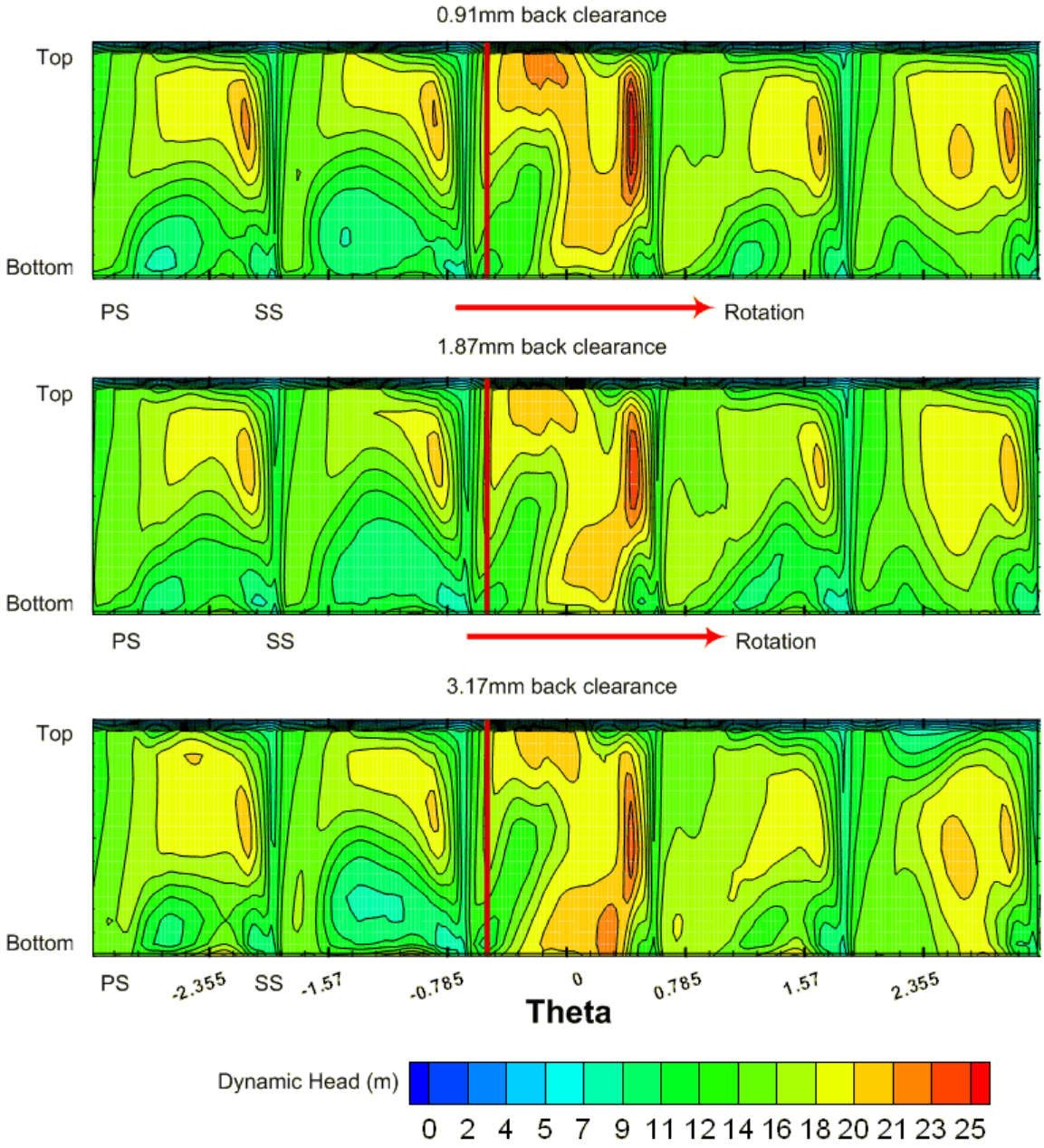

Figure E 47 The contour plots of dynamic head at the exit of the impeller without the balance holes at 28 liter/sec

(Note: Red vertical line is the location where the cutwater is located)

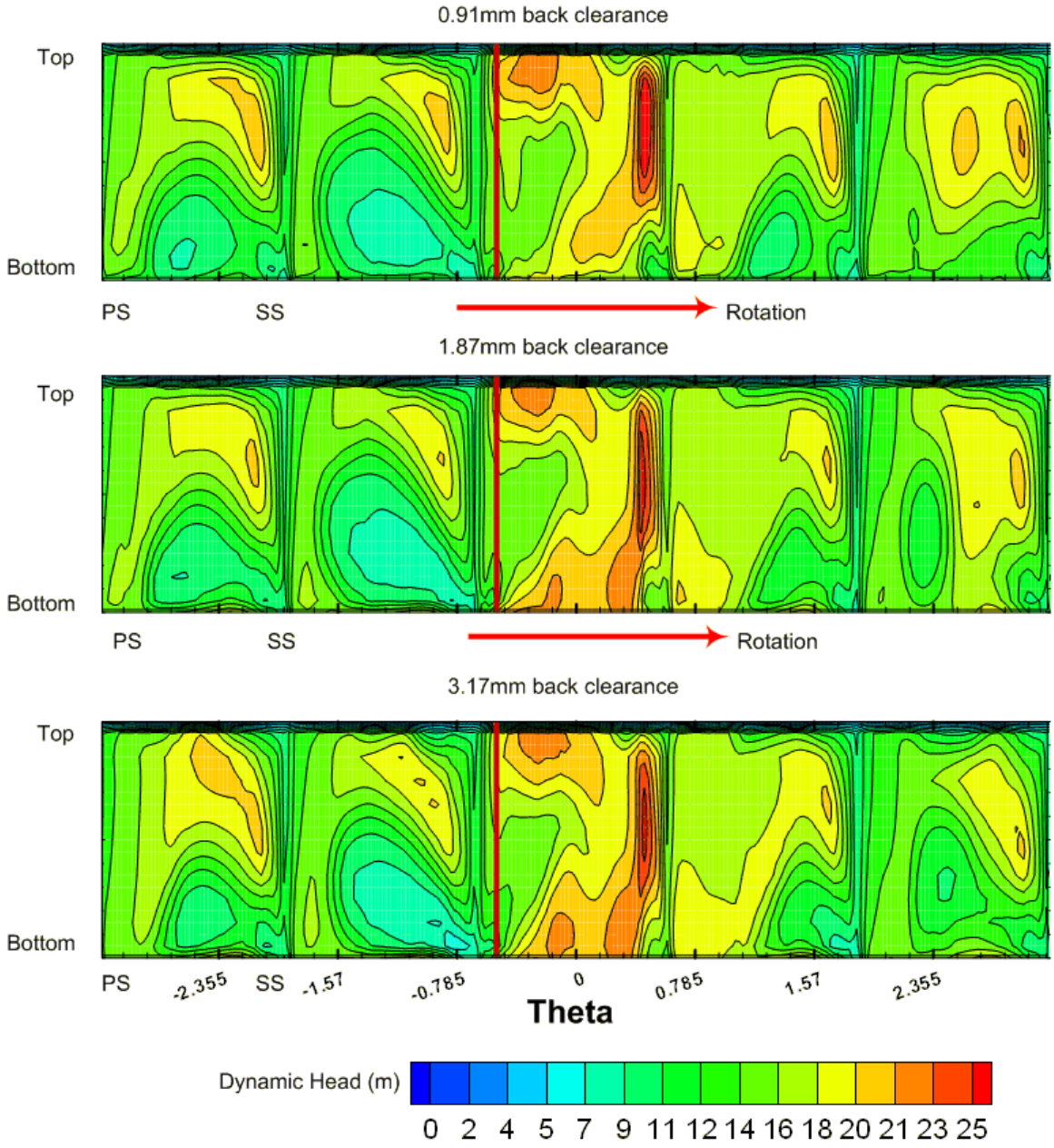

Figure E 48 The contour plots of dynamic head at the exit of the impeller without the balance holes at 25 liter/sec

(Note: Red vertical line is the location where the cutwater is located)

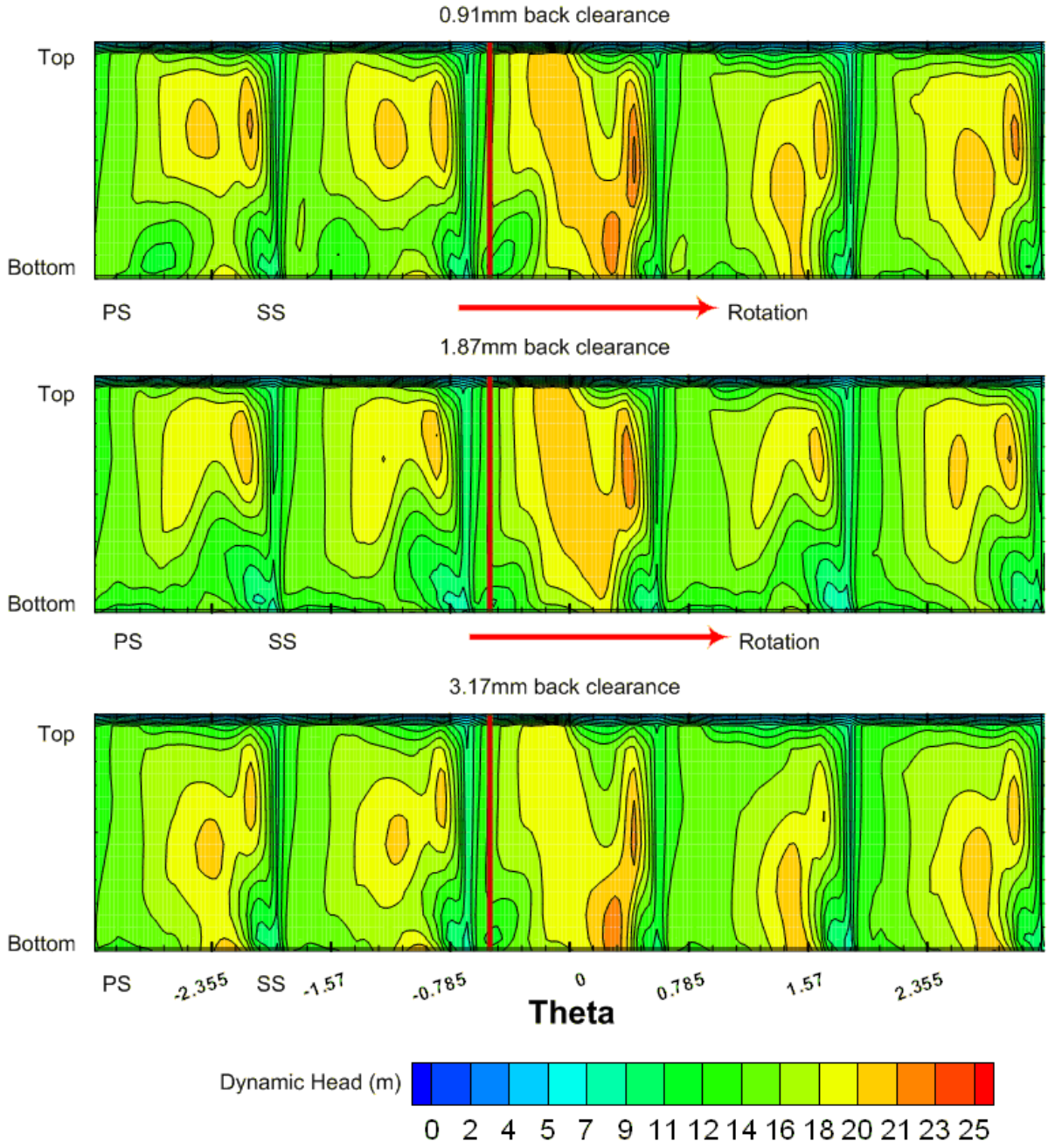

Figure E 49 The contour plots of dynamic head at the exit of the impeller with the balance holes at 31 liter/sec

(Note: Red vertical line is the location where the cutwater is located)

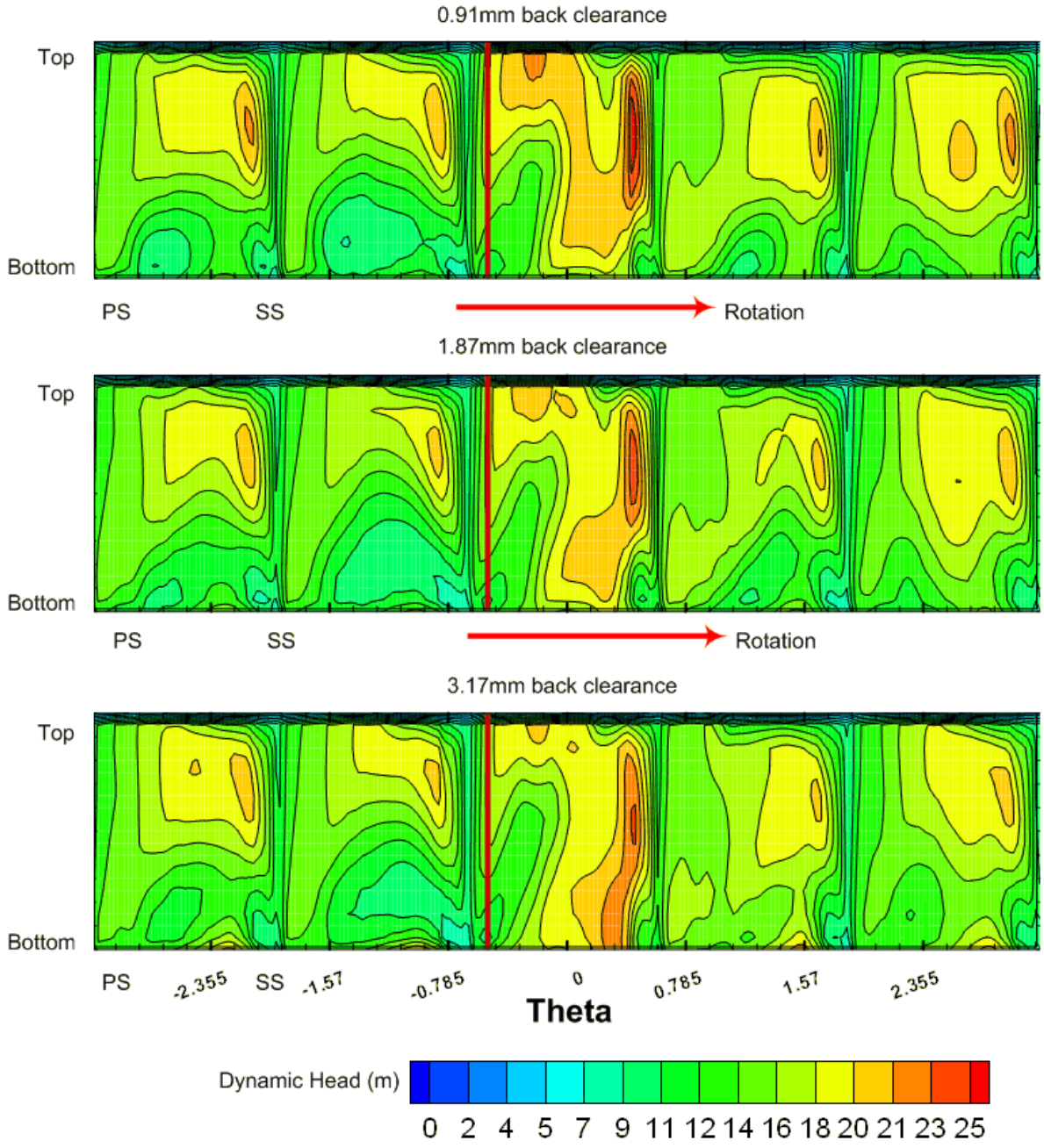

Figure E 50 The contour plots of dynamic head at the exit of the impeller with the balance holes at 28 liter/sec

(Note: Red vertical line is the location where the cutwater is located)

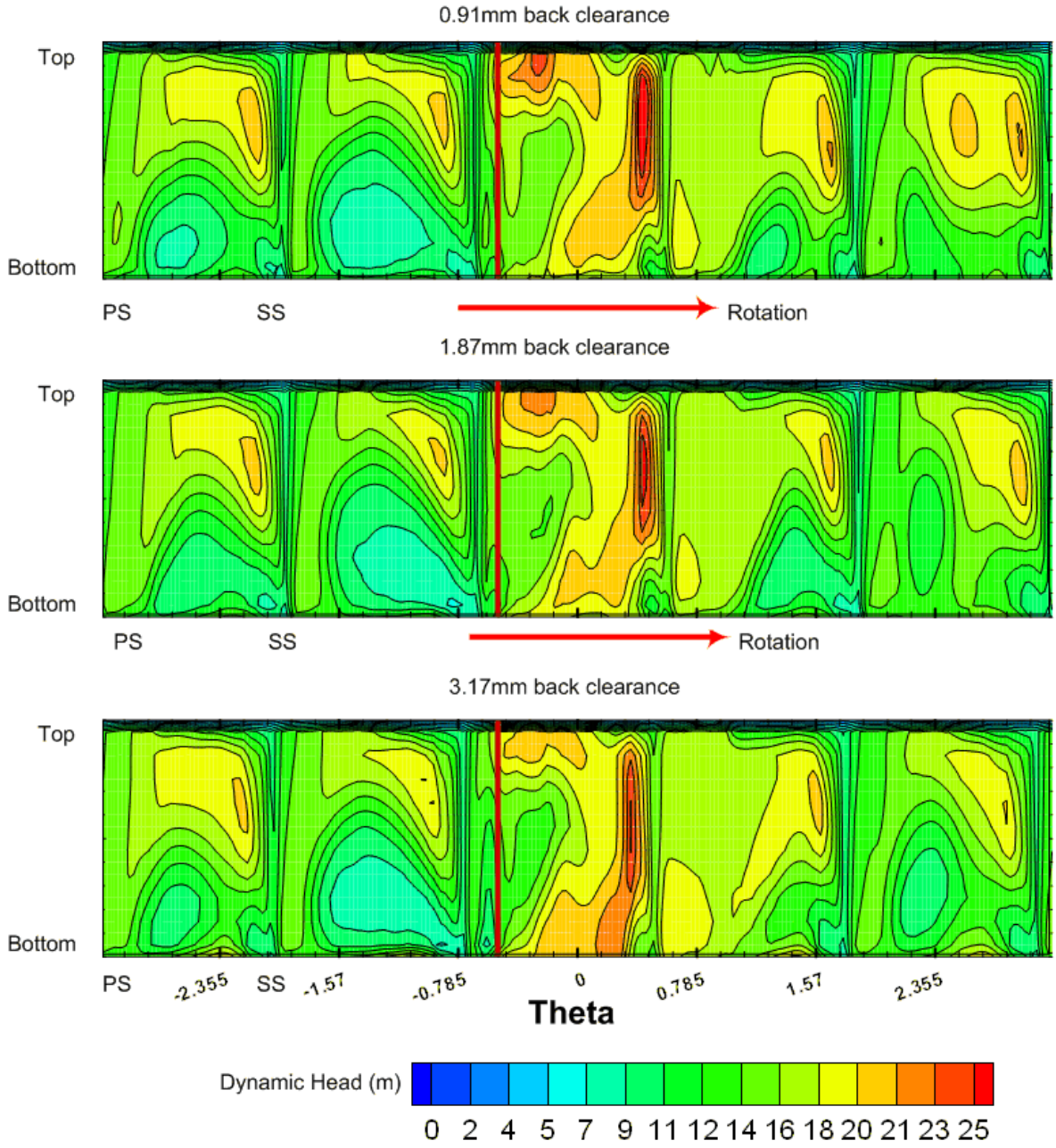

Figure E 51 The contour plots of dynamic head at the exit of the impeller with the balance holes at 25 liter/sec

(Note: Red vertical line is the location where the cutwater is located)

VITA

Sang Hyun Park is the son of Kil Yong Park and Eun Hee Cho. He was born in Seoul, Republic of Korea. He has a brother, Sang June. He graduated from Hwa Gok High School in 1995. In 1999, he received his Bachelor of Science degree in mechanical engineering from Yonsei University, Republic of Korea. In 2004, He received his Master of Science degree in mechanical engineering from Texas A&M University. His email address is parxang@hotmail.com. He may be reached at Sulzer Pumps Houston, 800 Koomey Rd., Brookshire, TX 77423.